Monitoring supraglacial hydrology on the Greenland Ice Sheet using remote sensing and machine learning

Emily Glen, BSc, MSc (Res)

Lancaster Environment Centre

Lancaster University

This thesis is submitted for the degree of *Doctor of Philosophy*

March 2025

Monitoring supraglacial hydrology on the Greenland Ice Sheet using remote sensing and machine learning

Emily Glen, BSc, MSc (Res)
Lancaster Environment Centre, Lancaster University
This thesis is submitted for the degree of *Doctor of Philosophy,* March 2025

Abstract

The Greenland Ice Sheet (GrIS) is experiencing accelerating surface melt rates, with supraglacial meltwater influencing ice dynamics, mass balance, and sea level rise. Yet key gaps remain in understanding the spatial and temporal evolution of supraglacial melt and hydrological features, especially for understudied features like slush. While traditional remote sensing methods are widely used, they often struggle to capture the complexity of these systems. Machine learning (ML) offers scalable, automated solutions suitable for large-scale or near-real-time monitoring, yet current applications remain limited by challenges in accuracy, generalisation, and training data availability. This thesis develops and applies satellite remote sensing and ML methodologies to improve the detection and mapping of supraglacial hydrology across the GrIS. In doing so, this thesis also produces new datasets that advance understanding of supraglacial meltwater distribution at ice-sheet scale, including detailed assessments of regional, interannual, and seasonal variability, with a focus on contrasting low and high melt years.

First, a comparative study of meltwater features in southwest Greenland during a low-melt year (2018) and a high-melt year (2019), using optical satellite imagery and threshold-based classification algorithms individually developed to delineate different components of the supraglacial hydrological system (i.e., supraglacial lakes, channels, and slush), reveals a substantial increase in meltwater extent, connectivity, and elevation in 2019. Slush emerges as a dominant yet previously under-recognized component of the supraglacial hydrological system. Second, a near-decadal, ice-sheet-wide analysis of slush from 2016 to 2024 using Sentinel-2 optical imagery and ML classification demonstrates that slush – underrepresented in existing meltwater inventories – is widespread, but highly variable, across regions and years. Third, to evaluate and optimise large-scale, cloud-based meltwater mapping, a systematic assessment of seven ML classifiers within Google Earth Engine identifies Random Forest as the most transferable across space and time, while Gradient-Boosted Decision Trees achieves the highest overall accuracy but are more sensitive to mislabelled training data.

Together, the findings in this thesis advance supraglacial hydrology monitoring by (1) establishing slush as an important component of the meltwater system, (2) revealing pronounced interannual variability and climate sensitivity in meltwater dynamics, (3) promoting a more holistic view of supraglacial hydrology as a continuum of interconnected features, and (4) evaluating the utility and scalability of various cloud-based ML approaches for large-scale meltwater mapping. These contributions enhance our understanding of meltwater distribution and dynamics on the GrIS and improve our capacity to monitor all components of supraglacial hydrology, including slush, over large spatial and temporal scales. These findings also lay the groundwork for optimizing ML-based classification approaches, with future implications for long-term monitoring and for assessing the impact of supraglacial hydrology on ice sheet stability in a warming climate – not only on the GrIS, but also on the Antarctic Ice Sheet and mountain glaciers worldwide.

List of publications

The research presented in Chapter 3 is published in *The Cryosphere*:

> **Glen, E.,** Leeson, A., Banwell, A. F., Maddalena, J., Corr, D., Atkins, O., Noël, B., and McMillan, M.: A comparison of supraglacial meltwater features throughout contrasting melt seasons: southwest Greenland, The Cryosphere, 19, 1047–1066, https://doi.org/10.5194/tc-19-1047-2025, 2025

The research presented in Chapter 4 and Chapter 5 is prepared as manuscripts to be submitted:

> **Glen, E.,** Banwell, A. F., Miles, K., Dell, R., McMillan, M., Maddalena, J., and Leeson, A. A. (2025). Supervised classification of slush on the Greenland Ice Sheet using Sentinel-2 satellite imagery. Intended for submission to JGR Earth Surface.

> **Glen, E.,** McMillan, M., Banwell, A. F., Parkes, D., Corr, D., and Leeson, A. A. (2025). Assessing the performance of machine learning algorithms in Google Earth Engine for cloud-based supraglacial meltwater feature classification on the Greenland Ice Sheet. Intended for submission to J Glaciology.

I am a named author on the following two papers. While this work is not included in the thesis, it played a fundamental role in shaping its direction and development:

> Corr, D., Zhang, C., McMillan, M., Leeson, A., **Glen, E**., Maddalena, J., Melling, L. (in preparation). Supraglacial hydrology coverage has increased on the Greenland ice sheet over the last decade. Intended for submission to Nature Climate Change.

> Melling, L., Leeson, A., McMillan, M., Maddalena, J., Bowling, J., **Glen, E**., Sandberg Sørensen, L., Winstrup, M., and Lørup Arildsen, R.: Evaluation of satellite methods for estimating supraglacial lake depth in southwest Greenland, The Cryosphere, 18, 543–558, https://doi.org/10.5194/tc-18-543-2024, 2024.

Acknowledgements

First and foremost, I extend my deepest gratitude to my supervisors, Alison Banwell, Amber Leeson, Mal McMillan, Katie Miles, and Jennifer Maddalena. Your guidance, expertise, and patience have been invaluable throughout this journey. A special thanks goes to Ali, who hosted me during my research trip to the University of Colorado, Boulder, and to Jenny, whose unwavering emotional support meant more than I can put into words.

This research was made possible by funding from the Engineering and Physical Sciences Research Council (EPSRC), the European Space Agency (ESA), and the Centre for Polar Observation and Modelling (CPOM), and I am incredibly grateful for the opportunities this made available.

Thank you to the Lancaster Glaciology Group–past and present members–you have been an incredible source of encouragement and have made academic life more enjoyable. A special mention goes to the LEC505 office girls–your friendship, support, and those shared bottles of wine (especially in Italy) made the hard days easier and the good days even better.

To my friends and family, who are one and the same–thank you for your endless support, patience, and encouragement. To Courtney and Arran, my best friends and constants in life, always there with unwavering support, laughter, and a good dose of reality when needed–life wouldn't be the same without you. To *the wains*, Nora and Goldie, who arrived during my PhD and brought plenty of joy (and just the right amount of chaos). To Jemma, my longest friend, who has been there through every phase of life–your ability to turn even the most stressful moments into something to laugh about has meant everything to me. To Karla, my soul mate in adventure–from exploring Alaska at the International Summer School in Glaciology to sharing whiskey in Reykjavik–I couldn't have asked for a better friend to navigate this PhD journey with. And to Rachel, my rock since undergrad, my biggest cheerleader, and the person who never let me doubt myself–your company throughout thesis writing made the process infinitely more bearable.

To my dad, my greatest supporter throughout this journey, whose encouragement never wavered and whose belief in me kept me going. To my mum, endlessly proud and always on the other end of the phone with encouragement–whether I needed it or not. To my step-mum Angela, whose sense of humour and steady support have lightened more than a few difficult days along the way. To my wee brother Marc, always

by my side and turning up wherever I go–whether in Colorado, Rome, or just when I need him most. To my wee sister Rachael, who is always checking in and never fails to make me laugh. And to my in-laws, Audrey and Jim, for your kindness and constant encouragement throughout this journey.

To Dusty and Ozzy, who brought comfort and calm through even the busiest of PhD days and are deeply missed. To Pepper, my dedicated office mate, who spent countless work-from-home days offering silent judgment, occasional keyboard interference, and excellent company through the long hours of writing.

To my gran, who would have been so proud.

And finally, to Ross, my husband–thank you for your endless patience, love, and unwavering support. For always knowing how to lift me up, for celebrating the highs, carrying me through the lows, and making sure there was life beyond the PhD. I couldn’t have done this without you.

Author’s Declaration

I declare that the work presented in this thesis is, to the best of my knowledge and belief, original and my own. The material has not been submitted, either in whole or in part for the award of a higher degree at this or any other university.

One chapter of this thesis has been published in a peer-reviewed journal. This section is clearly identified within the thesis and fully integrated into its structure.

Where research was conducted collaboratively, my individual contributions are explicitly stated within the relevant chapters and have been confirmed by my supervisor.

This thesis does not exceed the maximum permitted word length of 80,000 words. An approximate total word count is: 60,376.

Signed: Emily Glen
Date: 27/03/2025

Abbreviations and acronyms

a.s.l.	Above Sea Level
AI	Artificial Intelligence
AIS	Antarctic Ice Sheet
ASTER	Advanced Spaceborne Thermal Emission and Reflection Radiometer
AVHRR	Advanced Very High-Resolution Radiometer
B	Band
CART	Classification and regression trees
CNN	Convolutional Neural Network
CW	Central West
DEM	Digital Elevation Model
ELA	Equilibrium-Line Altitude
EROS	Earth Resources Observation Science
ESA	European Space Agency
FASTER	Fully Automated Supraglacial lake Tracking at Enhanced Resolution
FN	False Negative
FP	False Positive
GBDT	Gradient Boosted Decision Trees
GBI	Greenland Blocking Index
GEE	Google Earth Engine
GInd	Greenness Index
GrIS	Greenland Ice Sheet
ICESat	Ice, Cloud, and land Elevation Satellite
IMBIE	Ice sheet Mass Balance Inter-comparison Exercise
IoU	Intersection over Union
IPCC	Intergovernmental Panel on Climate Change
IQR	interquartile range
ISMIP	The Ice Sheet Model Intercomparison for the Coupled Model Intercomparison
KNN	K-nearest neighbour
L8	Landsat 8
LIDAR	Laser Imaging, Detection, and Ranging
MD	Minimum Distance
ME	Maximum Entropy
ML	Machine Learning
MODIS	Moderate Resolution Imaging Spectroradiometer
MSI	Multi- Spectral Instrument
NAO	North Atlantic Oscillation
NASA	National Aeronautics and Space Administration
NDSI	Normalised Difference Snow Index

NDWI	Normalised Difference Water Index
NE	Northeast
NEGIS	Northeast Greenland Ice Stream
NIR	Near Infra-Red
NO	North
NSIDC	National Snow and Ice Data Center
NW	Northwest
OA	Overall Accuracy
OLI	Operational Land Image
OOB	out-of-bag
RACMO	Regional Atmospheric Climate Model
RADAR	Radio Detection and Ranging
RCM	Regional Climate Models
RCP	Representative Concentration Pathways
RF	Random Forest
RGB	Red, Green, Blue
RMSE	Root Mean Square Error
RTE	Radiative Transfer Equation
SAR	Synthetic Aperture Radar
SD	Standard Deviation
SE	Southeast
SGL	Supraglacial Lake
SLR	Sea-Level Rise
SMB	Surface Mass Balance
SONAR	Sound Navigation and Ranging
SVM	Support vector machine
SW	Southwest
SWIR	Short-Wave Infra-Red
TIRS	Thermal Infrared Sensor
TN	True Negative
TOA	Top-of-Atmosphere
TP	True Positive
USGS	United States Geological Survey
VNIR	Visible Near Infra-Red

Table of contents

List of figures

List of tables

Chapter 1

Introduction and background

Chapter 1 introduces the Greenland Ice Sheet (GrIS), its geographical setting, and its sensitivity to atmospheric and oceanic forcing. It outlines the key processes governing the ice sheet's mass balance, with a focus on recent and ongoing changes driven by anthropogenic warming. This chapter provides an overview of the GrIS hydrological system, examining the production, transport, and storage of meltwater across supraglacial, englacial, and subglacial environments. The role of meltwater in influencing ice dynamics, firn structure, and ocean-driven melting is explored, followed by a discussion of future hydrological changes under different climate scenarios. The chapter concludes by considering the implications of these changes for Greenland's long-term stability and its contribution to global sea-level rise.

1.1 The Greenland Ice Sheet

This section provides an overview of the GrIS, emphasizing its importance in the climate system, its sensitivity to atmospheric and oceanic interactions, and its role in global sea-level rise. It begins by outlining the ice sheet's geographical setting and the key climate mechanisms governing its variability. It then explores the complex interactions between the ice sheet and atmospheric and oceanic processes, which both shape and respond to the GrIS's evolving dynamics. The discussion moves on to recent and ongoing changes, detailing accelerating ice mass loss driven by a combination of rising air temperatures, shifting precipitation patterns, and oceanic heat transport. It examines the key drivers of ice loss, including the increasing frequency of extreme melt events, atmospheric influences, and feedback mechanisms that amplify surface melting and ice sheet instability. Finally, the section explores mass balance trends, explaining the contributions of surface mass balance (SMB) and ice dynamics to overall ice loss, with insights from satellite-based monitoring techniques.

The GrIS is experiencing accelerated ice-mass loss due to rising air temperatures. Together with the Antarctic Ice Sheet (AIS) and mountain glaciers, it is one of the largest contributors to global sea-level rise (SLR). If fully melted, the GrIS would raise global sea levels by approximately 7.4 m (Bamber et al., 2018). The GrIS is projected to continue losing mass under all future emissions scenarios outlined by the Intergovernmental Panel on Climate Change (IPCC), including those limiting global warming to below 2°C (Oppenheimer et al.,

2019). Under the high-emission scenario (RCP8.5), projections indicate that the GrIS could contribute 100–180 mm to global SLR by 2100, with potential increases exceeding 700 mm by 2200 (Edwards et al., 2021; Goelzer et al., 2020). Even relatively small increases in sea level, such as 100–200 mm will disproportionately affect low-lying coastal regions, exacerbating flooding, storm surges, and erosion, thereby endangering infrastructure, economies, and livelihoods (Oppenheimer et al., 2019). Freshwater input from the GrIS has been linked to potential disruptions in ocean circulation (Rahmstorf et al., 2015), in turn affecting marine ecosystems by altering nutrient upwelling processes, with broader implications for oceanic biodiversity (Fichefet et al., 2003). Under optimistic scenarios, such as those consistent with strong mitigation efforts that limit warming to below 1.5–2°C, significant mass loss is still expected, necessitating robust monitoring to refine SLR predictions, freshwater flux estimates, and inform global climate adaptation strategies.

1.1.1 Geographical setting and climate

The GrIS, which covers approximately 80% of Greenland's landmass, is the largest body of ice in the Northern Hemisphere (Figure 1.1; NSIDC, 2024). It lies between the Arctic and Atlantic Oceans, is situated from 60 to 83° N and is confined around the majority of its margins by peripheral mountains. The ice sheet has an area of ~1.7 million km², a volume of ~ 2.9 million km³ and rises to its maximum elevation at two domes: the southern dome, which reaches ~3 km a.s.l. and the northern dome, which reaches ~3.3 km a.s.l. Ice flows towards the ocean from the divide between these domes, where it makes its way through a series of drainage networks to become channelised through valleys and fjords into outlet glaciers. The outlet glaciers draining the ice sheet are either land-terminating, such as the Russell Glacier, or marine-terminating, such as Jakobshavn Isbræ.

Figure 1.1: Overview map of Greenland with ice thickness, highlighting its high latitude and location between the Arctic Ocean and the Atlantic Ocean (Source: Eric Gaba (Wikimedia Commons user Sting), CC BY-SA 3.0, https://commons.wikimedia.org/w/index.php?curid=12566158).

The geographical setting of the GrIS makes it highly sensitive to interactions with large-scale atmospheric and oceanic circulation patterns (Figure 1.2). Atmospheric variability, particularly the North Atlantic Oscillation (NAO), strongly influences regional climate, with its negative phase weakening westerlies, enhancing high-pressure anomalies, and promoting increased summer melting, while its positive phase generally leads to cooler conditions and increased snowfall (Hanna et al., 2016; Noël et al., 2015). The Greenland Blocking Index (GBI) further modulates atmospheric circulation by controlling the persistence and intensity of high-pressure systems over Greenland, which can lead to prolonged melt events through enhanced solar radiation and cloud-free conditions (Tedesco and Fettweis, 2020; Tedesco et al., 2016; Woollings et al., 2018; Fettweis et al., 2013).

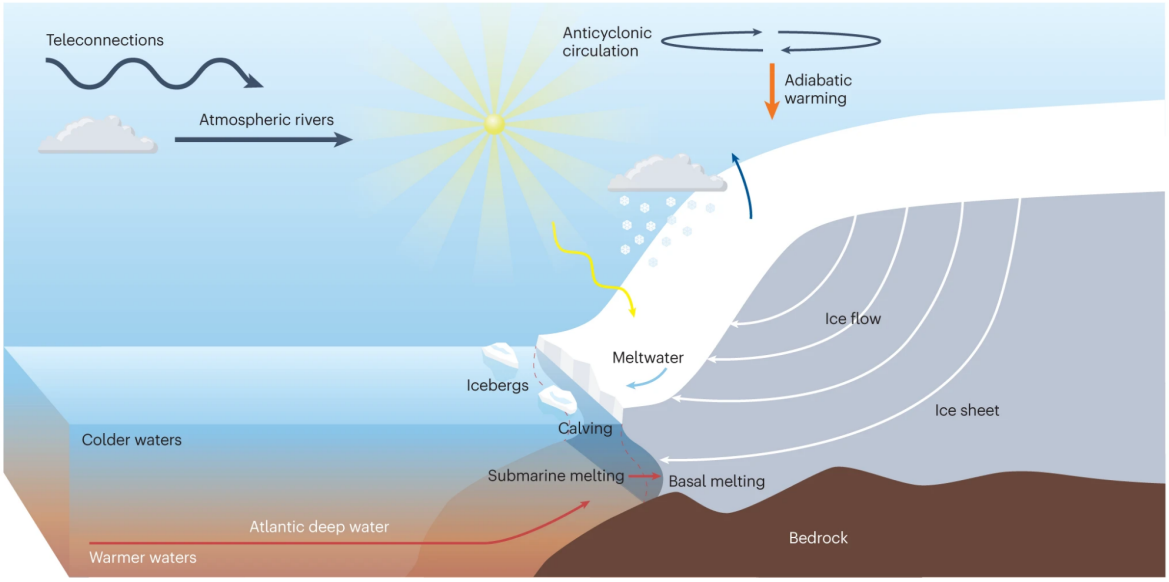

Figure 1.2: Weather, climate and hydrological processes influencing the GrIS (Source: Hanna et al., 2024).

In addition, Greenland's climate is further modulated by oceanic variability. For example, the North Atlantic Current transports warm Atlantic waters northward, influencing the temperature and salinity of waters reaching Greenland's fjords. This oceanic heat input is a key driver of basal melting for marine-terminating outlet glaciers, particularly where warm subsurface waters penetrate deep into fjords, enhancing ice-ocean interactions and accelerating ice loss (Straneo & Heimbach, 2013; Rignot & Mouginot, 2012). Oceanic forcing drives the retreat and thinning of marine-terminating glaciers in Greenland, primarily through submarine melting caused by warm Atlantic waters entering fjords (Straneo et al., 2012). Subglacial meltwater plumes, fueled by surface runoff, further enhance this melting by increasing heat exchange at the ice-ocean interface (Slater et al., 2022). Additionally, submarine melting can indirectly lead to glacier retreat through enhanced calving (O'Leary, and Christoffersen, 2013).

As well as being shaped by atmospheric and oceanic variability, the GrIS actively influences these systems. In the atmosphere, its high elevation and cold surface help establish large-scale pressure patterns, such as the GBI, which disrupts mid-latitude storm tracks and influences weather patterns across the Northern Hemisphere (Hanna et al., 2018; Tedesco et al., 2016). The ice sheet also affects moisture transport and precipitation patterns, while cold-air outflows contribute to regional circulation changes. In the ocean, freshwater discharge from the GrIS reduces surface salinity, weakening deep-water formation and slowing the Atlantic Meridional overturning circulation (AMOC), with potential consequences for global climate regulation (Böning et al., 2016; Rahmstorf et al., 2015). This influx of meltwater can also stratify the upper ocean, reducing vertical mixing and affecting sea ice dynamics.

Albedo, the fraction of solar radiation reflected by the Earth's surface, plays a crucial role in regulating regional and global climate. For ice sheets, where ice surfaces reflect a high proportion of incoming radiation, albedo is particularly important. The high reflectivity of the GrIS helps maintain locally cooler temperatures by limiting heat absorption. However, as melting increases, exposed bare ice and liquid water reduce albedo, leading to greater solar absorption and amplifying warming through a self-reinforcing feedback (Box et al., 2012).

1.1.2 Recent and ongoing changes of the Greenland Ice Sheet

The GrIS has undergone substantial changes in recent decades, with ice mass loss accelerating due to anthropogenic climate change (Otosaka et al., 2023; Hanna et al., 2021). Rising global temperatures, shifts in atmospheric circulation, and increasing oceanic heat content are driving rapid alterations in the ice sheet's surface and dynamic processes. Since the late 20th century, the impact of human-induced greenhouse gas emissions has surpassed natural climate variability as the dominant driver of temperature changes (IPCC, 2023), with Arctic regions, including Greenland, warming at more than twice the global average. This warming has led to record-high ice mass loss, driven by intensified surface melting, changing precipitation patterns, and enhanced ocean-driven basal melting of outlet glaciers.

This section examines recent and ongoing changes to the GrIS, exploring the key drivers of mass loss, the role of surface and oceanic processes, and the broader implications for future ice sheet stability. The focus is on changes since the late 20th century–a period marked by the strongest anthropogenic warming signal due to the rapid rise in greenhouse gas concentrations and associated radiative forcing, surpassing the influence of natural climate variability in earlier centuries (IPCC, 2023). The late 20th and early 21st centuries have also seen a significant increase in the availability of high-resolution observational records. Since the late 1970s, satellite data have provided continuous insights into ice mass loss trends and their climatic drivers, enabling robust assessments of recent changes.

While paleo-records indicate that the ice sheet has fluctuated over millennia, recent mass loss rates are comparable to the highest rates recorded in the early Holocene (~6,000 Gt per century) but are projected to exceed all natural Holocene variability under future warming scenarios (Briner et al., 2020). Modern ice sheet decline is driven by anthropogenic greenhouse gas emissions, which have led to record-high global temperatures, increased oceanic heat content, and shifts in atmospheric circulation that intensify ice loss (IPCC, 2023). The IPCC reports that human activities have caused approximately 1.1°C of global warming since 1850–1900, with Arctic regions warming at more than twice the global average (IPCC, 2021).

This anthropogenic warming has profoundly influenced the GrIS, with surface air temperatures across Greenland rising significantly in the 21st Century, particularly in coastal regions, which are warming faster than the interior and summit (Hanna et al., 2008; Box et al., 2009). Significant coastal warming of approximately +1.7°C in summer and +4.4°C in winter was observed between 1991 and 2019 (Hanna et al., 2021), with the largest

increases occurring in southern Greenland. Oceanic warming around southern Greenland, where sea surface temperatures have risen by up to +1.5°C in some regions since the late 1990s, is increasing basal melt, while atmospheric circulation patterns, like Greenland Blocking Episodes, have intensified surface melt during extreme events (McLeod & Mote, 2016).

Precipitation in the form of snow, which is crucial for maintaining the ice sheet's mass balance, is increasingly being replaced by precipitation in the form of rainfall in coastal areas. Here, annual rainfall has increased by approximately 50 mm per decade since the 1990s (Hanna et al., 2021; Loeb et al., 2024). Rainfall lowers the ice sheet's albedo, leading to more solar radiation absorption and faster surface melting, with rainfall-driven melt events now accounting for approximately 28% of total surface melt and having more than doubled in frequency since 1979 (Oltmanns et al., 2019). In August 2021, an atmospheric river –a narrow channel of concentrated moisture–brought unprecedented rainfall to Summit Station, extending melt conditions and amplifying ice loss through the melt–albedo feedback effect (Box et al., 2022). The rise in the occurrence of atmospheric rivers has brought more warm, moist air to Greenland, resulting in a +14% increase in annual rainfall and intensified surface melt during extreme events (Tedesco et al., 2020). Since 1979, the occurrence of moisture-rich air masses entering the region has risen by more than 6% (Mattingly et al., 2016).

The combined effects of warming temperatures, increased rainfall, and enhanced surface melt from oceanic and atmospheric forces make the GrIS especially vulnerable to climate change. Looking ahead, continued warming is expected to cause more frequent and severe melt events, further accelerating Greenland's ice mass loss. Hanna et al. (2024) predicts that rising temperatures, increasing variability in precipitation, and the growing influence of atmospheric rivers will intensify ice loss in the coming decades. The ISMIP6 projections for the GrIS estimate a sea-level rise of 90 ± 50 mm by 2100 under the high greenhouse gas concentration scenario RCP8.5, and 30 ± 17 mm under the low-emission scenario RCP2.6 (Goelzer et al., 2020). Other studies suggest that the ice sheet's committed contribution to sea-level rise by 2100 is at least 3.4 cm, with a minimum of 0.6 mm (Nias et al., 2023). However, uncertainty in these projections remains high due to factors such as ice sheet dynamics, regional climate variability, and the response of outlet glaciers to oceanic and atmospheric forcing.

Over recent decades, darkening of the ice sheet surface has intensified, further increasing melt rates. This trend is driven by processes such as snowmelt, snowline retreat, dust deposition (e.g., Dumont et al., 2014), and the growth of algae on ice surfaces (e.g., Cook et al., 2020). As these processes become more widespread, further declines in albedo are

expected, intensifying melt. Reduced surface albedo enhances melting through a self-reinforcing feedback loop that now affects over 97% of the GrIS and accounts for more than half of the observed increase in melting (Box et al., 2012; Tedesco et al., 2011). This cycle of decreasing albedo and increasing melt is an important driver of accelerating ice mass loss from the GrIS (Box et al., 2022).

Greenland has experienced an increasing frequency of extreme melt events in recent years, with notable examples in 2012 and 2019, amplifying surface mass loss from the ice sheet. The 2012 event was unprecedented, with 98.6% of the ice sheet's surface, including the summit, experiencing melt (Tedesco and Fettweis, 2020). Similarly, in 2019, another extreme melt event occurred, with 97% of the ice sheet surface experiencing melting within just three days (Sasgen et al., 2020). With progressing climate change, such extreme melt events are expected to occur more frequently and become more severe and persistent, further accelerating ice mass loss and contributing to global sea-level rise (Beckmann and Winkelmann, 2023).

1.1.2 Mass balance

This subsection provides an overview of the GrIS mass balance, outlining the key processes that govern its changes and their response to climate forcing. It first introduces the general principles of ice sheet mass balance, including the contributions of SMB and ice dynamics, followed by an overview of the primary satellite-based methods used to estimate mass balance. The discussion then shifts to recent trends in GrIS mass change, highlighting the increasing rates of ice loss, their implications for global SLR, and the relative contributions of SMB and ice dynamics over recent decades.

1.1.2.1 Overview of mass balance

Ice sheet mass balance is the net difference between mass gain (primarily through precipitation) and loss (through surface/subsurface melting and dynamic processes; Benn and Evans, 2010; Cogley et al., 2010). Mass loss from the ice sheet occurs through two primary mechanisms: SMB loss and dynamic ice loss. SMB refers to the net difference between mass gain through accumulation and mass loss through ablation on the surface of the ice sheet. Mass accumulates on top of the ice sheet through precipitation, condensation, and deposition; mass is removed from the surface through surface melting and subsequent runoff (melt – rainfall + refreezing; Lenaerts et al., 2019). Dynamic loss refers to mass loss through ice discharge directly to the ocean, i.e., through iceberg calving. Changes in ice discharge arise through ice flow fluctuations in the outlet glaciers fringing Greenland's coasts (King et al 2020; Enderlin et al., 2014). While evaporation and sublimation are also components of SMB, their contribution to mass loss is relatively minor in Greenland compared to the AIS where strong katabatic winds and arid conditions result in significantly higher sublimation rates (Van Wessem et al., 2018; Lenaerts and van den Broeke, 2012).

The mass balance of the GrIS is commonly estimated through satellite monitoring by using: fluctuations in Earth's gravitational fields using gravimetry (e.g. Groh et al., 2019; Velicogna et al., 2020), elevation and volume changes through altimetry (Simonsen et al., 2021; Sørensen et al., 2011; Sasgen et al., 2012), or input-output methods, using ice flow observations from optical and radar imagery (Mouginot et al., 2019; Rignot et al., 2019). Although these techniques can provide an estimate of the location, timing, and way mass is gained or lost from the ice sheet, each has limitations (Mankoff et al. 2021; Shepard et al., 2012). As such, the most comprehensive estimates of mass balance use combined measurements derived from all three geodetic methods (Figure 1.3; Shepard et al., 2012; The IMBIE team, 2020; Otosaka et al., 2023).

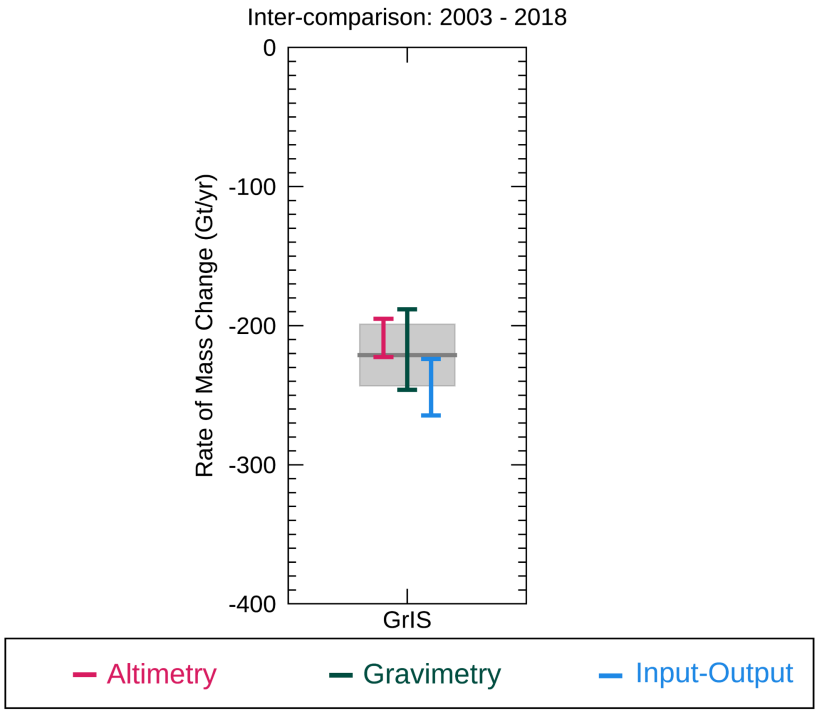

Figure 1.3: Comparison of ice sheet mass balance rates for the GrIS from 2003 to 2018, based on altimetry, gravimetry, and input–output methods (Source: Otosaka et al., 2023).

1.1.2.2 Recent changes in mass balance

The GrIS was in a near-balanced state in the 1970s, however, ice loss has substantially increased in the following decades (The IMBIE team, 2020). Recently, the GrIS has been subject to increased air (Hanna et al., 2021) and ocean (Straneo et al., 2013) temperatures, as well as decreased cloud cover through summer months (Hofer et al., 2017). Such conditions have caused the ice sheet to lose mass at an accelerated rate, leading to a negative mass balance every year since 1998 (Mouginot et al., 2019).

An ice sheet in a negative mass balance regime is actively contributing to SLR. The most recent estimates of mass balance of the GrIS show that each year from 1992 to 2020, the GrIS has lost 169 ± 9 Gt yr^{-1} on average, totalling to 4892 ± 457 Gt of ice, or a contribution of ~14 mm to global sea level (Otosaka et al., 2023). More recently, from 2002 - 2022, the ice sheet has lost mass at even greater rates, estimated at −255 ± 19 Gt yr^{-1} (Figure 1.4; Hanna et al., 2024). Within this negative trend, the mass balance of the GrIS has also experienced large variability (Sagden et al., 2020; The IMBIE team, 2020; Hanna et al., 2024), with ice loss ranging from 86 Gt yr^{-1} in 2017 to 444 Gt yr^{-1} in 2019 (Otosaka et al., 2023). For example, significant surface melt events occurred in 2010, 2012, and 2019 across the ice sheet, which lasted from several days to a few weeks, and produced annual mass loss

anomalies that were twice as large as those in prior and subsequent years, for example, 2012 compared to 2013 (Hanna et al., 2024; Figure 1.4).

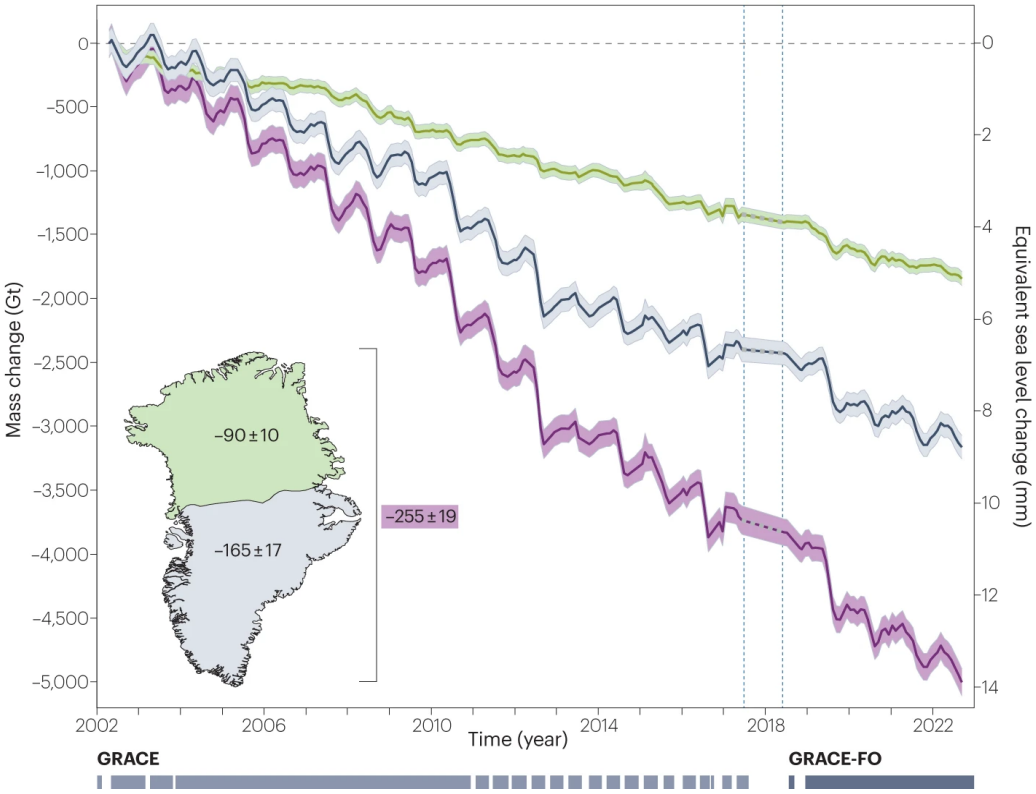

Figure 1.4: Time series of mass change and corresponding sea level equivalent for the GrIS from 2002 to 2022. Estimates are shown for the entire ice sheet (purple), as well as for the regions north (green) and south (grey) of approximately 72°N (Source: Hanna et al., 2024).

From 1992 to 2018, the GrIS has lost mass in near-equal parts through SMB (50.3 %) and dynamic mass loss (49.7 %; Figure 1.5; The IMBIE team, 2020). However, more recently (from 2007 - 2017), total mass loss was estimated to consist of 64% from SMB and 36% from ice dynamical processes (Otosaka et al., 2023). Between 1992 and 2018, an increasingly negative SMB compared to earlier periods contributed to a loss of 1964 ± 565 Gt of ice (Figure 1.5; The IMBIE team, 2020), which was driven by warming temperatures leading to increased melting and surface runoff (Hanna et al., 2021; Slater et al., 2021). Between 1992 and 2018, dynamic mass loss caused 1938 ± 541 Gt mass loss from the GrIS (The IMBIE team, 2020), with increased ice acceleration from Jakobshavn Isbræ and Southeast glaciers in the 2000s considerably contributing to the dynamical imbalance (Holland et al., 2008; Howat et al., 2008).

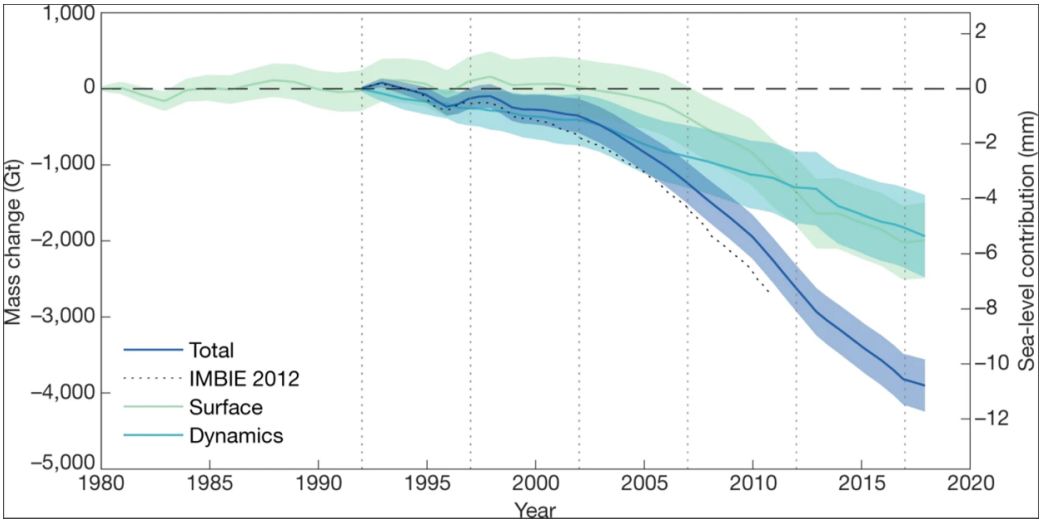

Figure 1.5: Cumulative anomalies in total mass, SMB and dynamic mass loss from the GrIS (Source: The IMBIE Team, 2020).

1.2 Greenland Ice Sheet hydrology

This section explores the hydrological processes of the GrIS, focusing on the production, transport, and storage of meltwater. It begins by outlining the surface energy balance governing meltwater production and the role of ice sheet facies in modulating meltwater runoff and storage. The discussion then examines supraglacial hydrology, detailing the formation, distribution, and seasonal evolution of meltwater features such as supraglacial lakes (SGLs), rivers, slush, and runoff pathways, which regulate surface water transport and influence ice sheet dynamics. It further explores the englacial hydrological system, highlighting the role of crevasses and moulins in routing meltwater from the surface to the bed. Finally, the section addresses subglacial hydrology, describing drainage system configurations and the influence of subglacial lakes on ice flow and meltwater flux.

1.2.1 Meltwater production and ice sheet facies

The surface melt process is governed by the energy exchange at the ice-atmosphere interface, where the net surface energy balance determines whether melting will occur (Hock, 2005). Although air temperature influences melt potential, actual melting only begins once the ice reaches its melting point of 0°C. Before this, any surplus energy is first used to warm the ice surface to 0°C, and only after this threshold is reached does additional energy contribute to surface melt (Benn and Evans, 2010). The ice sheet's response to melt is further modulated by the firn layer, which regulates runoff according to its variable storage capacity. During high melt conditions, the firn can become saturated, reducing its ability to

retain meltwater and thereby amplifying mass loss through increased runoff (Munneke et al., 2015; van den Broeke, 2008).

Melting of snow and ice accounts for the majority of ablation on the GrIS, particularly in the ablation zone, where annual mass loss exceeds accumulation (Cogley et al., 2010). The ablation zone, where the annual mass balance is negative, is characterized by exposed bare ice during the summer. In contrast, the accumulation zone, characterized by a positive annual mass balance, lies above the equilibrium line altitude (ELA) – the elevation where annual mass balance is zero (Box et al., 2022). The accumulation zone is further divided into three glacier facies: the dry snow zone, where melting is negligible; the percolation zone, where limited meltwater infiltrates snow and firn and refreezes; and the wet snow zone, where snow becomes fully saturated with meltwater by the end of the melt season (Figure 1.6; Benson, 1962; Nolin and Payne, 2007).

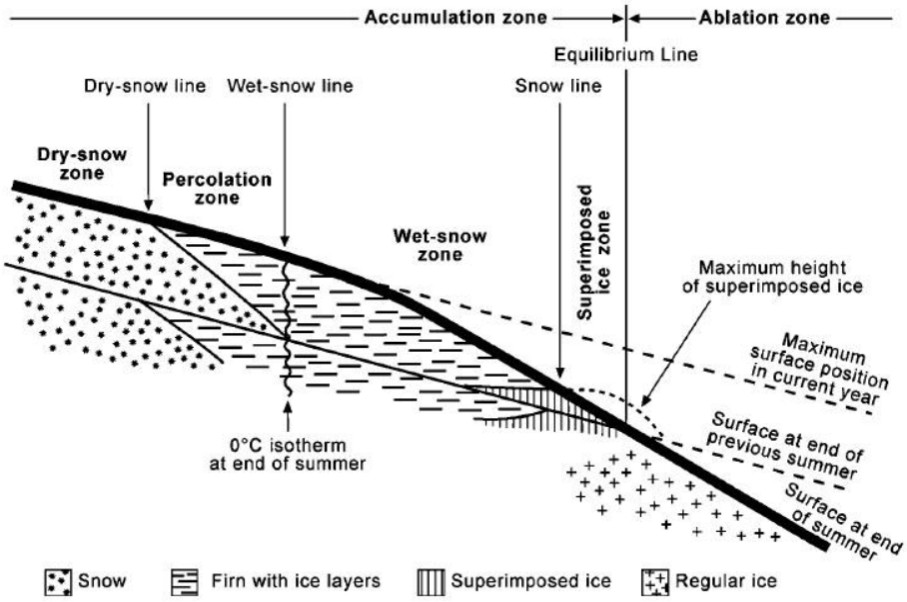

Figure 1.6: Cross section of a glacier showing near-surface ice and snow facies at the end of the ablation season (Source: Cuffey and Paterson, 2010).

Meltwater infiltrating the porous firn layer, a temporary storage system, can refreeze, be retained as liquid by capillary forces, or flow through perennial firn aquifers (Herron and Langway, 1980; Forster et al., 2014; Machguth et al., 2018). Over time, refreezing within the firn creates impermeable ice layers, slabs, or lenses that limit permeability and enhance surface runoff (Pfeffer et al., 1991; Machguth et al., 2016; MacFerrin et al., 2019; Culberg et al., 2024). When drainage is inefficient due to saturated firn, slush flows can occur, while lateral runoff across ice horizons reduces surface albedo and accelerates further melting (Charalampidis et al., 2015; Machguth et al., 2016).

1.2.2 Meltwater runoff

Meltwater that is not retained or refrozen flows across the ice sheet, following surface and basal topographic gradients to form complex networks of supraglacial hydrological features (Figure 1.7a). Storage and routing processes play a central role in regulating the timing, volume, and pathways of this runoff, shaping interactions between surface and basal hydrological systems. Ultimately, it drains into the ocean, driving ice mass loss and contributing to sea level rise. Beyond the ice sheet, the export of runoff influences freshwater fluxes to the surrounding ocean, with implications for ocean circulation and regional climate systems.

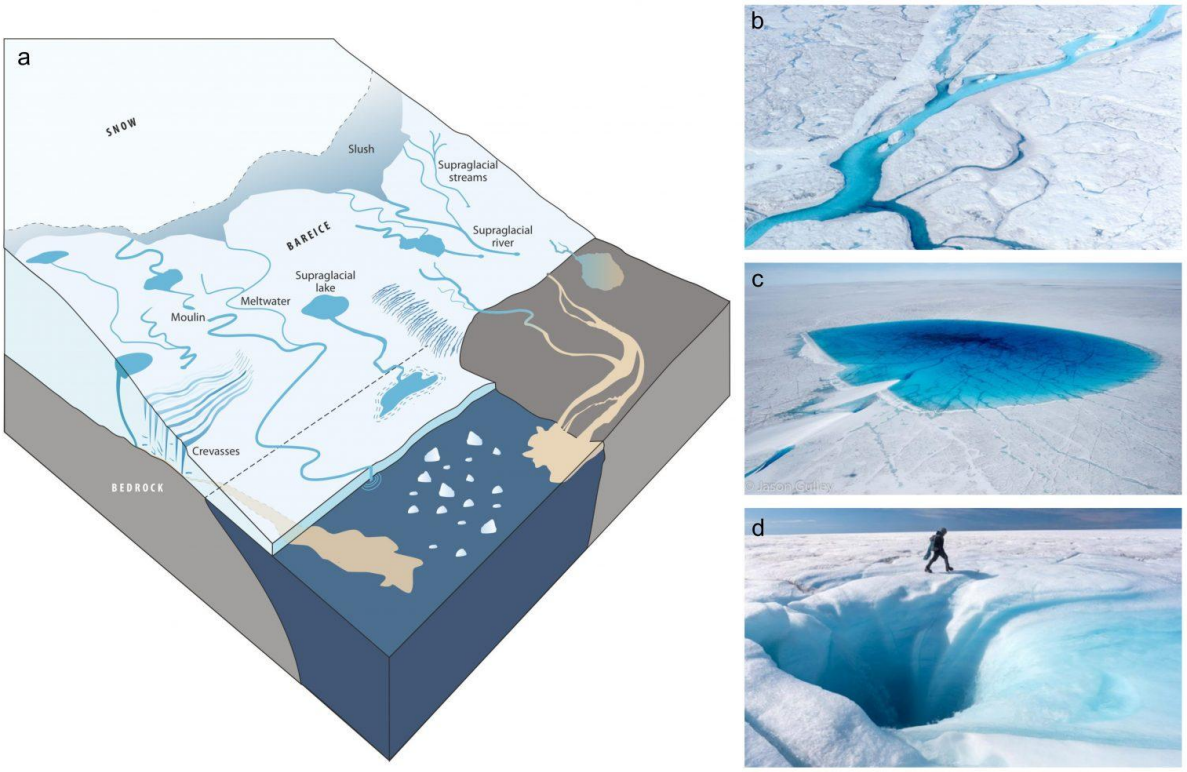

Figure 1.7: Components of the supraglacial hydrologic network on glaciers and ice sheets: (a) Diagram from Pitcher and Smith (2019); (b) Supraglacial channel on the ice surface; (c) an SGL; (d) Moulin funneling meltwater to the bed, influencing ice dynamics (Source: Lauren Rawlins, University of York, antarcticglaciers.org).

Runoff occurs primarily during the summer melt season, peaking in July and August when surface temperatures are highest. During this period, liquid water accumulates in SGLs (Figure 1.7c), rivers (Figure 1.7b), crevasses, and moulins (Figure 1.7d), forming an extensive drainage system that transports meltwater across the ice sheet surface and into the englacial and subglacial system (Banwell et al., 2016; Flowers, 2018; Hoffman et al., 2018).

Temporally, the extent of supraglacial drainage networks varies interannually, depending on atmospheric conditions and melt intensity. In extreme melt years, such as 2012, supraglacial meltwater channels were observed at elevations up to ~1850 m asl, with 11 ± 4% of the season's runoff originating from above this elevation (Machguth et al, 2016). Over the period 1991–2011, the mean ELA was ~1550 m asl, ranging from ~1240 to ~1830 m asl (van de Wal et al., 2012), reflecting the variability in runoff production and transport processes.

Across the ice sheet, meltwater runoff is most pronounced in the western and southwestern GrIS, where extensive ablation zones, dark bare-ice surfaces, and low albedo enhance melt intensity (Lenaerts et al., 2015; van den Broeke et al., 2017). Between 1991 and 2017, southwest Greenland alone contributed approximately 30% of the total GrIS runoff (Noël et al., 2019). Northern Greenland has also experienced increasing runoff due to the expansion of the ablation area, with the ELA rising by ~200 m in recent decades, contributing an additional 12 Gt yr^{-1} of meltwater runoff (Noël et al., 2019).

Longer and more intense melt seasons have significantly increased runoff in recent decades, a trend projected to continue under future warming scenarios. Observations from CryoSat-2 satellite altimetry indicate that between 2011 and 2020, runoff averaged 357 ± 58 Gt/yr, a 21% increase compared to the preceding three decades (Slater et al., 2021). Tedstone and Machguth (2022) demonstrated that the runoff limit, which they define as the highest elevation of supraglacial channel features, has risen between 1985–1992 and 2013–2020. This upward migration was most pronounced in the west (242 m), north (194 m), and northeast (59 m) sectors of the ice sheet, leading to an overall expansion of ~47,400 km^2 (29%) in the runoff area. Notably, this observed increase exceeds estimates from SMB models, indicating that current models may underestimate the extent of supraglacial drainage networks.

The increase in runoff is primarily driven by rising temperatures and longer melt seasons, which enhance surface melting and reduce refreezing within the firn. Warming-induced shifts in the ELA are exposing larger areas of the ice sheet to melt conditions, further expanding the runoff-producing area. Cloud cover has also emerged as a significant factor influencing

runoff. Van Tricht et al. (2016) found that clouds enhance meltwater runoff by ~33% relative to clear-sky conditions, primarily by suppressing meltwater refreezing rather than increasing direct melt. This accelerates bare-ice exposure, amplifying meltwater production and runoff fluxes. Additionally, changes in large-scale atmospheric circulation patterns are influencing seasonal and interannual variability in runoff, contributing to the observed 60% increase in runoff variability (Slater et al., 2021). Despite advancements in understanding meltwater runoff processes, substantial uncertainties remain such as feedback mechanisms involving climate warming, surface albedo changes, and cloud-radiation interactions, which present challenges for accurately modelling future runoff trends.

1.2.3 Supraglacial hydrology

Supraglacial hydrology refers to the network of meltwater features that form on the ice sheet surface, playing a critical role in the transport, storage, and redistribution of meltwater. As seasonal melting intensifies, liquid water accumulates and flows across the ice sheet, forming SGLs, channels, and slush-covered zones, which are key components of the broader hydrological system. The fate of this surface meltwater–whether it is stored, refrozen, or drained–significantly influences the GrIS mass balance, ice dynamics, and freshwater flux into the surrounding ocean. Understanding supraglacial hydrology is essential for accurately quantifying the GrIS's response to climate change and predicting its future contributions to sea-level rise. This subsection examines the formation, distribution, seasonal evolution, and long-term trends of key supraglacial meltwater features, highlighting their role in ice-sheet-wide hydrological processes.

1.2.3.1 Supraglacial lakes

1.2.3.1.1 Formation and distribution of supraglacial lakes

Meltwater runoff on the GrIS can accumulate in SGLs (Figure 1.7c), which form during the spring and summer melt season when meltwater pools in impermeable surface depressions in the ablation and lower accumulation zones (Box and Ski, 2007; McMillan et al., 2007; Sneed and Hamilton, 2007; Selmes et al., 2011). These SGLs exhibit a wide range of sizes, from just a few square meters to tens of square kilometres and can reach depths of several meters (Selmes et al., 2011; Box et al., 2012). Their locations are largely influenced by ice surface topography, which is shaped by underlying bedrock undulations (Echelmeyer et al., 1991; Gudmundsson, 2003; Selmes et al., 2011). SGLs are predominantly distributed between elevations of 1000 and 1600 m (Fan et al., 2025) but are often underdeveloped

above 1200 m a.s.l. and rarely form above 2000 m a.s.l. (Sundal et al., 2009; Lampkin, 2011; Chu, 2014; Fitzpatrick et al., 2014).

The first systematic study of SGLs was conducted by Echelmeyer et al. (1991), who documented SGLs ranging in size from 10 m² to 10 km² on Jakobshavn Isbræ. SGLs have since been identified to span across all regions of the ice sheet (e.g., Selmes et al., 2011). Early research primarily focused on basin-scale studies in western Greenland (e.g., McMillan et al., 2007; Sundal et al., 2009; Williamson et al., 2018a; Miles et al., 2017; Yang et al., 2021). However, more recent work has extended to the rapidly changing northern regions (Turton et al., 2021; Rawlins et al., 2023; Otto et al., 2022; Hochreuther et al., 2021) and the southeast (Everett et al., 2016).

Despite numerous regional-scale studies of SGLs, relatively few have examined their spatial distribution and evolution across the entire GrIS (Selmes et al., 2011, 2013; Hu et al., 2022; Zhang et al., 2023; Fan et al., 2025; Dunmire et al., 2025). Selmes et al. (2011) conducted one of the first pan-Greenland investigations, analysing SGL drainage behaviour across all regions of the ice sheet between 2005 and 2009. They observed that while SGLs were present in all regions, their distribution was uneven. The southwest region contained the majority (55%) of detected SGLs, with the northwest and northeast regions contributing 19% and 13%, respectively. Recent work by Fan et al. (2025) further expanded this understanding by producing the first annual, ice-sheet-wide database of maximum summer SGL extents, spanning 1985 to 2023. Using July and August Landsat imagery, they found that SGLs were primarily distributed in the northwestern, northeastern, and southwestern basins (Figure 1.8).

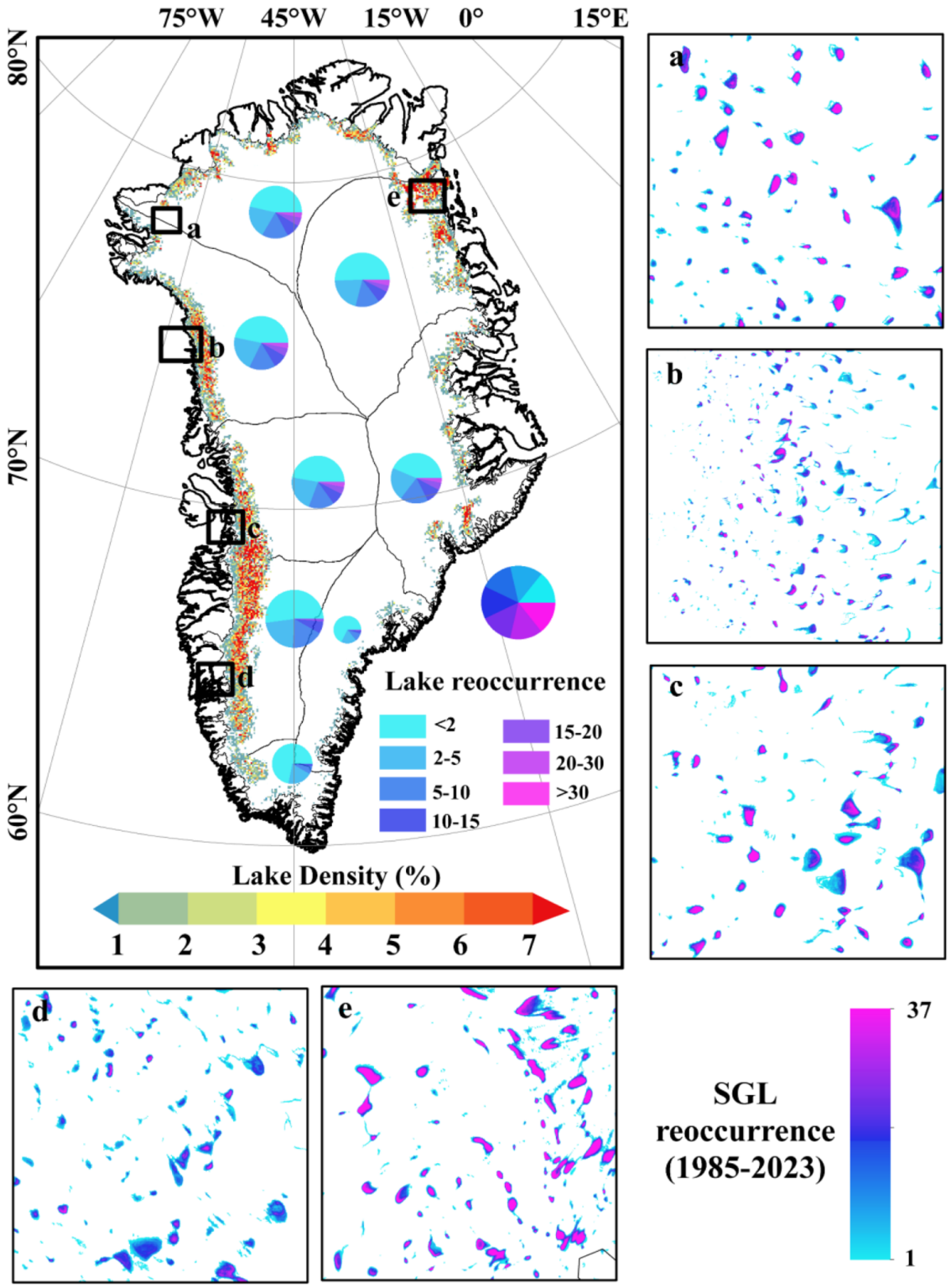

Figure 1.8: SGL reoccurrence (1985–2023) and spatial density on the GrIS and basins: (a) NO, (b) NW, (c) CW, (d) SW, and (e) NE. Pie chart shows reoccurrence class distribution and circle size reflects average SGL area (Source: Fan et al., 2025).

1.2.2.1.2 Seasonal evolution and dynamic behaviour of supraglacial lakes

SGLs first form near the ice margin early in the melt season and progressively appear at higher elevations as temperatures rise. Between spring and summer, these SGLs enlarge in area and depth, coinciding with the inland progression of surface melting (Box and Ski, 2007; McMillan et al., 2007; Sneed and Hamilton, 2007; Miles et al., 2017; Yang et al., 2021). SGLs are more likely to occur in areas with lower elevations and shallower slopes (Turton et al., 2021). However, during intense melt years, they become more established and reach increasingly higher elevations (Liang et al., 2012; Zhang et al., 2023).

SGLs on the GrIS either drain rapidly, drain slowly or refreeze. They can then become buried (Figure 1.9). Rapid drainage occurs in hours via hydrofracture, slow drainage occurs over days to weeks via channel incision and overflow. Hydrofracture-driven drainage happens when the hydrostatic pressure of a meltwater-filled crevasse propagates the fracture tip (Krawczynski et al., 2009), partially or fully draining the SGL. The likelihood and efficiency of hydrofracture depend on the local stress regime: under extensional stress, crevasses are more likely to open and propagate downward, facilitating rapid SGL drainage, whereas under compressive stress, crevasse propagation is inhibited, limiting the potential for hydrofracture-driven drainage. Early work estimates that approximately 10% of SGLs drain rapidly by hydrofracture across the GrIS (Selmes et al., 2011, 2013), however, more recent estimates suggest this figure is between 28% and 45% (Fitzpatrick et al., 2014).

Rapid drainage events are more common during high-melt years (Dunmire et al., 2025) and are less likely at higher elevations where extensional flow is reduced due to slower ice velocities and increased compressive stress, which inhibit crevasse propagation (Johansson et al., 2013). Poinar et al. (2015) argue that meltwater above 1600 m predominantly drains on the surface rather than through hydrofracture, though instances of rapid drainage above this elevation have been observed (e.g., Dunmire et al., 2025). In some cases, rapid drainage triggers cascading events, where strain rate perturbations induce nearby SGLs to drain (Christoffersen et al., 2018). Smaller SGLs, particularly those below 0.0495 km², are thought to be unlikely to trigger hydrofracture through 1 km-thick ice (Krawczynski et al., 2009). Potential factors influencing rapid drainage, such as SGL area, volume, water depth, ice surface velocity, surface strain rate, and cumulative melt and runoff, have been investigated, although they remain poorly constrained (Williamson et al., 2018b; Lutz et al., 2024). Recent studies suggest that SGL depth increases the likelihood of hydrofracture, as deeper SGLs exert greater hydrostatic pressure, promoting fracture propagation (Dunmire et al., 2025).

Slow drainage occurs when SGLs overflow their basins or when meltwater thermally incises surface channels after the rate of thermal erosion surpasses ablation (Catania et al., 2008; Banwell et al., 2012; Yang et al., 2016). Meltwater from these events flows down-glacier through shallow surface channels. SGLs that do not drain may freeze over and shrink at the end of the melt season as temperatures decrease (Selmes et al., 2013; Miles et al., 2017; Dunmire et al., 2025). Some SGLs remain partially liquid and are insulated beneath the ice, persisting through the winter in a buried state (Koenig et al., 2015; Miles et al., 2017; Dunmire et al., 2021).

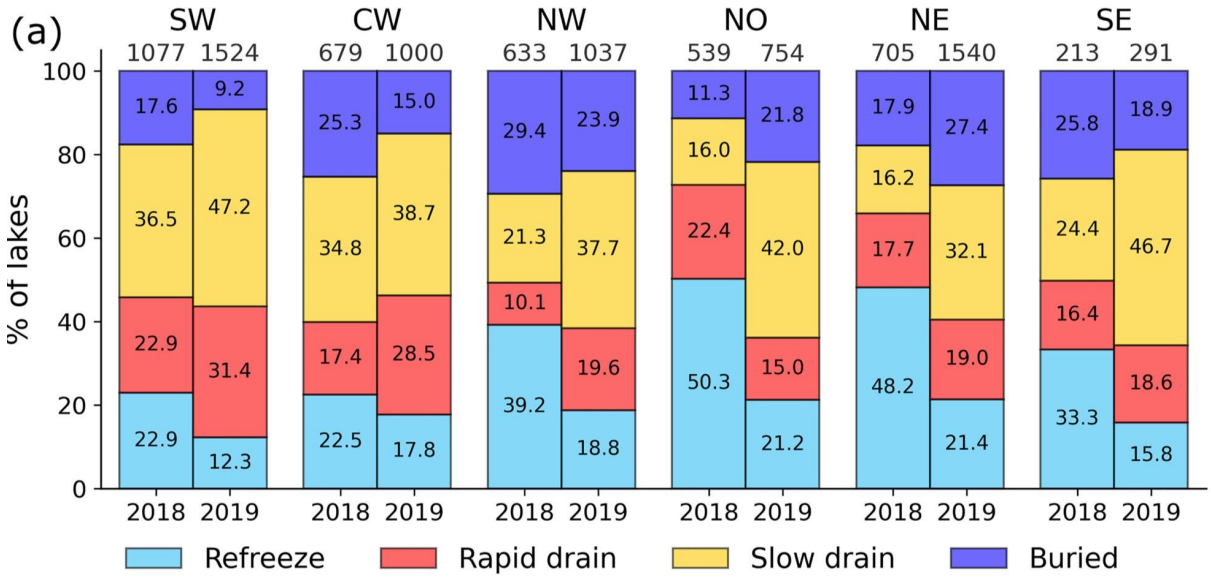

Figure 1.9: Percentage of SGLs on the GrIS that refreeze, drain rapidly, drain slowly, or become buried in 2018 (low melt year) and 2019 (high melt year), grouped by region (Source: Dunmire et al., 2025). Regional abbreviations: SW – Southwest, CW – Central West, NW – Northwest, NO – North, NE – Northeast, SE – Southeast.

1.2.2.1.3 Long-term trends in supraglacial lake extent and distribution

Although relatively few studies have systematically quantified long-term trends in the extent, distribution, and migration of SGLs across the GrIS, existing research indicates a progressive increase in SGL formation at higher elevations and an overall expansion in SGL area (Fan et al., 2025). However, extreme melt years drive substantial deviations from this trend, causing sharp increases in total SGL extent (e.g., Fitzpatrick et al., 2014). Ice-sheet-wide, SGLs have expanded in both size and number since the early 21st century, with an annual expansion rate of 51 km² in total SGL area and an annual upward migration of 10 m in maximum SGL elevation between 1985 and 2023 (Fan et al., 2025). Additionally, from 2014 to 2022, statistically significant increases in total meltwater volume have been observed across drainage basins in the north, east, and south of the ice sheet (Corr et al.,

2023), which reflects both a greater extent of supraglacial hydrological features and an increase in the depth and persistence of surface meltwater storage.

Regional trends reinforce these patterns of inland migration and SGL expansion. In northwest Greenland, SGLs have exhibited particularly strong growth in both area and elevation. Between 1985 and 2016, maximum and mean SGL elevations increased by 418 m and 299 m, respectively, while SGL coverage at high elevations (≥ 1200 m a.s.l.) expanded by over 2750% (Gledhill and Williamson, 2016). This inland migration coincided with a near-doubling of total regional SGL area and volume, with post-2000 accelerations largely driven by regional surface-temperature anomalies. A similar trend is evident in west Greenland where SGLs migrated inland between 2002 and 2012 (Fitzpatrick et al., 2014). While the number of SGLS varied annually, averaging 200 SGLS per year, total SGL area increased substantially during the high-melt years of 2010, 2011, and 2012 (Fitzpatrick et al., 2014). Additionally, Fitzpatrick et al. (2014) found that SGLs above 1400 m a.s.l. occupied 49% more area in record melt years compared to the 11-year mean.

1.2.2.2 Supraglacial channels

1.2.2.2.1 Formation and distribution of supraglacial channels

Supraglacial channels can be categorized as either rivers or streams (Smith et al., 2015). Supraglacial rivers are major, high-order channels that are evenly spaced and often terminate in moulins (Pitcher and Smith, 2019). In contrast, supraglacial streams are shallow, transient, and of lower stream order, often acting as tributaries to rivers (Smith et al., 2015). Supraglacial channels vary greatly in size and shape, ranging from just a few centimetres to several meters in width, and can extend for tens of kilometres before draining into SGLs, entering the englacial environment, or reaching the ocean (Yang and Smith, 2016; Rippin and Rawlins, 2021). Together, these stream-river systems serve as the primary pathways for transporting surface meltwater across the southwest of the ice sheet (Yang et al., 2016). The routing of water through these channels is largely controlled by surface topography, meaning that the locations of larger supraglacial streams remain relatively constant across melt seasons (Irvine-Fynn et al., 2011).

The formation of supraglacial channels is still not entirely understood but thought to occur when meltwater thermally incises the surface of the ice, with thermal erosion outpacing ablation rates (Yang et al., 2016). Meltwater originating from precipitation, surface melt, saturated slush, or overflow from water-filled moulins, crevasses, and SGLs contributes to the development of these channels (Chu, 2014). On steep surface slopes, ponded meltwater or slush is funnelled into narrow and shallow channels, which erode and expand over time

as the snowpack is melted. As the channels become more established, they facilitate increasingly efficient meltwater transport across the ice sheet surface (Chu, 2014).

The majority of research on supraglacial channels has been conducted in southwest GrIS, where dense networks of supraglacial rivers and streams dominate the ablation zone (Pritchard and Smith, 2019). In this region, drainage systems are characterized by closely spaced streams and rivers (Smith et al., 2015; Yang et al., 2016; Yang et al., 2021). In contrast, relatively little research has focused on supraglacial channels in other parts of the ice sheet, such as the northeast (e.g., Rawlins et al., 2023; Lu et al., 2021). In the dynamic Northeast Greenland Ice Stream (NEGIS) region, channel characteristics are closely tied to ice flow regimes. Areas dominated by ice deformation feature long rivers, whereas regions influenced by basal sliding are characterized by shorter rivers and larger SGLs (Lu et al., 2021).

Supraglacial rivers dominate surface meltwater drainage on the GrIS, forming the majority of the hydrological network and controlling meltwater transport across the ice sheet. In northeastern Greenland, rivers account for 83.8% of the supraglacial drainage system, compared to 62% in the southwest (Lu et al., 2021; Yang et al., 2021). However, while rivers control most of the meltwater area and facilitate rapid drainage, their role must be considered in relation to SGLs, which regulate meltwater storage and release. At higher elevations (>1600 m), rivers dominate due to steeper slopes that enhance transport efficiency, while SGLs are scarce due to the lack of topographic depressions. In contrast, lower elevations host more SGLs, which accumulate meltwater before eventually draining into river networks or moulins. Despite their smaller footprint, SGLs influence river distribution by acting as temporary reservoirs–delaying, regulating, and in some cases, enhancing downstream flow through overflow events. Thus, while rivers define the connectivity of the supraglacial drainage system, their function is shaped by interactions with SGLs, highlighting the interdependence between transport and storage mechanisms within the meltwater system.

1.2.2.2.2 Evolution of supraglacial channels

Supraglacial river systems are highly dynamic, evolving on both diurnal and seasonal timescales. Stream discharge follows a diurnal cycle, with peak flow occurring during periods of maximum solar radiation and decreasing at night (Ferguson, 1973). Seasonally, as temperatures rise in spring and summer, increased supraglacial runoff enables the formation and expansion of supraglacial river networks, which extend farther up-glacier as the melt season progresses and melting intensifies. Discharge is lowest at the beginning and end of

the melt season, reaching its peak in mid-summer (Holmes, 1955). During the early stages of channel development, high discharge volumes can significantly shape channel morphometry, often promoting meander formation. However, as rivers mature and their channels become more established, discharge has less of an effect on channel evolution, and the river's morphology stabilizes (Ferguson, 1973). In winter, lower temperatures cause channels to freeze and shut down, with potential erosion of channel pathways if water flow is insufficient. However, some remnant channels may persist and be reused the following season, making the location of river networks more predictable over time (Rippin and Rawlins, 2021; Pritcher and Smith, 2019).

2.2.2.2.3 Long-term trends of supraglacial channel networks

The long-term trends of supraglacial channel networks across the GrIS are not yet fully understood, with limited comprehensive studies tracking their evolution over extended periods. While there is growing evidence of significant changes in the distribution of supraglacial river networks over time, these trends are often obscured by interannual variability and the episodic nature of extreme melt years.

Rawlins et al. (2023) examined the seasonal and multi-annual behaviour of the supraglacial drainage network at Humboldt Glacier in northern Greenland, a region that has been experiencing significant changes due to warming temperatures. Using high-resolution Sentinel-2 (S2) imagery from 2016 to 2020, Rawlins et al. observed that the supraglacial drainage network exhibited considerable interannual variability, with substantial expansion during high-melt years such as 2019. In contrast, the network’s development was more limited in low-melt years, such as 2017 and 2018. This implicates extreme melt events as a key driver of the rapid expansion of supraglacial channels.

1.2.2.3 Supraglacial slush

Supraglacial slush, defined as fully water-saturated firn or snow, typically forms in the percolation zone of the GrIS. Slush formation occurs when meltwater percolation is impeded, either because the rate of meltwater production exceeds the firn's capacity to absorb water, leading to saturation at depth (Clerx et al., 2022; 2024), or due to low-permeability ice layers obstructing downward flow (MacFerrin et al., 2019).

When surface snow and ice reach saturation, drainage can mobilize the snow and firn, generating slush flows that propagate through topographic lows (e.g., Irvine-Fynn et al., 2011; Onesti, 1985; Onesti and Hestnes, 1989). Slush facilitates lateral meltwater transport by forming hydrologically connected zones that channel meltwater into supraglacial rivers

and SGLs (Holmes, 1955; Cuffey and Paterson, 2010). These zones also initiate and sustain supraglacial channels (Chu, 2014; Rippin and Rawlins, 2021). When slush fields connect to moulins or crevasses, they deliver meltwater to the ice-bed interface and the subglacial hydrological networks (Smith et al., 2021). Additionally, the refreezing of slush plays a key role in forming and expanding near-surface ice slabs. These ice slabs reduce firn's meltwater retention capacity and increase surface runoff (Machguth et al., 2016; Pfeffer et al., 1991; Harper et al., 2012; Miller et al., 2018; 2020). This process establishes a feedback loop: as thicker ice slabs impede downward percolation, they further contribute to slush formation (Covi et al., 2022; Machguth et al., 2016; MacFerrin et al., 2019; Miller et al., 2022; Jullien et al., 2023).

Although slush was first observed on the GrIS in the 1950s (Holmes, 1955), it has often been overlooked in meltwater mapping studies. Large-scale studies reveal that slush distribution aligns closely with runoff limits derived from optical satellite imagery (Machguth et al., 2023), while smaller basin-scale studies have identified slush primarily in the southwestern and northern regions of the GrIS (e.g., Covi et al., 2022; Rawlins et al., 2023). Previously, slush has been delineated on the GrIS only to eliminate it from supraglacial channel delineation efforts (Yang and Smith, 2012). Since slush accounts for nearly two-thirds of the meltwater area on the Roi Baudouin Ice Shelf, East Antarctica, and approximately half of the meltwater area across 56 other Antarctic ice shelves, which experience a climate similar to that of the GrIS (Dell et al., 2022; 2024), its exclusion from Greenland-based meltwater mapping efforts may lead to significant underestimation of total meltwater extent.

1.2.3 Englacial hydrology

The englacial hydrological system refers to the distribution of meltwater between the surface of the ice sheet and the base. Less is known about englacial hydrology compared to the supraglacial system since it is much more difficult to access in situ and monitor remotely. Meltwater flows into the englacial system via crevasses and moulins, which in turn provide pathways to the bed of the ice sheet. This subsection explores the formation and structural characteristics of crevasses and moulins, as well as their role in routing meltwater through the englacial system and into the subglacial drainage network.

1.2.3.1 Crevasses

Crevasses are open fractures in the ice sheet that can range from a few millimetres to tens of meters wide and tens of meters to kilometres long (Chudley et al., 2021, 2025). They are

surface expressions of glacier stress, formed by extensional flow, compression, or shear, and are intrinsically linked to glacier dynamics (Colgan et al., 2016). With increasing depth, ice overburden pressure causes crevasses to close; however, water pressure can widen and deepen fractures, propagating them through the full ice thickness via hydrofracture (Figure 1.10; van der Veen, 2007; Alley et al., 2005). This process enables crevasses to facilitate meltwater transfer to the subglacial system. Crevasse fields, which may capture up to half of the seasonal surface runoff, are believed to deliver more meltwater to the ice sheet bed than SGLs (Koziol et al., 2017). Crevasse fields allow for spatially distributed, slower meltwater drainage (Chu, 2014). Crevasses are increasing in extent, with a 13 ± 4% rise in the number of crevasses wider than 2 m in west Greenland observed between 1985 and 2009 (Colgan et al., 2011), potentially promoting increased water delivery to the basal system. Additionally, Chudley et al. (2025) found that crevasse volume increased by up to 25.3 ± 10.1% in southeast Greenland between 2016 and 2021, driven by accelerating ice flow.

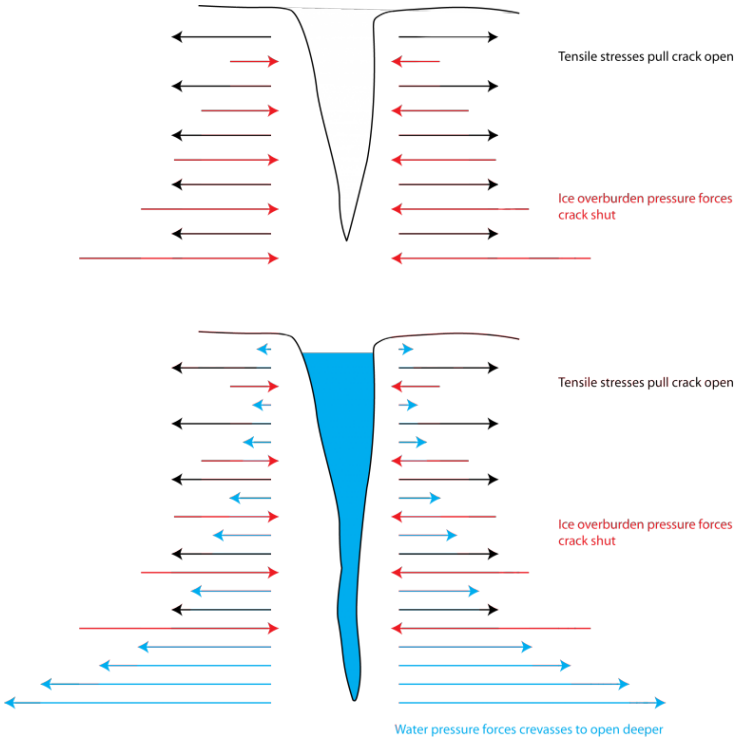

Figure 1.10: Controls on crevasse depth in valley glaciers. After Benn and Evans, 2010. (Source: Bethan Davies, Newcastle University, antarcticglaciers.org).

1.2.3.2 Moulins

Moulins (Figure 1.7d) are vertical ice channels that form through full-thickness fractures in crevasses, developing either during rapid SGL drainage events, where far-field tensile stress

exceeds the ice's fracture toughness, or through prolonged meltwater flow into a crevasse that causes it to enlarge (Hoffman et al., 2018). These features, which range in size from a few centimetres to tens of meters in diameter, enable rapid vertical drainage of meltwater to the en- and sub-glacial environments (Colgan et al., 2011). Moulins create efficient drainage pathways, driven by water pressure exceeding fracture strength and maintained by turbulent meltwater flow (Das et al., 2008; Krawczynski et al., 2009). Banwell et al. (2016) highlight the importance of moulin density and timing in determining the configuration of subglacial drainage on the GrIS, with higher densities facilitating earlier and more widespread basal channelization, while lower densities lead to delayed and more localized channel development. Once moulins have opened, they may act as surface-bed connections for the remainder of the melt season, enabling prolonged meltwater delivery to the ice sheet base (Joughin et al., 2008, Banwell et al., 2013, 2016; Hoffman et al., 2018).

1.2.4 Subglacial hydrology

Subglacial hydrology refers to water present at the base of a glacier, which can be an important control upon glacier dynamics. Water at the ice-bed interface originates from two primary sources: supraglacial inputs delivered to the bed through crevasses, fractures and moulins, and locally sourced basal meltwater produced by geothermal heat or frictional melting on the underside of the ice sheet. During the melt season (May - September), subglacial drainage is dominated by supraglacial inputs. This subsection examines the primary components of the subglacial hydrological system, focusing on drainage configurations and subglacial lakes, which together regulate the efficiency, connectivity, and impact of basal meltwater flow beneath the GrIS.

1.2.4.1 Subglacial drainage configurations

Theoretical models of subglacial drainage morphologies beneath the GrIS are largely derived from studies of Alpine glaciers due to the limited accessibility of the subglacial environment of the ice sheet (Hubbard and Nienow, 1997). Subglacial drainage systems of the GrIS are generally classified into two main configurations: efficient channelized systems and inefficient distributed systems, with a third weakly-connected drainage type recently proposed (Hoffman et al., 2016). Efficient systems include Röthlisberger or Hooke channels, carved upward into the ice (Röthlisberger, 1972), Nye channels, incised into the bed (Nye, 1976), or combinations of both. Inefficient drainage occurs through distributed mechanisms such as thin water films (Weertman, 1962), porous flow (Boulton and Jones, 1979), and linked-cavity systems, the dominant form, which develop as ice slides over bedrock protrusions (Kamb, 1987). The key difference between these configurations lies in their

response to fluctuations in water input. In distributed systems, increased meltwater supply raises water pressure, enlarges cavities, and lowers effective pressure. When discharge surpasses a critical threshold, the system transitions to a channelized configuration, where increased meltwater supply reduces water pressure due to the efficient expansion of channels driven by wall melting and viscous heat dissipation (Kamb, 1987; Röthlisberger, 1972; Schoof, 2010; Mankoff and Tulaczyk, 2017). While distributed systems dominate under low discharge and channelized systems during high discharge, these configurations are not mutually exclusive and can coexist and interact in the same region (Hubbard et al., 1995; Alley, 1996).

1.2.4.2 Subglacial lakes

Subglacial lakes, bodies of water stored beneath ice sheets or glaciers, play an important role in the subglacial hydrology system by acting to buffer the flux of meltwater to the ocean (Fricker et al., 2007; Siegert et al., 2016; Arthur et al., 2025). In Greenland, fewer than 100 subglacial lakes have been identified, mostly near the ice sheet margin where rapidly changing surface conditions challenge detection (Livingstone et al., 2022; Bowling et al., 2019). Subglacial lakes can be stable, maintaining a relatively constant volume, or active, periodically draining and refilling due to surface meltwater inputs that overcome the pressure of the overlying ice (Livingstone et al., 2022; Chandler et al., 2013). Active subglacial lakes, which fill and drain on annual to decadal timescales, influence ice flow by lubricating the ice-bed interface, altering ice discharge speeds, and transferring sediment and nutrients downstream (Siegfried and Fricker, 2018; Malczyk et al., 2020; Vick-Majors et al., 2020). Some active subglacial lakes are hydraulically connected to others, enabling water and sediment exchange (Smith et al., 2017). Observations, such as the 2011 drainage of a subglacial lake in Greenland, suggest these lakes can be fed by surface meltwater through moulins and drain via subglacial tunnels to the ice margin, temporarily impacting ice flow velocities downstream (Palmer et al., 2015).

1.3 Influence of meltwater on the Greenland Ice Sheet

In this section, the influence of meltwater on GrIS dynamics is examined through its interactions with the subglacial environment, ice properties, firn structure, and ocean-driven melting. Key feedback mechanisms, such as the melt-elevation and melt-albedo feedbacks, are discussed in the context of their role in amplifying ice sheet mass loss. The impact of meltwater on ice motion is analysed, highlighting how its delivery to the bed can either enhance or stabilize flow depending on subglacial drainage efficiency. Meltwater infiltration into firn is considered, focusing on its role in densification, ice slab formation, and the development of firn aquifers that regulate water storage and runoff. Finally, the contribution of surface-derived meltwater to oceanic melting at marine-terminating glaciers is explored, with emphasis on how subglacial discharge plumes enhance ice-ocean interactions and accelerate submarine melt.

1.3.1 Feedback mechanisms and albedo

Supraglacial meltwater plays an integral role in amplifying ice sheet mass loss through self-reinforcing feedback processes. One of the most significant is the melt-elevation feedback (Oerlemans, 1981), where substantial melting causes surface lowering, exposing the ice sheet to warmer atmospheric temperatures and enhancing further melt. This effect is compounded by the melt-albedo feedback, in which the transition from reflective snowpack to darker bare ice increases solar radiation absorption, further accelerating melting (e.g., Box et al., 2012). Additionally, biological darkening, driven by glacier algae colonizing exposed ice surfaces, can further reduce albedo and intensify melt (Cook et al., 2020). Ice sheet modelling and paleoclimate reconstructions suggest that once the melt-elevation feedback reaches a critical threshold, it can sustain irreversible ice loss (Levermann and Winkelmann, 2016).

Beyond these broad-scale feedbacks, supraglacial meltwater features–such as SGLs and slush –introduce additional albedo effects that enhance localized melting. The albedo of meltwater and slush is significantly lower than that of snow and bare ice, allowing greater absorption of solar radiation and reinforcing the melt-albedo feedback (Leeson et al., 2015; Lüthje et al., 2006). This process facilitates the expansion of supraglacial meltwater networks, as melting of surrounding snow and ice is enhanced (Lüthje et al., 2006; Box et al., 2012). Field and modelling studies underscore the magnitude of this effect: ablation beneath SGLs has been observed to be 70% to 170% greater than that of bare ice (Grüell et al., 2002; Lüthje et al., 2006), and the presence of slush on Antarctic ice shelves has been linked to a 2.8-fold increase in snowmelt (Dell et al., 2024).

The influence of these feedbacks extends beyond localized melt enhancement to broader atmospheric and climatic interactions. As seasonal albedo declines due to snowline retreat and increasing meltwater coverage, surface-atmosphere heat exchange is altered, modifying local temperature gradients and atmospheric circulation patterns. These effects, in turn, can further accelerate ice loss by influencing melt season duration and the spatial extent of surface melting.

1.3.2 Impact of meltwater on ice dynamics

When surface meltwater reaches the base of the GrIS, if the subglacial hydrological system is inefficient and distributed, then the additional water can increase water pressure at the ice-bed interface, countering the ice overburden pressure, reducing basal friction and increasing ice flow speed (Zwally et al., 2002). If the subglacial hydrological system is efficient and channelized then meltwater is evacuated more effectively, and an increase in basal water pressure does not occur (Bartholomew et al., 2010). An initial acceleration is commonly observed at the onset of each melt season when the subglacial hydrological system is inefficient and thus more susceptible to meltwater-induced speed-up (Bartholomew et al., 2010). This effect stabilises over the course of the melt season as the subglacial network evolves.

On longer timescales, increased surface melt has led to the development of more efficient drainage systems. This has actually resulted in reduced annual ice velocities in some marginal regions of the GrIS, despite increasing surface melt rates. For example, between 1985–1994 and 2007–2014, annual ice velocity in southwestern Greenland decreased by 12%, even as surface meltwater production increased by 50% (Tedstone et al., 2015). This reduction is attributed to the formation of larger, more frequent subglacial channels that act as low-pressure arteries, reducing water pressure across extensive areas (Tedstone et al., 2015; Stevens et al., 2016). However, in higher-elevation regions with lower basal water flux and greater overburden pressure, efficient drainage systems may not fully develop, allowing meltwater inputs to scale positively with ice motion. For instance, a ~2.2% increase in ice motion was observed between cooler and warmer years at 1840 m above sea level, where thick ice and limited drainage efficiency maintain higher subglacial water pressures year-round (Doyle et al., 2014).

Rapid drainage events from SGLs can temporarily overwhelm even efficient subglacial drainage systems. During these events, large volumes of water are transported to the ice-sheet bed, reducing subglacial effective pressure and causing significant short-term accelerations in ice velocity, sometimes up to 400% of pre-drainage levels (Shepherd et al.,

2009; Schoof et al., 2010; Bartholomew et al., 2012; Tedesco et al., 2013; Banwell et al., 2016). However, these accelerations are typically localized and short-lived, lasting hours to days, with ice flow decelerating to pre-drainage velocities shortly after, resulting in minimal net annual acceleration (~1 m yr^{-1}; Das et al., 2008). Beyond these immediate effects, SGL drainage events have longer-term influences on ice dynamics. For example, they can open new moulins which contribute to sustained meltwater delivery throughout the ablation season (Hoffman et al., 2018), aiding the seasonal transition from inefficient, distributed drainage to efficient, channelized systems (Bartholomew et al., 2010). This evolution reduces basal water pressure and thus promotes lower ice velocity over seasonal timescales.

1.3.3 Cryohydrologic warming

The infiltration of meltwater into the ice sheet influences its thermal structure through cryohydrologic warming (Phillips et al., 2010, 2013). As meltwater percolates into firn and ice, it refreezes, releasing latent heat that warms the ice, reduces its viscosity, and enhances deformation, facilitating further meltwater penetration and transport to englacial and subglacial environments. Over time, this process contributes to ice softening, increasing flow velocities and influencing long-term ice dynamics (Poinar et al., 2017). SGL drainage events can further accelerate warming by rapidly injecting large volumes of relatively warm meltwater into cold ice, releasing additional latent heat upon refreezing (Phillips et al., 2010, 2013; Poinar et al., 2017). This localized warming reduces viscosity, increases strain heating, and forms a feedback loop that promotes continued softening and flow acceleration, with lasting consequences for ice sheet dynamics, particularly in regions experiencing sustained meltwater input.

1.3.4 Effect of meltwater on firn

Firn, the transitional layer between fresh snow and glacial ice, covers ~78–92% of the GrIS with a thickness of up to 80 meters (Box et al., 2012; Fausto et al., 2018). Its porous structure acts as a buffer against meltwater runoff by allowing meltwater to percolate, be retained, and refreeze within its pore spaces (The Firn Symposium Team, 2024). Approximately 50% of Greenland's surface meltwater is currently stored or refrozen in the firn, reducing runoff to the ocean (Noël et al., 2018). However, climate warming has degraded firn by decreasing its thickness by 1–1.5 meters since 1980 and has reduced pore space by ~5% (Kuipers Munneke et al., 2015).

Meltwater infiltration into firn significantly alters its structure and properties (Figure 1.11). This process leads to firn densification, where porous, low-density snow transitions into

compacted, higher-density firn. This occurs as meltwater rounds and lubricates grains, increasing their size and enhancing compaction (Colbeck, 1982). Refreezing further increases firn density by filling pore spaces with ice, forming impermeable ice layers, lenses, and pipes that reduce permeability and water storage capacity (Braithwaite et al., 1994). Refreezing also releases latent heat, warming the surrounding firn and decreasing its capacity to refreeze subsequent infiltration, creating feedback loops between meltwater infiltration, thermal conditions, and firn structure (Vandecrux et al., 2020; The Firn Symposium Team, 2024). These processes can lead to the development of ice slabs (MacFerrin et al., 2019) and firn aquifers (Miège et al., 2016; Forster et al., 2014), which export meltwater from the firn to other parts of the hydrological system.

Ice slabs, which cover 60,400–73,500 km² of the ice sheet, have expanded by 37–44% in Greenland between 2012 and 2018 (Jullien et al., 2023; MacFerrin et al., 2019). These slabs form at lower elevations with high melt rates and limited snowfall, blocking vertical percolation and forcing meltwater to flow laterally. This contributes to surface runoff, supraglacial stream formation, and SGL expansion (Machguth et al., 2016; Tedstone et al., 2022). Firn aquifers, subsurface reservoirs of liquid water insulated by overlying snow, form in high-melt, high-accumulation areas where meltwater saturates the firn and resists freezing (Kuipers Munneke et al., 2015). Covering at least 21,900 km², these aquifers store significant water volumes, such as the 2.2–4.8 Gt reservoir at Helheim Glacier (Montgomery et al., 2017; Koenig, 2014). While aquifers delay surface runoff in the short term, they can drain to the ice-sheet bed through hydrofracture, supplying year-round water to subglacial systems and influencing seasonal ice velocity fluctuations (Poinar et al., 2017, 2019).

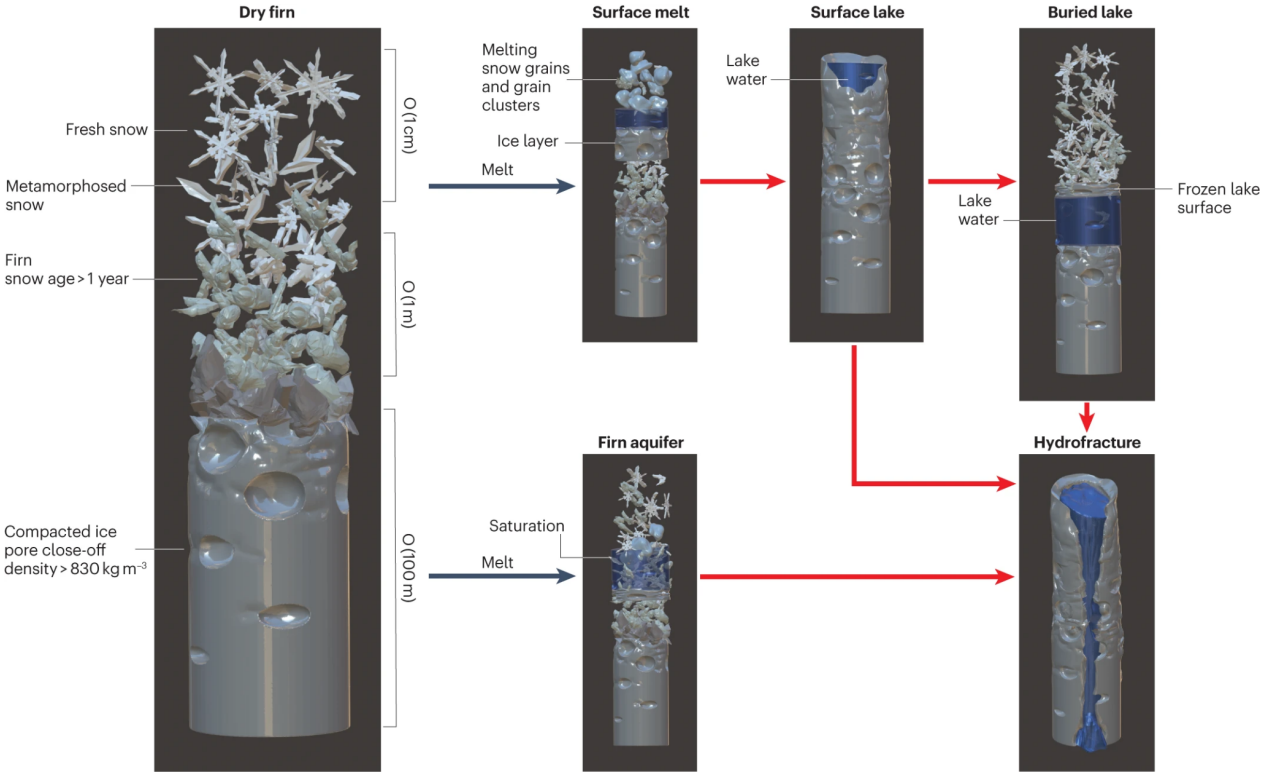

Figure 1.11: A diagram illustrating a dry firn column experiencing melting, which produces surface hydrological features like meltwater that could lead to hydrofracture (Source: The Firn Symposium Team, 2024).

1.3.5 Meltwater and ocean-driven melting

The release of surface-derived meltwater into the ocean plays a critical role in modulating submarine melting, calving, and fjord circulation at Greenland's marine-terminating glaciers (Figure 1.12). During the melt season, large volumes of supraglacial meltwater drain through the ice sheet and emerge at depth as subglacial discharge plumes. These buoyant plumes entrain warmer, saltier seawater as they rise along the glacier front, enhancing mixing across the ice-ocean boundary layer and accelerating submarine melting (Jenkins, 2011; Slater et al., 2018). While oceanic heat transport is a key driver of ice loss in Greenland's fjords, recent work suggests that the atmosphere plays a first-order role in governing submarine melting, particularly by regulating surface meltwater availability. Even in the absence of direct ocean warming, a warming atmosphere can amplify submarine melting by increasing meltwater discharge, which enhances heat transfer from the ocean to the ice (Slater and Straneo, 2022). At the ice sheet scale, atmospheric forcing dominates in some regions, such as northwest Greenland, whereas oceanic variability exerts stronger control in others, such as the south (Slater and Straneo, 2022).

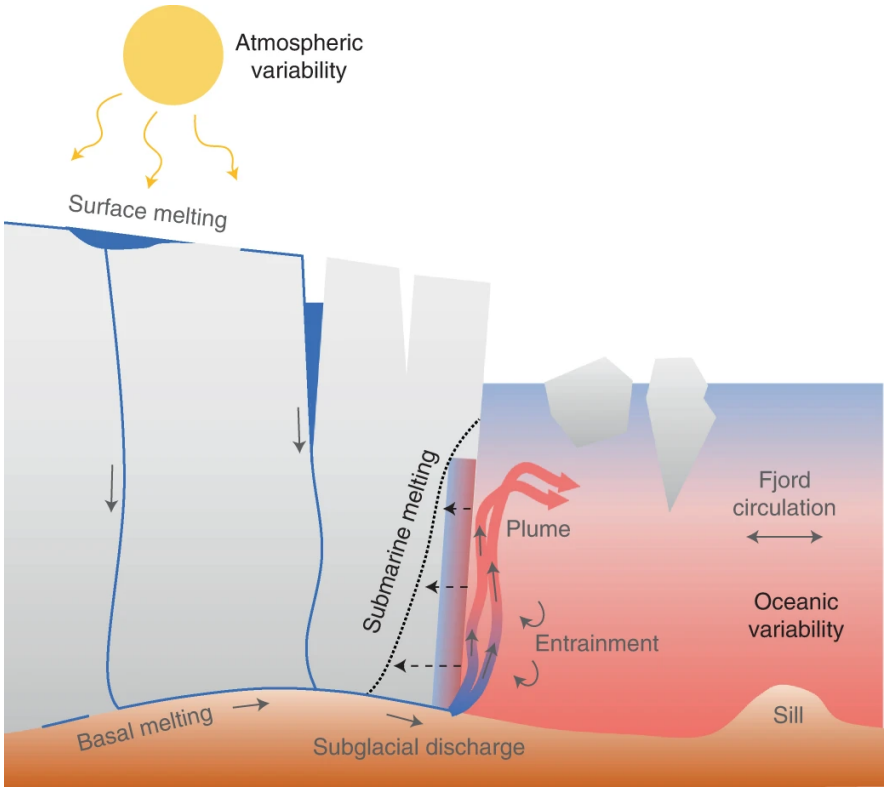

Figure 1.12: Schematic of submarine melting at marine-terminating glaciers being driven by subglacial discharge plumes, which entrain warm fjord waters and are influenced by both atmospheric meltwater input and oceanic heat availability. (Source:* Slater and Straneo, 2022*).

1.4 The future of meltwater and its influence on the Greenland Ice Sheet

Under all future emissions scenarios outlined by the IPCC–ranging from low-emission pathways such as RCP2.6 to high-emission pathways like RCP8.5–Greenland's atmosphere is projected to warm, leading to intensified surface melt (Fettweis et al., 2013; IPCC, 2021). As such, the GrIS is expected to undergo profound changes in its hydrological system, with increased meltwater production influencing surface processes, ice dynamics, and firn structure. This section examines these projected changes, focusing on the inland expansion of SGLs and their role in enhancing basal lubrication, contributing to cryo-hydrologic warming, and impacting seasonal ice flow acceleration. The implications of evolving subglacial drainage efficiency for ice dynamics are considered, highlighting regional differences in long-term flow trends. Changes in firn properties, including reductions in firn thickness, air content, and meltwater storage capacity, are explored in the context of their role in the expansion of ice slabs, which amplify runoff and accelerate sea-level rise. Finally, the increasing frequency and intensity of extreme melt events are assessed, with emphasis on their role in mass loss and long-term ice sheet stability.

1.4.1 Expansion of supraglacial lakes

Future projections suggest that SGLs will form at even higher elevations, extending further inland where gentler surface slopes may allow them to grow larger (Figure 1.13; Leeson et al., 2015; Luthje et al., 2006). Leeson et al. (2015) estimate that under RCP 4.5 and RCP 8.5 scenarios, SGLs could expand inland by 103 km and 110 km, respectively, by 2060. This expansion is expected to increase the total SGL-covered area on the GrIS by 48–53%. As SGLs expand, surface melting may be further amplified due to albedo-driven impacts, with projected increases in meltwater volume of 0.7–0.8% – more than double the current contribution from SGLs and equivalent to an additional 6.6–8.5 Gt of meltwater per year across the ice sheet. Up to half of these newly formed SGLs may grow large enough to drain, enhancing basal lubrication but may also contribute to cryo-hydrologic warming, particularly in regions with inefficient subglacial drainage. Under RCP 4.5, Leeson et al. (2015) estimate that between 4–51% of SGLs could become large enough to hydro-fracture, while under RCP 8.5, this number rises to between 8–50%, potentially triggering rapid drainage events. Consistent with these trends, Ignéczi et al. (2016) project that SGL volumes will increase by 113% under RCP 4.5 and 174% under RCP 8.5 by the late 21st century, with the most substantial growth in the northeastern sector of the ice sheet and more moderate increases in the west.

While large, sudden meltwater inputs to the bed from SGL drainages can trigger short-term accelerations, these events often promote rapid channelization, limiting their long-term impact on ice velocity (Das et al., 2008; Hoffman et al., 2011). However, Poinar et al. (2015) find that crevasses–and thus moulins–are unlikely to form above ~1600 m, limiting direct drainage from SGLs at higher elevations. Consequently, meltwater in these regions primarily flows via surface streams to existing moulins downstream, suggesting that the inland expansion of SGLs will have a limited impact on extending melt-induced seasonal ice flow acceleration. However, studies have observed SGL drainage events at elevations >1600 m a.s.l.; for example, Yang et al. (2021) found that at elevations > 1600 m, 21% of SGLs drain into moulins on southwest GrIS during the 2015 melt season.

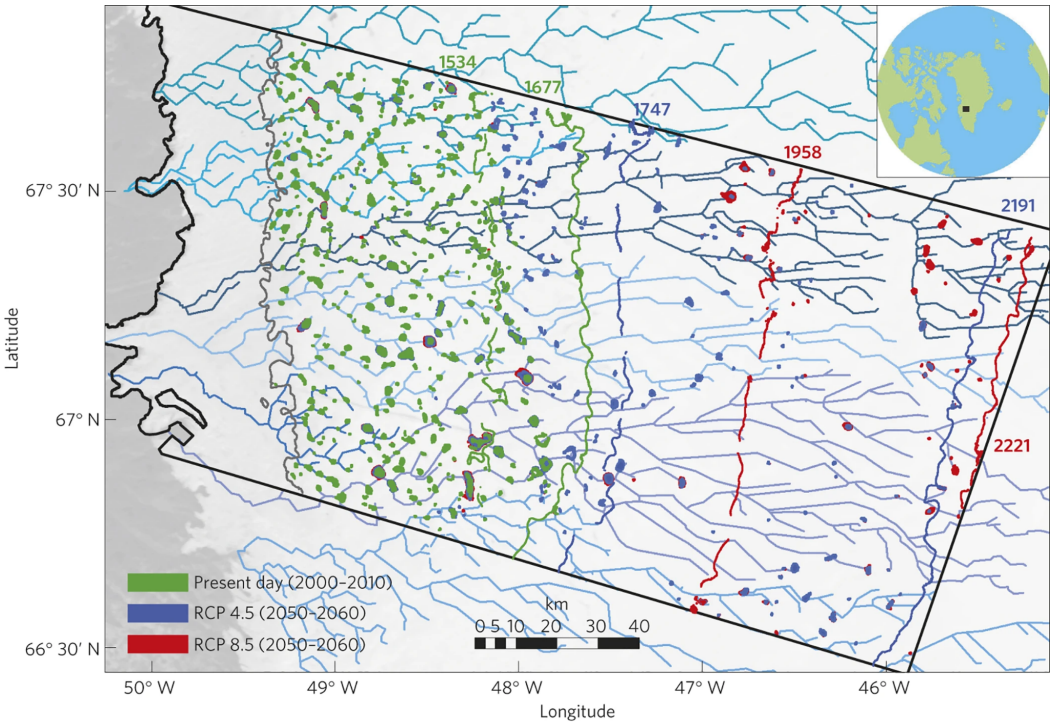

Figure 1.13: the projected expansion of SGLs under different climate scenarios (Source: Leeson et al., 2015).

1.4.2 Future ice dynamics

It has been suggested that in land-terminating systems, dynamic changes due to enhanced meltwater will be limited in future due to the compensating effect when increased meltwater drives the development of efficient subglacial drainage (e.g., Nienow et al., 2017; Tedstone et al., 2013; Sole et al., 2013). Davison et al. (2019) suggest that future increases in runoff may enhance seasonal ice flow variability but lead to contrasting long-term trends across the ice sheet. In regions with well-connected drainage systems, annual ice flow will likely decline due to increased drainage efficiency and reduced basal water pressure, while further inland,

areas with developing hydrological connectivity may experience increased ice flow unless self-regulation mechanisms expand.

1.4.3 Meltwater in firn

It is likely that future climate changes will impact the firn layer of the GrIS, both directly through increased surface melt and indirectly via alterations in hydrological features such as ice slabs and firn aquifers (The Firn Symposium Team; Lenaerts et al., 2020; Fettweis et al., 2013; Flowers, 2018). Reduced snowfall, increased refreezing, and the expansion of the ablation zone are expected to decrease firn thickness, air content, and meltwater storage capacity. These changes will diminish the firn's ability to buffer meltwater, leading to increased runoff and amplifying the GrIS's contribution to global sea-level rise. The extent of these impacts will depend on future warming trajectories, with strong mitigation efforts offering the most effective means to limit firn degradation and its cascading effects on the ice sheet and global sea levels.

A key factor in this process is the expansion of ice slabs. MacFerrin et al. (2019) project that the area covered by ice slabs will approximately double by 2050, significantly accelerating runoff from the ice sheet interior as meltwater infiltration decreases. Although runoff from the top of ice slabs has contributed less than one millimetre to global sea-level rise so far, this contribution is projected to grow substantially as ice slabs expand inland in a warming climate. By 2100, runoff over ice slabs is expected to contribute between 7 to 33 mm under moderate-emissions scenarios and 17 to 74 mm under high-emissions scenarios (MacFerrin et al., 2019). This represents approximately double the estimated runoff from Greenland's high-elevation interior, as predicted by SMB models that do not account for the presence of ice slabs. Without accounting for ice slabs, regional climate models may significantly underestimate future meltwater discharge.

Compounding this issue, Noël et al. (2022) predict that peak firn refreezing will occur around the year 2126 ± 14 under extreme warming scenarios, driven by increased meltwater production saturating the firn layer. Beyond this peak, the GrIS's ability to retain meltwater will sharply decline as firn porosity decreases and ice lenses expand, limiting percolation and refreezing capacity. This reduction in firn refreezing will result in greater surface runoff and reduced meltwater storage, amplifying the GrIS's contribution to sea-level rise more than twenty-fold compared to recent decades. Even under moderate warming, peak refreezing is expected by the year 2172 ± 20, reflecting the long-term susceptibility of firn to persistent meltwater input. In contrast, low-end warming scenarios stabilize firn refreezing capacity

after 2100, highlighting the importance of mitigation efforts in preserving the firn's role as a critical meltwater buffer.

1.4.4 The role of extreme melt events

Extreme melt events are expected to increase in both frequency and intensity on the GrIS. Frequent extreme events under high emission scenarios could raise sea level by 20 to 450 mm and reduce ice sheet area by an additional 6,000 to 26,000 km² by the year 2300 compared to scenarios without such extremes (Beckmann & Winkelmann, 2023). While extreme events can temporarily reduce surface velocities due to surface thinning, the combined effects of dynamic processes and SMB amplify mass loss, raising sea level contributions by over 30% compared to SMB-only models by 2300 (Beckmann & Winkelmann, 2023). However, Ing et al. (2024) demonstrated that late-season extreme melt events contribute only ~2% more annual ice discharge compared to scenarios without such speed-ups. While these events can induce temporary acceleration of GrIS motion, with velocities increasing by up to ~240%, their isolated impact on net mass loss via ice discharge remains limited.

Chapter 2

Techniques for identifying supraglacial hydrology via remote sensing

To effectively monitor and study supraglacial hydrology, a variety of methods have been employed. Traditional approaches, such as field-based observations and airborne surveys (e.g., Gleason et al., 2016), have provided invaluable data but are limited logistically and by both spatial and temporal coverage. More recently, numerical models (e.g., Leeson et al., 2012; Gantayat et al., 2023) have been developed to simulate hydrological processes, but their accuracy depends on the quality and resolution of input data. This thesis focuses on satellite remote sensing of supraglacial hydrology.

This chapter introduces the topic of satellite remote sensing for supraglacial meltwater mapping and provides an overview of the L8 and S2 missions, the main data sources used in this thesis. Methods for delineating supraglacial hydrology in satellite imagery are reviewed, including manual delineation, image thresholding, and machine learning (ML) based approaches. The chapter concludes by addressing the challenges and limitations of satellite remote sensing in this context, highlighting key knowledge and capability gaps that inform the aims and objectives of this thesis.

2.1 Satellite remote sensing

Remote sensing is a technique used to collect information from the Earth's surface by sampling reflected and emitted electromagnetic radiation, typically from airborne or spaceborne instruments (Horning, 2008). In Glaciology, remote sensing has become indispensable for studying vast, often inaccessible regions over extended timescales. Advancements over the past 50 years have transformed cryospheric research, allowing continuous, large-scale observation of ice sheets and glaciers (Tedesco, 2015). On the GrIS, satellite data have been essential for tracking mass balance, analyzing ice velocity over multi-decadal timescales and improving understanding of ice sheet hydrology.

Remote sensing instruments are either passive or active: the former is when a sensor measures reflected solar radiation from the Earth's surface, and the latter is when the sensor emits a beam which measures reflected backscatter from a target. Passive instruments typically employ multi- or hyper-spectral sensors, and resolve in the optical, thermal, and microwave parts of the electromagnetic spectrum. Passive sensors are unable to resolve the surface of the Earth in dark or cloudy conditions, which can be a major limitation when

studying regions like Greenland and Antarctic as they endure periods of polar night through winter.

The spatial resolution of these sensors varies, and as such, so does the type of information retrieved. Coarse-resolution examples of passive remote sensors (i.e. those with a spatial resolution greater than 250 m) include The Moderate Resolution Imaging Spectroradiometer (MODIS) and Advanced Very High Resolution Radiometer (AVHRR). Owing to the fine temporal resolution of these sensors, data acquired has been successfully used to characterize rapidly evolving supraglacial hydrology on the AIS and GrIS (e.g. Sundal et al., 2009; Williamson et al., 2017; Selmes 2011, 2013; Morriss et al., 2013), although this is at the expense of detecting small-medium and narrow features. Medium-resolution passive sensors (those with a spatial resolution between 10 – 250 m) are capable of resolving smaller-scale supraglacial meltwater features, such as small SGLs (e.g. Williamson et al., 2018b) and rivers (e.g. Yang et al., 2019). Examples of such sensors include S2, Landsat 1 – 9, and Advanced Spaceborne Thermal Emission and Reflection Radiometer (ASTER). Medium scale sensors have been used to map supraglacial hydrology and extract meltwater characteristics both regionally (e.g. Otto et al., 2022; Dell et al., 2020; Arthur et al., 2020; Rawlins et al., 2023) and ice-sheet wide (e.g. Zhang et al., 2023; Corr et al., 2022; Stokes et al., 2019).

Active remote sensors can operate in cloudy and dark conditions and are capable of penetrating materials such as snow and firn (e.g., Benedek and Willis; Miles et al., 2017). These sensors include Radio Detection and Ranging (RaDAR), Laser Imaging Detection and Ranging (LiDAR), and Sound Navigation and Ranging (SoNAR). In recent years, Synthetic Aperture Radar (SAR) has been increasingly used to detect surface and subsurface lakes on the GrIS and AIS. Unlike optical imagery, which relies on direct visual contrast, SAR identifies differences in the backscatter signal of SGL features relative to the surrounding environment. However, interpreting SAR signals can be challenging due to factors such as scattering effects, surface roughness, and the complexity of subsurface reflections (Miles et al., 2017). Sentinel-1 (S1), for example, has been employed to map both surface and subsurface lakes on the GrIS (Jiang et al., 2022; Miles et al., 2017; Dunmire et al., 2021; Benedek and Willis, 2020). While SAR is effective for certain applications, it is less suitable for detecting features like slush because of its sensitivity to surface roughness and the complex scattering associated with variable meltwater conditions. Additionally, SAR cannot measure the depth or volume of SGLs, as microwave signals are strongly attenuated in water, preventing penetration below the surface.

NASA's Ice, Cloud, and land Elevation Satellite (ICESat-2) laser altimeter is an active sensor capable of directly measuring SGL depths from space (e.g., Arndt and Fricker, 2024; Lutz et al., 2024; Melling et al., 2024). This is possible because its green laser light penetrates the water's surface, allowing the detection of photons reflected from both the SGL surface and the SGL bed. Although ICESat-2 provides highly accurate depth measurements, its spatial coverage is limited to narrow, one-dimensional ground tracks that are widely spaced. As a result, it offers detailed information along specific paths but lacks continuous coverage across large areas.

High-resolution optical imagery, such as L8 and S2, has been particularly useful for surface hydrology studies, particularly the monitoring of meltwater features such as SGLs, channels and slush (Williamson et al., 2017, 2018a; Hochreuther et al., 2021; Rawlins et al., 2023; Yang et al., 2019; Lu et al., 2021; Miles et al., 2017; Yang et al., 2021). The integration of multiple satellite sensors is now commonly employed to optimize trade-offs between resolution and return period, improving our understanding of meltwater feature evolution both within and between melt seasons. While fieldwork remains crucial for ground-truthing and process studies, the integration of remote sensing with in situ measurements continues to drive advancements in ice sheet hydrology.

2.1.1 Landsat 8

The Landsat mission, orchestrated by NASA and the USGS, has allowed for uninterrupted monitoring of the Earth's surface since 1972 by providing moderate scale resolution multi-spectral imagery. The Landsat 8 (L8) satellite was launched in 2013. The L8 satellite undergoes a sun-synchronous near polar orbit around the earth at an altitude of 705 km, with a 185 km swath and a repeat cycle of 16 days.

The L8 satellite has two sensors onboard: The Operational Land Imager (OLI) and the Thermal Infrared Sensor (TIRS). OLI captures data across eight short-wave multispectral bands at 30 m resolution, and a single panchromatic band at 15 m resolution (Band 8; Table 2.1). TIRS collects data from two longwave infrared bands at 100 m resolution (Band 10 and 11). Both OLI and TIRS are push-broom sensors, using linear arrays of detectors to capture imagery line by line as the satellite moves along its orbit. Unlike older whisk-broom sensors, which scan side-to-side with a single detector, push-broom sensors acquire data more efficiently. OLI and TIRS operate in tandem to collect multispectral and thermal data simultaneously.

L8 imagery (Figure 2.1) has been frequently used to detect, measure, and monitor supraglacial hydrology on both the AIS (e.g. Stokes et al., 2019; Banwell et al., 2021; Moussavi et al., 2020; Dell et al., 2020; Corr et al., 2022; Arthur et al., 2020) and GrIS (e.g. Pope et al., 2016; Williamson et al., 2018b; Miles et al., 2017; Yang et al., 2021).

L8 data are free of charge and can be acquired from the USGS EROS EarthExplorer website: https://earthexplorer.usgs.gov/.

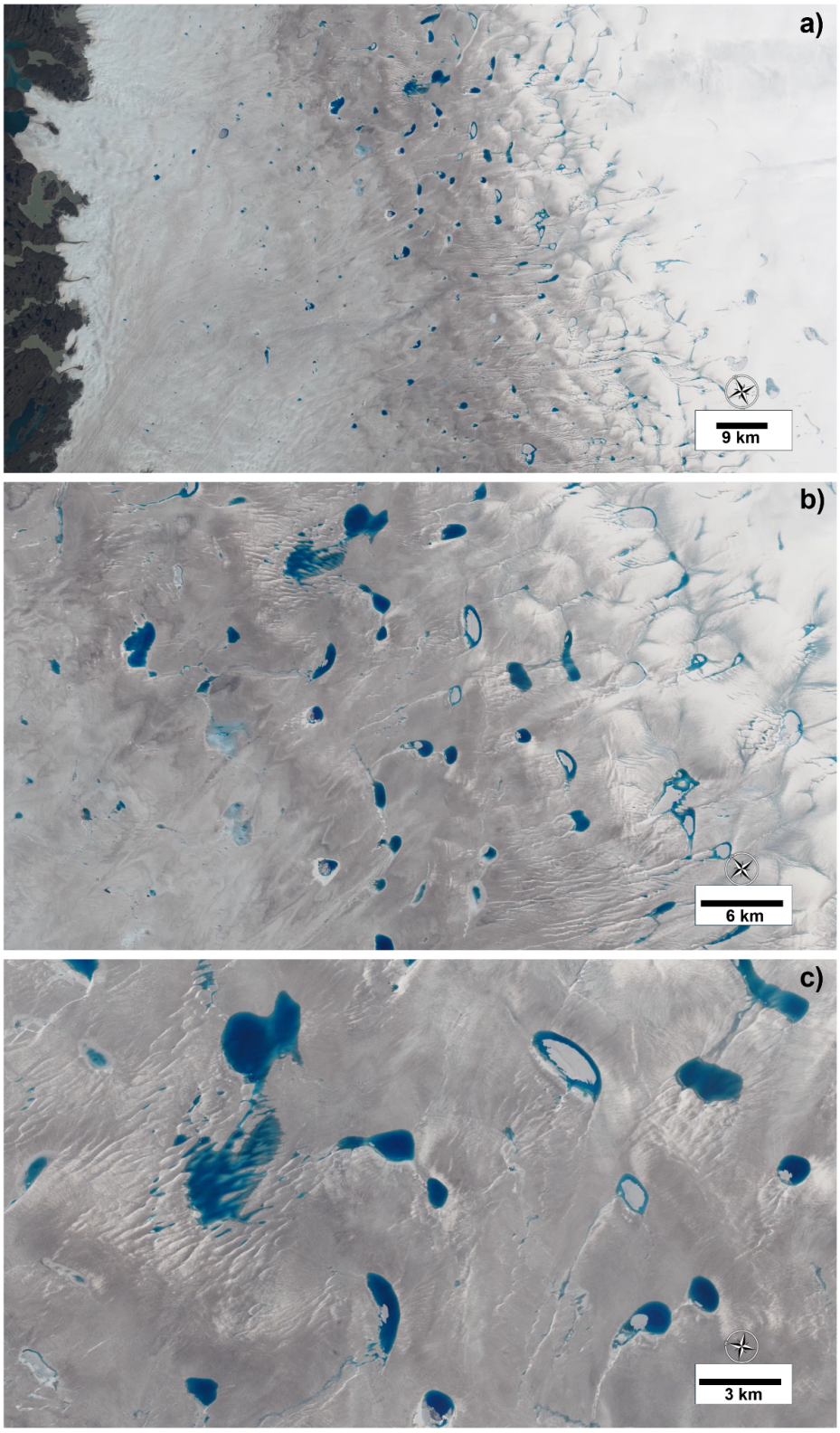

Figure 2.1: SGLs on the western GrIS, derived from NASA/USGS L8 imagery on July 12, 2014, at a) 9 km, b) 6 km, c) 3 km. The image is a composite of red, green, and blue channels (bands 4, 3, and 2). Source: (Dr. Allen Pope and NASA's Goddard Space Flight Center, https://svs.gsfc.nasa.gov/11973/).

Table 2.1: L8 bands, their central wavelength and resolution

L8 Bands	Central Wavelength (μm)	Resolution (m)
Band 1 - Coastal aerosol	0.44	30
Band 2 - Blue	0.48	30
Band 3 - Green	0.56	30
Band 4 - Red	0.655	30
Band 5 - Near Infrared (NIR)	0.865	30
Band 6 - SWIR 1	1.61	30
Band 7 - SWIR 2	2.2	30
Band 8 - Panchromatic	0.59	15
Band 9 - Cirrus	1.37	30
Band 10 - Thermal Infrared (TIRS) 1	10.895	100
Band 11 - Thermal Infrared (TIRS) 2	12.005	100

2.1.2 Sentinel-2

ESA's S2 mission provides high resolution multispectral satellite imagery, which is used throughout this thesis. The mission comprises two identical satellites: S2-A (launched in 2015) and S2-B (launched in 2017). The S2 satellites are situated in the same sun-synchronous orbit, although they are phased at 180 to ensure a high revisit time. Separately, the S2 satellites have a revisit time of 10 days, which is reduced to 5 days when combined. The satellites orbit the earth at an altitude of 786 km and have a swath of 290 km. A third satellite, Sentinel-2C, was launched in 2024 and became operational in early 2025 to ensure mission continuity and maintain high temporal coverage as S2-A nears the end of its design lifetime.

Both satellites carry a Multi-Spectral Instrument (MSI): a push-broom sensor which samples 13 spectral bands. MSI senses from Visible (VNIR) and Near Infra-Red (NIR) to the Short Wave Infra-Red (SWIR), with four bands at spatial resolution of 10 m, six bands at 20 m and three bands at 60 m (Table 2.2).

Owing to its fine spatial resolution and frequent revisit time, S2 data (Figure 2.2) has been used to resolve the characteristics and evolution of meltwater of the surface of both the AIS (e.g. Moussavi et al., 2020; Kingslake et al., 2017; Bell et al., 2017; Stokes et al., 2019; and GrIS (e.g. Williamson et al., 2018b; Hochreuther et al., 2021; Rawlins et al., 2023; Yang et al., 2019; Lu et al., 2021).

S2 and L8 data can also be combined to produce a dataset with a higher temporal sampling than using just one sensor or the other, which allows for fine temporal and spatial scale tracking of meltwater evolution (e.g. Williamson et al., 2018; Moussavi et al., 2020; Corr et al., 2022). Although, it should be noted that, due to the differing radiometric and spatial properties of each sensor, merging these data can be challenging.

S2 data can be acquired freely from the Copernicus Open Access Hub: https://scihub.copernicus.eu/.

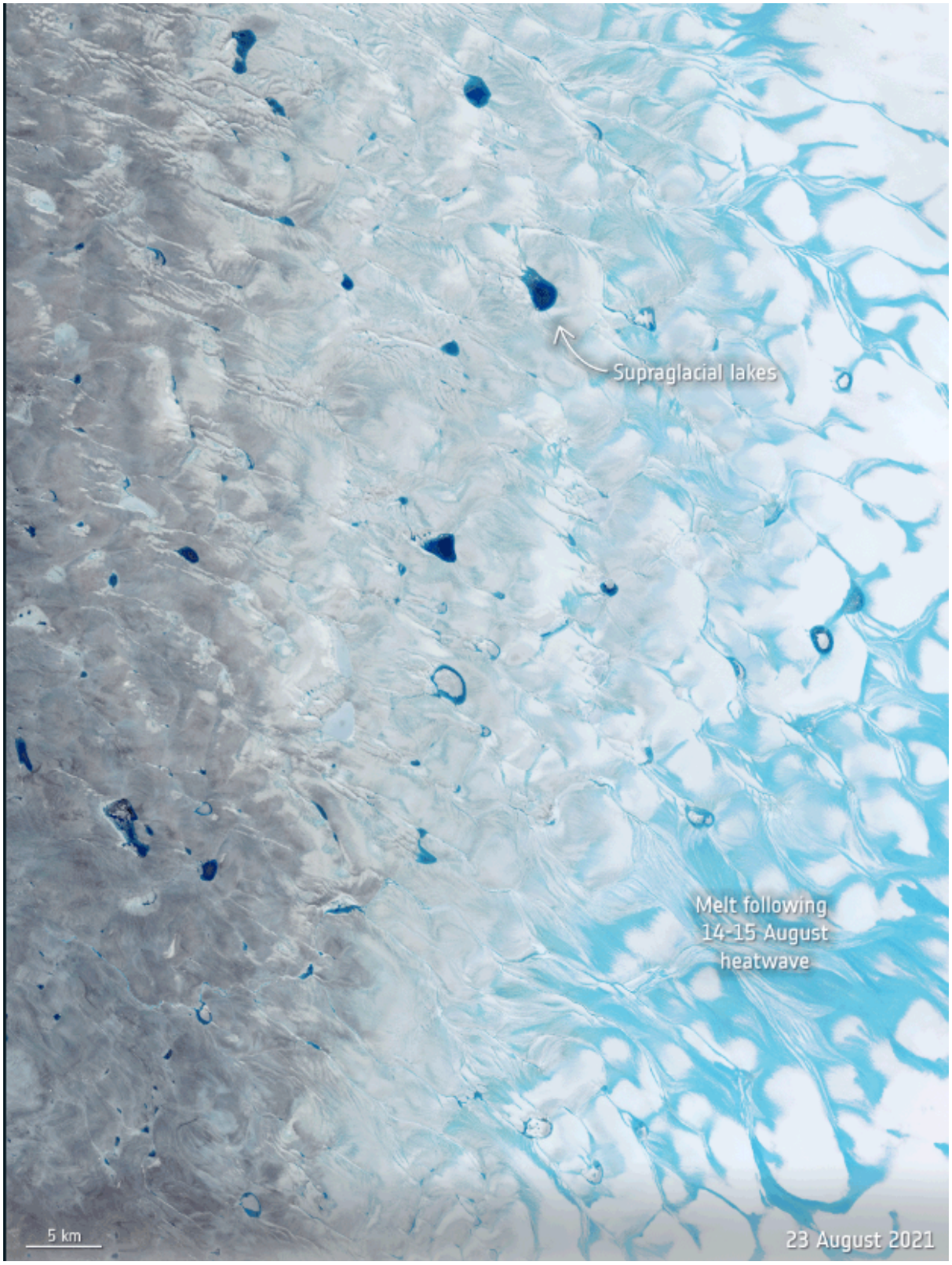

Figure 2.2: Animated Gif of changes in meltwater and SGLs on the GrIS from August 1 to August 23, 2021, derived from Copernicus S2 imagery. Credit: ESA, contains modified Copernicus S2 data (2021), processed by ESA. (Source: https://www.esa.int/ESA_Multimedia/Images/2022/05/Meltwater_and_surface_lakes_on_the_Greenland_ice_sheet).

Table 2.2: S2 bands, their central wavelength and resolution

S2 Bands	Central Wavelength (μm)	Resolution (m)
Band 1 - Coastal aerosol	0.443	60
Band 2 - Blue	0.49	10
Band 3 - Green	0.56	10
Band 4 - Red	0.665	10
Band 5 - Vegetation Red Edge	0.705	20
Band 6 - Vegetation Red Edge	0.74	20
Band 7 - Vegetation Red Edge	0.783	20
Band 8 - NIR	0.842	10
Band 8A - Vegetation Red Edge	0.865	20
Band 9 - Water vapour	0.945	60
Band 10 - SWIR - Cirrus	1.375	60
Band 11 - SWIR	1.61	20
Band 12 - SWIR	2.19	20

2.2 Supraglacial meltwater feature delineation methods

Mapping SGLs, channels, and slush areas enables researchers to quantify seasonal and interannual changes in melt extent, assess potential impacts on ice sheet dynamics, and improve predictions of meltwater runoff into the ocean. Additionally, understanding the spatial and temporal evolution of these features provides insight into ice-sheet-wide hydrological connectivity and the efficiency of supraglacial-to-subglacial meltwater transfer. Since surface meltwater can contribute to dynamic ice loss through hydrofracture and basal lubrication, as well as directly to SLR via runoff into the ocean, accurately delineating these features is essential for constraining projections of Greenland's future contribution to global sea level. Various methods have been developed to classify meltwater features in satellite imagery, ranging from manual delineation to automated approaches that leverage spectral indices, image thresholding, and ML. Below, this section provides a review of these methods, highlighting their strengths and limitations.

2.2.1 Manual delineation

Manual delineation has been widely used to map meltwater features on the GrIS. This method involves interpreting satellite imagery and manually tracing SGL and channel outlines using visual cues, band combinations, or indices like the Normalized Difference Water Index (NDWI). In Greenland, studies such as McMillan et al. (2007) and Lampkin and VanderBerg (2011) have utilized manual delineation to identify 292 and 1,190 SGLs from ASTER and Landsat-7 imagery, respectively. The key advantage of manual delineation lies in its precision, as it allows researchers to incorporate expertise and prior knowledge to identify complex or subtle features that automated methods might miss. However, this approach is labour-intensive, time-consuming, and prone to user bias (Langley et al., 2016; Williamson et al., 2017). Due to these limitations, semi- and fully-automated methods are now preferred for large-scale assessments. These approaches leverage advanced algorithms and ML techniques to efficiently analyse large datasets, providing consistent and objective detection of meltwater features across regional to ice-sheet-wide scales (Stokes et al., 2019; Moussavi et al., 2020).

2.2.2 Thresholding

Image thresholding is the standard approach for mapping supraglacial hydrology on the Earth's ice sheets (Moussavi et al., 2020; Stokes et al., 2019; Williamson et al., 2017; Corr et al., 2021). First applied to the GrIS by Box and Ski (2007), this method classifies pixels as 'water' or 'non-water' based on an optimized threshold. Open water appears dark blue in optical satellite imagery due to stronger red light attenuation relative to blue light. NDWI

exploits these spectral properties to distinguish meltwater features from ice and snow (Morriss et al., 2013; Liang et al., 2012; Pope et al., 2016; Yang and Smith, 2012; Sneed and Hamilton, 2007; Box and Ski, 2007).

Originally developed for terrestrial applications, NDWI combines NIR and green wavelengths to enhance open water detection while minimizing interference from soil and vegetation (McFeeters, 1996). However, its suitability for ice sheets is limited, as snow, ice, and firn exhibit low NIR reflectance (Yang and Smith, 2012). To address this, most recent studies use NDWI_ice (Yang and Smith, 2012), which applies a red/blue reflectance threshold (typically 0.2–0.5) better suited to glaciological environments (Fitzpatrick et al., 2014). While effective, NDWI_ice can misclassify features with similar spectral signatures (e.g., rocks, clouds, shadows) and struggles with detecting shallow or narrow meltwater bodies (Arthur et al., 2020). Refining thresholding techniques can reduce classification errors and improve accuracy (Moussavi et al., 2020). A more robust classification method, integrating NDWI_ice with the Normalized Difference Snow Index (NDSI; Hall et al., 1995), has been successfully applied to five East Antarctic ice shelves, reducing misclassification of clouds and rocks and improving detection of shallow SGLs (Moussavi et al., 2020). Corr et al. (2021) extended this approach across all Antarctic ice shelves, achieving high accuracy (98.7%–98.3%) for S2 and L8 imagery.

To further improve classification, additional processing steps–such as masking non-water features–are required, often supplemented by manual refinement. While thresholding has been used to delineate shallow surface water and slush on the Greenland (Yang and Smith, 2013) and Antarctic (Bell et al., 2017) ice sheets, few studies explicitly focus on slush detection. Lower NDWI_ice thresholds (e.g., 0.12–0.14) have been applied for this purpose, but further research is needed to refine these methods.

Identifying supraglacial rivers in satellite imagery is challenging due to their narrow widths (< 30 m) and spectral similarity to slush, which complicates differentiation using traditional remote sensing techniques (Yang and Smith, 2012). Thresholding methods alone are insufficient for detailed mapping of these hydrological networks, necessitating advanced processing approaches. Yang and Smith (2013) introduced the first automated method for extracting supraglacial channels, later refined in subsequent studies (Yang et al., 2016; 2019; Figure 2.3). Their approach, applied to WorldView, S2, and Landsat imagery, combines NDWI with noise reduction via a band-pass filter, Gabor filtering to highlight river cross-sections, and a path-opening operator for improved connectivity (Yang et al., 2019; Lu et al., 2021; Yang et al., 2021). This method demonstrates high accuracy (~97.8%), with a true positive rate of ~94.3% and a false positive rate of ~1.8% on L8 imagery (Yang et al.,

2016). Under optimal conditions, it can detect rivers as narrow as ~3 m in 15 m L8 imagery (Yang et al., 2016).

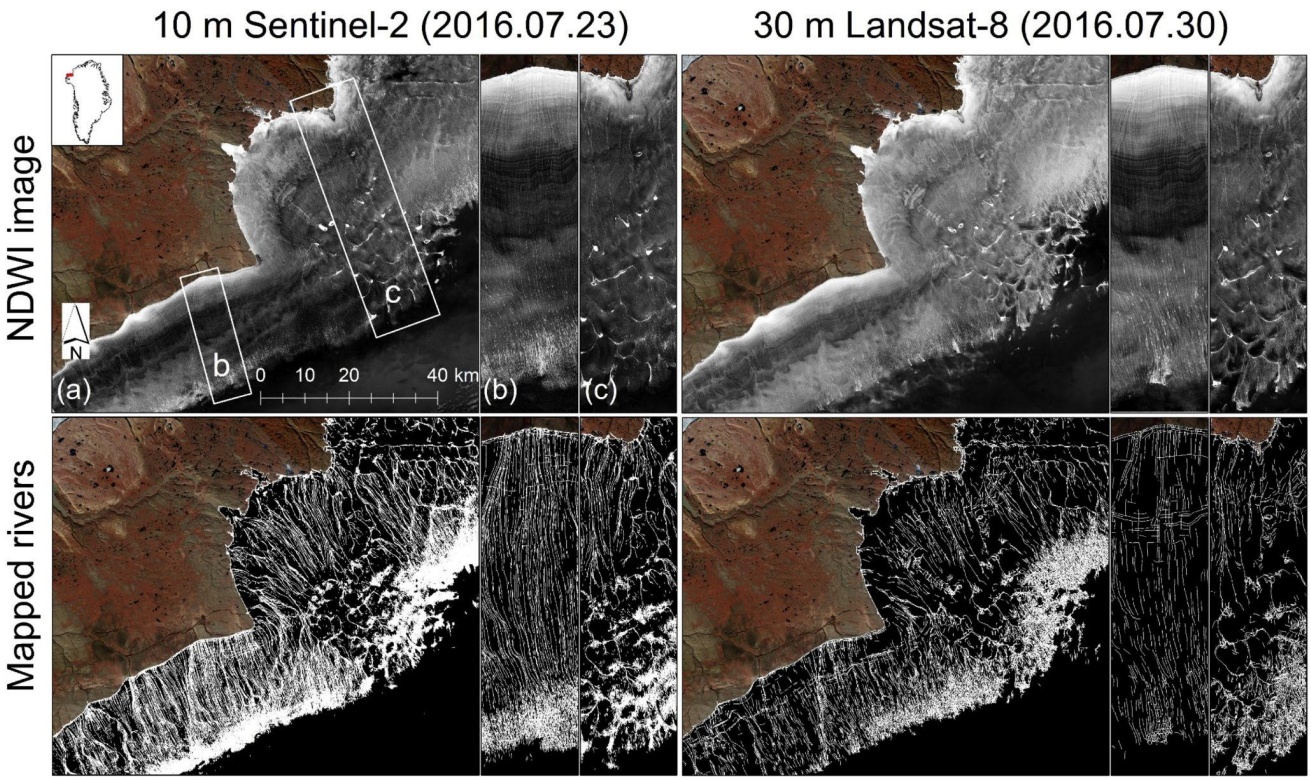

Figure 2.3: Supraglacial river networks on the northwest GrIS, mapped from 10 m S2 (23 July 2016) and 30 m L8 (30 July 2016) images (Source: Yang et al., 2019).

2.2.3 Machine learning

ML is a subset of artificial intelligence (AI) that enables systems to improve their performance autonomously by learning from data, without explicit programming. It builds models that simulate human learning, allowing systems to identify patterns, make predictions, and generalize to unseen data. ML algorithms can be broadly categorized into three main types: supervised learning, unsupervised learning, and reinforcement learning.

Supervised learning algorithms use labelled training data to perform classification. The model learns by adjusting its weights as input data is processed, comparing predictions to the actual labels, and refining itself based on the results. This process includes cross-validation to avoid overfitting or underfitting. The model continues to adjust until it reaches the desired accuracy or learning plateaus. Once trained, the model can apply the learned relationships between input variables and outcomes to classify new, unseen data. Unsupervised learning algorithms group unlabelled data by identifying patterns, similarities,

and differences within the data. These algorithms do not require human intervention or labelled data. Instead, they allow the system to independently discover hidden structures or relationships in the data, such as clustering similar data points together or reducing the dimensionality of the data. Reinforcement learning allows models to self-correct through trial and error, using environmental feedback (positive or negative) to improve performance without labelled data. The algorithm is rewarded for desired outcomes and penalized for undesired ones, gradually optimizing its actions over time. Deep learning, a specialized branch of ML, leverages multiple layers of neural networks to process complex data and solve intricate tasks by simulating the decision-making process of the human brain.

While ML has been applied to satellite imagery analysis since the 1990s (e.g., Charlebois et al., 1993), its use in supraglacial hydrology mapping is more recent. Random Forest is the most widely used classifier in this field and is often combined with clustering methods (e.g., k-means), which group spectrally similar pixels to support training data creation. It has demonstrated high accuracy in mapping SGLs in Antarctica (Dirscherl et al., 2020; Dell et al., 2022, 2024), Greenland (Yuan et al., 2020; Hu et al., 2022; Wang and Sugiyama, 2024; Lutz et al., 2023), and mountain glaciers (Wangchuk & Bolch, 2020). More recently, deep learning techniques, such as Convolutional Neural Networks (CNNs) and U-Net, have shown promise in SGL mapping, often in combination with RF for enhanced segmentation (Dirscherl et al., 2021b; Niu et al., 2023). Despite these advances, ML is still underutilized in this field, with a limited range of classifiers employed.

ML-based classification has shown promising results in limited-area studies across both the GrIS and AIS (e.g., Dell et al., 2022; Dirscherl et al., 2020; Hu et al., 2022; Lutz et al., 2024). However, a major barrier to the widespread application of ML in meltwater mapping is the lack of high-quality training data. One promising strategy to overcome this limitation is hybrid learning, which combines supervised and unsupervised methods to reduce dependence on large manually labelled datasets. Unsupervised clustering techniques, such as k-means, can generate initial training datasets that are later refined using expert validation, improving efficiency (Dell et al., 2022; Halberstadt et al., 2020).

2.2.4. Machine learning classifiers used in this thesis

This section gives an overview of the ML classifiers that are used in Chapters 4 and 5 of this thesis.

i. K-means clustering

K-means clustering is an unsupervised classification technique that partitions data into a predefined number of clusters based on similarity (Figure 2.4). It has been applied in supraglacial meltwater mapping, either as a standalone method or in combination with supervised approaches, achieving overall classification accuracies exceeding 90% (Dell et al., 2022, 2024; Halberstadt et al., 2020). K-means offers advantages such as computational efficiency, simplicity, and independence from labelled training data. However, its accuracy depends on selecting an appropriate number of clusters and can be affected by spectral overlap between surface types, requiring manual validation and post-processing (e.g., Dell et al., 2022).

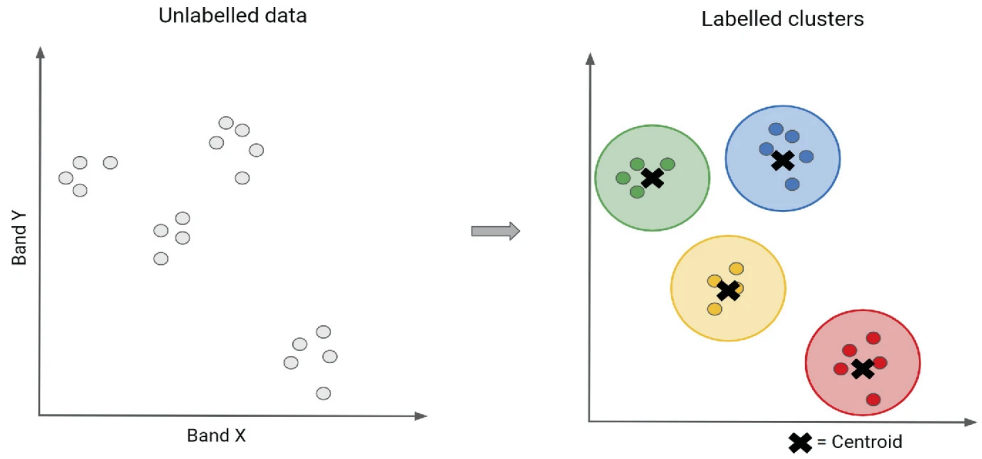

Figure 2.4: A visual representation of K-means clustering. On the left, unlabelled data points are distributed in feature space. On the right, the K-means algorithm has grouped the data into clusters, each represented by a different colour, with black crosses indicating the centroids of each cluster (Source: Cardille et al., 2024).

ii. Classification and regression trees (CART)

Classification and regression trees (CART) is a decision tree algorithm (Figure 2.5) that classifies data by recursively splitting it into subsets based on feature values, forming a tree-like structure (Breiman et al., 1984). It has been applied in supraglacial hydrology mapping in a single study, Halberstadt et al. (2020), where it achieved validation accuracies up to 91.4%. While CART effectively identifies SGLs, its reliance on binary splits can make it sensitive to variations in input data, potentially leading to overfitting in complex glaciological environments.

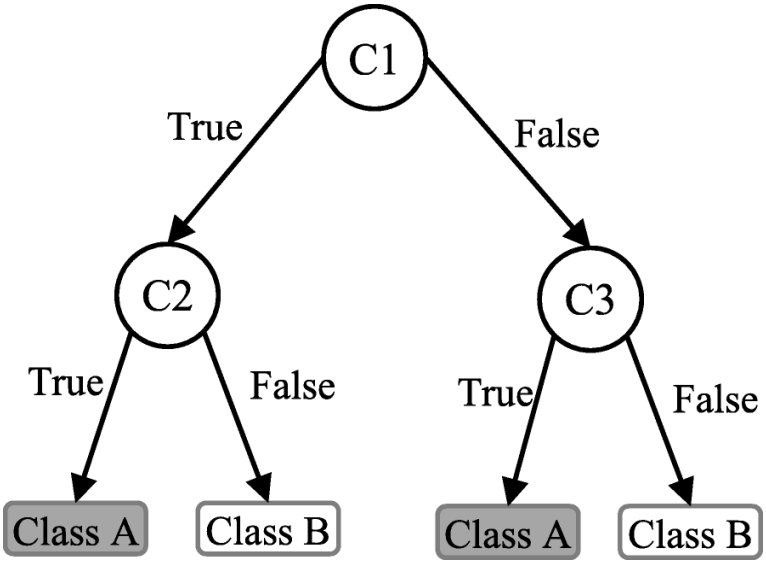

Figure 2.5: A decision tree illustration where circles represent variables (C1, C2, and C3) and rectangles indicate classification outcomes (Class A and Class B). Each branch is labelled 'True' or 'False,' reflecting the result of the preceding node's test, guiding the classification process (Source Uddin et al., 2019).

iii. Random Forest (RF)

Random forest (RF) is a supervised ensemble classifier that constructs multiple decision trees from subsets of training data, collectively forming a "forest" to determine the most probable classification outcome (Figure 2.6; Breiman, 2001). It has recently been applied to mapping supraglacial hydrological features, including SGLs (Dirscherl et al., 2020, 2021; Halberstadt et al., 2020; Yuan et al., 2020; Dell et al., 2022, 2024), returning pixel-based accuracies of 92.6% (Halberstadt et al., 2020). RF offers advantages such as low computational cost, parallel processing, simple parameter tuning, and robustness against overfitting, making it effective for handling complex and noisy data, such as satellite imagery. However, RF's accuracy depends on the quality and of its training data, and in heterogeneous ice-sheet environments with varying snow, ice, and meltwater conditions, it may struggle with generalization.

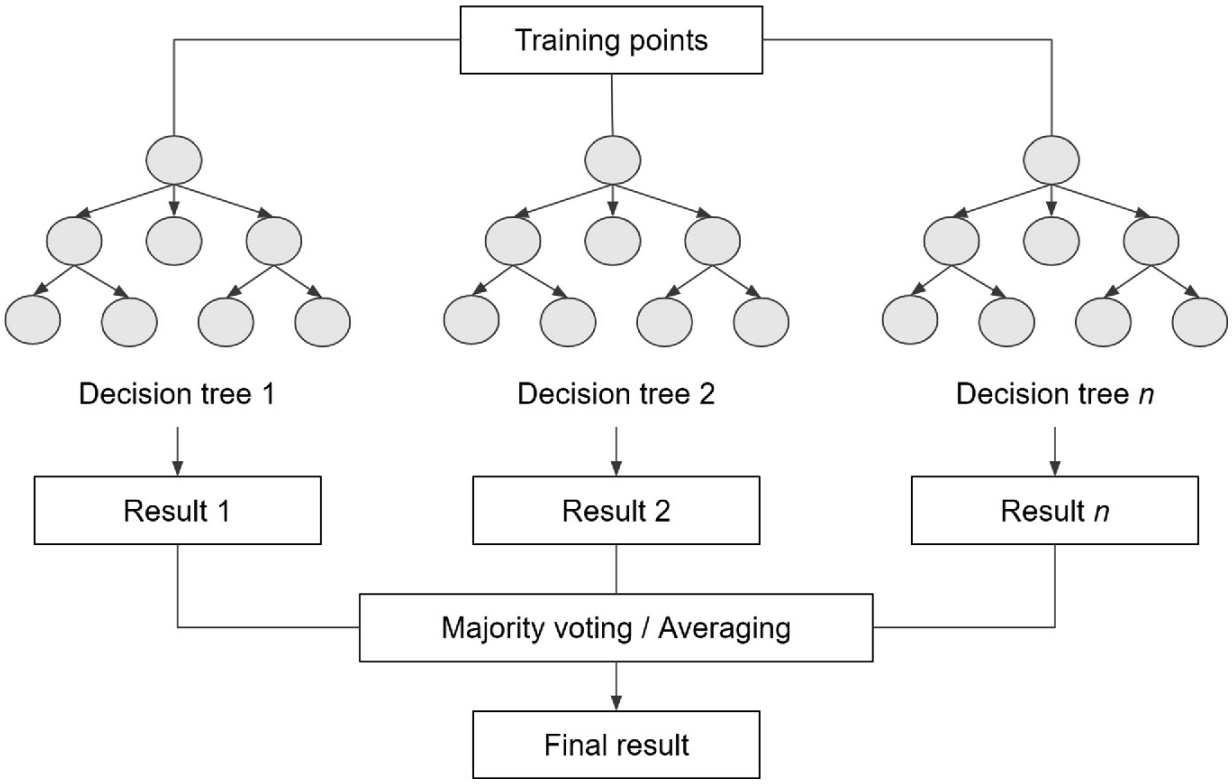

Figure 2.6: A conceptual illustration of a RF classifier. Multiple decision trees are trained on different subsets of the training data, and their individual predictions are combined using majority voting (for classification) or averaging (for regression) to produce the final result (Source: Cardille et al., 2024).

iv. Gradient Boosted Decision Trees (GBDT)

Gradient Boosted Decision Trees (GBDT) is a supervised ML algorithm that builds an ensemble of decision trees sequentially, with each tree improving upon the errors of the previous one (Figure 2.7; Friedman, 2001). Unlike RF, which trains trees independently in parallel, GBDT follows a boosting approach where each new tree is trained to correct the residual errors of the previous trees, resulting in an optimized predictive model. However, GBDT can be computationally expensive and sensitive to hyperparameter tuning, which may affect its scalability and generalization. In the cryosphere, one of the few applications is IceBoost, a GBDT-based framework used to model glacier ice thickness (Maffezzoli et al., 2024). Despite its demonstrated success in various remote sensing applications, GBDT has not yet been applied in supraglacial hydrology studies.

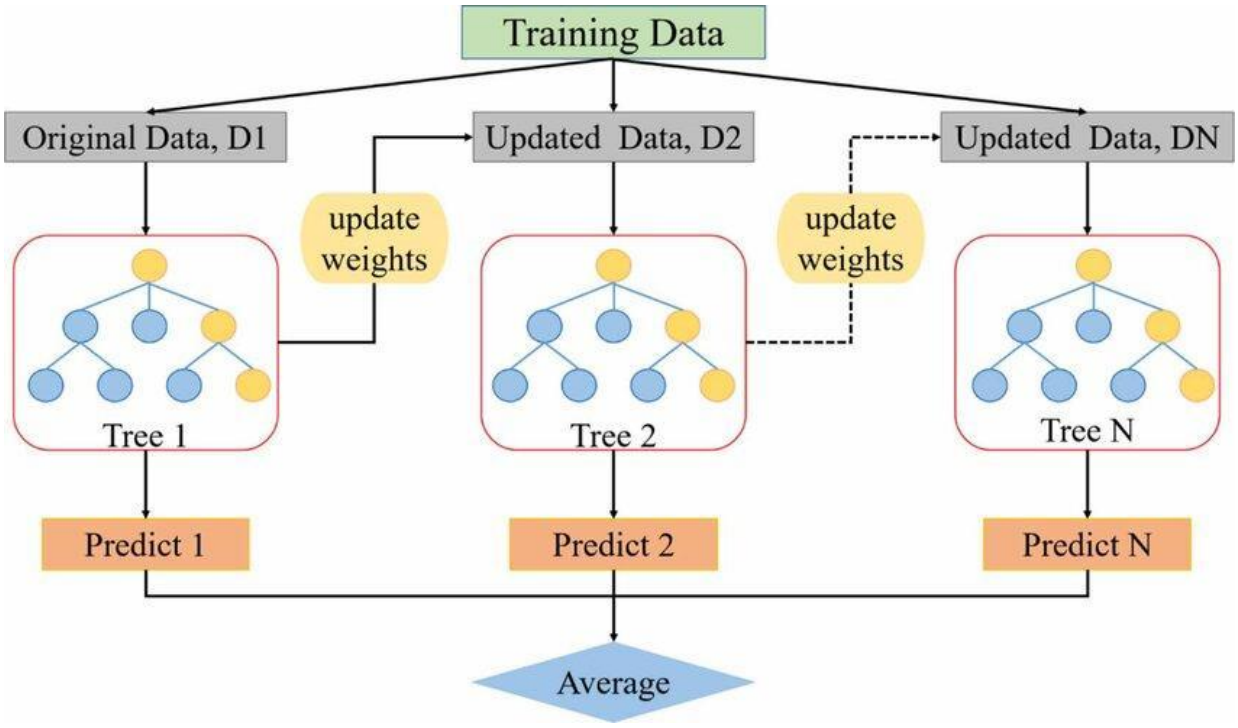

Figure 2.7: Flow chart of a GBDT model. The process begins with the original training data (D1), which is used to train the first decision tree. In subsequent iterations, the dataset is updated (D2, D3, DN), and additional trees (Tree 2, Tree N) are trained with updated weights. The predictions from all trees (Predict 1, Predict 2, Predict N) are then averaged to produce the final prediction (Source: Zhang et al., 2024).

v. Support Vector Machine (SVM)

Support Vector Machine (SVM) is a supervised learning algorithm that classifies data by drawing the best possible boundary, called a hyperplane, to separate different classes (Figure 2.8; Cortes and Vapnik, 1995; Rüping, 2001). It finds the hyperplane that maximizes the margin between the closest data points from each class, serving as a decision boundary for classifying new data points based on their position relative to it. SVM is computationally demanding, particularly for large remote sensing datasets, and its performance is highly sensitive to parameter tuning and kernel selection, which can impact classification accuracy and generalization. SVM has not been widely applied in supraglacial hydrology mapping, with the only notable study, Halberstadt et al. (2020), finding that while SVM achieved high validation accuracy (up to 94.9%), it tended to miss some shallow SGL areas. However, it demonstrated strengths in reducing cloud shadow misclassification and correctly identifying SGLs in low-sun-elevation scenes. Additionally, SVM has been effectively applied to classify diverse ice-sheet and glacial features, including blue ice areas, meltwater channels, and crevasse fields, in East Antarctica using integrated optical and SAR datasets (Choukset et al., 2021).

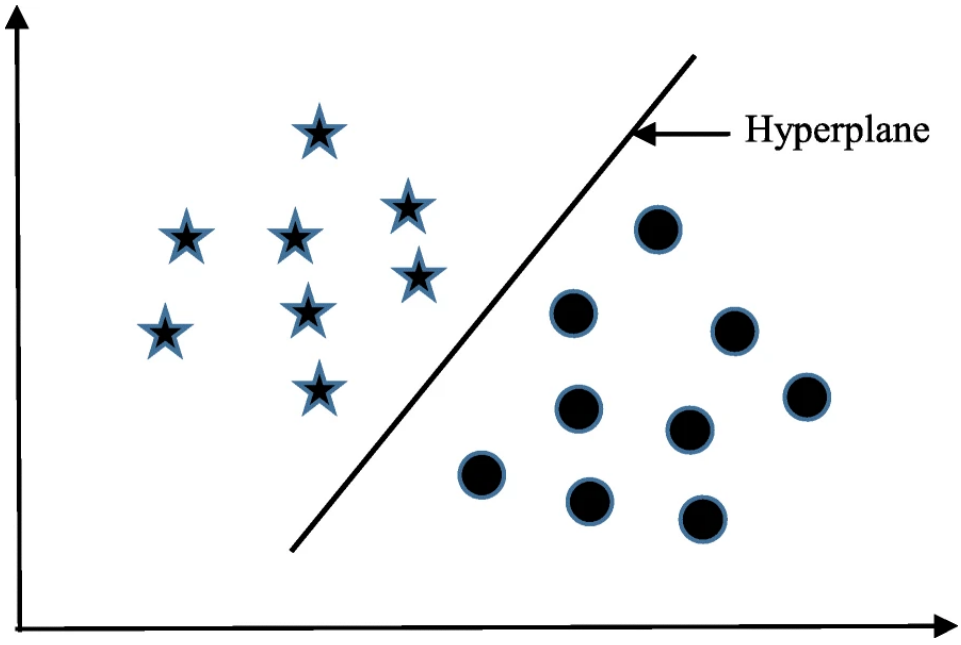

Figure 2.8: A simplified representation of the SVM process, where a hyperplane is identified to maximize the separation between the 'star' and 'circle' classes (Source: Uddin et al., 2019).

vi. K-nearest neighbour (KNN)

The K-nearest Neighbour (KNN) algorithm, introduced by Cover and Hart (1967), is one of the simplest and earliest classification methods (Figure 2.9). It is a non-parametric, supervised learning technique that classifies or makes predictions about a data point's group based on the proximity to other data points. The "K" in KNN refers to the number of nearest neighbours considered when determining the classification or prediction, with each neighbour voting to determine the outcome. Different values of "K" can lead to varying classification results for the same data point. Despite its simplicity, KNN has limitations, particularly when working with high-dimensional data. It often does not scale well with large datasets and is prone to overfitting. While KNN has not yet been applied to supraglacial hydrology delineation, it has been used effectively in other areas of cryospheric research, such as avalanche forecasting (Brabec and Meister, 2001) and predicting Arctic sea ice cover (Lin et al., 2023).

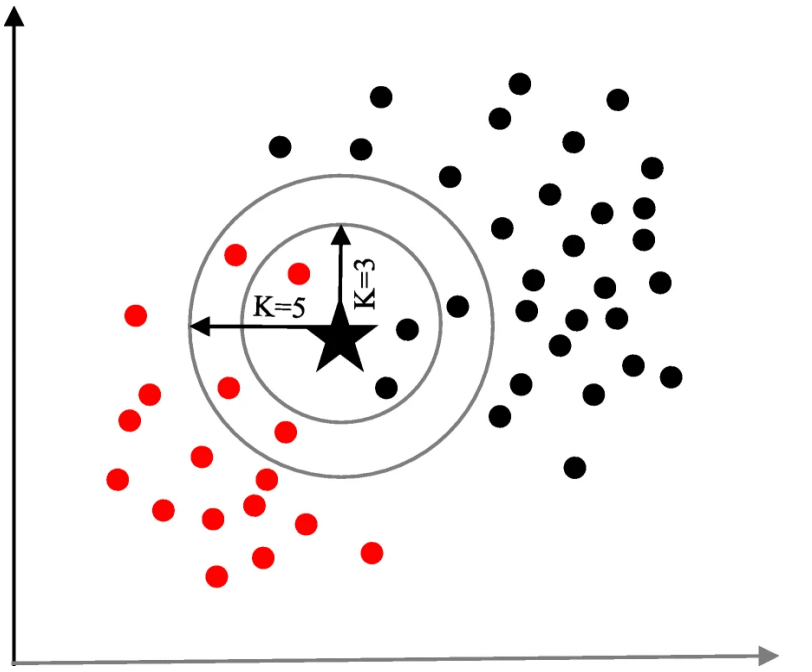

Figure 2.9: A basic demonstration of the K-nearest neighbour algorithm. For K = 3, the sample point ('star') is categorized as 'black' because it is surrounded by more neighbours from the 'black' class. However, when K = 5, the same sample point is classified as 'red' due to a higher number of neighbours from the 'red' class. (Source: Uddin et al., 2019)

vii. Minimum Distance (MD)

Minimum Distance (MD) is a classification method that assigns pixels to the class with the closest mean spectral value, using distance metrics like Euclidean, Mahalanobis, or cosine distance (Figure 2.10). While MD is simple and computationally efficient, it relies only on the class mean, which can be problematic with overlapping spectral distributions. In Halberstadt et al. (2020), MD was applied to classify SGLs on the Amery Ice Shelf. The method showed varying performance, with validation accuracies ranging from 46.8% using Euclidean distance to 74.4% using Mahalanobis distance.

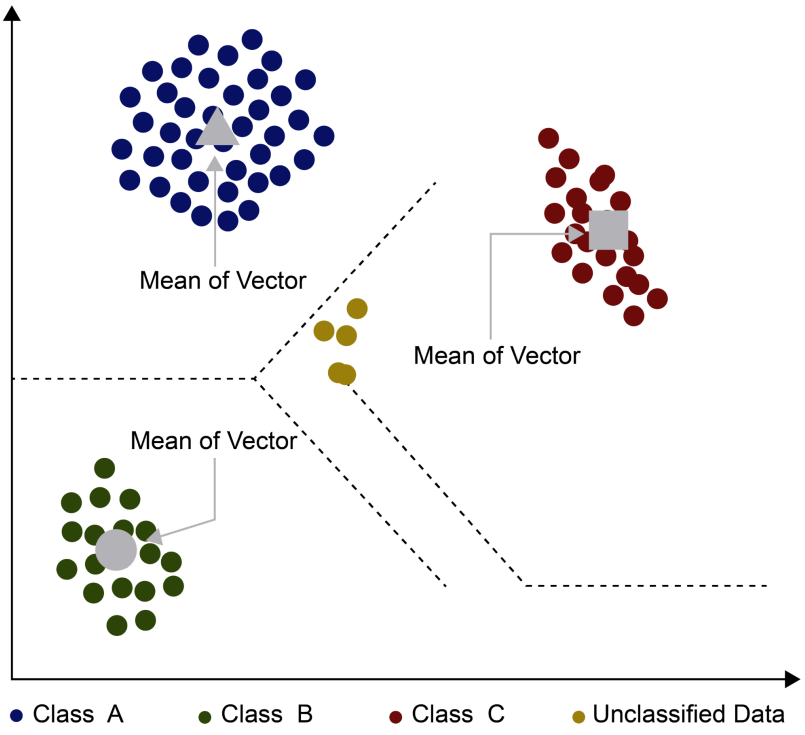

Figure 2.10: Schematic of a Minimum Distance classifier. This method classifies data points based on their distance from the mean vector of each class, where unclassified data points (shown in yellow) are assigned to the class (blue, green, or red) with the closest mean vector (represented by squares). The dashed lines indicate the decision boundaries between the classes (Source: Razaque et al., 2021).

vii. Maximum Entropy (ME)

Maximum Entropy (ME) is a statistical model that predicts the most likely distribution of an outcome based on known environmental conditions, with the aim of maximizing entropy (or randomness) subject to these constraints (Phillips et al., 2004). While ME has not been widely applied in supraglacial hydrology mapping, it was used by Halberstadt et al. (2020) to classify SGLs on Antarctic Ice Shelves. In this study, ME achieved a high validation accuracy of 90.8% in certain cases. However, its performance varied significantly across application scenes from different regions, with accuracy dropping as low as 42.6% for some scenes on the Amery and Roi Baudouin Ice Shelves.

2.2.5 Google Earth Engine

Google Earth Engine (GEE) has become an important tool for large-scale satellite image analysis, providing the computational power and cloud-based infrastructure necessary to study supraglacial hydrology across vast regions like the GrIS. By leveraging high-performance cloud computing, GEE enables rapid processing of large datasets, significantly reducing the time required for complex analyses (Gorelick et al., 2017). It integrates multi-temporal datasets from sensors such as Landsat, Sentinel, and MODIS, allowing comprehensive spatiotemporal analyses without the need for local storage (Gorelick et al., 2017). Additionally, GEE provides built-in ML capabilities, enabling users to train and apply classification models directly within the platform. Its extensive catalogue of preprocessed datasets, including topographic, climatic, and land cover data, further supports large-scale hydrological studies by facilitating multi-source data fusion and automated feature extraction.

In this thesis, GEE is used to process S2 and L8 imagery, which serve as the primary datasets for mapping supraglacial meltwater features. The platform supports automated classification and feature extraction using both threshold-based methods (e.g., NDWI-based approaches; Tuckett et al., 2021) and ML techniques (e.g., Wang et al., 2024; Dell et al., 2022, 2024; Dirscherl et al., 2020). Its ML capabilities facilitate efficient model training, validation, and deployment using large, high-resolution datasets, enabling scalable and automated supraglacial hydrology mapping (Halberstadt et al., 2020; Dell et al., 2022). For example, GEE's RF classifier, often combined with k-means clustering, has been successfully used to map meltwater features across entire ice sheets, demonstrating its effectiveness in large-scale applications (Dell et al., 2022; Zhu et al., 2022).

GEE has been previously applied to supraglacial hydrology research, with recent studies in Antarctica (Halberstadt et al., 2020; Dell et al., 2022, 2024; Tuckett et al., 2021) and Greenland (Zhu et al., 2022; Hu et al., 2021; Wang et al., 2024) highlighting its potential for

automating meltwater mapping and supporting scalable ML applications. However, despite these advancements, significant knowledge gaps remain. The extent to which different ML algorithms perform and generalize across diverse spatial and temporal conditions on the GrIS is not well understood. Additionally, the training data requirements necessary to optimize classifier performance remain unclear. Addressing these gaps is crucial for improving the robustness and transferability of ML-based meltwater mapping and informing the design of future large-scale supraglacial hydrology monitoring efforts.

2.2.6 Supraglacial lake depth quantification

Estimating SGL depth is more complex than simply determining their area, and several methods are employed to estimate depth. In-situ techniques, such as boat surveys or remote-controlled vehicles, provide accurate depth data but are resource-intensive and impractical for large-scale or remote studies (Tedesco et al., 2014; Box and Ski, 2007). Empirical models, based on field data and remote sensing, can estimate SGL depth but are typically region-specific and less applicable on a larger scale (Pope et al., 2016; Tedesco and Steiner, 2011).

Laser altimetry offers precise depth measurements by detecting laser reflections from the lakebed (Arndt et al., 2024; Lutz et al. 2024; Melling et al., 2024), with recent work developing fully automated method for determining SGL depths along ICESat-2 tracks (e.g., Arndt et al. 2024). However, its limited spatial coverage (only along satellite tracks) and coarse temporal resolution make it unsuitable for tracking rapid SGL changes (Melling et al., 2024). DEMs, such as ArcticDEM, calculate depth by comparing elevations of empty and filled basins. They offer high spatial resolution but poor temporal coverage, limiting their ability to capture dynamic SGL depth changes (Das et al., 2008; Lampkin and VanderBerg, 2011).

Physics-based models, like the radiative transfer equation (RTE), estimate depth using light attenuation in the water column (Sneed and Hamilton, 2007; Philpot, 1989; Williamson et al., 2018a). The depth z is calculated by equation 2.1:

$$z = \frac{ln(Ad - R\infty) - ln(Rw - R\infty)}{g}, \tag{2.1}$$

where *Ad* is lakebed reflectance, $R\infty$ is the reflectance of optically deep water, *Rw* is the satellite measured reflectance value of a water pixel, and *g* is the attenuation coefficient rate associated with losses in upward and downward directions through the waterbody.

For L8 data, SGL depths using the RTE are derived by averaging the red and panchromatic TOA reflectance values, with lakebed reflectance obtained from the average of the first non-water pixel surrounding the SGL. The reflectance of optically deep water is either taken as the darkest ocean pixel or set to zero if absent. The attenuation coefficients are 0.38 for the panchromatic band and 0.75 for the red band (Williamson et al., 2018a; Pope et al., 2016). For S2, depths are calculated similarly using the red TOA reflectance, but the lakebed reflectance is averaged over the first three surrounding pixels, and the attenuation coefficient is set to 0.83. The reflectance of optically deep water is assumed to be zero (Williamson et al., 2018a).

Williamson et al. (2018a) applied this method to both the red and green bands of S2 imagery and validated the results against L8 data, finding that the method worked well with the red band, with an RMSE of 0.6 meters. However, when the green band was used, the depth estimates were found to be exceptionally high, likely due to spectral sensitivity issues at greater depths, and were therefore excluded from the final analysis. While the RTE is widely used and applicable at large scales, it has limitations in its application to deeper SGLs (> 3.5 meters), where the red wavelengths of light used in the calculation become saturated, leading to overestimates of depth (Williamson et al., 2018a). The RTE also requires assumptions, such as homogeneous SGL bottoms and low turbidity.

To compare different depth estimation techniques, Melling et al. (2024) used ArcticDEM digital elevation models, ICESat-2 photon refraction, and the RTE applied to S2 imagery across five SGLs in southwest Greenland (Figure 2.11). The results showed a high level of agreement between the ArcticDEM and ICESat-2 methods (Pearson's r=0.98), indicating that these two techniques produce similar depth estimates. However, the RTE had notable limitations, overestimating SGL depth by up to 153% when using the green band and underestimating depth by up to 63% when using the red band. The study identified that the largest source of uncertainty in RTE-based estimates was the reflectance values at the lakebed, which are empirically derived and subject to significant variability. Similarly, Lutz et al. (2024) highlighted the sensitivity of RTE-based methods to parameter selection, noting that empirical approaches, particularly those calibrated with ICESat-2 and in situ sonar data, offer more reliable depth estimates under clear atmospheric conditions and low-sediment environments.

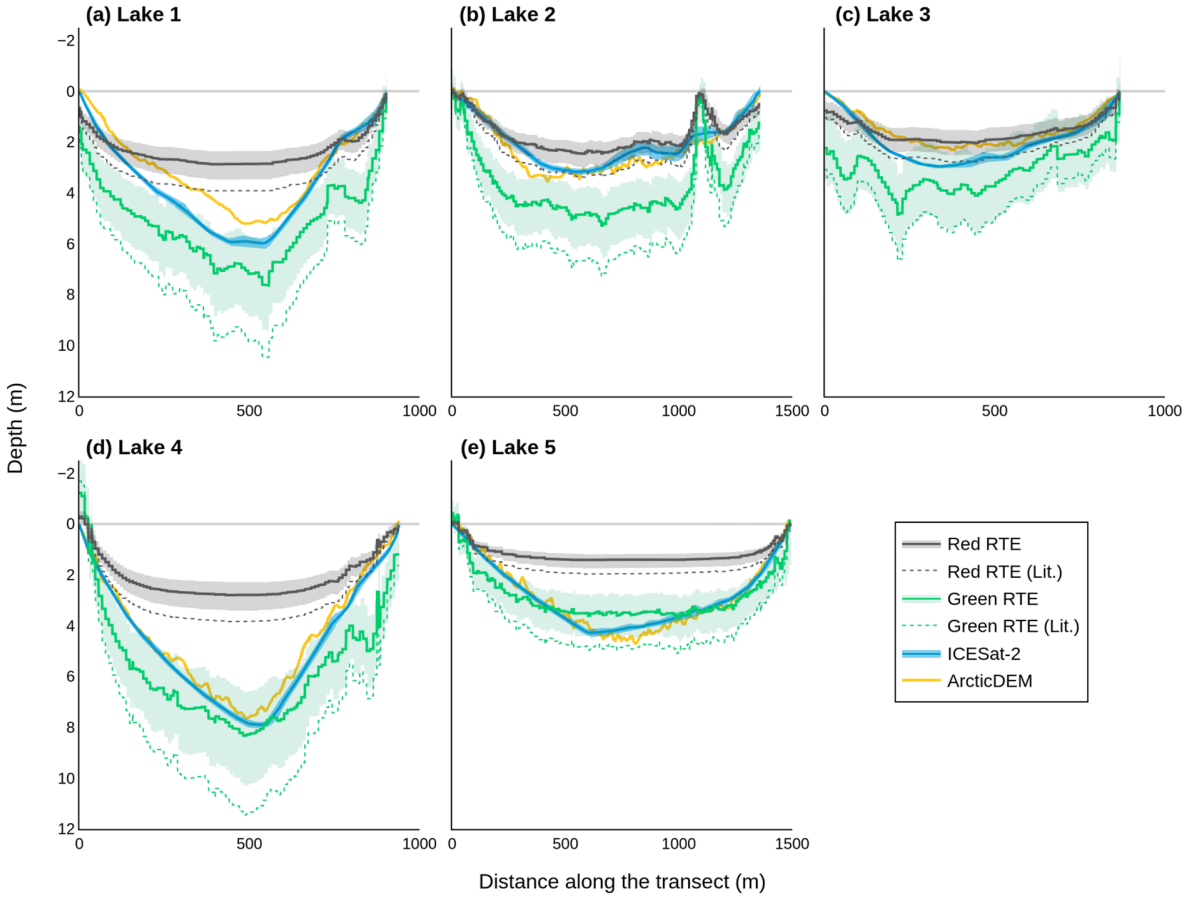

Figure 2.11: SGL depth estimates from the band-specific RTE, ArcticDEM, and ICESat-2 along transects. 'Lit.' refers to RTE values previously used in earlier literature (Source: Melling et al., 2024).

2.2.7 Supraglacial lake tracking

In addition to traditional methods for quantifying the area and depth of SGLs on the GrIS, several approaches have been developed to monitor their evolution and drainage dynamics over time. One such method, demonstrated by Selmes et al. (2011, 2013), involved manually inspecting MODIS data to visually analyse changing SGL shapes and textures, offering insights into drainage dynamics. This manual approach was time-consuming and relied on low spatial resolution MODIS data.

Rapid SGL drainage events, occurring in hours, pose challenges for satellite detection due to sensor revisit times. However, a dual-sensor approach combining optical and radar imagery can enhance spatial resolution and temporal coverage for better tracking of SGL dynamics. For example, Miles et al. (2018) used L8 and S1 data to track SGLs in western Greenland during the 2015 summer season, detecting SGL dynamics with a 25-40 m resolution and 3-day revisit time. Although this approach effectively detected SGL dynamics, it could not estimate SGL volumes and was unsuitable for areas with saturated firn. The Fully

Automated Supraglacial Lake Tracking at Enhanced Resolution (FASTER) algorithm, developed by Williamson et al. (2018a), uses both L8 and S2 imagery to track SGLs across the southwestern GrIS. This method offers a spatial resolution of 10-30 m and a revisit time of approximately 4 days, with an error of about 1.1 days. FASTER improves upon earlier techniques by offering finer spatial resolution, though it still faces limitations as it does not categorise refreezing events. The FASTER algorithm has also been applied to track both circular (i.e., SGLs) and linear water bodies (i.e., channels) across Antarctic Ice Shelves (Dell et al., 2020).

Previous studies on SGL behaviour are either outdated, low-resolution, or focused on basin-scale analysis. Dunmire et al. (2025) introduced a novel time-series classification model to automatically categorize SGLs across the GrIS into four groups: refreezing, rapidly draining, slowly draining, and transitioning to buried subsurface lakes (Figure 2.12). Using optical and microwave imagery with advanced deep learning, this model improves automatic classification. However, with a 6-day window for detecting rapid drainage events, it may still miss some events.

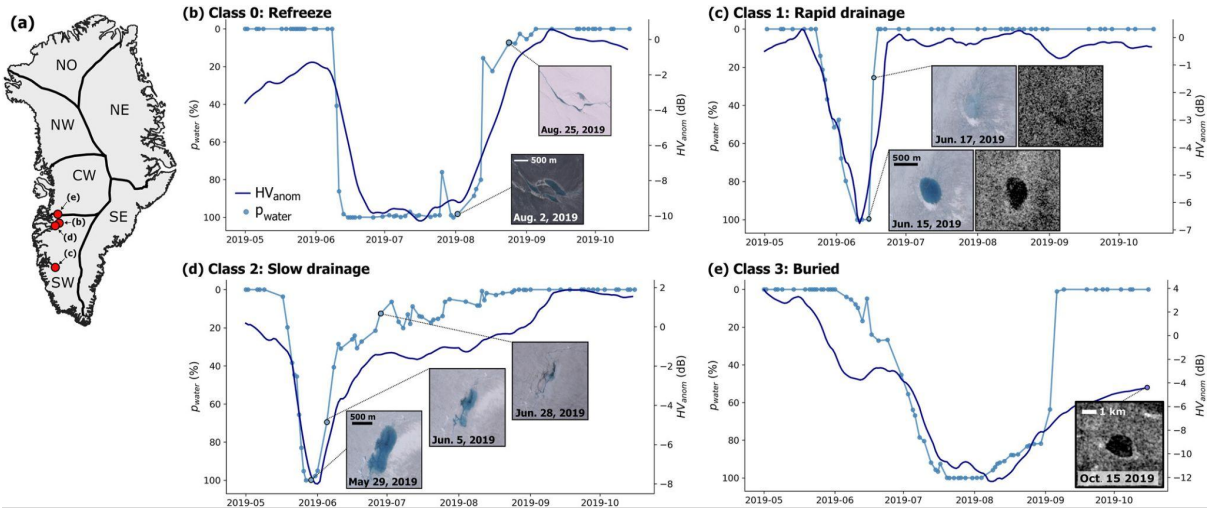

Figure 2.12. Time series of optical and microwave data for GrIS SGL behaviour groups: (b) refreezing, (c) rapidly draining, (d) slowly draining, and (e) buried (Source: Dunmire et al., 2025).

2.3 Knowledge and capability gaps in remote sensing of supraglacial hydrology

In the review above, key knowledge gaps have been identified relating to the use of remote sensing to resolve and understand supraglacial hydrology. These gaps fall into several categories: 1) Process-level knowledge gaps, where fundamental uncertainties remain in the physical processes governing supraglacial hydrology, for example, in the formation, distribution, and evolution of meltwater features such as SGLs, channels, and slush. 2) methodological accuracy, where the accuracy and reliability of traditional remote sensing and ML approaches limit the ability to fully characterize supraglacial hydrology, often leading to misclassifications or biases in feature detection and interpretation; and 3) technological challenges, computational constraints and the scarcity of high-quality training data hinder large-scale, automated mapping efforts. Below, each of these knowledge gaps are explored in more detail, beginning with process-level uncertainties before addressing methodological accuracy and technological limitations.

2.3.1 Process-level knowledge gaps

Compared to slush, SGLs and supraglacial channels have been more extensively studied, providing a relatively stronger understanding of their formation, evolution, and impacts on the ice sheet. However, uncertainties remain, for example, the response of all supraglacial meltwater features to extreme melt years–events that are likely to become more frequent with climate change–remains uncertain, especially in comparison to low-melt years.

Slush, in particular, remains poorly studied despite its known role in hydrological connectivity, runoff processes, and albedo, as demonstrated in AIS studies (e.g., Dell et al., 2022, 2024). Previous GrIS mapping efforts have largely overlooked slush, limiting our ability to assess its distribution, evolution, and temporal variability.

Despite forming a highly interconnected system, supraglacial meltwater features are typically studied in isolation (e.g., Box & Ski, 2007; Selmes et al., 2011; Williamson et al., 2017; Sundal et al., 2009; Smith et al., 2015; Greuell & Knap, 2000; Machguth et al., 2023; Tedstone & Machguth, 2022). While some studies have attempted a more holistic approach (e.g., Rawlins et al., 2023; Zhang et al., 2023), their spatial and temporal coverage remains limited. Additionally, many regional studies overlook key meltwater features, such as slush and smaller SGLs that do not meet hypothesized area thresholds for rapid drainage initiation (i.e., Krawczynski et al., 2009). At the same time, large-scale assessments often lack the spatial and temporal resolution needed to resolve key hydrological processes, highlighting a second major category of knowledge gaps: methodological limitations.

2.3.2 Methodological accuracy

The detection and classification of supraglacial meltwater features present significant methodological challenges due to the indistinct spectral and physical characteristics of SGLs, channels, and slush. Traditional remote sensing approaches, particularly thresholding methods, have been widely used to delineate meltwater features (as described in the review above). However, these methods often rely on a single, generalized threshold, which fails to capture the spectral nuances between different meltwater features, leading to incomplete or inaccurate classifications. To improve accuracy, more detailed, feature-specific classification methods have been developed, such as approaches that account for the linear morphology of channels (e.g., Yang et al., 2015) or the shallow nature of slush (e.g., Bell et al., 2017). While these methods enhance classification precision, they have typically been applied in isolation rather than in combination. Integrating these feature-specific approaches is necessary to achieve a more comprehensive and accurate classification of supraglacial hydrology.

While traditional remote sensing methods–whether manual or semi-automated–may be effective in basin-scale settings, they are time-intensive and impractical for large-scale, repeat monitoring, especially given the increasing volume of satellite imagery. ML presents a promising alternative, yet its application to supraglacial hydrology remains somewhat limited. Most studies have relied on RF or selected deep learning models (e.g., Wangchuk & Bolch, 2020; Hu et al., 2021; Dirscherl et al., 2020, 2021; Dell et al., 2022, 2024; Yuan et al., 2020; Halberstadt et al., 2020; Wang & Sugiyama, 2024; Hu et al., 2022; Lutz et al., 2024), with little consideration of alternative algorithms. Additionally, there is no clear consensus on the optimal training data requirements for supraglacial meltwater classification, including dataset size and labelling strategies. A key challenge lies in balancing data quantity and quality: insufficient training data may limit model accuracy, while excessive data can lead to inefficient training and diminishing returns. Further uncertainty exists regarding the balance between manual and automated labelling and the extent to which models trained on one region or melt season can generalize effectively to others.

To improve supraglacial meltwater classification accuracy, there is a need for both feature-specific approaches and large-scale ML-based methods. Feature-specific classification techniques allow for high-precision delineation of individual meltwater features, ensuring accuracy at localized scales. Meanwhile, ML enables automated, scalable classification across ice-sheet-wide datasets.

2.3.3 Technological challenges

While ML approaches offer scalability and automation, their effectiveness is constrained by broader technological challenges. Large-scale monitoring of supraglacial hydrology is hindered by computational limitations, which limit the widespread implementation of ML-based methods across the GrIS. Traditional approaches relying on locally downloaded satellite imagery are slow, require substantial storage, and are impractical for large-scale and near-real-time analysis. Recent advances in cloud computing and ML offer scalable solutions, but these technologies remain underexplored in supraglacial hydrology. Cloud-based platforms such as GEE provide opportunities for large-scale analysis, yet adoption in this field has been limited. Expanding the use of ML algorithms implemented in the cloud could enable more efficient, comprehensive and timely monitoring of supraglacial meltwater features.

An integrated approach that combines regional-scale analyses, ice-sheet-wide assessments, and ML advancements has the potential to address all of the gaps outlined above and improve large-scale monitoring of supraglacial meltwater features. Regional-scale analyses provide essential context for understanding the processes driving supraglacial hydrology, offering insights that can inform larger-scale classifications. Ice-sheet-wide assessments, in turn, enable the quantification of broader trends and spatial variability. Finally, ML advancements enhance the scalability and efficiency of these classifications, ensuring they remain adaptable to diverse supraglacial conditions.

This thesis is structured around these key themes. First, it examines how interannual variability influences supraglacial hydrology at a regional scale. Second, it expands the focus to quantify and track the evolution of slush across the GrIS. Third, it develops and evaluates ML-based methods to improve the scalability and accuracy of supraglacial meltwater mapping. These themes form the basis of the research objectives outlined in the following section.

2.4 Thesis aims and objectives

Understanding the spatial and temporal dynamics of surface hydrology on the GrIS is critical for predicting its response to climate change and its contribution to global sea level rise. Supraglacial meltwater features, including SGLs, channels, and slush, play a key role in influencing ice dynamics, SMB, and meltwater routing to the ice sheet bed and the ocean as discussed in Chapter 1. However, several key knowledge and capability gaps limit our understanding of these processes, as outlined in Section 2.3.

To address these gaps, this thesis aims to advance understanding of: 1) how GrIS supraglacial meltwater features evolve over time and 2) how best to monitor them at scale. To achieve this, three main objectives have been defined, which together will allow these overarching aims to be met. These objectives are as follows:

1. **Understand how the distribution, evolution, and morphology of supraglacial meltwater varies within, and between, high and low melt years (Chapter 3).** This objective directly addresses the process-level knowledge gap by examining how interannual variability in summer temperatures influences the distribution and evolution of SGLs, channels, and slush. By comparing these features in contrasting melt seasons, this research provides insight into the sensitivity of meltwater features to extreme melt conditions, which are becoming increasingly frequent due to climate change. This research also contributes to a more holistic understanding of supraglacial hydrology beyond the isolated treatment of individual features, using different feature-specific methods to distinguish between SGLs, rivers, and slush more effectively.
2. **Understand the spatial and temporal distribution of slush on the GrIS (Chapter 4)**. This objective directly addresses a major methodological limitation by developing methods for mapping slush on the GrIS and applying these methods to classify its extent and variability. Mapping slush over multiple years provides insights into its distribution, variability, and evolution at an ice-sheet-wide scale, addressing process-level knowledge gaps by improving understanding of slush dynamics and its role in supraglacial hydrology. This work also contributes to addressing technological challenges for meltwater feature mapping by deploying scalable monitoring approaches on a cloud-based platform and thus capturing slush meltwater features across large spatial scales and tracking their evolution over time.
3. **Optimise the performance of and understand the trade-offs between ML classifiers deployed in the cloud**. By assessing accuracy, transferability, and scalability, this objective identifies the most effective approaches for large-scale,

automated mapping of supraglacial meltwater features. By determining the most effective ML approaches for supraglacial hydrology mapping, this objective directly supports the thesis aim by optimising ML and remote sensing-based methods for large-scale meltwater monitoring. By focusing on cloud-based ML methods, this objective enhances the scalability and efficiency of supraglacial hydrology monitoring and achieves the thesis aim by establishing the foundations for improved automated meltwater mapping on the GrIS.

Together, these objectives provide a detailed view of recent supraglacial meltwater evolution on the GrIS and contribute to the development of improved monitoring tools. By first examining the distribution, evolution, and morphology of supraglacial meltwater features in southwest Greenland under contrasting melt conditions, Chapter 3 establishes how interannual variability influences surface hydrology, highlighting the role of slush as an important yet often overlooked component of the meltwater system. Building on these findings, Chapter 4 expands the focus to an ice-sheet-wide assessment of slush, mapping its distribution and evolution from 2016 to 2024 using S2 imagery and ML. This large-scale analysis provides insights into slush variability both within and between different melt seasons, offering a broader perspective on its hydrological significance across the GrIS. Chapter 5 evaluates the performance of ML classifiers for supraglacial feature delineation. By assessing classifier accuracy, transferability, and computational efficiency, this research identifies the most effective approaches for automated mapping, ultimately improving long-term monitoring of supraglacial hydrology in a changing climate. Finally, in Chapter 6, the thesis findings are synthesized, explored within a broader context, and potential directions for future research are discussed.

Chapter 3

A comparison of supraglacial meltwater features throughout contrasting melt seasons: Southwest Greenland

Emily Glen[1,2], Amber Leeson[1,2], Alison F. Banwell[3], Jennifer Maddalena[1,2], Diarmuid Corr[1,2], Olivia Atkins[4], Brice Noël[5], Malcolm McMillan[1, 2]

[1] Lancaster Environment Centre, Lancaster University, Lancaster, UK

[2]UK Centre for Polar Observation & Modelling, Lancaster University, Lancaster, UK

[3] Cooperative Institute for Research in Environmental Sciences (CIRES), University of Colorado Boulder, Boulder, USA

[4] Department of Earth Sciences, University of Oxford, Oxford, UK

[5] Laboratoire de Climatologie et Topoclimatologie, University of Liège, Liège, Belgium

Correspondence to: Emily Glen (e.glen@lancaster.ac.uk)

The following work was originally published in *The Cryosphere* on 6 March 2025 (Glen et al., 2025). This version has been slightly revised for inclusion in the thesis, with supplementary material from the manuscript now integrated into the main text.

This paper was edited by Horst Machguth and reviewed by Andrew Tedstone and one anonymous referee.

EG, AL and AFB conceptualised the research. AL, AFB, JM, and MM contributed to the scientific content, technical details, and overall structure of this paper. DC developed the code to automatically delineate meltwater features. OA provided manually digitised meltwater features. BN provided RACMO2.3p2 data. EG carried out the main body of work and drafted the manuscript. All co-authors contributed to discussion of results and editing of the manuscript.

Abstract

Over recent decades, the Greenland Ice Sheet (GrIS) has lost mass through increased melting and solid ice discharge into the ocean. Surface meltwater features such as supraglacial lakes (SGLs), channels and slush are becoming more abundant as a result of the former and are implicated as a control on the latter when they drain. It is not yet clear, however, how these different surface hydrological features will respond to future climate changes, and it is likely that GrIS surface melting will continue to increase as the Arctic warms. Here, we use Sentinel-2 and Landsat 8 optical satellite imagery to compare the distribution and evolution of meltwater features (SGLs, channels, slush) in the Russell-Leverett Glacier catchment, southwest Greenland, in relatively high (2019) and low (2018) melt years. We show that: 1) supraglacial meltwater covers a greater area and extends further inland to higher elevations in 2019 than in 2018; 2) slush – generally disregarded in previous Greenland surface hydrology studies - is far more widespread in 2019 than in 2018; 3) the supraglacial channel system is more interconnected in 2019 than in 2018; 4) a greater number, and larger total area, of SGLs drained in 2019, although draining SGLs were, on average, deeper and more voluminous in 2018; 5) small SGLs (≤ 0.0495 km^2) - typically disregarded in previous studies - form and drain in both melt years, although this behaviour is more prevalent in 2019; and 6) a greater proportion of SGLs refroze in 2018 compared to 2019. This analysis provides new insight into how the ice sheet responds to significant melt events, and how a changing climate may impact meltwater feature characteristics, SGL behaviour and ice dynamics in the future.

3.1. Introduction

Over recent decades, the Greenland Ice Sheet (GrIS) has undergone substantial mass loss, totalling 4,892 ± 457 Gt of ice from 1992 to 2020 (Otosaka et al., 2023). This mass loss has arisen through a reduction in surface mass balance (SMB), as well as dynamic factors; with meltwater runoff now being the main contributor to ice loss (Mouginot et al., 2019; van den Broeke et al., 2016; The IMBIE Team, 2020; Hanna et al., 2024). Increased surface melt, driven by atmospheric warming, causes a direct reduction in mass through surface runoff. Since the early 1990's, the GrIS has experienced a total mean summer temperature increase of ~1.7°C (Hanna et al., 2021), with a commensurate increase in surface meltwater production through an increase in melt extent as well as enhanced local melt rates (van As et al., 2012; Hall et al., 2013), and surface runoff has risen by 33-50% since the early 2000s (Trusel et al., 2018). Surface melting on the GrIS has migrated to higher elevations since 2000 (Gledhill and Williamson, 2018), and meltwater features, including supraglacial lakes (SGLs), channels and slush, have also migrated inland (Howat., et al., 2013; Tedstone and Machguth, 2022). This trend is expected to continue as the climate warms further - temperatures are predicted to increase by up to 6.6 °C by 2100 (Hanna et al., 2021) - with models suggesting that, relative to the period 2000 – 2010, meltwater features on the GrIS will extend 110 km further inland by 2060 under extreme warming/emission scenarios (Leeson et al., 2015).

Supraglacial melt on the GrIS can create meltwater features by ponding in SGLs, flowing in channels, and saturating snow and firn to create supraglacial slush. SGLs generally form in late spring or early summer, enlarging in area and depth throughout the melt season as they accumulate water (McMillan et al., 2007; Sneed and Hamilton, 2007; Selmes et al., 2011). SGLs can drain rapidly in hours by hydrofracture (Das et al., 2008; Doyle et al., 2013; Williamson et al., 2018a), slowly in days to weeks via channel incision and overflow (Hoffman et al., 2011; Tedesco et al., 2013), become buried in snow then persist into winter (Benedek and Willis, 2021; Dunmire et al., 2021), or refreeze at the end of the melt season (Selmes et al., 2013). Moulins, often created by SGL hydrofracture events (e.g. Das et al., 2008; Tedesco et al., 2013), allow supraglacial meltwater to access the ice sheet base, where the location and timing of meltwater injection can modulate ice flow (Zwally et al., 2002; Bartholomew et al., 2010; 2012; Hoffman et al., 2011; Sole et al., 2011; Nienow et al., 2017). Once moulins have opened, they may act as surface-bed connections for the remainder of the melt season, enabling meltwater to impact ice dynamics over monthly-to-seasonal timescales (Joughin et al., 2008, Banwell et al., 2013, 2016; Hoffman et al., 2018). Supraglacial channel systems are the main way in which surface meltwater is transported as runoff across the southwest GrIS (Yang et al., 2016). Supraglacial channels may direct

meltwater towards moulins and crevasses, where meltwater can access the ice sheet base and influence ice velocity (Bartholomew et al., 2010, 2012; Nienow et al., 2017), or channels can transport meltwater directly off the ice sheet and into the ocean (Yang et al., 2019). Meltwater can also travel laterally across the ice sheet surface through slush fields, which are features that have been identified on the ice sheet as early as the 1950s (Holmes, 1955). Slush fields can initiate or reopen supraglacial channel routes (Miller et al., 2018; 2020; Clerx et al., 2022; Machguth et al., 2023). Refrozen slush and SGLs can create low-permeability ice slabs, which inhibits water storage in the underlying firn and, in turn, increases ice-surface runoff and ultimately contributes to global sea-level rise (MacFerrin et al., 2019; Tedstone and Machguth, 2022).

As meltwater runoff is the main contributor to GrIS mass loss (The IMBIE Team, 2020; Otosaka et al., 2023), the distribution of supraglacial meltwater on Greenland has been the focus of several modelling (e.g. Banwell et al., 2012; Leeson et al., 2012; Arnold et al., 2015) and remote-sensing (e.g. Yang and Smith., 2013; McMillan et al., 2007; Selmes et al., 2011; Williamson et al., 2017, 2018a; Miles et al., 2017; Yang et al., 2021; Lu et al., 2021; Turton et al., 2021; Rawlins et al., 2023; Zhang et al., 2023) studies. Previously, the characteristics and behaviour of medium to large SGLs (defined as > 0.0495 km²; where this value was inferred to correspond to the minimum lake size required to fracture to the ice-sheet bed (Krawczynski et al., 2009)), have been studied in single melt-seasons (e.g. Williamson et al., 2017, 2018a; Miles et al., 2017). Although several multi-seasonal studies have been conducted, they have often been limited by coarse spatial resolution data and hence have ignored small SGLs (≤ 0.0495 km²) (e.g. Selmes et al., 2013; Fitzpatrick et al., 2014). This approach has often been justified by the understanding that larger volumes of water are needed to hydrofracture through kilometre or so thick ice (Krawczynski et al., 2009). However, since small SGLs tend to form at the ice margin where the ice is thinner, it is possible that small SGLs may trigger hydrofracture and perturb ice dynamics in marginal areas (Williamson et al., 2018a).

Supraglacial meltwater on the GrIS exists in different forms and previous remote-sensing studies have predominantly focussed on SGLs, channels and slush as separate entities (e.g. Box and Ski, 2007; Selmes et al., 2011; Williamson et al., 2017; Yang and Smith, 2016; Sundal et al., 2009; Smith et al., 2015; Greuell and Knap, 2000; Machguth et al., 2023; Tedstone and Machguth, 2022). Although there have been a handful of studies that have focussed on mapping and analysing the supraglacial hydrological system as a whole (e.g. Rawlins et al., 2023; Zhang et al., 2023; Yang et al., 2021), the vertical drainage of meltwater features through the ice sheet via hydrofracture was not considered. Likewise, some studies included buried lakes (e.g. Dunmire et al., 2021; Miles et al., 2017), although supraglacial

slush features were ignored. Despite recent research, little is known about how the distribution of all forms of supraglacial meltwater features, including SGLs, slush, and channels, differs as a whole system across fine spatial and temporal scales, and how this varies between high and low melt years.

Since the distribution and dynamics of supraglacial meltwater has a profound influence on the mechanisms contributing to mass loss from the GrIS, it is important to understand its evolution and distribution, especially since high melt years - presumably more conducive to surface melt and meltwater ponding - are becoming more frequent as the climate warms. In this study, we compare the distribution, evolution and morphology of all supraglacial meltwater features in the Russell-Leverett Glacier catchment, southwest Greenland, in the low melt year of 2018, to the relatively high melt year of 2019. We delineate SGL, slush and channel features using a variety of Normalised Difference Water Index (NDWI) thresholding methods tailored to each meltwater feature and applied to both Landsat 8 and Sentinel-2 optical satellite imagery. Our dataset includes small (i.e., SGLs > 0.0018 km² and ≤ 0.0495 km²) and shallow (i.e., slush) meltwater features, which are important, but have been overlooked in previous mapping studies, as well as the previously more commonly included, large SGLs (i.e., > 0.0495 km²) and channels (i.e., linear meltwater features > 1000 m long). We also compare the drainage dynamics and hypsometry of SGLs, and partition SGLs into those that drain versus those that refreeze in the low and high melt seasons. Together, these data provide new insights into how a warming climate - where high melt years become the norm - may influence the spatial and temporal distribution of supraglacial meltwater features and the drainage dynamics of SGLs.

3.2. Methods

3.2.1. Study area

We focus on a ~5800 km² area of Southwest Greenland: the Russell-Leverett Glacier catchment (Figure 3.1, orange star). The surface drainage catchment is derived from the digital elevation model, ArcticDEM version 3 (Porter et al., 2022) at 1 km resolution. The catchment is land terminating and meltwater is transported from the ice sheet margin oceanward by both Watson and Isortoq proglacial rivers. The study area is well known for prevalent supraglacial hydrology features including SGLs, channels, and moulins (e.g., Bartholomew et al., 2010; Sundal et al., 2009; Smith et al., 2015; Fitzpatrick et al., 2014; Yang et al., 2021).

3.2.2. Study years

We focus on two GrIS melt seasons: the relatively low melt year of 2018, and the relatively high melt year of 2019. The 2018 melt season was anomalously cold ice-sheet wide, with a summer temperature anomaly of -1.5 °C relative to the 2002–2016 mean (Sasgen et al., 2020). The maximum daily extent of supraglacial melt in 2018 reached 44% of the total ice sheet area, only slightly above the 1981-2010 mean of 40% (Tedesco et al., 2019). In contrast to the 2018 melt season, the 2019 melt season was exceptionally warm, with some regions on the ice sheet reaching a summer mean temperature anomaly of +1.5 °C relative to 2002–2016 (Sasgen et al., 2020). Maximum daily extent of supraglacial melt in 2019 reached 60% of the total ice sheet area, greatly exceeding the 1981-2010 mean of 40% (Tedesco et al., 2019).

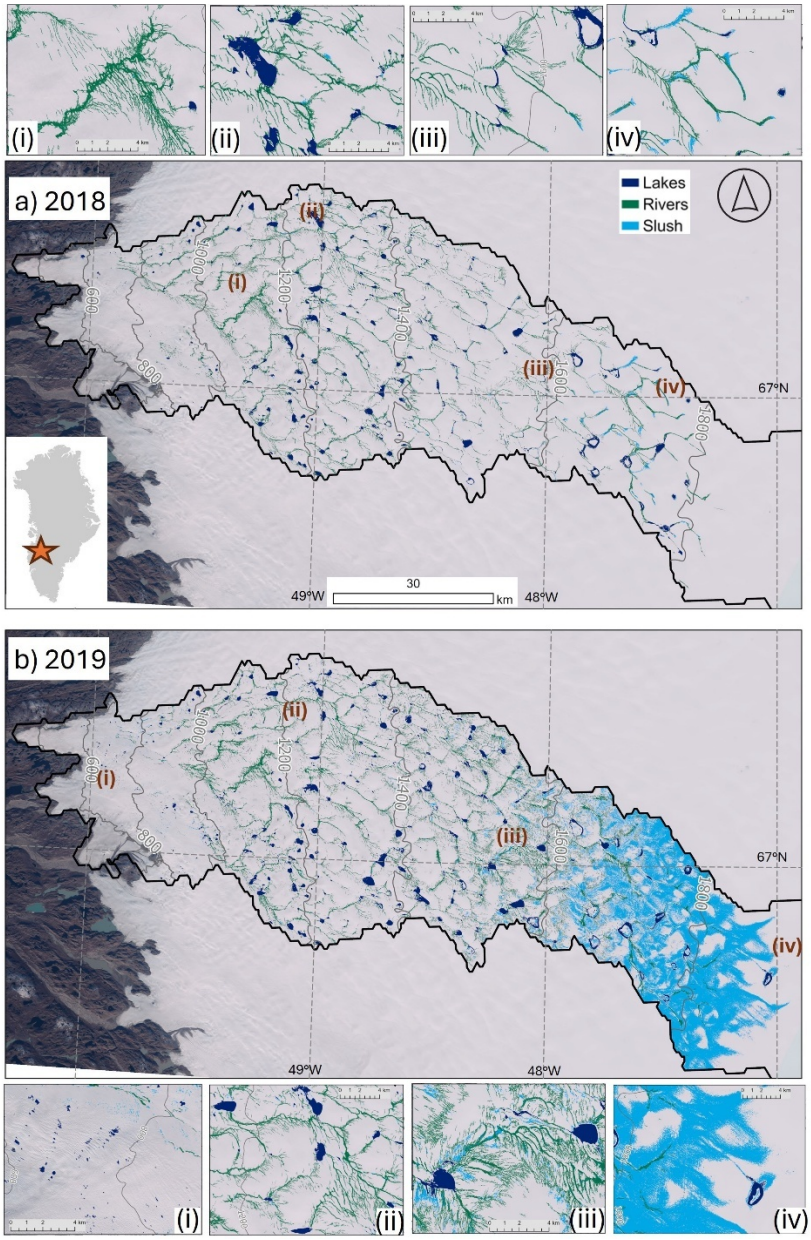

Figure 3.1: Maximum areal extent of all supraglacial meltwater features in (a) 2018 and (b) 2019 within the Russell-Leverett Glacier catchment derived from ArcticDEM (black outline). Slush is light blue, channels are green, and SGLs are dark blue. Elevation contours from the ArcticDEM are shown in grey (m a.s.l.). Background is a true colour Sentinel-2 image acquired on 26/09/2019. Inset depicts the location of the catchment within southwest GrIS. a(i) depicts a supraglacial channel system, a(ii) shows SGLs linked with channels, a(iii) is an example of underdeveloped SGLs in the ~1600 m a.s.l. region of the catchment, a(iv) depicts slush and channels in the percolation zone (~1700 m a.s.l.). b(i) shows small SGLs close to the margins of the catchment, b(ii) highlights interconnected channels and SGLs, b(iii) shows interconnected SGLs, channel and slush, b(iv) depicts high-elevation (˜1900 m) slush, channels and the highest elevation SGL (1880 m) in our 2019 dataset.

3.2.3. Satellite imagery and pre-processing

All available imagery from both the Landsat 8 Operational Land Imager (hereafter 'L8') and the Sentinel-2 Multispectral Instrument (hereafter 'S2') sensors was acquired from 1 May to 30 September for both 2018 and 2019 melt seasons (Table A.1). We initially limited the cloud cover to < 50% based on the image metadata. However, after manual inspection, it appeared that some white ice/snow was misclassified as cloud. Therefore, we manually checked all available images and included misclassified images (labelled with > 50% cloud cover) in our dataset. Images with a sun angle < 20° were discarded due to difficulties in accurately differentiating meltwater features from adjacent features under these conditions (Halberstadt et al., 2020). 10 L8 images and 18 S2 images were used for 2018, and 16 L8 and 63 S2 images were used for 2019, corresponding to a mean temporal sampling of ~ 5 days and ~ 2 days in 2018 and 2019, respectively.

L8 data were downloaded as Level-1T geometrically and radiometrically calibrated images in the form of Digital Numbers. The L8 Level-1T data were converted to Top-Of-Atmosphere (TOA) reflectance using individual image metadata and equations provided in the Landsat 8 Data Users Handbook (USGS, 2019). L8 bands 2 (blue), 3 (green), 4 (red) and 5 (NIR), which have a spatial resolution of 30 m, were pan-sharpened to a 15 m resolution using intensity hue saturation methods (Rahmani et al., 2010), to better match the 10 m resolution of S2 data. L8's bands 6 (SWIR) and 10 (thermal infrared), which have a spatial resolution of 30 and 100 m, respectively, were resampled using nearest neighbour interpolation. S2 data were downloaded as Level 1-C orthorectified TOA reflectance products with sub-pixel multispectral registration. S2 bands 1 (Coastal Aerosol) and 11 (SWIR) have a spatial resolution of 60 m and 20 m, respectively, and so were resampled using nearest neighbour interpolation to match the finer (10 m) resolution of bands 2 (blue), 3, (green), 4 (red) and 8 (NIR).

3.2.4. Image masking

Prior to meltwater delineation, rock and cloud masks are created and applied to each L8 and S2 image to reduce classification errors, using methods by Corr et al. (2022), which are summarised here and in Figure 3.2, where all threshold values are also stated. The addition of masks allowed for better separation between deep meltwater features, rocks, clouds, and shaded snow areas. For L8 images, rock masks were created using the thermal infrared band, blue band, and red band. For S2 imagery, rock masks were created by applying the Normalised Difference Snow Index (NDSI), created by Hall et al. (1995), as well as additional blue and green filters, which applied separately, to remove snow and clouds.

Clouds were masked from L8 imagery using the NDSI, Short-Wave Infrared band (SWIR), and blue band. Clouds were masked in S2 imagery using the SWIR band, SWIR-Cirrus band, and blue band. We took the threshold values for these masks directly from Corr et al. (2022; Figure 3.2).

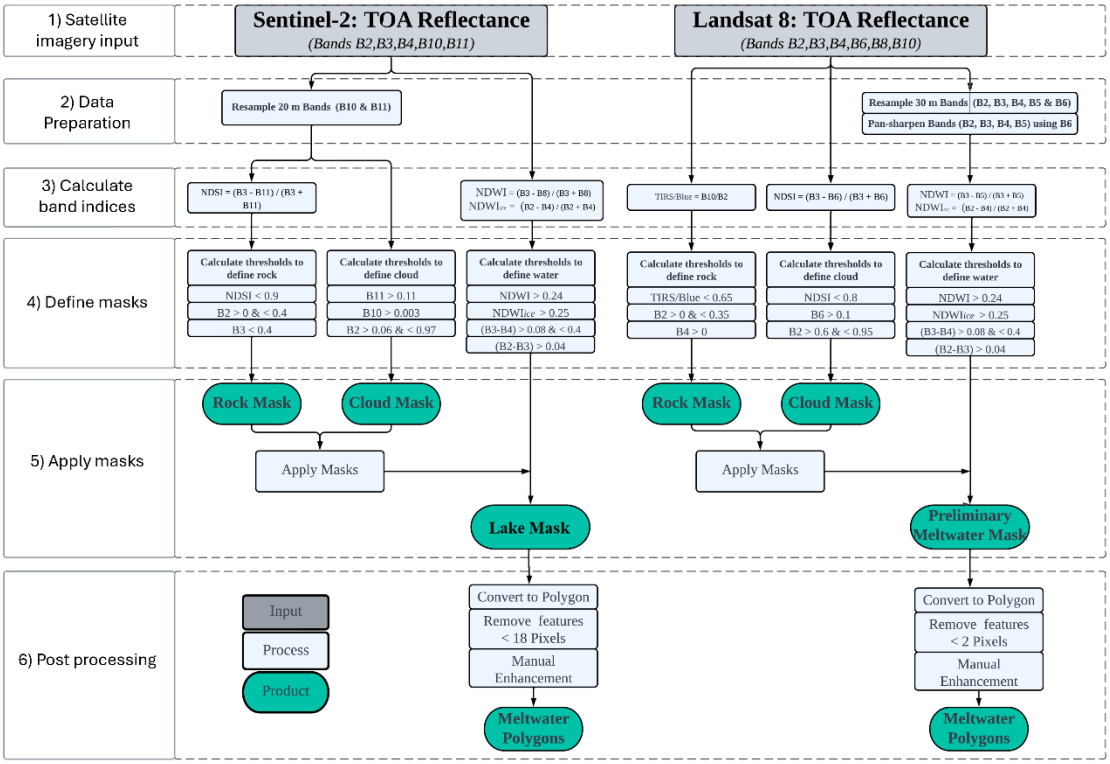

Figure 3.2: Workflow of SGL delineation by NDWI thresholding and additional filtering on Sentinel-2 (left) and Landsat 8 (right) image scenes, following methods adapted from Corr et al. (2022). Top of Atmosphere (TOA) reflectance values are used as input. Normalised Difference Snow Index (NDSI), Normalised Difference Water Index (NDWI), NDWI adapted for ice (NDWI_ice) and additional band (B) combinations are used to mask imagery and define meltwater. The wavelengths of each numbered band are taken from the Sentinel-2 User Handbook and Landsat 8 Data User Handbook (see Data Availability section).

3.2.5. Supraglacial lake delineation

We delineate SGLs from the masked L8 and S2 imagery following Corr et al. (2022) (Figure 3.2). We apply the NDWI calculated from the ratio of green and NIR wavelengths (McFeeters, 1996), in addition to the NDWI adapted for ice (NDWI_ice), which utilises the ratio of blue and red wavelengths and better accounts for the supraglacial conditions of the GrIS (Yang and Smith, 2013). For both L8 and S2 imagery, NDWI values > 0.24 and NDWI_ice values > 0.25 were classified as water pixels with all other pixels designated as not water (Figure 3.2). Our chosen threshold values are in line with those from previous

studies, which typically lie between 0.15 and 0.30 (e.g., Williamson et al., 2018a; 2018b; Miles et al., 2017; Bell et al., 2017; Stokes et al., 2019; Yang and Smith, 2013). For both L8 and S2 imagery, after application of the NDWI and NDWI_ice, we implemented two further threshold values to better distinguish meltwater features from surrounding ice/snow: the green band subtracted by the red band, and the green band subtracted by the blue band, again using the values from Corr et al. (2022) (Figure 3.2).

After SGLs had been delineated, binary lake/non-lake masks were created from all L8 and S2 scenes. In line with similar studies undertaken in Antarctica (Stokes et al., 2019; Dell et al., 2020; Langley et al., 2016), SGLs ≤ 0.0018 km² (≤ 2 L8 and ≤ 18 S2 image pixels) were removed from the binary meltwater images to reduce misclassification errors. The same area threshold was used for both L8 and S2, despite these sensors' different resolutions, in order to maintain consistency in the processing of data from both sensors. In our study, 'small lakes' are defined as SGLs > 0.0018 km² and ≤ 0.0495 km². The final stage of SGL delineation was to convert binary meltwater images to polygon features.

3.2.6. Supraglacial slush delineation

Before delineating slush, we first applied rock, cloud and SGL masks to each individual L8 and S2 image. As our preliminary analysis indicated that crevasses were often confused as slush, in line with findings of Rawlins et al. (2023), we applied a crevasse mask (Chudley et al., 2021). Having applied this mask, we delineated slush using methods adapted from Bell et al. (2017) and Yang and Smith (2013). Whereas Bell et al. (2017) and Yang and Smith (2013) used just a single NDWI threshold, we used two separate NDWI and NDWI_ice thresholds to identify shallow water and slush, which is consistent with our SGL identification method (Corr et al., 2022) (Section 2.5). In our study, we found that using these two separate thresholds (> 0.14 and > 0.15 for the NDWI and NDWI_ice, respectively) optimized slush identification while minimizing misclassifications with other meltwater features. These thresholds were determined through iterative testing against true-colour images, evaluating a range of potential values (from 0.1 to 0.2 in increments of 0.01). The iterative process involved visually comparing the classified slush areas with their appearance in true-colour images, allowing us to identify thresholds that best matched the observed spatial extent of slush. Binary slush masks were then created and converted to polygon features for analysis.

3.2.7. Supraglacial channel delineation

Supraglacial channels have different physical and spectral characteristics to SGLs, and thus we delineated channels using channel-specific methods developed by Yang et al. (2015).

We extracted channels based on their Gaussian-like cross-sections and longitudinal open-channel morphometry. All meltwater features were first enhanced by calculating the NDWI for the image. A band-pass filter, which is ramped between 1/200 and 1/40 m^{-1} (Yang et al., 2015), was then applied to remove low frequency background and high frequency noise. This was followed by applying Gabor filtering to amplify the cross-section of small channels with widths < 2 pixels. A path opening operator (with a minimum length of 20 pixels) was then implemented to produce better channel connectivity. We then removed any features < 1000 m in length to reduce classification uncertainties. To account for variations in environmental conditions across the different tiles, a pixel brightness threshold of 5 for lower-elevation ('_T22WEV_') S2 tiles and all L8 tiles, and 10 for higher-elevation ('_T22WFV_') S2 tiles (Table A.1), out of 255 was then used to extract the channels (Lu et al., 2020; Rawlins et al., 2023). We again tested threshold values in our study against true colour images to optimize channel delineation in select tiles, a process consistent with approaches in other studies where thresholds are manually adjusted to ensure consistent feature extraction (e.g., Zhang et al., 2023). Masks were then applied to remove all features (rock, cloud, SGL, slush, crevasse) not related to channels, before delineated channel features were polygonised.

3.2.8. Post-processing meltwater feature polygons

To account for the detection of false positives and/or negatives in the polygon features, manual enhancement was undertaken for all image acquisitions used in the study by comparing the appearance of supraglacial meltwater on true colour composite images. Polygons which incorrectly identified supraglacial meltwater were manually removed, and undetected meltwater features such as deep SGL centres and narrow channels were manually added.

To calculate meltwater feature statistics from each meltwater feature polygon, the mean elevation of each individual waterbody polygon was extracted from the ArcticDEM 100 m mosaic, which represents median elevation values from data acquired between 2011 and 2017 (Porter et al., 2018). Mean ice thickness values for every meltwater feature were extracted from BedMachine Greenland v4 at a 150 m spatial resolution (Morlighem et al., 2017; 2022).

To evaluate meltwater channel interconnectivity, we calculated the channel drainage density of the catchment (e.g. Yang et al., 2019). For each day of available imagery, we calculated the total channel length of each channel centreline and divided this value by the area of the catchment (5800 km^2).

3.2.9. Uncertainty analysis of meltwater feature area

The uncertainty associated with using a dual sensor (L8 and S2 imagery) approach is generally low in our study. We calculate that the greatest uncertainties between meltwater features delineated from the two different sensors are observed during peak season (3 July), with an R^2 of 0.93 and RMSE = 0.1 km² at this time.

An evaluation between meltwater feature areas derived from L8 and S2 images was undertaken to determine whether sensor resolution impacts SGL detection accuracy. Individual lake areas of overlapping lake polygons across the whole catchment, derived from L8 and S2 images from 8 June, 3 July and 29 August 2019, were compared. We found a strongly significant relationship between both lake area datasets on all of these three dates (with R^2 values of 0.98 on 8 June, 0.93 on 3 July and 0.98 on 29 August; Figure 3.3). There were no overlapping S2 and L8 images in the 2018 melt season to compare. Although it has previously been shown that S2 imagery can detect meltwater at the boundaries of hard to distinguish lakes more accurately than L8 (i.e. Arthur et al., 2020a), here we conclude that sensor resolution does not have a significant impact on our ability to accurately detect meltwater or calculate SGL area, and both sensors can be used in conjunction for such analysis.

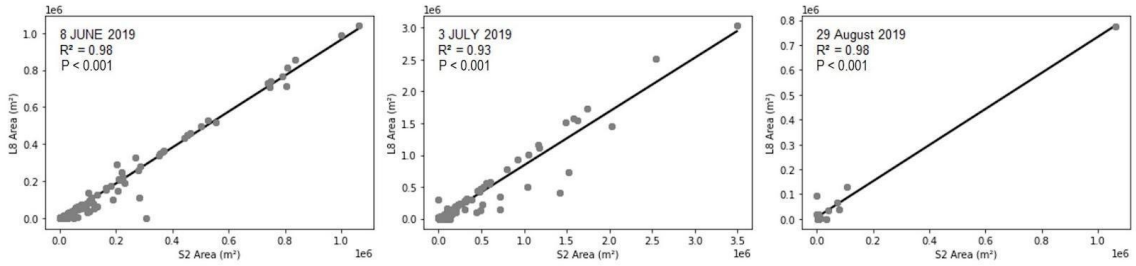

Figure 3.3: Lake area frequency distribution from three overlapping Landsat 8 and Sentinel-2 image scenes throughout the 2019 melt season.

In the absence of extensive ground truth data, it is very difficult to assess the accuracy of calculated meltwater feature areas, and this is an acknowledged challenge in the literature (e.g., McMillan et al., 2007; Sundal et al., 2009; Leeson et al., 2012; Corr et al., 2022). To provide an indicative estimate of the confidence in our meltwater delineation methods, we therefore compare our dataset to a fully manually delineated dataset, in line with the methods employed by other meltwater mapping studies (e.g. Corr et al., 2022; Arthur et al., 2021). Two ‘experts’ (i.e. glaciologists with extensive expertise in Greenland surface hydrology mapping) manually digitised meltwater features (categorised as SGLs, streams and slush based on physical appearance) from eight true colour composite S2 images

spanning across the 2018 and 2019 melt seasons. In comparing the areas of the manually and automatically derived datasets, we find that the mean difference between meltwater feature area manually derived by experts and area automatically delineated in our dataset to be 0.06 km². This reflects both the uncertainty in the automated and manual mapping procedures, and with the challenges of mapping small lakes and slush. While the number and size of features vary between scenes, total mapped meltwater area per image typically ranged from ~10 to 80 km², indicating that a mean difference of 0.06 km² per feature is relatively minor in context. Nonetheless, this figure provides only an indicative estimate of delineation uncertainty in the absence of ground truth data.

3.2.10. Calculating supraglacial lake depth and volume

Water depth for each SGL pixel was determined using the physically-based radiative transfer model used in a variety of prior studies (e.g., Sneed and Hamilton, 2007; Banwell et al., 2014; Pope et al., 2016; Williamson et al., 2018a; Macdonald et al., 2018). This algorithm calculates meltwater feature depth assuming that light penetrating a water column is attenuated with depth (Philpot, 1989). An assumption is made that the optical properties of the meltwater features are not altered by wind-driven surface roughness or column-integrated particulate matter. The lake bottom albedo is taken to be homogenous (Sneed and Hamilton, 2007). Depth, *z*, is calculated using equation 3.1:

$$z = \frac{ln(Ad - R\infty) - ln(Rw - R\infty)}{g}, \quad (3.1)$$

where *Ad* is lakebed reflectance, *R*∞ is the reflectance of optically deep water, *Rw* is the satellite measured reflectance value of a water pixel, and *g* is the attenuation coefficient rate associated with losses in upward and downward directions through the waterbody.

For L8 data, depths were determined by an average of both red and panchromatic TOA reflectance values (after Williamson et al., 2018a, Macdonald et al., 2018, and Pope et al., 2016). *Ad* was obtained from the average reflectance of the first non-water pixel surrounding each feature, determined by a single pixel (30 m) buffer around meltwater features. *R*∞ was determined in each individual image as the darkest open ocean pixel and if deep water was not present in an image, *R*∞ was taken to be 0 (Sneed and Hamilton, 2007; Banwell et al., 2019; Dell et al., 2020). Following Williamson et al., (2018a) the value of *g* was taken to be 0.3817 for the panchromatic band and 0.7504 for the red band (after Pope et al., 2016).

For S2 data, depths were determined by using the red TOA reflectance value, after Williamson et al. (2018a). Due to S2's finer spatial resolution compared to L8, *Ad* was determined by the average reflectance of the first three pixels surrounding the waterbody, as

opposed to just one surrounding pixel for L8. $R\infty$ was taken to be 0, as for L8 (see above), and a g value of 0.8304 was taken from Williamson et al. (2018a).

For both the L8 and S2 imagery, meltwater feature volumes were then calculated by taking the sum of depths multiplied by the pixel area. We assume an uncertainty of 21.2% on these volume estimates, after Melling et al., (2023), who compared meltwater feature depth and volume determined by the same radiative transfer algorithm to those determined from the ArcticDEM, for five SGLs in the Russell-Leverett catchment. It should also be noted that this method may be less accurate in higher elevation regions due to the prevalence of slush that may alter the reflectance of surrounding pixels (Melling et al., 2023).

3.2.11. Tracking lakes through time

The seasonal evolution and drainage dynamics of SGLs within the catchment were tracked using the Fully Automated Supraglacial Lake Tracking at Enhanced Resolution (FASTER) algorithm developed by Williamson et al. (2018a). Using this algorithm, we created maximum meltwater extent array masks for both the 2018 and 2019 melt seasons by superimposing individual SGL masks derived from each image. We then applied FASTER to these SGL masks and used it to track changes in SGL area and volume between images, which also enabled us to detect SGL drainage events.

In addition to simply detecting SGL drainage, Williamson et al. (2018a) also used the FASTER algorithm to partition between rapid and slow SGL drainage events based on a 4-day sampling period. However, given the paucity of our data in 2018 relative to 2019, we performed an assessment of the temporal sampling that would be required in order to robustly determine whether a meltwater feature drained rapidly or slowly. Our findings show that data with a temporal sampling of two to three days is required for such partitioning, while the typical temporal sampling of data in 2018 is only five days. As such, in this study, we restrict our analysis to assessing drainage of any kind, regardless of timeframe.

We use our 2019 dataset of SGLs to highlight the influence of the timescale of image availability on rapid and slow SGL drainage events. An SGL was determined to drain rapidly if > 80% of its volume was lost over a period of 1-5 days, and an SGL was determined to drain slowly if it lost 20% of its volume over any time period (Figure 3.4a). The proportion of rapid drainage events changes when the time threshold changes, highlighting how the number of drainage days used to determine a rapid drainage event can alter results considerably; the difference between 3 days and 4 days is particularly notable. The typical time that previous studies have used to determine a rapid SGL drainage event is 4 days (Figure 3.4b).

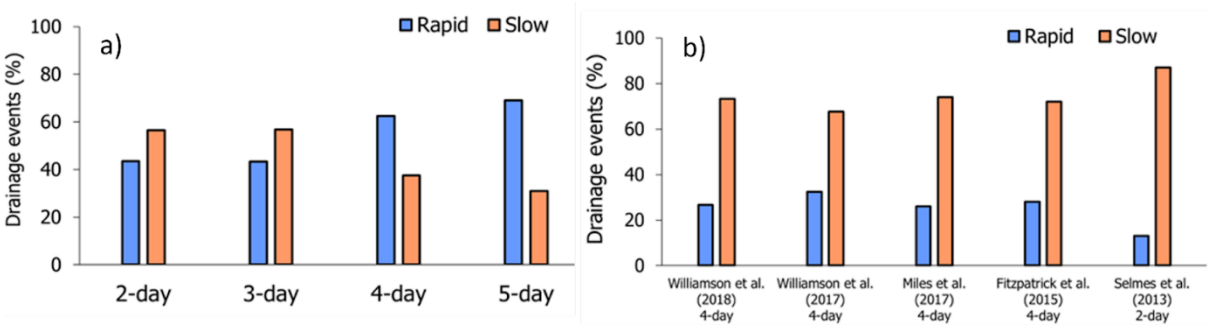

Figure 3.4: Partitioning of lake drainage events. a) Percentage of rapid and slow SGL drainage events in 2019 (y axis) and the number of days determining rapid drainage (x axis). b) Frequency of rapid and slow SGL drainage events from previous SW Greenland studies.

An SGL was determined to have drained when > 20% of its liquid volume appeared to have been lost over any time period and if it did not gain volume in any subsequent image through the melt season. An SGL was determined to have refrozen if it: 1) lost > 20% of its volume with no volume regain in subsequent imagery; 2) the mean air temperature was ≤ 0°C +/- 1°C during, and over the two days before, the volume loss event; and 3) the volume loss period lasted at least 72 hours. Mean air temperature was extracted from the RACMO 2 m air temperature data (see Section 2.12) at the centroid of each meltwater feature during, and over the two days preceding, the volume loss event. The > 72-hour event threshold duration reflects the fact that SGL refreezing does not happen instantaneously after the onset of negative temperatures. To provide some validation for our approach, we have cross referenced a subset of our refreezing lakes with two independent datasets of buried lakes acquired from SAR imagery in both years (Dunmire et al., 2021; Zheng et al., 2023).

To provide some validation for our approach to determine if an SGL has refrozen or not, we cross referenced a subset of our refreezing lakes with two independent datasets of buried lakes acquired from SAR imagery in both years (Dunmire et al., 2021; Zheng et al., 2023) (Figure 3.5). This is undertaken under the assumption that refrozen lakes essentially become buried lakes after refreezing. We find good agreement in the locations of refreezing lakes in our dataset when compared to the other two datasets. We suggest that differences in the locations of these refrozen lakes are due to differing NDWI thresholds used to produce the three datasets.

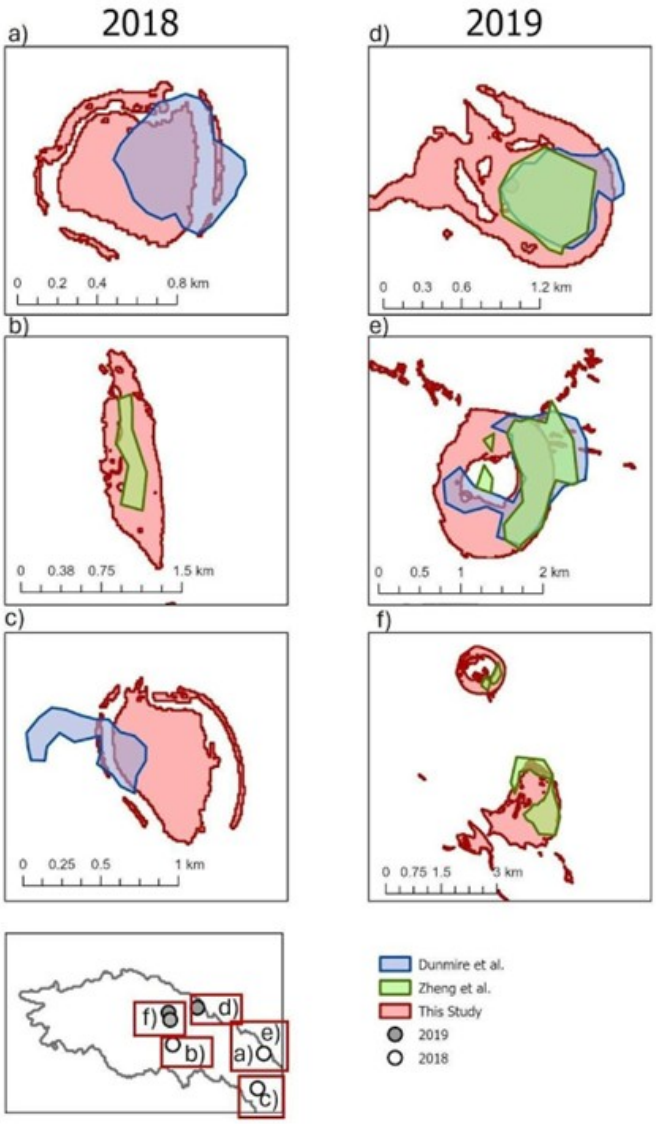

Figure 3.5: Cross referencing a subset of refreezing lakes in this study with maps of subsurface lakes acquired from SAR imagery in both 2018 (left) and 2019 (right). Blue: dataset from Dunmire et al. (2021); green: dataset from Zheng et al. (2023); red: Data from this study. Coordinates of lakes in WGS 1984 UTM Zone 22N: a) 47.3861245°W 66.9952765°N, b) 48.4755826°W 67.0147779°N, c) 47.4456300°W 66.8319809°N, d) 48.2075289°W 67.1934572°N e) 47.3873357°W 66.9953815°N , f) 48.5521200°W 67.1620352°N.

In addition to ‘drain’ and ‘refreeze’ SGL behaviour classes, we also included an ‘unknown’ behaviour class. An SGL was classified to have ‘unknown’ behaviour if the patterns of area and volume decline are not in accordance with that of a draining or refreezing SGL, as described above.

3.2.12. Regional air temperature and surface melt

To calculate temperature anomalies for the Russell-Leverett Glacier catchment for our melt seasons of interest (i.e. 2018 and 2019), we used mean daily values of 2 m air temperature from 1958 to 2019 from the Regional Atmospheric Climate Model (RACMO2.3p2, hereafter 'RACMO') at 5.5 km spatial resolution and further statistically downscaled to a 1 km grid (Noël et al., 2018; 2019). We additionally used the air temperature data to partition between SGL drainage and refreezing (Section 2.11 above).

We also extracted daily mean values of total melt (ice and snow) from RACMO throughout both 2018 and 2019 melt seasons for the catchment. Previous studies have shown that RACMO performs well compared to automatic weather station data along the K-Transect (e.g., Noël et al., 2018).

3.3. Results

3.3.1. Meltwater feature distribution in each melt season

Our detailed mapping shows that the distribution of meltwater features differs between the 2018 and 2019 melt seasons. We compute the maximum meltwater areal coverage as a percentage of the catchment area (i.e., the total area where liquid water is observed to be present on at least one day of the melt season) to be 6.3% in 2018 and 20.8% for 2019 (Figure 3.1). In 2018, channels make up the largest proportion of meltwater features by area, with a cumulative maximum areal coverage of 4.5% of the catchment area, followed by SGLs (1.5%) and slush (0.3%) (Figure 3.1a; Table A.2). In comparison, in 2019, slush covers the largest area of the catchment, with a cumulative maximum areal coverage of 12.3% of the catchment area, followed by channels (6.4%) and SGLs (2.1%) (Figure 3.1b).

Meltwater extends from the margin to 265 km (1815 m a.s.l.) and 315 km (1920 m a.s.l.) inland in 2018 and 2019, respectively. SGLs and channels have a similar median elevation of ~ 1350 m a.s.l. in the 2018 melt season (Figure 3.6). In comparison, in 2019, the median elevation of SGLs and channels is 1250 and 1500 m a.s.l. (~ 100 m lower and 150 m higher than 2018), respectively. Slush is concentrated over higher elevations in 2019 than in 2018 (Figure 3.6). The elevation range of slush in 2018 is 800 – 1700 m a.s.l., whereas in 2019, slush is concentrated over a smaller range and at higher elevations of 1200 – 2000 m a.s.l. Slush features are situated at the higher elevations compared to the other meltwater features, with a maximum elevation of ~ 1600 m a.s.l. in 2018 and a higher maximum elevation of ~ 1700 m a.s.l. in 2019. In both years, SGLs also tend to be larger in area at

higher elevations, coincident with lower surface slopes at these elevations (Figure 1; Figure 3.7).

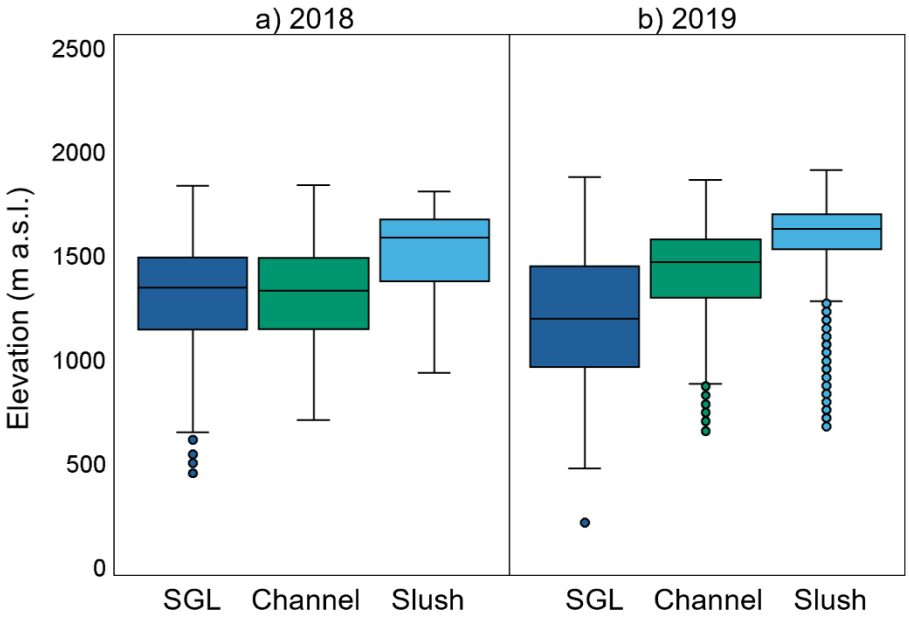

Figure 3.6: Boxplots showing the hypsometry of supraglacial lakes, channels, and slush features in 2018 (a) and 2019 (b). The black horizontal line represents the median, the edges of the box indicate the 25th and 75th percentiles, the whiskers are equal to the 5th and 95th percentiles, and outliers represent the full elevation distribution.

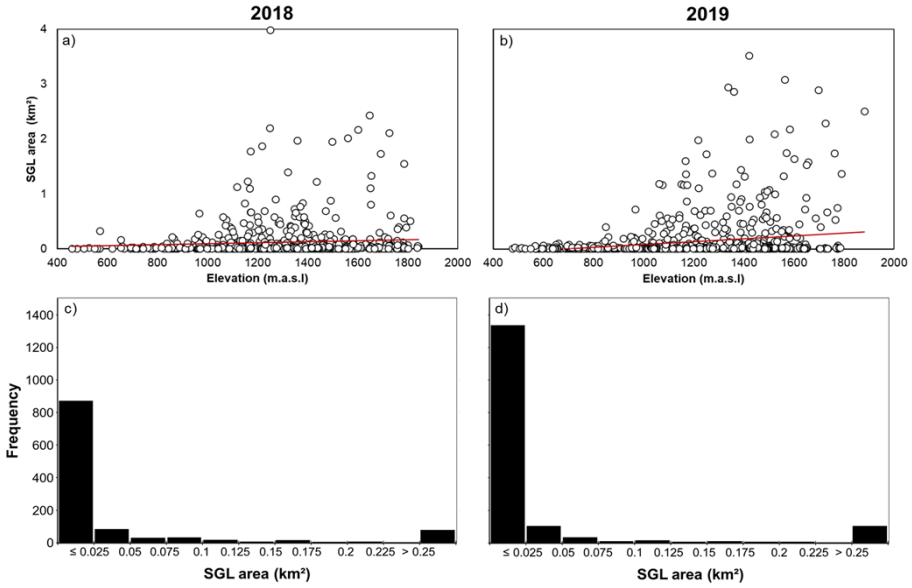

Figure 3.7: Scatter plots (a) and (b) displaying the relationship between SGL area and elevation for 2018 and 2019, respectively. Histograms (c) and (d) showing the frequency distribution of SGL areas separated into 10 different bins for 2018 and 2019, respectively.

3.3.2. Meltwater feature evolution through each melt season

3.3.2.1. Supraglacial lakes

SGLs appear earlier in the 2019 melt season than in 2018. In 2018, SGLs first appear on 5 June (Figure 3.8a), whereas in 2019, they first appear approximately one month earlier on 9 May, following a ~ + 11 °C temperature anomaly in early May 2019 (Figure 3.8b). In 2018, total SGL area and volume gradually increase from 5 June by 1.9 $km^2\ d^{-1}$ and 0.002 $km^3\ d^{-1}$, respectively, until 18 June. Both total SGL area and volume then remain relatively steady until 13 July, when both peak at 40 km^2 and 0.05 km^3, respectively (Figure 3.8a). Both SGL area and volume abruptly decrease by 4.3 $km^2\ d^{-1}$ and 0.004 $km^3\ d^{-1}$, respectively, from 19 to 24 August 2018, coinciding with lower surface air temperatures and melt rates.

Rates of increase of area and volume are slightly lower in 2019 (1.1 $km^2\ d^{-1}$ and 0.001 $km^3\ d^{-1}$, respectively), than in 2018. However, these rates are sustained over a longer period of time in 2019, throughout May and June, resulting in a peak area and volume that is higher in 2019 than in 2018, at 56 km^2 and 0.07 km^3, respectively. The 2019 peak also occurs earlier in the melt season, on 20 June (Figure 3.8b). From then onwards through the remainder of the 2019 melt season, SGL area and volume decrease at an average rate of 1.1 $km^2\ d^{-1}$ and 0.001 $km^3\ d^{-1}$, respectively, which represents a more gradual decline than in 2018. The disappearance of all SGLs occurs only slightly later in 2019 (on the 26 August), than in 2018 (on 21 August). In both melt seasons, SGLs initially form at low elevations (~1000 m a.s.l.), migrating inland to higher elevations as the melt seasons progress.

Small SGLs (i.e., > 0.0018 km^2 and ≤ 0.0495 km^2) are more abundant in 2019 than in 2018 (Figure 3.9). In both years, small SGLs are most prevalent at the start of the melt season at low elevations (Figure 3.1a (i)). In 2018, small SGLs make up 86% of all SGLs that form within the first month (June), and are situated at a mean elevation of 1040 m a.s.l. In 2019, small SGLs make up 89% of all SGLs that form within the first month (May), and are situated at a lower mean elevation of 950 m a.s.l.

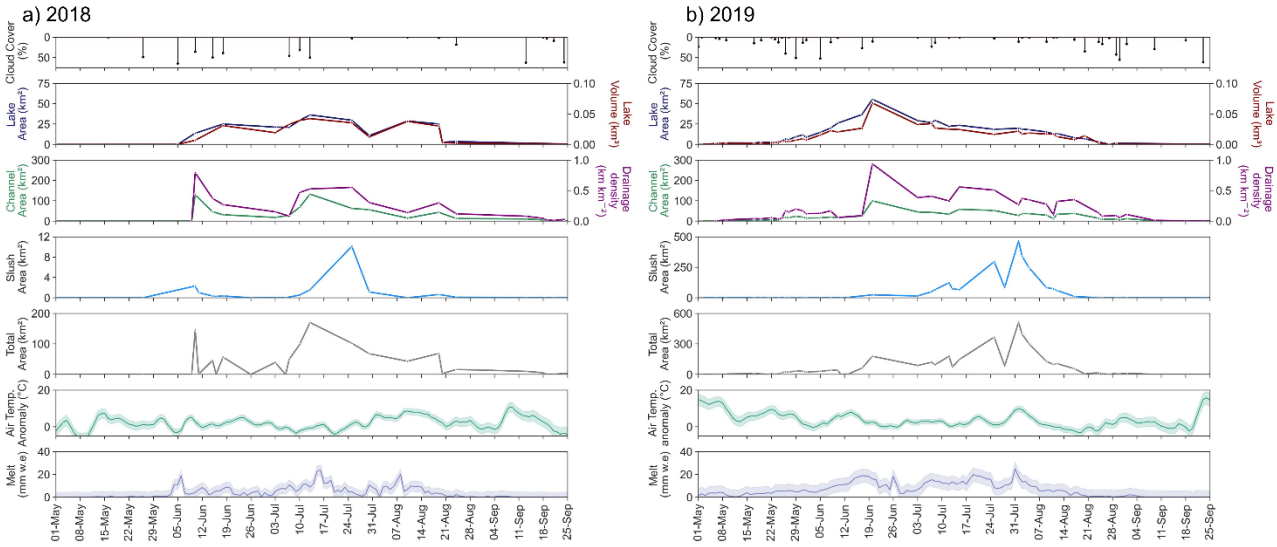

Figure 3.8: Time series of total areas of SGLs (dark blue), channels (green), slush (light blue) and all meltwater features (grey) in (a) 2018 and (b) 2019 from L8 and S2 imagery. SGL volume is given in red and channel drainage density is given in purple. Also shown is cloud cover percentage (black bars), RACMO 2 m air temperature anomaly (light green line) from the 1958 - 2019 catchment average with the spatial standard deviation (light green shading), and RACMO total daily melt (mm w.e.; light blue line) with the spatial standard deviation (light blue shading). Note that the y-axis ranges are different for the slush and total areas between (a) and (b).

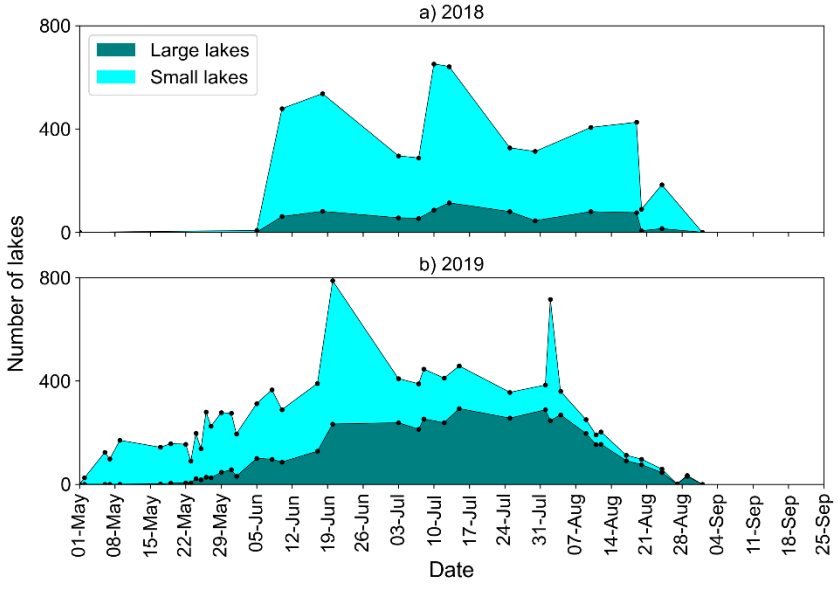

Figure 3.9: The total number of SGLs observed throughout the 2018 (a) and 2019 (b) melt seasons, partitioned into large (> 0.0495 km²; teal green) and small (> 0.0018 km² and ≤ 0.0495 km²; aqua blue) SGLs. The black solid circles indicate the days on which measurements were acquired.

3.3.2.2. Supraglacial channels

In both 2018 and 2019, dense, dendritic drainage networks of supraglacial channels form, allowing for meltwater connectivity across the majority of the catchment towards the ice-sheet margin and proglacial area (Figure 3.1). In both years, channels are observed to expand up glacier from lower elevations (~800 m a.s.l.) to higher elevations (~1800 m a.s.l.) as the melt seasons progress (Supplementary Animation 1 and 2, Section A.1.).

In 2018, a large channel network (~125 km²) abruptly appears on 10 June after a spike in melt, before reducing by 4.9 km² d^{-1} until 3 July (Figure 3.8a). Total channel area then increases by 11.5 km² d^{-1} and peaks at ~ 130 km² on 13 July 2018, coinciding with peak melt. Channel area in 2018 then gradually reduces by 4.2 km² d^{-1} to ~ 15 km² by 10 August. We then observe a small 3.2 km² d^{-1} increase in total channel area to ~ 45 km² on 19 August 2018, followed by a 1.1 km² d^{-1} reduction in total channel area by 30 September.

In 2019, supraglacial channels appear earlier in the melt season compared to 2018, following the observed behaviour of SGLs (Section 3.2.1). Total channel area remains low throughout most of May (~ 4 km²) but then increases at a rate of 3.6 km² d^{-1} to reach a peak of 100 km² on 20 June (coinciding with maximum SGL areal extent) (Figure 3.8b). This peak is less than in 2018 (130 km²) and earlier in the melt season by 23 days. After the peak, total channel area in 2019 then decreases by 4.2 km² d^{-1} to 45 km² on 3 July, where it remains mostly steady until it begins to taper off on 24 August, reducing by 0.4 km² d^{-1} until channel features are no longer visible by 28 September.

The drainage density of the supraglacial channel network throughout both 2018 and 2019 follows a similar pattern to the total channel area (Figure 3.8). In 2018, the drainage density peaks in mid-June at 0.8 km km^{-2} (Figure 3.8a). In 2019, the drainage density also peaks in mid-June, although at a greater value of 1 km km^{-2} (Figure 3.8b). The density of the drainage network is consistently higher on average in 2019 compared to 2018, where it experiences distinct peaks and troughs.

3.3.2.3. Supraglacial slush

The evolution of supraglacial slush also differs throughout each melt year. In 2018, the total area of slush within the catchment follows a similar trend to channels and is mostly observed as extensions of channel features in the percolation zone (~ 1500 m a.s.l.) in mid-July (Figure 3.1a (iv)). The areal extent of slush remains low for most of the 2018 season, ranging from 0.02 km² on 6 July (by 0.53 km² d^{-1}) to a peak of ~10 km² on 25 July, which is when it reaches its maximum elevation of 1800 m a.s.l. (Figure 3.8a). Following this peak,

total slush area reduces by 0.4 km² d^{-1} until it reaches 0.65 km² on 19 August and then remains low until the end of the 2018 melt season.

Conversely, in 2019, slush is the most dominant meltwater feature in terms of areal coverage and, unlike in 2018 where it looks like extended channels, in 2019 it is characterised as patches of dense, light blue meltwater, with poorly defined boundaries (Figure 3.1b (iv)). In 2019, slush first develops at ~1500 m a.s.l. in mid-June and migrates up-glacier through July by occupying topographic lows, before stabilising in early-August at a maximum elevation of ~ 2000 m a.s.l. (i.e. 200 m higher than 2018) (Supplementary Animation 1 and 2, Section A.1.). The total area of slush remains low until it becomes established in late-June, when it increases from 14.9 km² on 3 July by 15.6 km² d^{-1} to peak at 466 km² on 1 August, which is 47 times larger than in 2018 (Figure 3.8b). The total area of slush then reduces in area by 19.4 km² d^{-1} until it ceases to be observed on 24 August 2019.

3.3.3. Modes of supraglacial lake evolution

3.3.3.1. Supraglacial lake drainage

Of the 1011 and 1495 SGLs that form in 2018 and 2019, respectively, 43% (432) and 44% (650) are observed to drain (either rapidly or slowly) (Table 3.1). In both melt seasons, drainage of SGLs occurs at increasing elevations and distances inland from the ice margin as the melt seasons progress (Figures 3.10a and b). The total meltwater volume drained from SGLs is similar in each year (0.54 km³ and 0.50 km² for 2018 and 2019, respectively), but the total drained meltwater area in 2019 is nearly double that in 2018 (59 km² and 99 km², respectively) (Table 3.1). However, the mean SGL drainage volume is greater in 2018 than in 2019 (1.3 $x10^{-3}$ km² and 7.7 $x10^{-4}$ km², respectively). In both years, the SGLs that drain early in the melt season are typically small lakes (Figure 3.10; Figure 3.11). For example, in 2018 and 2019, respectively, 83% and 87% of SGLs that drain in the first month of each season are classed as small SGLs (Figure 3.10). We also find that in 2018 and 2019, respectively, 47% and 67% of small SGL drainage events occur where the ice sheet is < 1 km thick.

Drainage events in 2018 are sporadic and spread over time throughout the melt season, with most drainage occurring in July and August (Figure 3.12a). The greatest number of drainage events in 2018 occur between elevations of 1200 and 1600 m a.s.l. We identify fewer SGL drainage events at the highest elevations in the catchment, with two notable exceptions being large events that occurred on 6 and 19 August 2018 (between 1600 - 2000 m a.s.l.). In comparison, in 2019, drainage events are more frequent and concentrated in time, occurring ~ a month earlier in the season, and predominantly in June and early-July (Figure 3.12b).

Similar to 2018, drainage frequency is greatest between 1200 and 1600 m a.s.l.; however, there is notably less volume of water that drains at the highest elevations in 2019. We identify more drainage events at low elevations in 2019 compared to 2018.

Table 3.1: Statistics of SGLs that drain, refreeze or have unknown behaviour in 2018 and 2019. DOY is the 'day of year' in 2018 and 2019. DOY sampling is calculated by averaging the start drainage DOY and the end drainage DOY. Percentage values are proportions of the sum of the total meltwater areas or volumes over each melt season.

	2018			2019		
Statistic	*Drainage*	*Refreeze*	*Unknown*	*Drainage*	*Refreeze*	*Unknown*
Frequency (n)	432	129	450	650	59	786
n (%)	43	13	44	43	4	53
Total volume (km^3)	0.54	0.065	0.0035	0.50	0.12	0.0015
Total volume (%)	89	11	< 1	80	19	1
Mean volume (km^3)	1.3e-3	5.0e-4	7.9 e-6	7.7e-4	2.8e-4	1.8e-6
Total area (km^2)	59	12	3.5	99	23	3.5
Total area (%)	80	16	4	79	19	2
Mean area (km^2)	0.14	0.091	0.0079	0.15	0.40	0.0044
Mean depth (m)	1.7	1.4	0.73	1.4	1.8	0.53
Mean event DOY	195	200	n/a	159	166	n/a
Mean DOY sampling (± days)	6	6	n/a	2	5	n/a
Mean elevation (m a.s.l.)	1224	1459	n/a	1130	1262	n/a

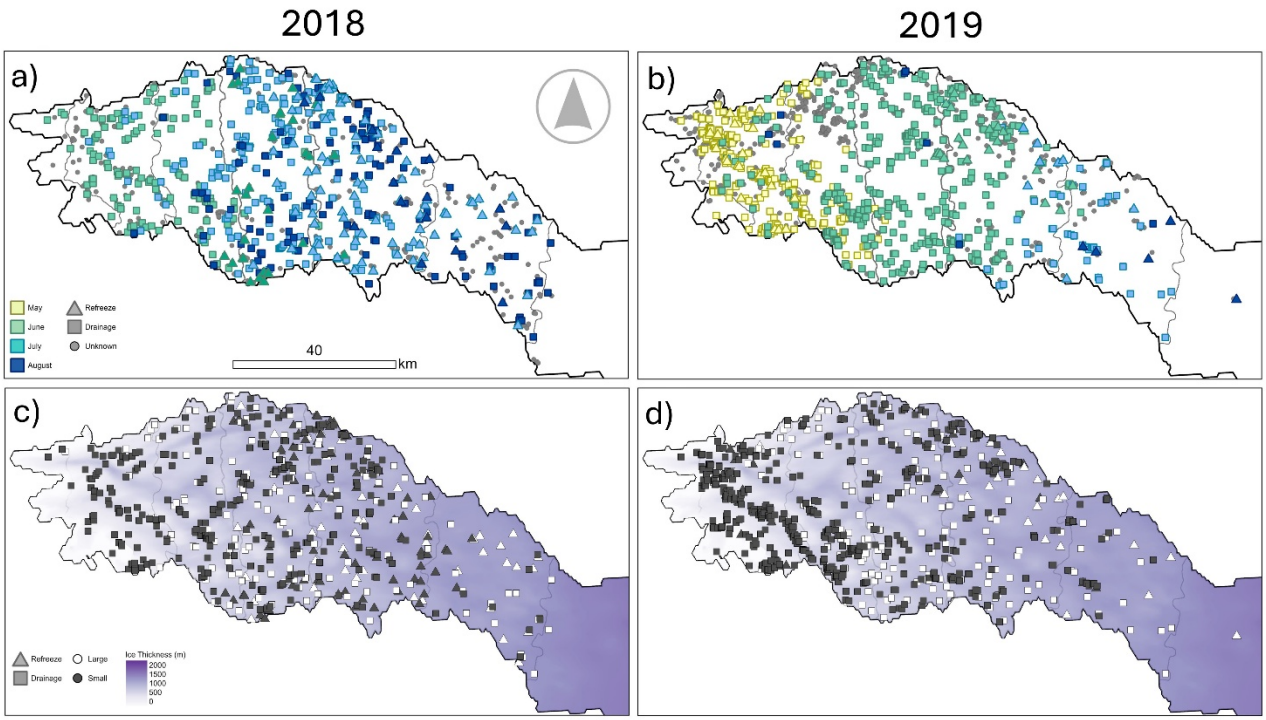

Figure 3.10: SGLs that drain, refreeze or have unknown behaviour in the Russell-Leverett Glacier catchment in 2018 (left) and 2019 (right). (a) and (b) depict the timing of SGL drainage (square) and SGL refreezing (triangle) events in 2018 and 2019, respectively. SGLs of unknown behaviour are represented by small grey circles. (c) and (d) depict small (≥ 0.0018 and ≤ 0.0495 km²; black) and large (>0.0495 km²; white) SGL drainage (square) and SGL refreezing (triangle) events in 2018 and 2019, respectively. Light to dark purple gradient represents ice sheet thickness in metres. SGLs of unknown drainage/refreezing behaviour are not shown in panels c and d.

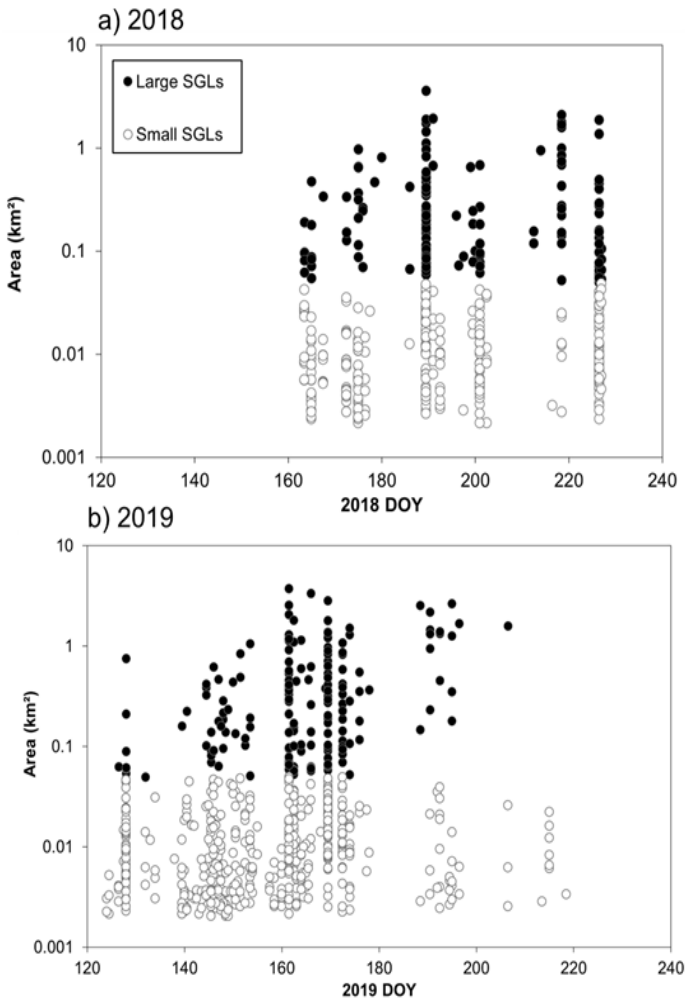

Figure 3.11: Seasonal variation in the area of draining SGLs in 2018 (a) and 2019 (b). The area of large draining SGLs (>0.0495 km²; solid black circles) and small draining SGLs (≥ 0.0018 and ≤ 0.0495 km²; open circles) is plotted on a logarithmic scale against the day of the year (DOY).

3.3.3.2. Supraglacial lake refreezing

In 2018, 13% (129) of SGLs refreeze, corresponding to 31% of total SGL area (12 km²) and 11% of total SGL volume (0.065 km³) (Table 3.1). In 2019, 4% (59) of SGLs refreeze, corresponding to 14% of total SGL area (23 km²) and 19% of total SGL volume (0.12 km³). On average, SGLs refreeze at higher elevations in 2018 (~1460 m a.s.l.) than in 2019 (~ 1260 m a.s.l.) (Table 3.1). The mean SGL refreezing elevation in 2018 is ~200 m higher than the mean drainage elevation and the mean SGL refreezing elevation in 2019 is ~100 m higher than the corresponding mean drainage elevation. In 2018, refreezing tends to occur at higher elevations (> 1200 m a.s.l.) where ice is thicker (Figure 3.10c; Figure 3.12). In 2019, refreezing typically occurs at elevations < 1000 m a.s.l. across the catchment, as well as in the northern area of the catchment between 1600 and 2000 m a.s.l. (Figure 3.10d;

Figure 3.12). We observe that ~12 SGLs appear to refreeze at lower elevations in May 2019, but limitations in temporal sampling prevent full characterisation of their subsequent dynamics.

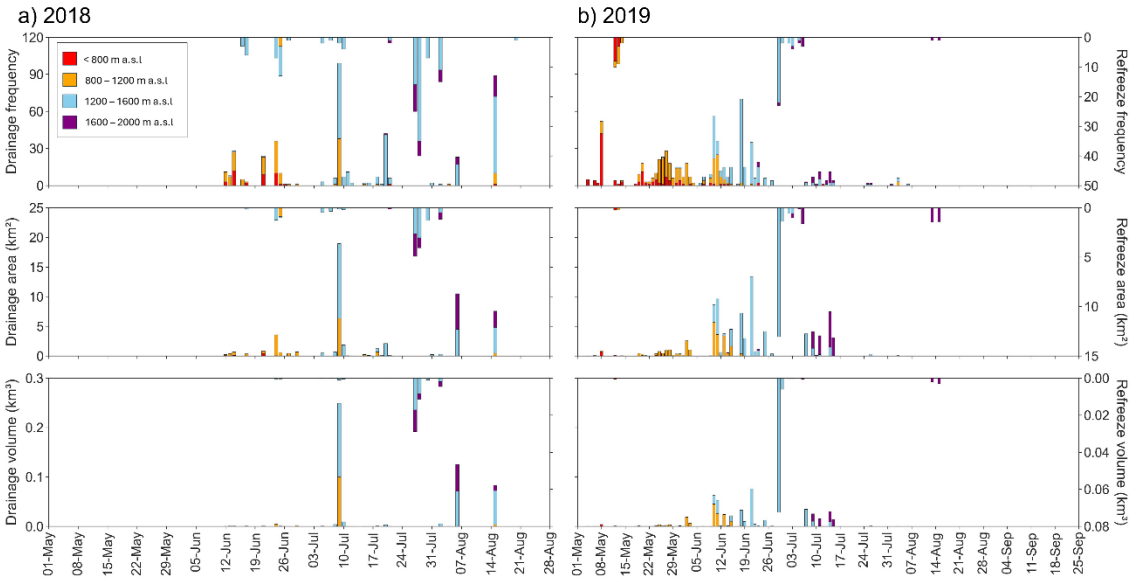

Figure 3.12: Time series of SGL drainage and refreeze within the Russell-Leverett catchment in a) 2018 and b) 2019, partitioned into elevation bands. From top to bottom: frequency of drainage/refreeze events (i.e., the number of features that drained or refroze); total daily area loss; total daily volume loss. Bars extending upward correspond to drainage events (left y-axis), while bars extending downward correspond to refreezing events (right y-axis). The data is colour-coded based on elevation: <800 m a.s.l. (red), 800–1200 m a.s.l. (orange), 1200–1600 m a.s.l. (blue), and 1600–2000 m a.s.l. (purple).

3.4. Discussion

By comparing meltwater features within the Russell-Leverett Glacier catchment between the high melt season of 2019 and the relatively lower melt season of 2018, we identify a clear contrast in supraglacial meltwater distribution, evolution and SGL behaviour. As Greenland's climate warms, exacerbated by Arctic amplification and climate/ice-sheet feedback processes, the frequency of high melt years like 2019 will likely increase (e.g., Hanna et al., 2024). By examining supraglacial meltwater behaviour during 2019–a year with warmer-than-average temperatures–we gain insight into how the ice sheet responds to large amounts of melt, contributing to our understanding of its future evolution in a changing climate. Our study also provides an assessment of the extent to which previously poorly mapped and understudied supraglacial hydrological features (such as small SGLs and slush) may play a role on the broader en- and sub-glacial systems, particularly in the context of a warmer climate.

3.4.1. Meltwater features at high elevations

We observe that meltwater features tend to extend further inland to higher elevations in the high melt year of 2019 than in the lower melt year of 2018 (Figure 3.6). This is in keeping with previous studies that found meltwater features tend to reach increasingly higher elevations during more intense melt years (e.g., Sundal et al., 2009; Liang et al., 2012; Lüthje et al., 2006). While these studies primarily focused on SGLs, our results indicate that channels and slush can typically coexist with SGLs across similar elevation bands, although slush is more commonly observed at higher elevations compared to SGLs and channels. The formation of channel, slush and SGL features at higher elevations in more intense melt seasons is indicative of the substantial surface runoff present in these regions during these periods. It has been previously reported that moulins are present at higher elevation regions in our study area (> 1600 m a.s.l., e.g., Yang et al., 2021). As such, it is possible that meltwater produced at high elevations may be routed to the bed through these moulins, in turn reaching areas where the subglacial hydrological system is relatively inefficient, which may cause temporary and localised speed up events (Leeson et al., 2015). The formation of meltwater features within the high elevation percolation zone may result in densification of firn and possibly ice slabs (e.g., MacFarren et al. 2019; Jullien et al., 2023), reducing the firn's meltwater storage capability and leading to enhanced supraglacial meltwater runoff in subsequent years (Machguth et al., 2016; Nienow et al., 2017).

3.4.2. Slush

We identify that the maximum spatial extent of peak slush area in 2019 is an order of magnitude greater, and extends to higher elevations, relative to 2018 (Figures 3.6 and 3.8). This is likely due to higher surface melt rates in 2019, especially above the equilibrium-line altitude. In previous work, the 'slush limit' has been used as an indicator of the visible runoff limit, representing the upper boundary where meltwater runoff is directed to the ocean and contributes to mass loss (Gruell and Knap, 2000; Tedstone and Machguth, 2022; Machguth et al., 2023; Clerx et al., 2022). Our study therefore suggests that the upper visible runoff limit is higher in the 2019 melt season compared to the 2018 melt season. Tedstone and Machguth (2022) found that the visible runoff area of the entire GrIS has increased by 29% between 1985 and 2020 and it is likely that projected warming may drive this limit upwards. We note that while our study–and indeed others that have used optical satellite imagery–can only detect slush on the ice surface, slush may also exist within the subsurface snowpack (Clerx et al., 2022). As such, our methodology of mapping slush from optical imagery

provides a minimum bound for slush extent, because the total slush area may be even greater than what we can observe from optical imagery alone.

The refreezing of slush at high elevations may have a long-term influence on the runoff from the GrIS by forming near-surface ice slabs, which act as aquitards, restricting meltwater percolation into the firn and reducing retention capacity (Machguth et al., 2016; MacFerrin et al., 2019; Miller et al., 2022; Jullien et al., 2023). As high melt years like 2019 become more frequent, it is likely that slush will become more prevalent, leading to the formation and expansion of low-permeability ice slabs, preconditioning the ice sheet surface for greater ponding and surface runoff in future years. This is potentially already occurring at Humboldt Glacier in North Greenland, where a previous study identified the earlier activation of the supraglacial hydrologic system and longer melt-seasons in years following widespread slush events (Rawlins et al., 2023).

Most prior mapping studies of Greenland's supraglacial hydrology, such as those by McMillan et al. (2007), Selmes et al. (2011), Williamson et al. (2017, 2018a), and Miles et al. (2017), have focused on SGLs, while others, including Smith et al., (2015), Yang et al. (2021), Lu et al. (2021), and Turton et al. (2021), examined meltwater channels and drainage patterns. However, these studies largely overlooked slush, which our findings show accounts for a significant proportion of the total meltwater area. In our study, slush accounts for ~ 59 % of total meltwater area in our study area of southwest Greenland in 2019. The exclusion of slush in these previous studies likely led to underestimations of meltwater extent.

The presence of widespread slush is likely to lower the surface albedo and hence increase solar absorption relative to ice or snow, thus influencing the surface energy balance. In Antarctica, Dell et al. (2024) found that slush accounted for ~ 50% of total meltwater area across 57 ice shelves around the continent. As variations in surface albedo due to slush (and ponded water) are not currently accounted for within surface energy balance routines in regional climate models, Dell et al. (2024) went on to calculate that modifying the surface albedo in a regional climate model to reflect the lower albedo of surface meltwater caused snowmelt to increase by 2.8 times across a subset of five ice shelves. That finding, combined with our observations in southwest Greenland, highlight the importance of including slush when mapping supraglacial meltwater across both of Earth's ice sheets. We further advocate for the refinement of regional climate models to account for slush’s impact on albedo, which will likely enhance the accuracy of modelled surface meltwater production.

3.4.3. Interconnectivity

The density and area of the supraglacial channel network provides an indication of meltwater interconnectivity across the catchment (Figure 3.8). Overall, we observe that the channel interconnectivity is more developed in the higher melt year of 2019 than in the relatively low melt year of 2018. The configuration of the supraglacial channel network has implications for both the routing of supraglacial meltwater, as well as the magnitude, location and timing of meltwater delivery to the en- and sub-glacial environment (e.g. Banwell et al., 2013; 2016; Smith et al., 2021). At lower elevations, meltwater routing is more efficient than at higher elevations (e.g. Smith et al., 2015) due to steeper gradients, crevassing, and minimal surface snow cover. Nonetheless, as air temperatures increase, as observed in 2019, so may the density and extent of the drainage network, with channel formation also extending to higher elevations (e.g., Yang et al., 2023), even in flatter, snow-covered regions, as demonstrated in our study.

A future increase in channel drainage density may also allow for amplified interactions between supraglacial channels and thin fractures, potentially leading to a slow mode of stream-driven hydrofracture via reactivation of existing fractures, with potential implications for cryo-hydrological warming at depth and decreased ice viscosity (Chandler and Hubbard, 2022).

3.4.4. Modes of supraglacial lake evolution

We show that previously understudied small SGLs (≥ 0.0018 km² and ≤ 0.0495 km²) form and drain in both melt years, although these features are more abundant in the high melt year of 2019 (Figure 3.9). Small SGLs tend to form and drain earlier in each melt season, and at lower elevations, than larger SGLs. This is likely because crevassing is more prevalent at lower elevations (Das et al., 2008) and smaller surface topographic undulations in these regions (Johansson et al., 2013) limit SGL growth. This allows small SGLs to reach their maximum volumes earlier in the melt season, when they may drain earlier via overflow. Although we do not partition slow and rapid SGL drainage in this study, it is reasonable to assume that moulins are created when small SGLs drain rapidly, which may then modulate ice dynamics on intra-seasonal time scales by providing access points for meltwater runoff to reach the ice sheet base throughout the remainder of the melt season (Banwell et al., 2016). While small SGLs contribute a relatively small proportion to the overall drainage flux across the melt season (3.5% in 2018 and 3.1% in 2019), their importance lies in the timing of their drainage. These events typically occur early in the season, when the subglacial hydrological system is inefficient due to limited preceding meltwater input (e.g., Bartholomew et al., 2010)

and may accelerate the transition to a more efficient subglacial configuration. The drainage of small SGLs dominates the first month of each melt season (e.g., June 2018 and May 2019), accounting for the majority (>80%) of drainage events. This early-season activity may contribute to the initial development of the subglacial hydrological system, potentially affecting when and where an efficient drainage network is established.

Furthermore, in both melt years studied, over a third of small SGLs drained in areas where ice thickness is less than 1 km, making it plausible that their drainage pathways extended to the bed, if they drained rapidly via hydrofracture. If so, moulin density at these lower elevations may be higher than previously reported (Banwell et al., 2016; Hoffman et al., 2018). This challenges the previous assumption that smaller lakes are unlikely to trigger hydrofracture through 1-1.5 km thick ice (Krawczynski et al., 2009), which was stated as the reason for why studies such as Miles et al. (2017) and Williamson et al. (2018a) restricted analyses to SGLs larger than 0.0495 km². Our observations suggest that small SGLs may play a more significant role in meltwater routing than previously recognised, particularly during high melt years such as 2019, when small lakes were approximately 15% more abundant, formed earlier in the melt season, and occurred at lower elevations compared to 2018. We suggest that including SGLs smaller than 0.0495 km² in future remote-sensing and modelling-based studies is important for better understanding where, when, and how much supraglacial meltwater is routed to the ice sheet bed, and the associated implications for ice dynamics.

We have identified that a greater number, and larger total area, of SGLs drained in 2019 compared to 2018, however our observations show that in both years a similar total volume of water drained. Interestingly, we find that SGLs which drained in the low melt year of 2018 were typically deeper and greater in volume than those that drained in the high melt year of 2019; a finding that is in line with those of Dunmire et al. (2024). It is possible that SGLs in 2019 were unable to reach greater depths due to increased ice speeds in 2019, perhaps resulting from rapid lake drainage events in the Spring, which in turn temporarily increased local ice velocity and hence tensile stress, triggering additional rapid SGL drainages (e.g., Christoffersen et al., 2018) relatively early in the melt season and thereby preventing SGLs in 2019 filling to their 2018 depths (Dunmire et al., 2024). Also, the increased supraglacial channel network interconnectivity that we observe in 2019 relative to 2018 may have provided a mechanism for meltwater to overflow out of SGLs via basin-side incision, thus preventing deeper SGLs from forming in 2019.

We find that a greater proportion of SGLs refreeze in 2018 (13%) compared to 2019 (4%), likely due to reduced number of lakes that drain in 2018, compounded by the cooler surface

air temperatures in 2018. If SGL refreezing on the GrIS becomes less common in the future, then a greater proportion of liquid meltwater will be available to drain to the ice sheet's base and/or be routed as supraglacial runoff towards the ocean. Additionally, open water in SGLs has a lower albedo than frozen SGLs, thereby resulting in increased melting through the positive melt-albedo feedback.

In both melt years, we find that SGLs more commonly drain than refreeze, and that refreezing typically occurs at higher elevations than drainage. This is in keeping with the findings of Johansson et al. (2013), Selmes et al. (2013) and Dunmire et al. (2024). The majority of the SGLs that we observe to refreeze do so at relatively high elevations (1250 to 1450 m a.s.l.), which is to be expected due to lower air temperatures, shallow surface slopes making SGL drainage via lateral surface overflow less likely (e.g. Raymond and Nolan, 2000), and thicker ice inhibiting rapid, vertical drainage through hydrofracture (e.g., Krawczynski et al., 2009). We acknowledge that, given the temporal sampling of our dataset, it is difficult to unequivocally distinguish between SGLs that drain and refreeze, and that consequently our partitioning method has several limitations. Our method only accounts for lake surface refreezing (i.e. lakes that form a cap of ice on their surface) and not full-thickness freeze through, and it is therefore possible that liquid meltwater may still persist under the refrozen surface. This may lead to the drainage of meltwater outside of the melt season when the subglacial drainage system is more likely to be inefficient and ice flow is more sensitive to meltwater input (e.g., Benedek and Willis, 2021). Dunmire et al. (2021) found that, in southwest Greenland in the 2018 and 2019 melt seasons, 87 and 80 buried lakes were identified, respectively, and we assume that these features were likely classified as refreezing events in our study. Finally, we note that some uncertainty in our study may exist because SGLs can lose volume through multiple mechanisms in a single melt season; for example, by undergoing both partial drainage and refreezing (e.g. Gantayat et al., 2023).

3.4.5. Limitations of using the 2019 melt season as a proxy for future warming

Using the relatively high melt season of 2019 to investigate how the GrIS responds to intensified warming offers valuable insights into the impact that future changes in climate may have on the ice sheet's hydrology and dynamics. Nonetheless, it is clear that using a single high melt year like 2019 to directly infer future conditions has inherent limitations, due to the fact that surface properties are dependent upon changes that occur over multiple seasonal cycles (e.g., Hanna et al., 2024). Beyond melt intensity and duration, for example, surface and near-surface properties such as snowpack thickness, firn air content, and the

presence of ice slabs partially control supraglacial meltwater and slush field extents. Ice slabs, for example, act as aquitards that prevent the vertical percolation of meltwater down into the firn and instead facilitate supraglacial runoff (MacFerrin et al., 2019; Jullien et al., 2023), while a thinner snowpack leads to faster saturation and slush expansion (Harper et al., 2012; Machguth et al., 2016). Therefore, while the 2019 melt season provides a snapshot of potential future melt and supraglacial hydrological conditions, it is essential to consider the broader context of multi-year climatic trends and the development of features such as ice slabs when fully assessing the GrIS's response to ongoing climate change.

3.5. Conclusion

In this study, we have undertaken a detailed mapping and intercomparison of the distribution and dynamics of supraglacial meltwater features across the Russell-Leverett Glacier catchment in the high melt year of 2019 and the comparatively low melt year of 2018. Through this, we have aimed to establish deeper insights into how the GrIS's hydrological system responds to variations in atmospheric temperature forcing. As such, this work contributes to an improved understanding of how rising air temperatures and more intense melt events may impact the hydrology of the GrIS in the future. This research provides detailed observations of GrIS hydrology, offering new insights that can help to inform the representation of hydrological processes in the physical models that are used to make projections of future mass balance and sea level rise.

As high melt years like 2019 become more common in the future, our study suggests that the GrIS may experience increased surface meltwater ponding and transport, with more interconnected and efficient supraglacial channel systems at higher elevations on the ice sheet, potentially leading to increased meltwater flow to the ice sheet base via moulins. Additionally, greater slush extents in these high melt years, which lowers surface albedo and reduces surface permeability when it refreezes, may further increase ice sheet surface runoff and hence decrease mass balance. Moreover, the formation and drainage of smaller SGLs during higher melt years like 2019 may enhance surface-to-bed connections early in the melt season, which has implications for the representation of subglacial hydrology and hence ice flow velocities in models. Furthermore, the complex relationship between meltwater drainage and melt intensity, highlighted by deeper SGLs in the low melt year as well as similar total drainage volumes in both high and low melt years, also demonstrates the need for nuanced representation of surface hydrology when coupling climate and ice sheet models.

Two of the most novel aspects highlighted in our study are the widespread presence of slush and small SGLs. We suggest that these previously poorly mapped and/or under-studied

supraglacial hydrological features may exert a significant impact on glacio-hydrological systems, especially in future warmer melt years. Future work should therefore focus on understanding the longer-term distribution and evolution of slush on the GrIS. To better estimate melt on the GrIS, we recommend that slush, and crucially its effect on albedo, should be incorporated into regional climate models to improve projections of the future behaviour of the GrIS. Additionally, better identification and representation of small SGLs in future remote-sensing and modelling studies will improve understanding of meltwater routing under climate change, which is vital for understanding the complex processes that will influence the response of the GrIS to a warming climate.

Chapter 4

Supervised classification of slush on the Greenland Ice Sheet using Sentinel-2 satellite imagery

Emily Glen[1,2], Alison F. Banwell[3], Katie Miles[1,2], Rebecca L. Dell[4,5], Jennifer Maddalena[1,2], Malcolm McMillan[1, 2], Amber A. Leeson[1,2]

[1] Lancaster Environment Centre, Lancaster University, Lancaster, UK

[2]UK Centre for Polar Observation & Modelling, Lancaster University, Lancaster, UK

[3] Cooperative Institute for Research in Environmental Sciences (CIRES), University of Colorado Boulder, Boulder, USA

[4] Scott Polar Research Institute, Lensfield Road, Cambridge, UK

[5] British Antarctic Survey, High Cross, Madingley Road, Cambridge, UK

Correspondence to: Emily Glen (e.glen@lancaster.ac.uk)

This following work is prepared for publication to be submitted for publication as: ‘Supervised classification of slush on the Greenland Ice Sheet using Sentinel-2 satellite imagery’

EG and AFB conceptualised the research. AL, AFB, KM, JM, and MM contributed to the scientific content, technical details, and overall structure of this paper. RD originally developed the code to delineate slush, which was further edited by EG. All co-authors contributed to discussion of results and editing of the manuscript.

Abstract

Surface melt on the Greenland Ice Sheet (GrIS) has intensified in recent decades, accelerating mass loss and transforming supraglacial hydrology. Yet the extent and behaviour of slush – fully saturated firn or snow – remain poorly constrained, despite its critical role in meltwater storage, routing, and refreezing. Here, we present the first GrIS-wide classification of slush, based on over 300,000 Sentinel-2 images and a supervised Random Forest classifier implemented in Google Earth Engine. This near-decadal (2016–2024), high-resolution (10 m) dataset maps slush distribution across six major drainage basins covering the entire ice sheet. On average, slush covers ~4.2% of the GrIS each summer (~73,300 km²), with strong interannual variability: peak coverage reached 8.3% (144,800 km²) during the extreme melt year of 2019, dropping to 1.4% (24,400 km²) in the low melt year of 2018. Notably, around 40% of slush (~29,300 km²) occurs in areas with low-permeability subsurface features such as ice slabs and firn aquifers. Slush alone covers up to 14.5 times more area than lakes and streams identified in previous studies, revealing it as the dominant form of surface meltwater on the GrIS. We further show that machine learning classification outperforms traditional thresholding techniques, providing a robust and scalable approach for slush detection. As climate change drives more frequent and prolonged melt seasons, slush is likely to become a defining feature of the melt regime – promoting lateral meltwater flow, surface refreezing, and albedo reduction – and must be incorporated into hydrological models and ice-sheet mass balance projections.

4.1. Introduction

The Greenland Ice Sheet (GrIS) has experienced a negative mass balance for several decades, losing ice at a rate of −255 ± 19 Gt yr^{-1} from 2002 to 2022 (Otosaka et al., 2023), with supraglacial melting being the principal driver of this mass loss (IMBIE, 2020). Between 1991–2019, the mean summer air temperature on the GrIS increased by approximately 1.7°C (Hanna et al., 2021). This warming has led to enhanced supraglacial melt rates – e.g., a 21% increase in supraglacial runoff between 2011 and 2020 compared to the previous three decades (Slater et al., 2021). Supraglacial melt extents and meltwater features have also increased in area and elevation (Mouginot et al., 2019; van den Broeke et al., 2016; Leeson et al., 2015; Howat et al., 2013). For example, the maximum meltwater runoff elevation shifted inland by as much as 329 m between the years 1985 and 2020 (Tedstone and Machguth, 2022). In some regions, supraglacial melt has reached areas of the percolation zone that were previously subject to little melt (Tedesco, 2007; Fettweis et al., 2011).

First observed in the 1950s (Holmes, 1955), slush is defined as fully water-saturated firn or snow and is expressed on a glacier or ice sheet surface as blue hued features in optical satellite imagery. Slush usually forms when a low-permeability ice layer prevents the vertical percolation of meltwater deeper into the snowpack, a process which typically occurs in the percolation zone of the GrIS. Slush facilitates lateral meltwater transport, as meltwater flows more easily through slush than through compacted snow or firn (Clerx et al., 2022), creating hydrologically connected zones that channel meltwater into supraglacial rivers and lakes (Holmes, 1955; Cuffey and Paterson, 2010). This network may form new supraglacial channels or reactivate existing ones, enhancing meltwater routing (Chu, 2014; Rippin and Rawlins, 2021). When channels within slush fields connect to moulins or crevasses, they can direct meltwater to the ice-bed interface, lubricating the ice sheet's base and accelerating ice flow, driving dynamic ice loss (Smith et al., 2021). Slush zones also promote the up-glacier expansion of the drainage network as the snowline retreats and supraglacial runoff increases (Rawlins et al., 2023). The refreezing of slush contributes to the formation of extensive near-surface ice layers, often called 'slabs', which reduce the meltwater retention capacity of firn (Machguth et al., 2016; Pfeffer et al., 1991; Harper et al., 2012; Miller et al., 2018; 2020), in turn promoting rapid runoff of meltwater across the ice sheet surface. In the southwestern GrIS, newly formed ice slabs enable supraglacial rivers originating from slush fields to flow at elevations as high as 1840 m a.s.l. (Machguth et al., 2016; Tedstone and Machguth, 2022).

Meltwater mapping studies in Greenland have largely overlooked the presence of slush, with only a limited number monitoring either small-scale slush distribution or the slush limit, which is defined as the highest elevation where water-saturated material is visible and has been used as a proxy for the runoff limit on the GrIS (Machguth et al., 2022). In southwest Greenland, Covi et al. (2022) found slush formed up to 1900 m elevation in intense melt years but remained below 1750 m in low melt years (2016 and 2021). Rawlins et al. (2023) identified slush within the supraglacial drainage network at Humboldt Glacier (2016–2020) but did not distinguish it from river features. Glen et al. (2025) compared meltwater features in low- and high-melt years within the Watson catchment, southwest Greenland (2018 and 2019, respectively), finding slush extended to higher elevations and covered a significantly larger area in 2019. Gruell and Knap (2000) found that the slush limit along the K-Transect (~1720 m a.s.l.) remained consistent in high-melt years (e.g., 1990, 1991, 1995) which they attribute to a density barrier preventing slush formation above it. Tedstone and Machguth (2022) observed a 29% increase in the slush limit from 1985 to 2020 using Landsat imagery, while Machguth et al. (2022) identified a maximum slush elevation of ~2080 m a.s.l. using MODIS data (2000–2022). In Antarctica, Dell et al. (2024) reported that slush comprised 50% of the meltwater area across 57 ice shelves, suggesting previous studies may have underestimated meltwater volumes, both in Antarctica and Greenland. Furthermore, Dell et al. (2024) demonstrated that including surface melt-albedo feedbacks in regional climate models increased modelled snowmelt by 2.8-fold, emphasizing the need to incorporate slush in meltwater mapping and climate modelling studies.

While optical remote sensing techniques have been widely employed to detect and monitor supraglacial lakes (SGLs) and streams on the GrIS (e.g., McMillan et al., 2007; Selmes et al., 2011; Williamson et al., 2017, 2018; Miles et al., 2017; Yang et al., 2021; Lu et al., 2021; Turton et al., 2021; Zhang et al., 2023), a notable gap exists in the development of remote sensing techniques to map slush. For instance, thresholding methods, such as the commonly used Normalised Difference Water Index (NDWI), are effective for delineating meltwater features, but often fail to capture the subtleties of slush due to its spectral similarity to other supraglacial meltwater features and its indistinct boundaries (e.g., Rawlins et al., 2023; Yang and Smith, 2012). Machine Learning (ML) classification methods have recently shown promise as an alternative to image thresholding for meltwater classification in both Greenland and Antarctica, for instance using Random Forest (RF) algorithms (e.g., Hu et al., 2022; Halberstadt et al., 2020; Wangchuk et al., 2020; Yuan et al., 2020; Dirscherl et al., 2020) and deep learning methods (e.g., Qayyum et al., 2020; Wu et al., 2020; Jiang et al., 2022; Lutz et al., 2023). Dell et al. (2022; 2024) utilised a k-means clustering algorithm to create training classes from Landsat 8 imagery, subsequently training a RF classifier to

delineate both slush and SGLs on Antarctic ice shelves. This approach was shown to enhance classification accuracy by incorporating spatial context and object characteristics, making it particularly useful for distinguishing slush from other supraglacial meltwater features. However, no previous study has explored the use of ML classification methods for slush detection in Greenland.

Here, we aim to quantify the spatial-temporal distribution of slush across the entire GrIS from 2016 to 2024, analysing both the ice sheet as a whole and across six distinct basins that together represent the full extent of the GrIS. Following the methods of Dell et al. (2022; 2024) for Antarctic ice shelves, we use Google Earth Engine (GEE), to delineate slush by employing: i) a k-means clustering algorithm to generate training classes; and ii) a RF classifier, both applied to Sentinel-2 imagery. In doing so, we aim, for the first time, to better understand the spatial distribution, extent, and evolution of slush on the GrIS over nine summers.

4.2. Methods and study area

We conduct our analysis across the entire GrIS, split into six basins: Southwest (SW), Central West (CW), Northwest (NW), North (NO), Northeast (NE) and Southeast (SE) (Figure 4.1) (Mouginot and Rignot, 2019). To classify slush, we largely follow the approach outlined by Dell et al. (2022, 2024) but adapted to the GrIS (Figure 4.2) as detailed in the following sections. A summary of all steps is provided in Figure 4.2.

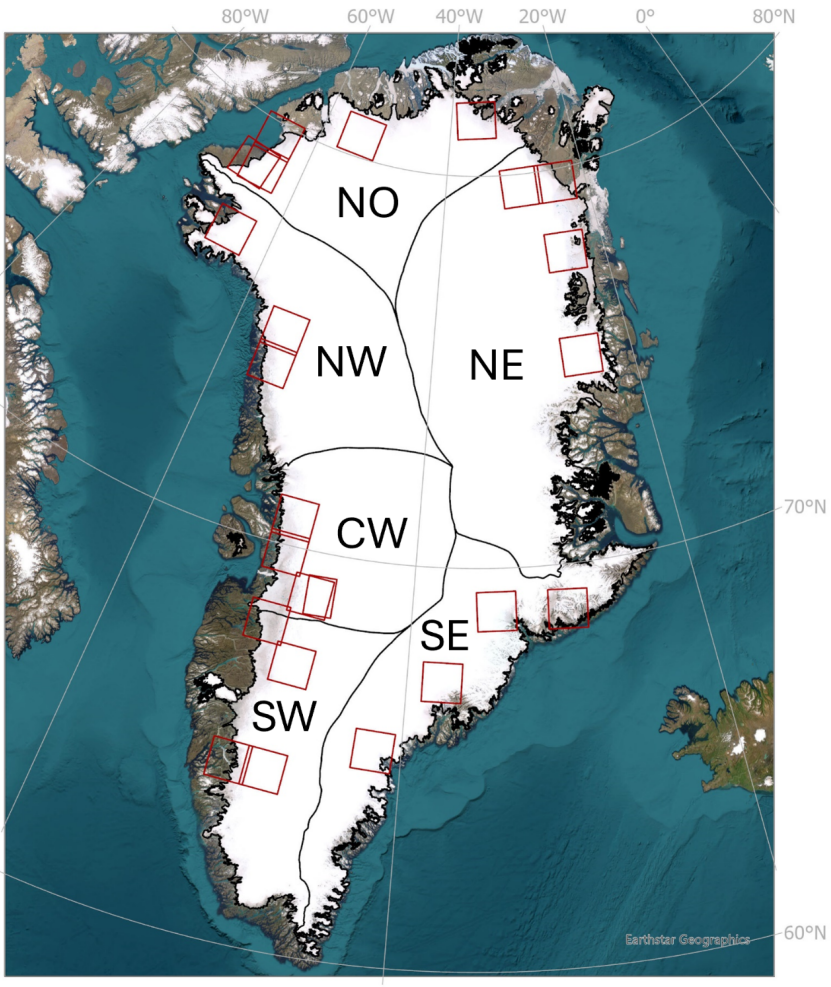

Figure 4.1: Overview map of Greenland separated into six drainage basins*: *Southwest (SW), Central West (CW), Northwest (NW), North (NO), Northeast (NE) and Southeast (SE) **(Mouginot and Rignot, 2019)**. ***Red boxes indicate footprints of the 24 training/validation images used to train and validate the RF classifier used in this study. Base map source: Esri, Maxar, Earthstar Geographics, and the GIS User Community.***

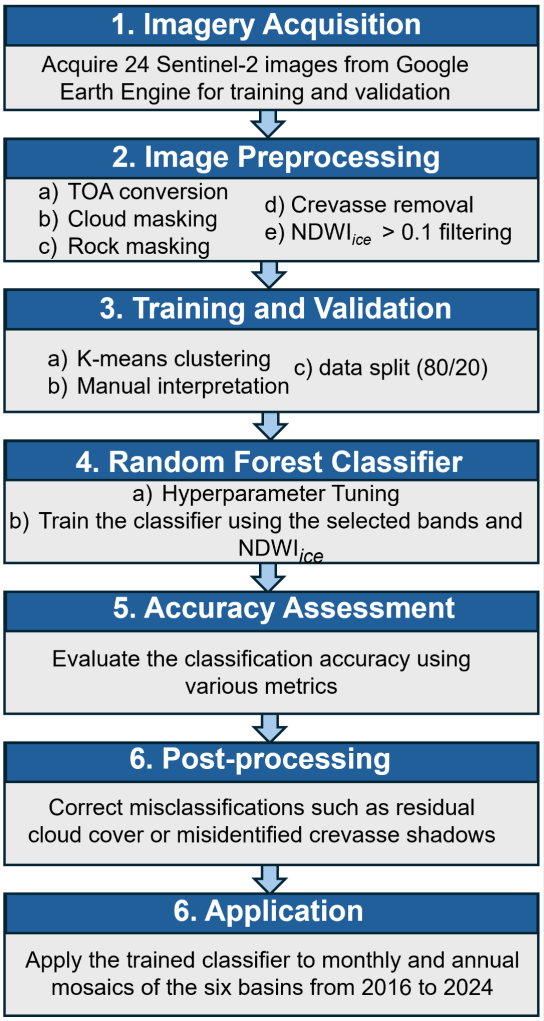

Figure 4.2: Flowchart of slush classification processes following Dell et al. (2022) for Antarctic ice shelves, adapted in this study for the GrIS.

4.2.1. Image pre-processing

4.2.1.1. Sentinel-2 imagery

We acquired and pre-processed Sentinel-2 (S2) Multi-Spectral Imager (MSI) Level 1C data from the GEE data catalogue, processing a total of 329,229 images from 2016 - 2024. ESA's S2 mission provides high-resolution multispectral imagery via two satellites, S2A (launched in 2015) and S2B (launched in 2017), in a sun-synchronous orbit, with a combined temporal revisit time of 5 days. Images were converted to Top-Of-Atmosphere (TOA) reflectance using a scaling factor of 10,000 (ESA, 2015). We ensured that all S2 images had a sun elevation angle of > 20° to better differentiate water bodies from adjacent features (Halberstadt et al., 2020), and that images were limited to cloud cover of < 25%. We use all the S2 MSI bands for analysis, which are detailed in Table 4.1.

Table 4.1: Sentinel-2 satellite bands, their central wavelengths, spatial resolutions, and how each band was used in the study.

Sentinel-2 bands	Description	Central Wavelength (μm)	Resolution (m)	Use
Band 1	Coastal aerosol	0.443	60	Training/validation Classification
Band 2	Blue	0.49	10	Cloud Mask Rock Mask Water Mask Greenness Index Training/validation Classification
Band 3	Green	0.56	10	Rock Mask Greenness Index Training/validation Classification
Band 4	Red	0.665	10	Cloud Mask Water Mask Greenness Index Training/validation Classification
Band 5	Vegetation Red Edge	0.705	20	Training/validation Classification
Band 6	Vegetation Red Edge	0.74	20	Training/validation Classification
Band 7	Vegetation Red Edge	0.783	20	Training/validation Classification
Band 8	NIR	0.842	10	Training/validation Classification
Band 8A	Vegetation Red Edge	0.865	20	Cloud Mask Training/validation Classification
Band 9	Water vapour	0.945	60	Training/validation Classification
Band 10	SWIR - Cirrus	1.375	60	Cloud Mask Training/validation Classification
Band 11	SWIR	1.61	20	Cloud Mask Rock Mask Training/validation Classification
Band 12	SWIR	2.19	20	Greenness Index Training/validation Classification

4.2.1.2. Image masking

A cloud detection algorithm, based on thresholds from Corr et al. (2022), was applied to each S2 image, with a 1 km buffer added to account for cloud shadows. To exclude rock outcrops, we used a modified Normalised Difference Snow Index (NDSI; Moussavi et al., 2020), adding a 1 km buffer for complete removal. A crevasse mask, generated from ArcticDEM (Porter et al., 2023) at 2 m resolution, was applied to avoid confusion between crevasses and meltwater features (Chudley et al., 2021). Following Dell et al. (2022), all meltwater features, including slush, were isolated using a NDW_*ice* threshold. Although Dell et al. (2022) used a threshold of > 0.1 for Antarctica, for Greenland, we increased this threshold to > 0.12 (Yang and Smith, 2013) to account for differing albedo and reflectance properties between ice sheets. A B2 threshold of > 0.03 was also applied to exclude

shadows from rocks/crevasses and other non-meltwater features (Dirscherl et al., 2020; Corr et al., 2021). After applying this automated masking process, any residual cloud, rock, and crevasse features were manually removed through visual inspection, ensuring only meltwater features were analysed in the later processing steps. While we did not quantify the exact proportion of features requiring manual removal, the automated masking process was largely effective. Residual features that necessitated manual correction were generally limited to smaller, less distinct elements such as faint cloud shadows or crevasse artifacts. These instances were more prevalent in regions with subtle spectral variability or complex topography, but overall, the manual intervention required was minimal.

4.2.2. Label generation for model training and validation

For each basin, we selected 24 S2 tiles (four per basin) for training and validation (Table B.1). These tiles were manually chosen from the 2016–2024 melt seasons (01 May to 30 September), ensuring minimal cloud cover (< 20%) with a range of solar elevations varying between 42° and 75°. This selection aimed to capture a broad range of supraglacial melt conditions and spectral characteristics. Each image was clipped to the boundaries of the six drainage basins (Figure 4.2).

Training and validation data were generated from the 24 pre-processed S2 images using k-means clustering, following Halberstadt et al. (2020) and Dell et al. (2022). K-means clustering refines cluster boundaries and improves accuracy by revealing spectral patterns that may be missed through manual methods, combining automated clustering with manual interpretation.

The k-means algorithm clustered pixels based on spectral characteristics, using bands B1 through B12 and NDWI_ice, with 100,000 pixels sampled per image and between 5 and 70 clusters created. Clusters were manually interpreted to distinguish 'slush' from ‘non-slush' classes. Slush was identified as water-saturated features appearing as dense, light blue patches in true-colour images, while non-slush encompassed all other features (e.g., SGLs, channels, rock, snow, ice, cloud, cloud shadows, sediment, and cryoconite). Misclassified areas were masked, and 2,000 pixels from each class were randomly selected for a balanced training dataset. The data were then split randomly, with 80% used for training and 20% for validation.

4.2.3. Training and validation

Following Dell et al (2022, 2024), the classification of slush from S2 satellite imagery was performed using a RF classifier, implemented within GEE (ee.Classifier.smileRandomForest). This ensemble learning method trains multiple decision trees on random subsets of data and features, classifying by majority voting (Breiman, 2001). In this study, the RF classifier was applied to spectral bands B1 through B12, as well as the NDWI_ice (Dell et al., 2022). The incorporation of multiple spectral bands and the NDWI_ice helped ensure that both spectral and spatial variations in surface conditions were captured, improving the accuracy of the classification. Hyperparameters were tuned by comparing performance on training and validation datasets, ensuring the model generalised well to unseen data. Performance was evaluated using metrics derived from the confusion matrix for the validation data. While no specific target metric was predefined, hyperparameter tuning was stopped when the model achieved stable performance on the validation dataset, with no significant improvement in key metrics.

4.2.3.1. Hyperparameter testing

We determined hyperparameter values specific to our study by comparing the training and validation datasets, selecting those that yielded the highest accuracy with the lowest computational time (Figure 4.3). We tuned each hyperparameter individually, starting with the most impactful ones, such as the number of trees, based on their theoretical importance and observed influence on model accuracy. We then used these values as fixed inputs for subsequent tuning. This approach contrasts with Dell et al. (2022, 2024), who relied on default settings for their analyses, and gives our study a more precise product with the highest possible accuracy. The RF classifier's hyperparameters were set with 50 trees, a bag fraction of 0.7, and a minimum leaf population of 20, balancing accuracy and overfitting control. A cap of 500 maximum nodes, a seed of 30 for reproducibility, and 10 variables per split provided a robust structure while managing computational efficiency. Further details on these hyperparameters and their impact are provided in Table 4.2.

Feature importance analysis (Figure 4.3) highlighted B2 and B3 as the most influential spectral bands for slush detection. Hyperparameter tuning showed that increasing the number of trees improved accuracy up to around 50 trees, with diminishing returns beyond this point. The out-of-bag (OOB) error decreased until about 40 trees, after which it stabilised. Increasing the minimum leaf population and maximum nodes also improved accuracy, while the random seed caused only minor fluctuations. However, further increases

in these parameters yielded only marginal accuracy gains, which did not outweigh the additional computational cost.

Table 4.2: Hyperparameter settings for the RF Classifier, detailing our chosen values for key parameters (see section 4.2.3.1)

Hyperparameter	Value	Description
Number of Trees	50	Controls the number of trees in the forest. More trees improve stability and accuracy but increase computational demand.
Bag Fraction	0.7	Fraction of the training data used for each tree. A lower value increases variance in the predictions made by individual trees, while a higher value reduces it but may introduce bias.
Minimum Leaf Population	20	Minimum number of samples required at a leaf node to prevent overfitting by ensuring sufficient data per leaf.
Maximum Nodes	500	Limits the number of nodes per tree, balancing complexity and simplicity.
Seed	30	Ensures reproducibility by initialising the random number generator used for tree building.
Variables per Split	10	Controls the number of randomly chosen variables that are considered at each split in a tree.

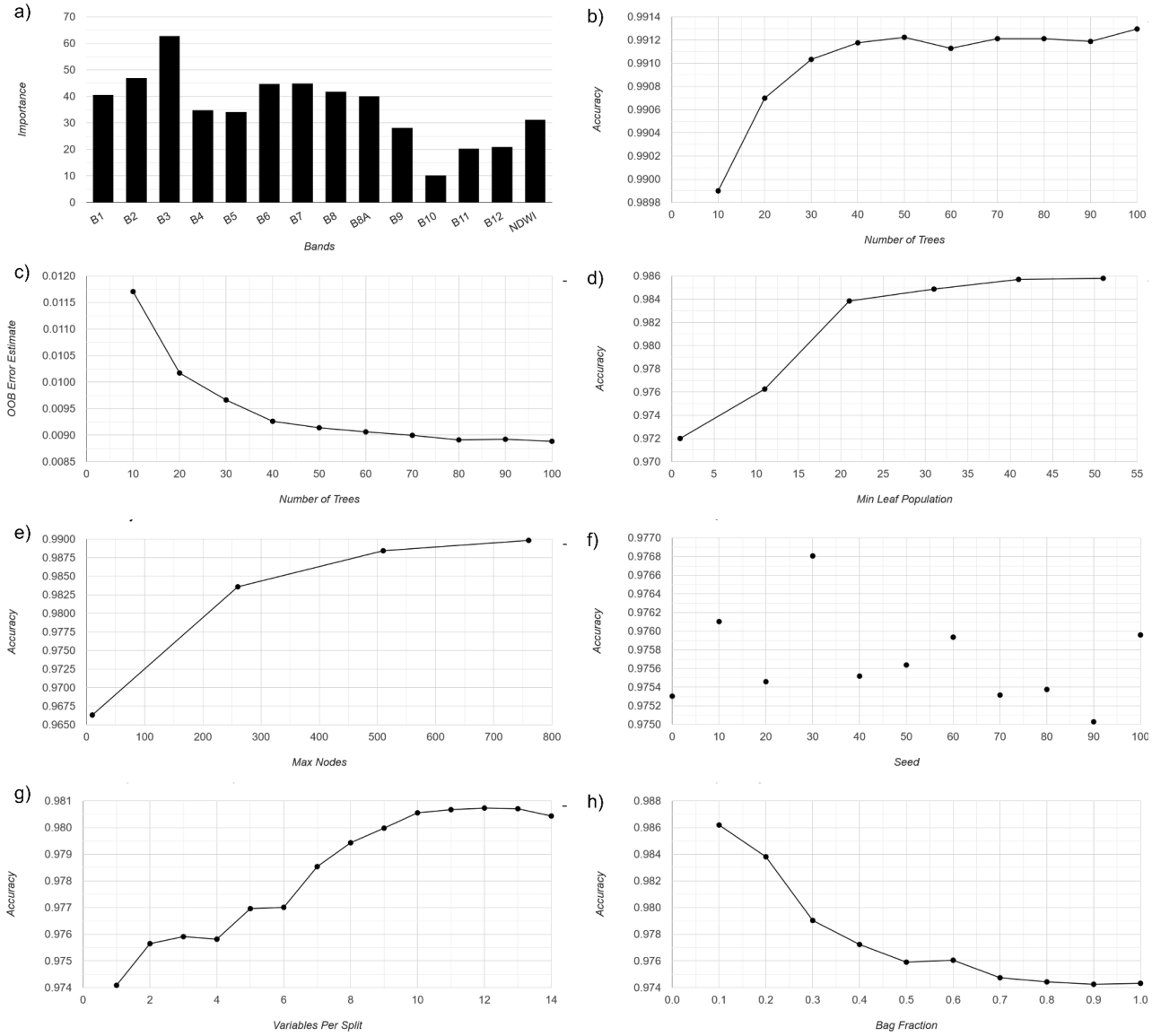

Figure 4.3: Hyperparameter tuning results for the accuracy of the RF classifier in our study. a) The feature importance for the selected bands used in classification. b) The effect of the number of trees on model accuracy. c) The OOB error estimate as a function of the number of trees. d) The accuracy in relation to the minimum leaf population. e) The accuracy versus the maximum number of nodes per tree; f) The effect of different random seed values on accuracy. g) The accuracy as it relates to the number of variables considered per split. h) The accuracy versus the bag fraction.

4.2.3.2. Accuracy assessment

To evaluate the RF classifier's performance, we analysed confusion matrix metrics (Figure 4.4; Table 4.3; Table 4.4). The model achieved an overall accuracy of 97.5%, with 74,969 true positives and 1,000 false negatives for 'slush', and 6,755 true negatives with 1,133 false positives for ‘non-slush’. Precision was 85.6% for 'non-slush' and 98.7% for 'slush', while recall was 87.1% for 'non-slush' and 98.5% for 'slush'. The F1-scores were 86.4% and 98.6% for 'non-slush' and 'slush', respectively. The Kappa statistic of 0.85 indicates strong agreement between predictions and true classes, showing the classifier's performance is well above chance.

Table 4.3: Definitions and formulas of performance metrics used for evaluating RF classification.

Metric	Description	Formula
Precision	Represents the proportion of correctly classified positive instances out of all instances predicted as positive. Reflects the reliability of positive predictions.	$Precision = \frac{TP}{TP + FP}$
Recall	Indicates the proportion of actual positive instances correctly identified by the model. Reflects the model's ability to detect true positives	$Recall = \frac{TP}{TP + FN}$
F1-Score	Balances precision and recall by calculating their harmonic mean. Useful when both metrics are critical for evaluating model performance, especially in imbalanced datasets.	$F1 = 2 \cdot \frac{precision \cdot recall}{precision + recall}$
Overall Accuracy (OA)	Measures the proportion of correctly classified instances across all classes. Provides a general performance metric but can be misleading for imbalanced datasets.	$OA = \frac{TP + TN}{TP\ + TN + FP + FN}$
Kappa Coefficient (κ)	Evaluates the level of agreement between classification results and reference data, accounting for random chance. Useful for assessing reliability across datasets.	$k = \frac{P_o - P_e}{1 - P_e}$

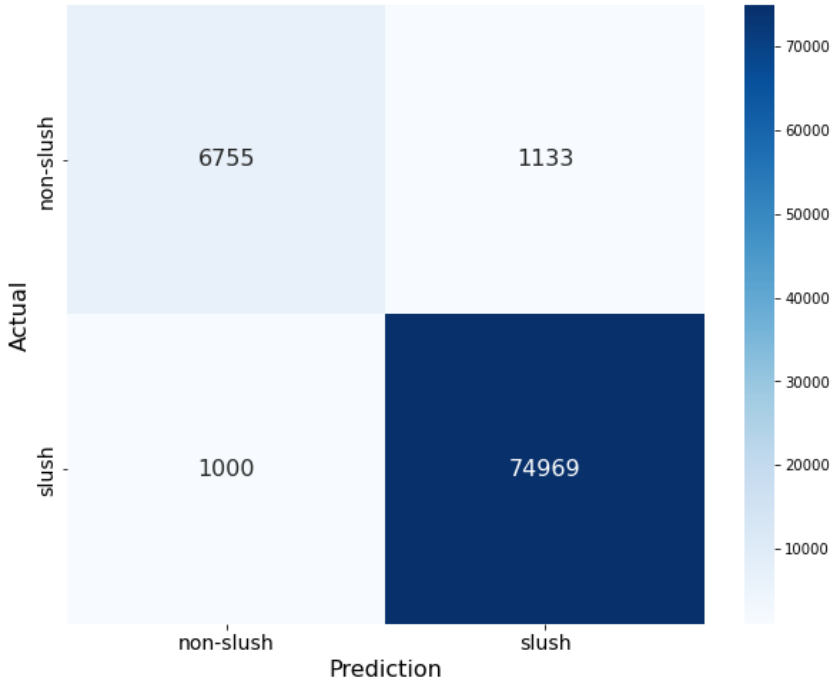

Figure 4.4: Confusion matrix for the RF classifier applied to slush detection. The matrix compares predicted versus actual values, with two classes: "slush" and "non-slush." The vertical axis represents the actual labels, while the horizontal axis represents the predicted labels. The colour bar on the right indicates the scale of the number of observations, with darker shades representing higher counts.

Table 4.4: Performance metrics derived from the confusion matrix of the RF classifier used for slush detection.

	Precision (%)	**Recall (%)**	**F1-score (%)**	**True Positives (TP)**	**False Positives (FP)**	**False Negatives (FN)**	**True Negatives (TN)**
Non-slush	*85.6*	*87.1*	*86.4*	*6,755*	*1,133*	*1,000*	*74,969*
Slush	*98.7*	*98.5*	*98.6*	*74,969*	*1,000*	*1,133*	*6,755*

4.2.4 Application of trained RF model

Once trained, the supervised RF classifier was applied across all six drainage basins (Figure 4.1) to S2 imagery between 2016 and 2024. To prepare the S2 imagery for classifier application, after filtering based on spatial bounds of each basin, we filtered and pre-processed the images using the same process described above in Section 4.2.1. Before applying the NDWI_ice > 0.12 filter (Yang and Smith, 2012), we created both monthly (May–September) and annual Sentinel-2 mosaics by selecting, at each pixel location, the image with the highest NDWI_ice value from all available observations, following Dell et al. (2022).

The supervised classifier was then applied to each image mosaic. Similar to other studies (e.g., Corr et al., 2023; Dell et al., 2022), manual post-processing was performed on each mosaic to address and correct clear misclassifications, including residual cloud cover and shaded regions near crevasses and fjords. Approximately 5-7% of pixels from the final mosaics were identified as misclassifications and removed from the dataset. The elevation of slush was determined for each mosaic by using values extracted from the ArcticDEM at a 100 m spatial resolution (Porter et al., 2023).

4.2.5. Comparison to other methods

We compare a subset of our RF classification results to two thresholding methods. Masking for these comparisons follows the approach described in Section 4.2.1.2. This comparison serves to validate our RF classification by assessing its performance relative to alternative approaches and evaluating the consistency of slush detection across methodologies.

4.2.5.1. Normalised Difference Water Index

We compared our results with those from Glen et al. (2025), using thresholds of NDWI > 0.14 (McFeeters, 1996) and NDWI_ice > 0.15 (Yang and Smith, 2012) for slush identification. These indices leverage green/NIR and blue/red band ratios, respectively, to optimize slush detection under supraglacial conditions (bands detailed in Table 4.1). NDWI (equation 4.1) and NDWI_ice (equation 4.2) are defined as:

$$NDWI = \frac{B3 - B8}{B3 + B8} \quad (1)$$

$$NDWI_{Ice} = \frac{B2 - B4}{B2 + B4}$$

(2)

4.2.5.2. Greenness Index

We also compared results with the Greenness Index (Gind) from Covi et al. (2022), which detects slush by emphasizing green reflectance relative to blue and red while reducing cloud interference using shortwave infrared. Gind (equation 4.3) is defined as:

$$G_{ind} = \frac{3 \cdot B3}{B2 + B3 + B4} - 2 \cdot B12$$

(4.3)

A threshold of Gind > 1 was applied to classify slush (bands detailed in Table 2.1).

4.3. Results

4.3.1. Spatial distribution of slush across the Greenland Ice Sheet

Over the whole ice sheet, mean summer (1st May to 30th September) slush coverage between 2016 and 2024 was ~4.2%, with the greatest extent within the ice marginal areas (i.e. 10 - 20 km inland), though slush extended up to a maximum of 170 km inland in the SW basin (Figure 4.5). The SW basin showed the highest mean slush coverage over all summers (5.5%), followed by the NO basin (4.8%). NE, CW, and NW basins showed 3%, 1.9%, and 1.8% slush coverage respectively, while the SE exhibited the lowest coverage (0.6%).

Over multiple melt seasons, persistent slush was most notable in the NE and NO basins, where 8.7% (915 km²) and 4.6% (487 km²) of slush-covered areas remained each year from 2016 to 2024 (Figure 4.5; Figure 4.6). Despite the SW basin having the highest proportion of its basin covered by slush on average, slush persistence over multiple seasons in the SW basin was more variable between melt seasons compared to NE and NO basins, with only 0.4% (51 km²) of the slush area consistently present each year. The SE basin showed minimal and less variable slush formation over seasons, with only 0.5% (43 km²) of slush area consistently present (Figure 4.5; Figure 4.6).

We identify that the spatial configuration and pattern of slush varied by basin and year (Figure 4.7). In the NW (Figure 4.7(a)), slush appeared as linear, river-like features with dispersed boundaries, as observed in 2021. In the CW (Figure 4.7(b)), slush in 2022 appeared to connect SGLs. In the SW (Figure 4.7(c)), slush blanketed extensive areas with patches of exposed snow, as seen in 2023. In the NO (Figure 4.7(d)), a dendritic network of narrow, web-like slush tributaries channelled meltwater across the northern ice sheet, as observed in 2017. In the NE (Figure 4.7(e)), meltwater collected in SGLs and streams within a slush matrix, forming a distinct slush line boundary in 2019. Finally, in the SE (Figure 4.7(f)), slush formed preferentially around rocky outcrops, observed in 2023. These highlighted examples illustrate notable configurations of slush in each basin, but these patterns were not necessarily consistent every year. The spatial distribution of slush varied depending on the melt season, with some years exhibiting different or less distinct configurations.

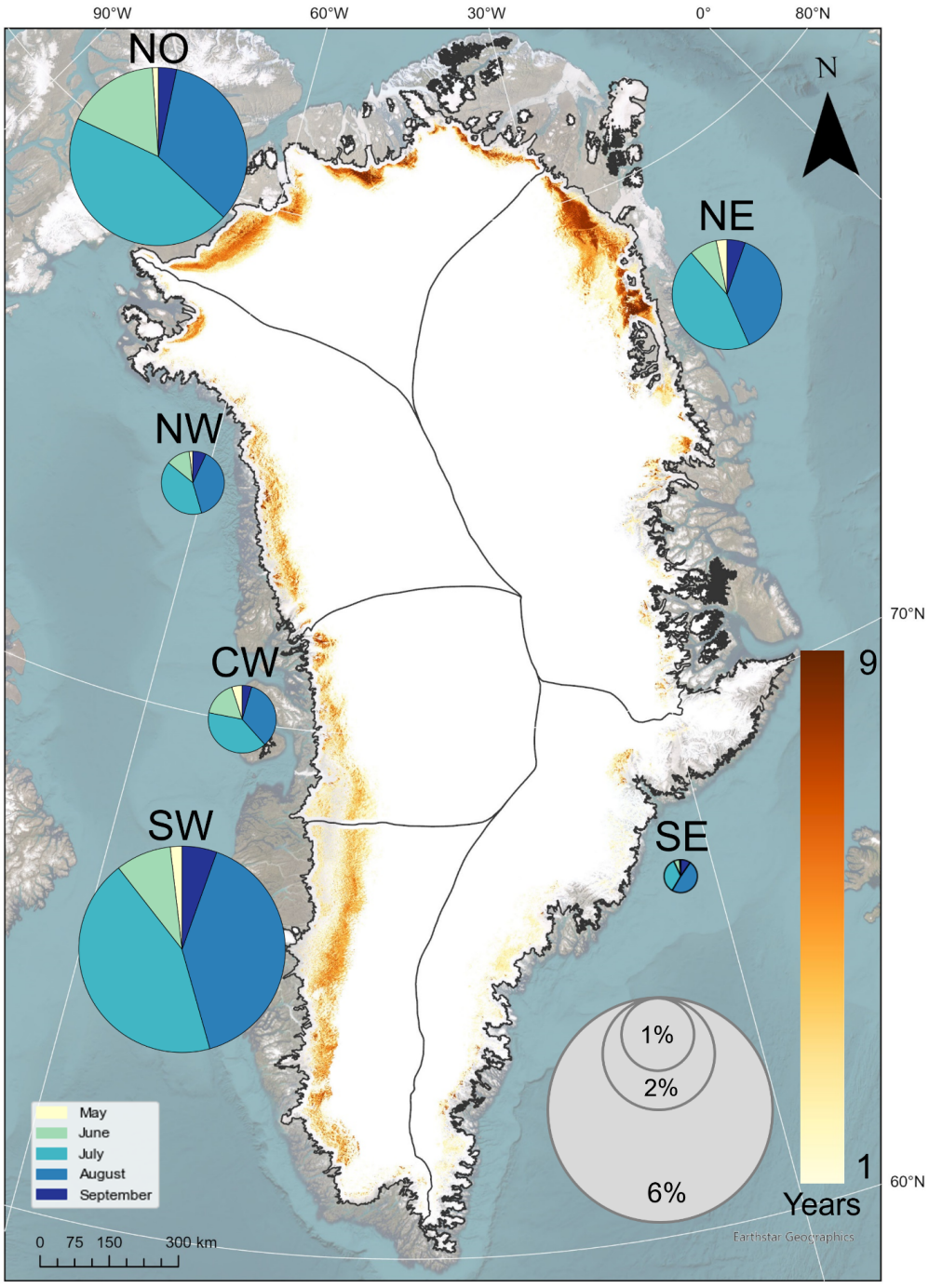

Figure 4.5: Slush persistence and average coverage across basins during the summer months (1st May to 30th September). Slush persistence is represented by a colour bar on a scale from 1 (light yellow) to 9 years (dark orange). The average slush coverage for each basin is illustrated by the size of the circles, which reflect the average slush coverage value across all years from 2016 to 2024, calculated by averaging the slush-covered area annually. Within each circle, pie charts display the mean monthly distribution of slush coverage averaged over all nine melt seasons. Base map source: Esri, Maxar, Earthstar Geographics, and the GIS User Community.

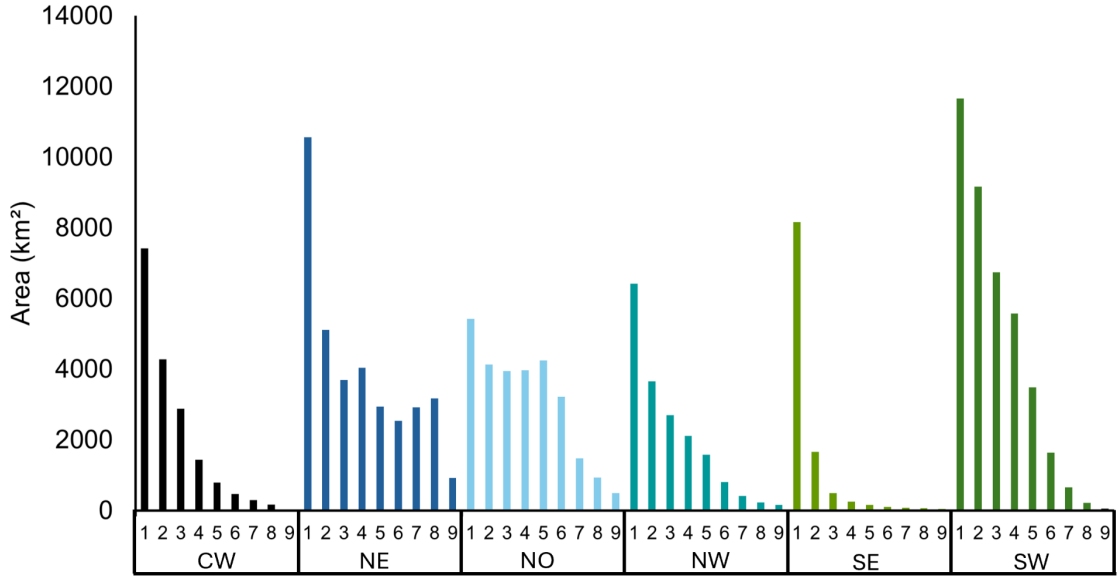

Figure 4.6: Slush persistence across the six basins of the GrIS from 2016 to 2024. The x-axis represents the persistence from 1 to 9, where 9 indicates slush presence in all nine years of the study period. The y-axis shows the total slush area (km²) for each score by basin (see Figure 4.5).

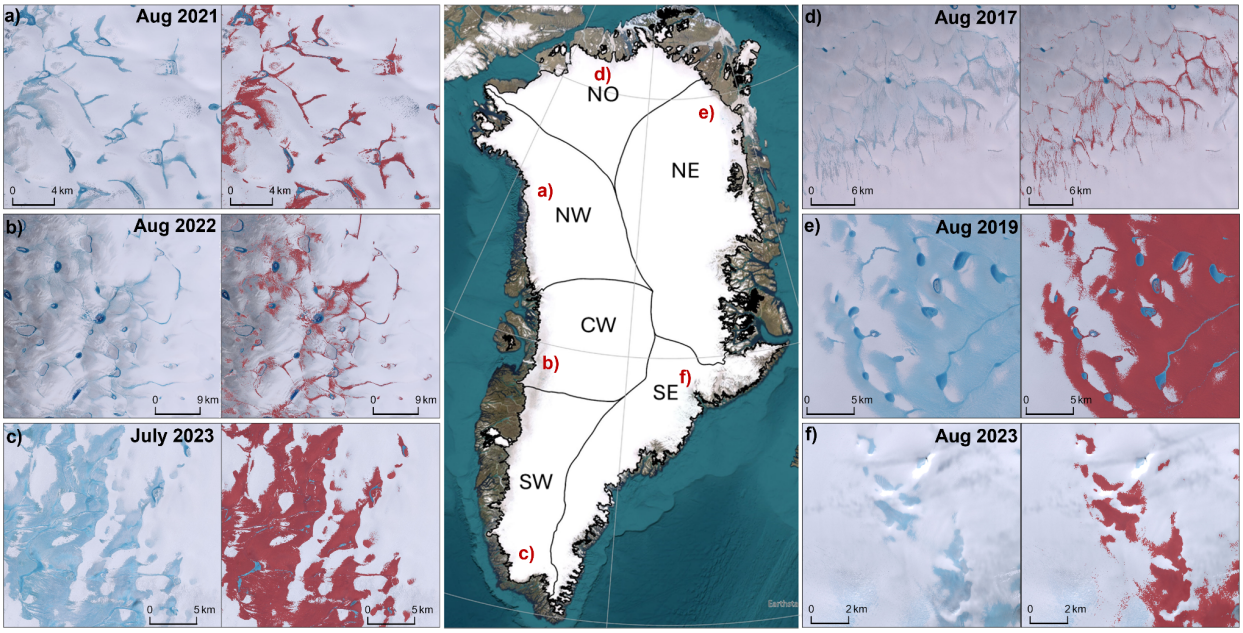

Figure 4.7: Examples of the spatial distribution of slush for six selected areas basins of the GrIS (locations shown in the central panel) shown using S2 RGB imagery (left) and classified slush areas (red) overlaid on the imagery (right). (a) NW: linear, river-like features with dispersed boundaries (2021); (b) CW: slush connecting SGLs (2022); (c) SW: extensive areas of slush with exposed snow patches (2023); (d) NO: dendritic, web-like tributaries channelling meltwater (2017); (e) NE: SGLs and streams within a slush matrix, forming a distinct slush line boundary (2019); (f) SE: slush forming around rocky outcrops (2023). Base map source for central GrIS panel: Earthstar Geographics.

Figure 4.8 highlights correlations in slush extent between the six basins over the study period. The highest Pearson correlation coefficient values are between the NO and NW (0.76), and the SW and CW, basins (0.84). In contrast, the SE exhibits weaker correlations with other basins, such as with CW (0.35). We also see moderate correlations of the NE with western basins, including SW (0.53) and CW (0.68).

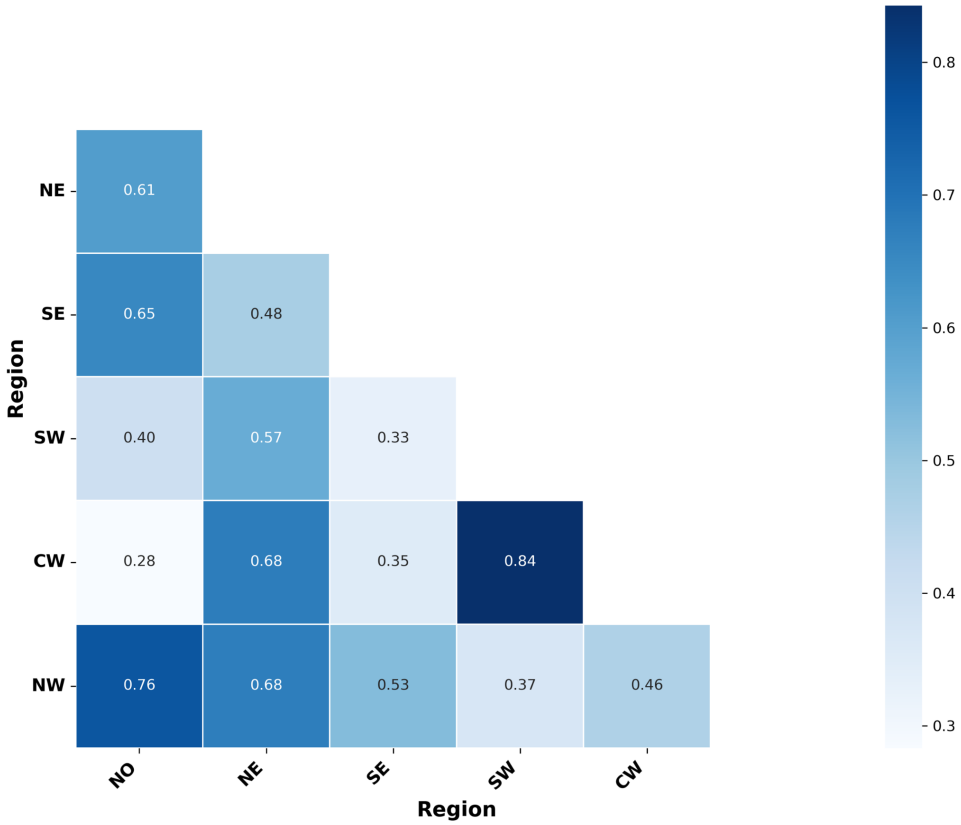

Figure 4.8: Correlation matrix of slush extent on GrIS basins from 2016–2024. Each cell represents the Pearson correlation coefficient, with values ranging from -1 to 1, where blue indicates stronger positive correlations, and red indicates weaker correlations.

4.3.2. Elevation trends and variability of slush

Slush consistently formed at the highest elevations in the SW basin, with the mean of annual maximum elevations ranging from 1740 m a.s.l. in 2017 to 1880 m a.s.l. in 2021 (Figure 4.9; 4.10). Similarly, the SE basin exhibited high elevations, with a mean maximum elevation of 1800 m a.s.l. in 2023. In contrast, the NO basin recorded the lowest elevations overall, with a maximum of 1370 m a.s.l. in 2023 and a minimum of 1140 m a.s.l. in 2018. The CW basin displayed the greatest variability, with annual maximum elevations ranging from 1380 m a.s.l. in 2020 to 1770 m a.s.l. in 2019 (Figure 4.9; 4.11).

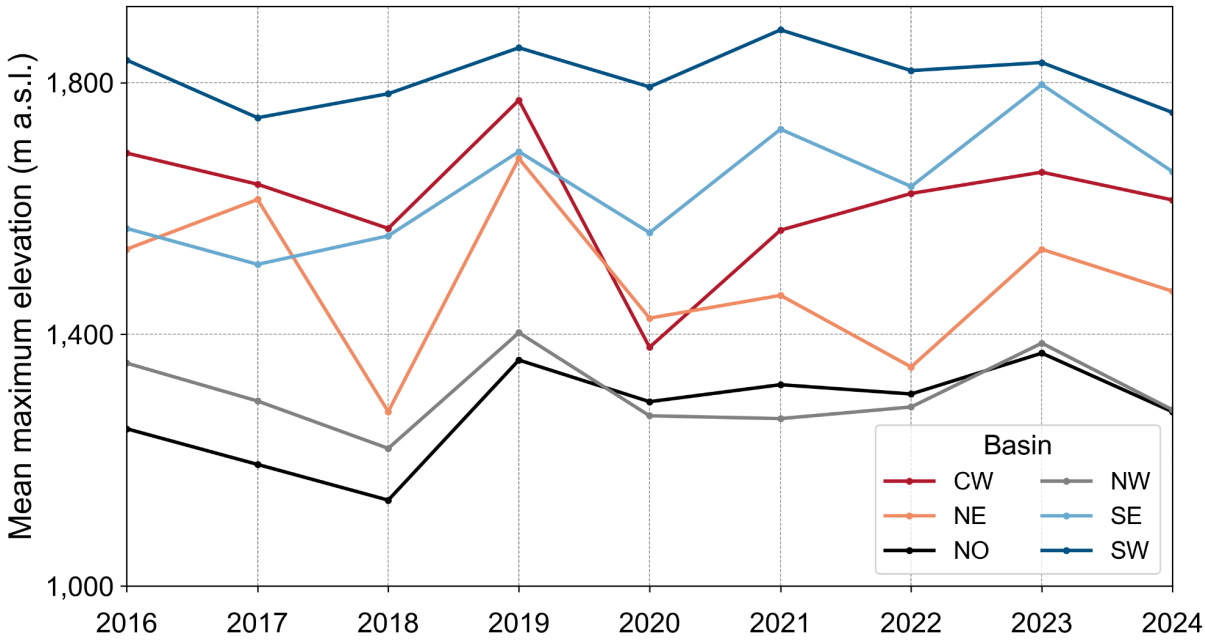

Figure 4.9: Annual time series of the mean maximum elevation (m a.s.l.) of slush within each of the six basins of the GrIS from 2016 to 2024: CW (deep red), NE (orange), NO (black), NW (grey), SE (light blue), and SW (dark blue).

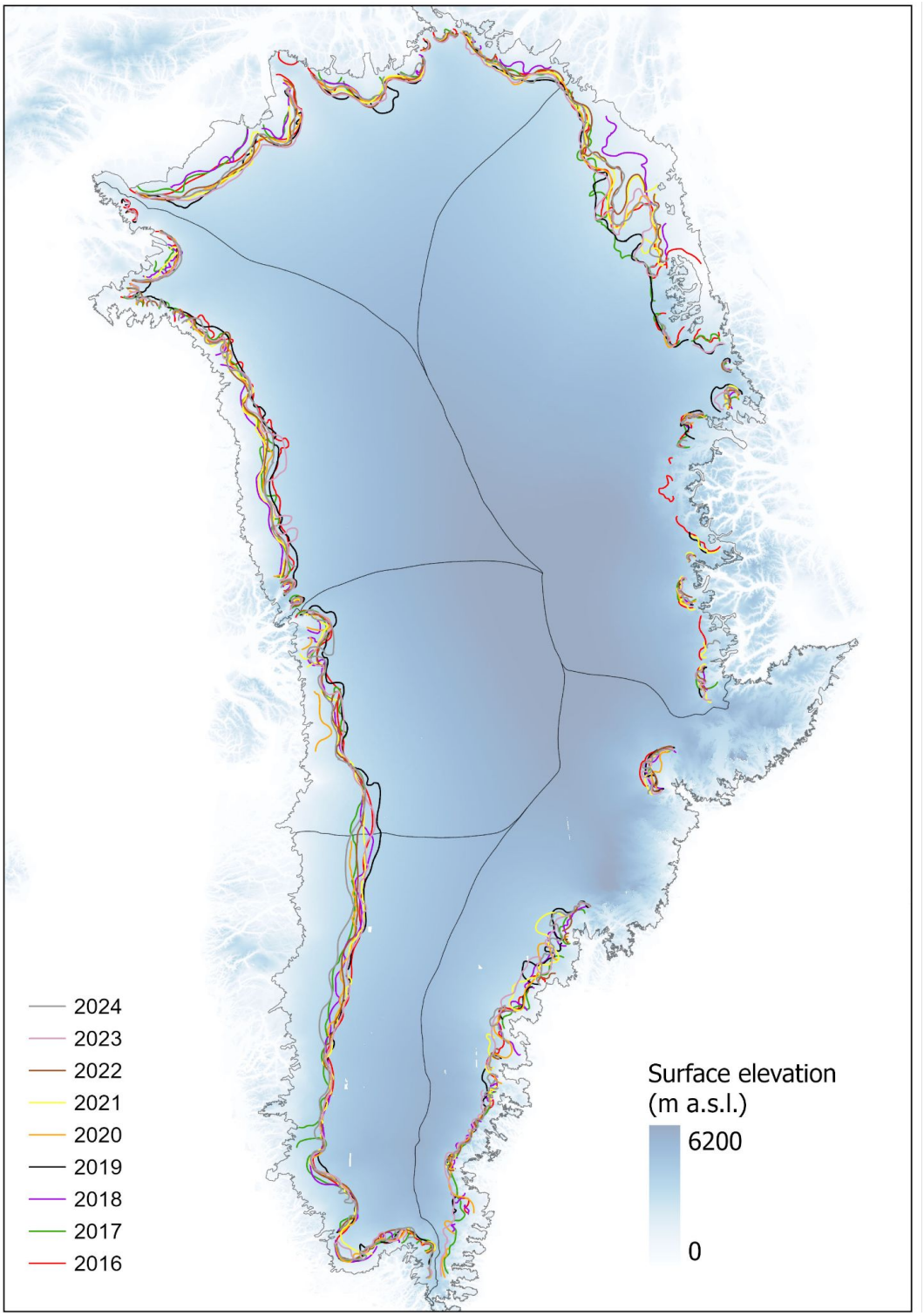

Figure 4.10: Annual maximum slush elevation limits across the GrIS between 2016 to 2024. Base map is surface elevation from the ArcticDEM.

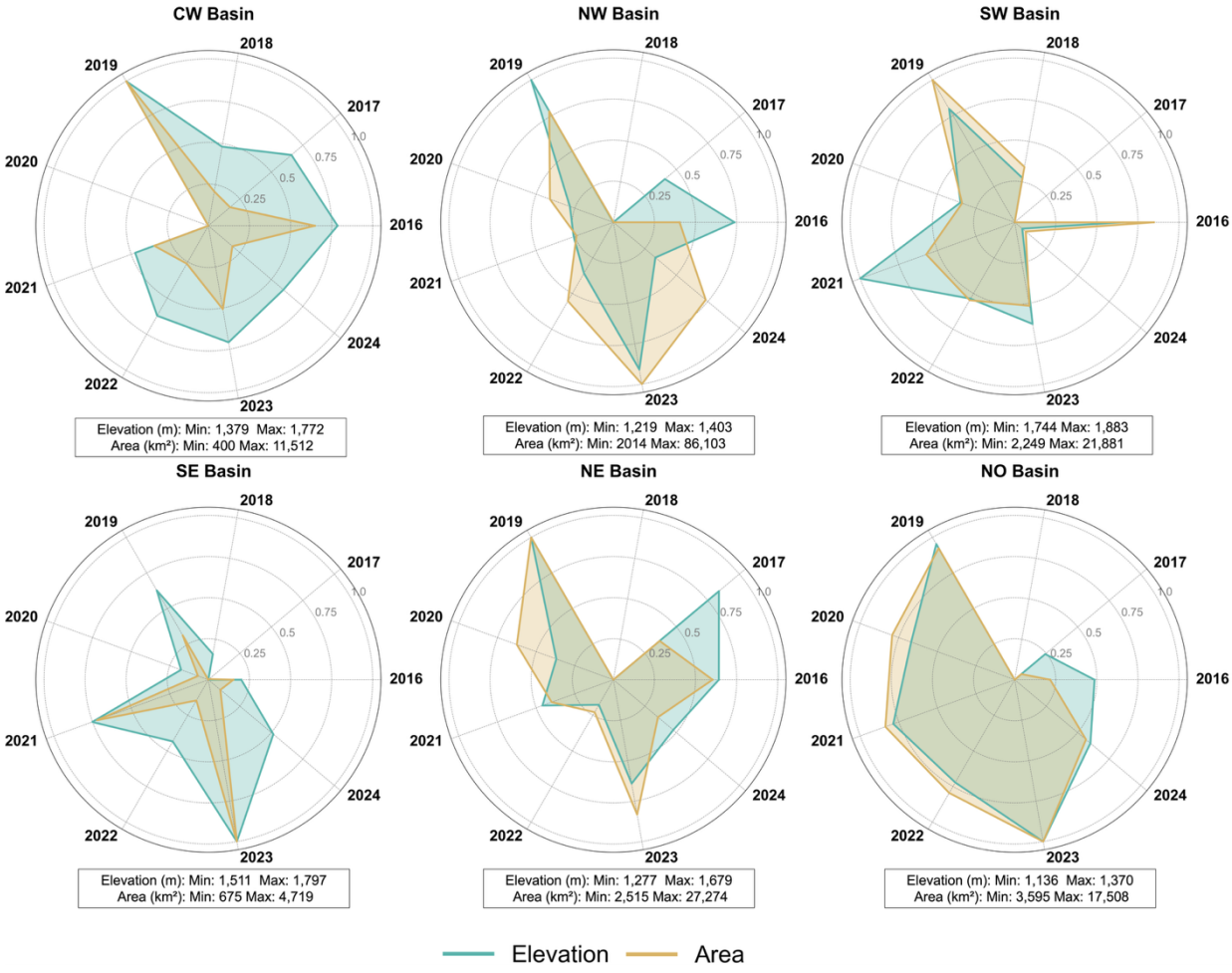

Figure 4.11: Radar charts showing the interannual variability in slush formation across different basins on the GrIS from 2016 to 2024. Each chart displays normalised values for slush area (orange) and elevation (blue). Under each plot, each basin's minimum and maximum elevations, as well as areas, are stated.

4.3.3. Inter-annual variability of slush across Greenland

4.3.3.1. Ice-sheet wide variability

Between 2016 and 2024, slush formation was consistently observed across all basins on the GrIS during the summer months of May to September (Figure 4.5; 4.12; 4.13). The lowest area of slush coverage occurred in 2018 (1.4%; 24,400 km²), while the highest was recorded in 2019 (8.3%; 144,800 km²). No statistically significant trend in slush area was observed over the study period.

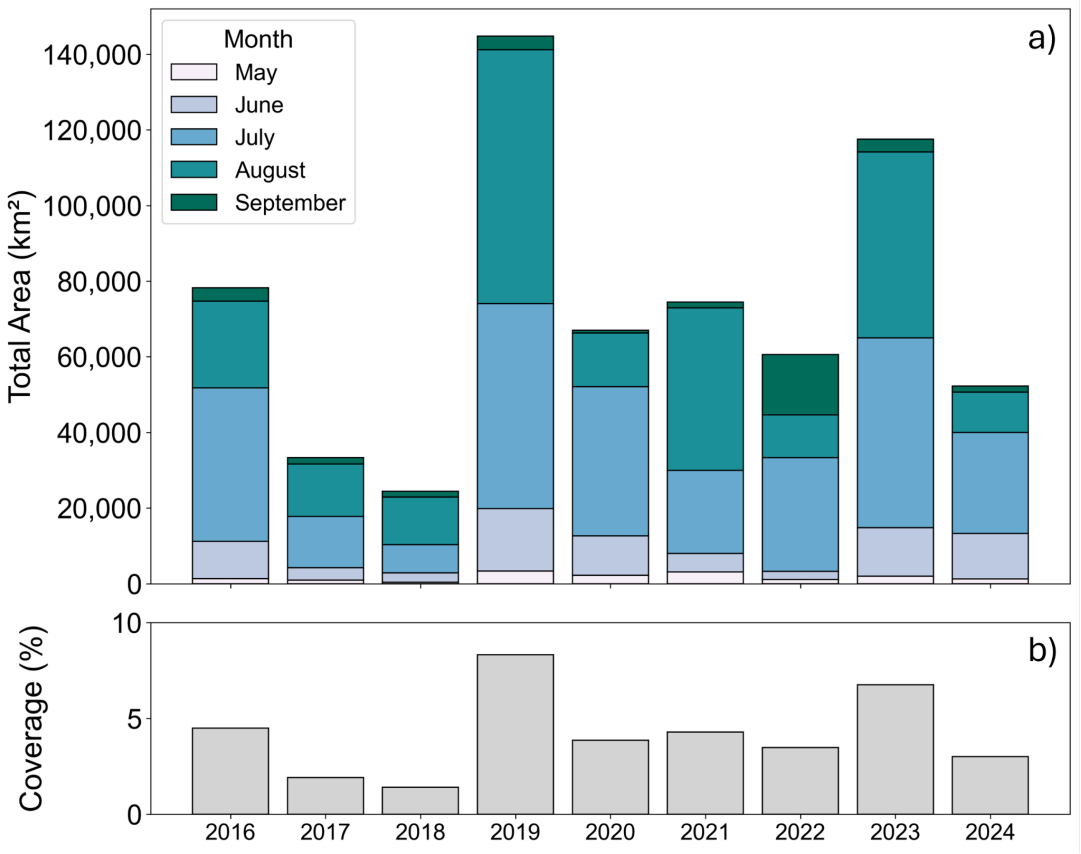

Figure 4.12: Total slush area across the GrIS from 2016 to 2024. a) Cumulative slush area by month (May to September) for each year. b) Percentage of total ice sheet area covered by slush annually.

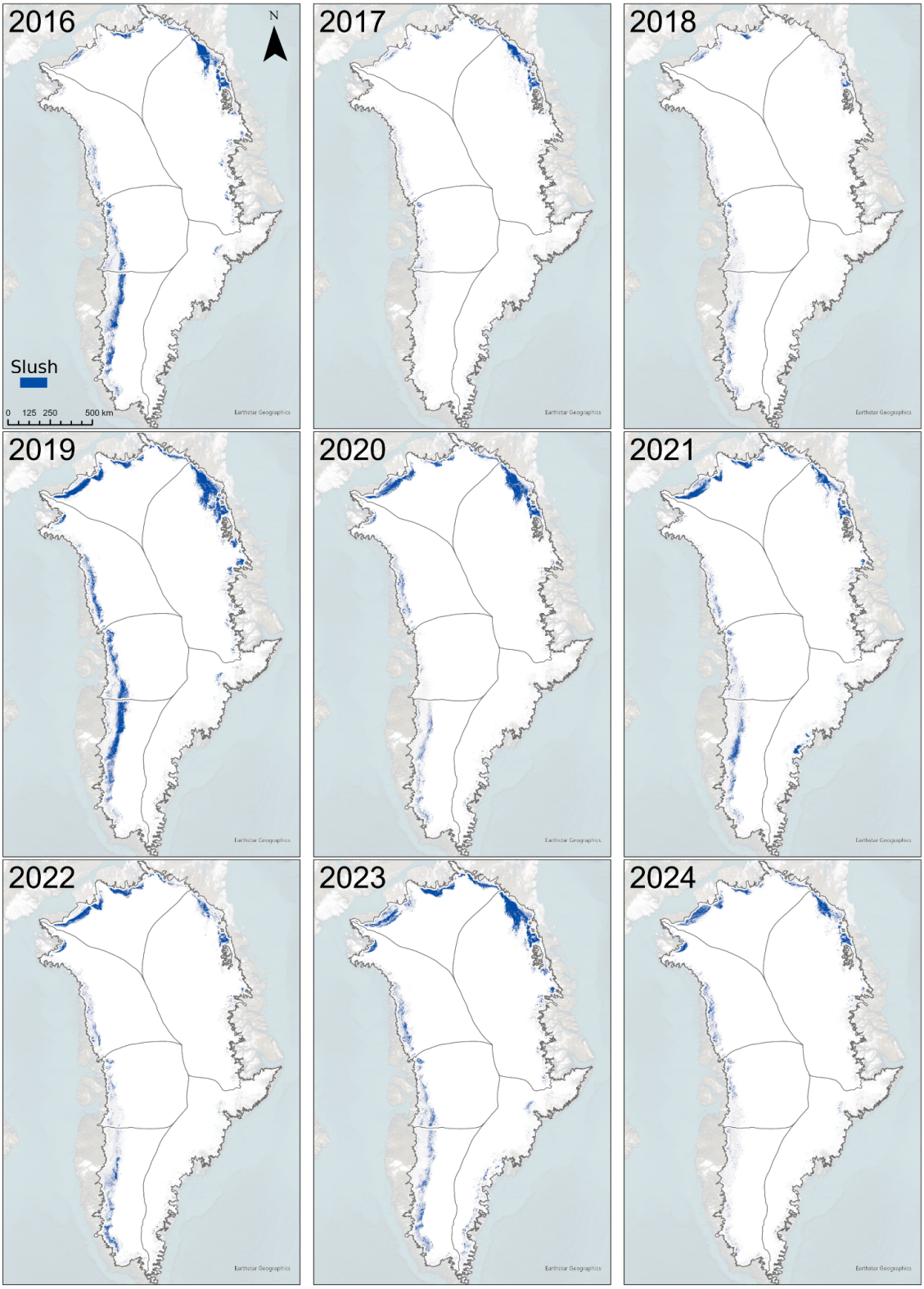

Figure 4.13: Ice sheet wide spatial distribution of slush (navy blue) from 2016 - 2024. Base map source: Earthstar Geographics.

4.3.3.2. Regional variability

From 2016 to 2024, slush presence across the GrIS varied by basin (Figure 4.14). The SW basin recorded the highest peak area of slush in 2019 at 9.6% (20,100 km²), while the NO basin peaked at 7.2% (17,500 km²) in 2023. The NE basin held the largest absolute slush presence in 2019 at 5.6% (27,290 km²). The NW and CW basins peaked at 3.1% (8,600 km²) in 2023 and 5.0% (11,500 km²) in 2019, respectively. The SE basin remained consistently low, ranging from 0.45% (1,000 km²) in 2018 to 1.8% (5,000 km²) in 2023.

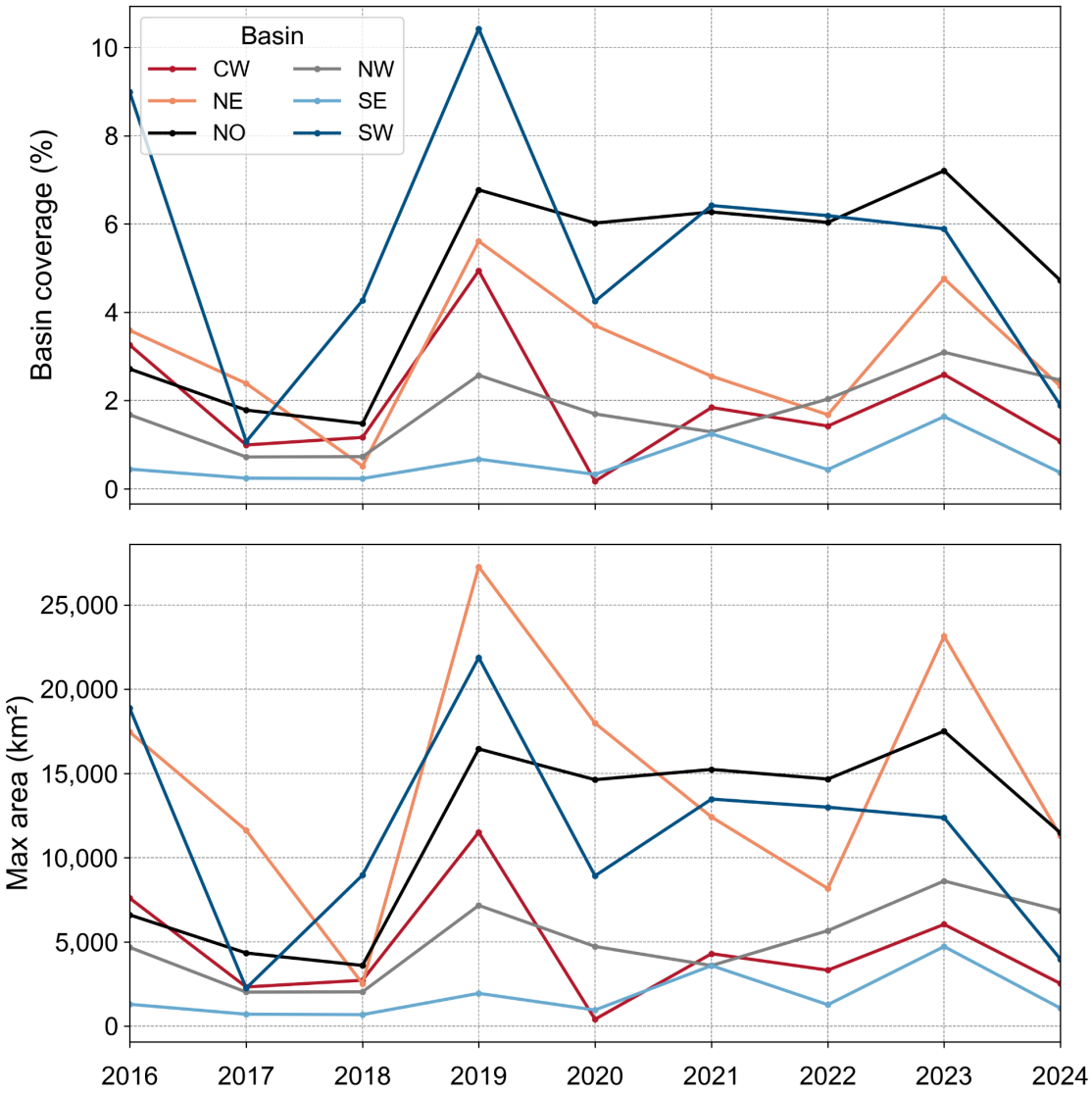

Figure 4.14: Annual time series of slush coverage and maximum area within each of the six basins of the GrIS from 2016 to 2024: CW (deep red), NE (orange), NO (black), NW (grey), SE (light blue), and SW (dark blue). The top panel shows the percentage of basin coverage, and the bottom panel depicts the maximum area (in km²) of slush across the six basins.

4.3.4. Intra-annual variability of slush across Greenland

4.3.4.1. Ice sheet wide variability

Monthly slush coverage across the GrIS from May to September (2016–2024) showed considerable variability (Figure 4.15). In all years, slush area was greatest in July and August (averaging 1.7% and 1.6%, respectively). May and September exhibited the lowest coverage for all years, typically below 0.2%, with September being the most variable month and May the least variable (Figure 4.15).

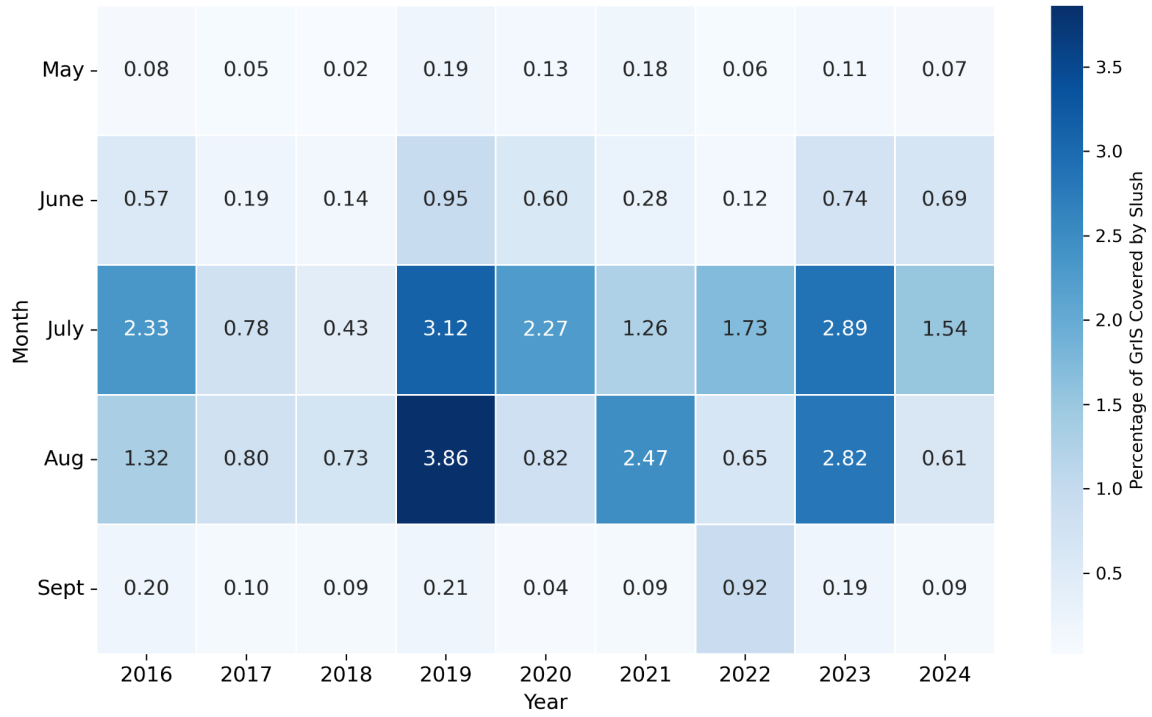

Figure 4.15: Heatmap illustrating the percentage of the GrIS covered by slush from 2016 to 2024, organised by month. Each cell represents the percentage of slush coverage for a specific month and year, with darker shades indicating higher coverage percentages.

4.3.4.2. Regionally

As seen ice-sheet wide, July and August were the primary months for slush coverage across all basins, with smaller extents in May and September (Figure 4.16). July accounted for the peak slush coverage in NW (40%), CW (40%), SW (44%), NE (45%), and NO (45%), with a slight reduction into August (Figure 4.5). SE, however, peaked in August, showing a substantial 41% increase over July. The SW basin showed the most pronounced increase in mean monthly slush area across basins (which was calculated from May to September for 2016–2024), rising from under 1,000km² in May to 6,700 km² in July (Figure 4.16). The SE basin consistently maintained the lowest slush area, remaining under 1,000 km² throughout the melt season and peaking slightly above 500 km² in August.

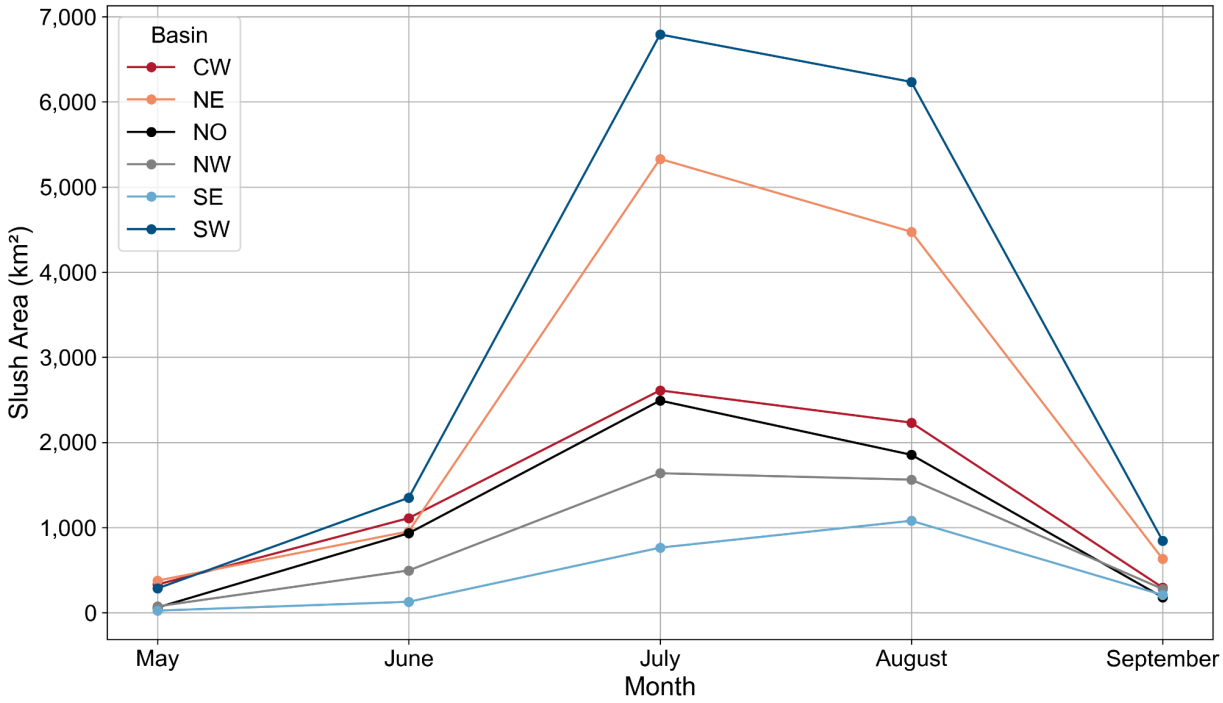

Figure 4.16: Mean slush area across the six GrIS basins from May to September, calculated as the mean slush area for each month over a nine-year period from 2016 to 2024. CCW (deep red), NE (orange), NO (black), NW (grey), SE (light blue), and SW (dark blue).

Throughout our study period we identify two distinct peaks in slush coverage: one in August 2019 and another later in the season in September 2022 (Figure 4.17; 4.18). In August 2019, the SW basin recorded the largest slush area at 18,000 km² (9% basin coverage), the highest observed across all basins during the study period (Figure 4.17), with an example of its spatial distribution shown in Figure 4.19(a). The NW (5,060 km²; 3%), NE (11,700 km²; 4%), and CW (7,100 km²; 3%) basins also reached their highest extents in August 2019. September 2022 marked a late-season peak in slush area across most basins, with the SW basin again recording the highest extent for September at 6,800 km² (3%) (Figures 4.17, 4.18), with an example of its spatial distribution shown in Figure 4.19(b). In September 2022, the NO and NE basins recorded 3,000 km² (1%) and 2,700 km² (1%), respectively, roughly equivalent to their August values in the same year, while the SE basin showed a more typical September with only 600 km² (0.2%) of slush.

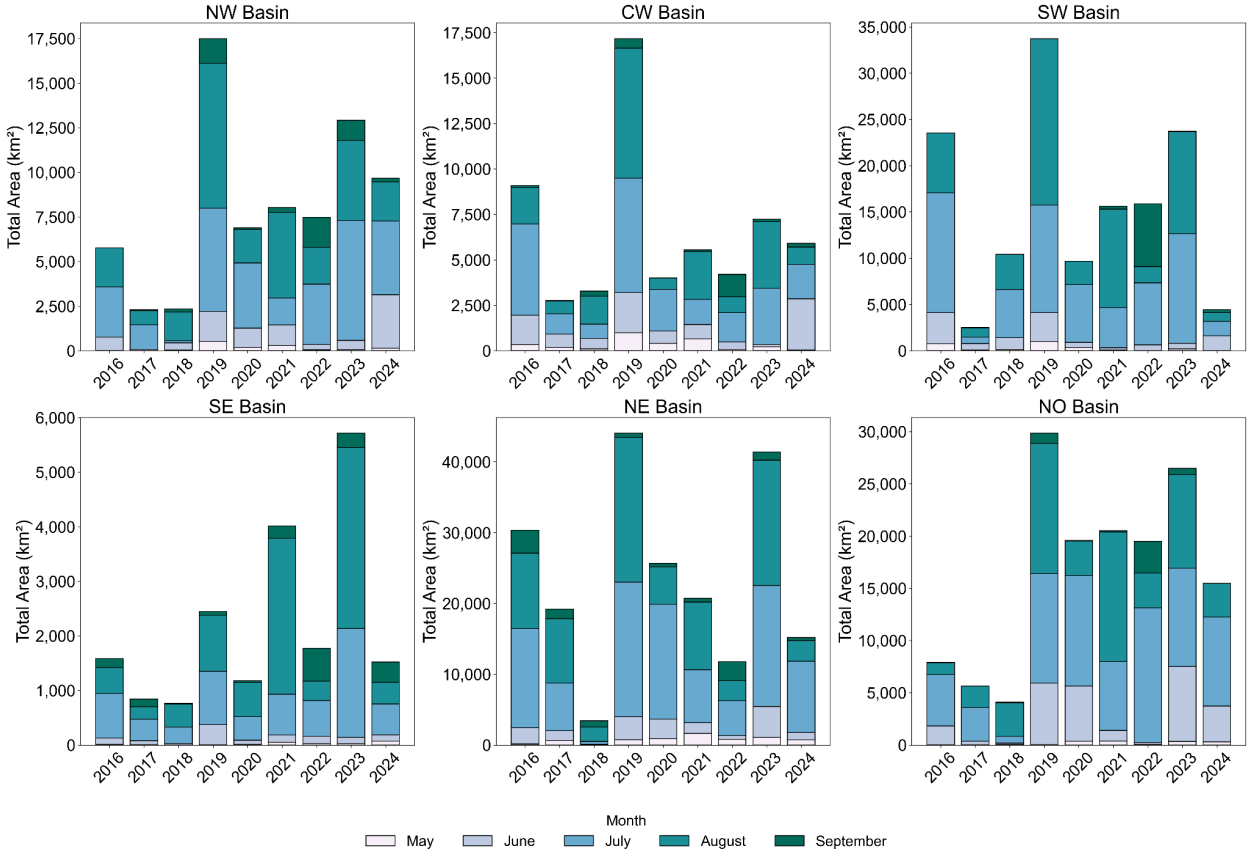

Figure 4.17: Bar plots illustrating the total area (in km²) covered by slush across different basins of the GrIS from 2016 to 2024. Each subplot represents a specific basin (NW, CW, SW, SE, NE, NO), with the total area segmented by month: May, June, July, August, and September.

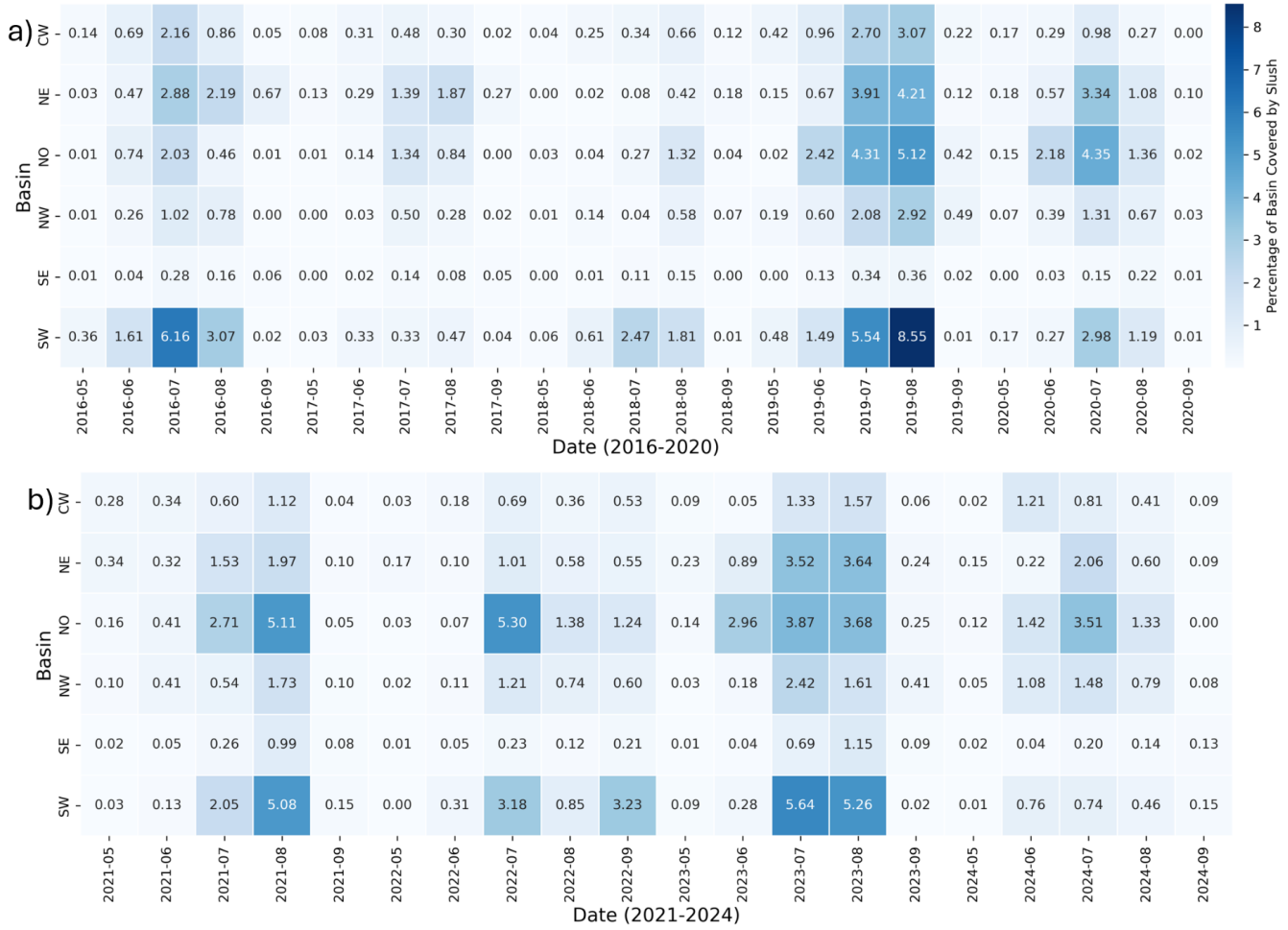

Figure 4.18 Heatmap depicting the percentage of slush coverage in the basins of the GrIS. a) spans from May 2016 to September 2020 and b) spans from May 2021 to September 2024. Each cell represents the percentage of the respective basin covered by slush for a specific month. The colour gradient illustrates the range of coverage, with darker shades indicating higher percentage values.

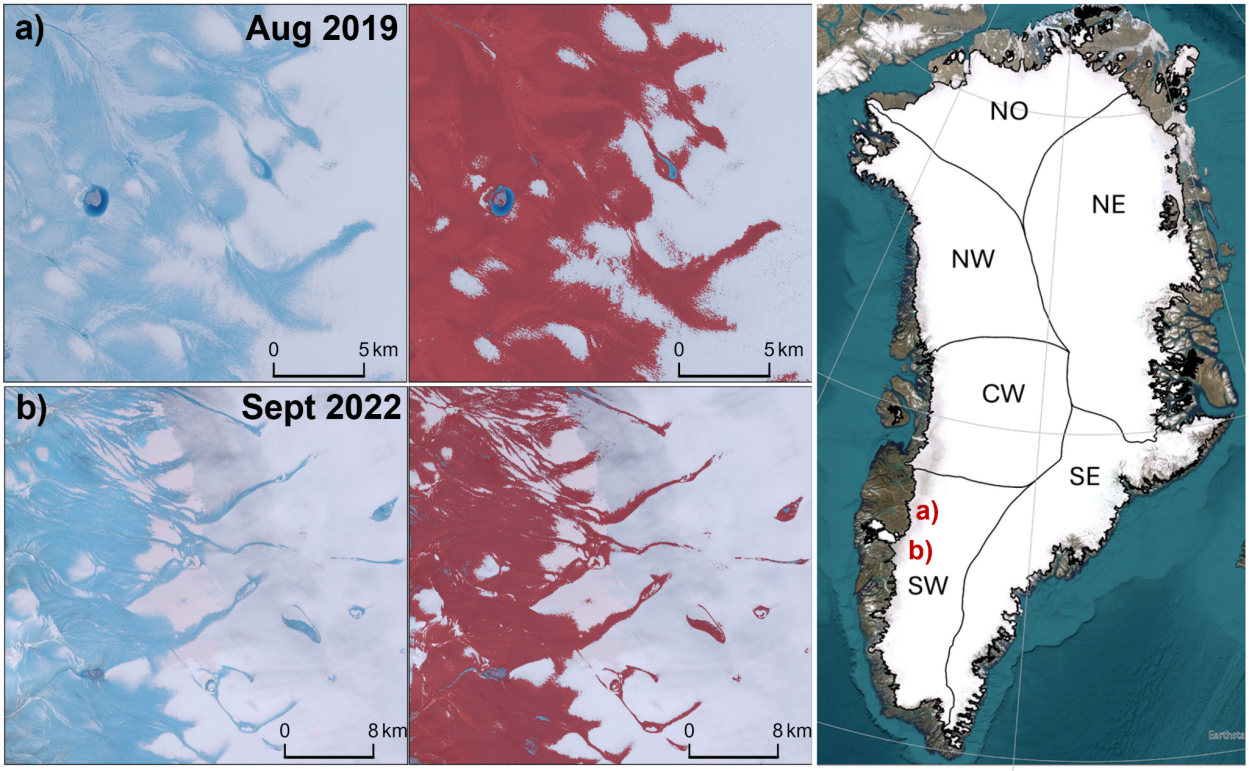

Figure 4.19: Examples of the spatial distribution of slush in a) August 2019 and b) September 2022, shown using S2 RGB imagery (left) and classified slush areas (red) overlaid on the imagery (right). Base map source: Earthstar Geographics.

4.3.5. Comparison of slush detection methods

To evaluate the performance of the RF classifier and its agreement with alternative threshold-based slush detection methods, its classifications were compared with those derived from NDWI and Gind across the six basins (Tables 4.5; 4.6). We determined how closely the spatial distribution of slush identified by RF corresponds to that detected by NDWI and Gind, which was assessed using the extent of spatial overlap between RF and the other methods, classification metrics (Recall, Precision, and F1-score), as well as visual comparisons of classified outputs across selected basins and years.

4.3.5.1 Quantitative Comparison

RF showed better agreement with NDWI than with the Gind method, as evidenced by higher Recall values, F1-Scores, and larger spatial overlap between RF and NDWI classifications compared to RF and Gind classifications (Tables 4.5; 4.6). Overlap between areas where both the RF and NDWI methods detect slush was substantial in basins such as the SW (733 km²), and the CW (41 km²). In contrast, overlap in slush detection areas between the RF and Gind results were consistently lower, peaking at 436 km² in SW and dropping to just 11 km² in CW, emphasizing a weaker spatial correspondence.

The classification metrics of Recall and Precision reinforced the findings described above. RF's Recall values were consistently higher when compared to NDWI than when compared to Gind, ranging from 0.55 (SE) to 0.73 (CW) in NDWI comparisons, versus 0.53 (SE) to 0.65 (NW) in Gind comparisons (Tables 4.5; 4.6). Again, these results suggest that RF more effectively captured the slush features identified by NDWI than those identified by Gind.

Precision values were more comparable across the two method comparisons, with RF achieving between 0.66 (NW) and 0.79 (CW) against NDWI, and between 0.64 and 0.78 against Gind. This reflects RF's consistent ability to classify slush features with minimal false positives, regardless of the comparison method (Tables 4.5; 4.6). However, F1-scores, which balance Precision and Recall, were generally higher in NDWI comparisons (ranging from 0.56 in SE to 0.76 in CW) than in Gind comparisons (ranging from 0.51 in NO to 0.68 in NW). This further supports the finding that RF classifications align more closely with NDWI classifications than with Gind classifications.

4.3.5.2. Visual Assessment

Figure 4.20 presents three examples visually comparing RF classification results with NDWI and Gind methods with optical imagery of three areas of the GrIS for reference. These qualitative comparisons help to further illustrate the differences in classification patterns and errors associated with each classification method.

In the optical image of the CW basin (Figure 4.20a), NDWI and RF showed closer agreement in their classification of slush features, while Gind identified fewer slush features overall. Based on our visual analysis of optical imagery, Gind misclassified lake boundaries as slush more frequently than NDWI and RF.

In the NO basin (Figure 4.20 b), a complex image with cloud cover and mosaicking artifacts was intentionally selected to evaluate the methods. NDWI heavily overestimated slush in this image, misclassifying a substantial portion of clouds as slush. RF captured more detail than either thresholding method, successfully identifying linear slush streams between the clouds without misclassifying the clouds themselves. Gind, while avoiding the misclassification of clouds, detected very limited slush compared to RF.

In the SW basin (Figure 4.20c), NDWI and RF exhibited relatively good agreement in identifying dispersed slush features. RF also detected additional slush areas in the centre of the image that were not captured by either NDWI or Gind. The image contained limited cloud cover, which was not misclassified as slush by any method. Through visual inspection, Gind misclassified a shallow lake in the scene as slush and showed weaker agreement with RF compared to NDWI in this basin.

***Table 4.5: Performance metrics (Recall, Precision, F1-Score) and spatial overlap areas of slush for the comparison of RF classifications with NDWI across the six GrIS* basins.**

RF VS. NDWI										
Image	**Region**	**Date**	**Overall Agreement**	**Kappa**	**Precision**	**Recall**	**F1-Score**	**RF Area (km²)**	**NDWI Area (km²)**	**Overlap Area (km²)**
1	CW	Aug-18	0.96	0.52	0.79	0.73	0.76	86.04	67.82	41.33
2	SW	Aug-19	0.68	0.35	0.79	0.68	0.64	2019.85	758.16	733.17
3	NW	Aug-21	0.82	0.31	0.66	0.65	0.66	134.74	126.68	54.77
4	NO	Aug-22	0.77	0.29	0.66	0.64	0.65	353.22	299.01	142.12
5	SE	Aug-23	0.85	0.16	0.76	0.55	0.56	400.55	71.90	47.15
6	NE	Aug-24	0.9	0.25	0.71	0.59	0.62	430.4	176.25	88

***Table 4.6: Performance metrics (Recall, Precision, F1-Score) and spatial overlap areas of slush for the comparison of RF classifications with Gind across the six GrIS* basins.**

RF VS. G_{ind}										
Image	**Region**	**Date**	**Overall Agreement**	**Kappa**	**Precision**	**Recall**	**F1-Score**	**RF Area (km²)**	**G_{ind} Area (km²)**	**Overlap Area (km²)**
1	CW	Aug-18	0.94	0.16	0.64	0.56	0.58	86.04	33.19	11.06
2	SW	Aug-19	0.61	0.21	0.75	0.6	0.54	2019.85	461.64	435.64
3	NW	Aug-21	0.87	0.38	0.78	0.65	0.68	134.74	66.21	44.5
4	NO	Aug-22	0.79	0.1	0.84	0.53	0.51	353.22	27.97	25.03
5	SE	Aug-23	0.85	0.1	0.77	0.53	0.52	400.55	39.26	27.14
6	NE	Aug-24	0.91	0.14	0.78	0.54	0.56	430.4	61.76	39.98

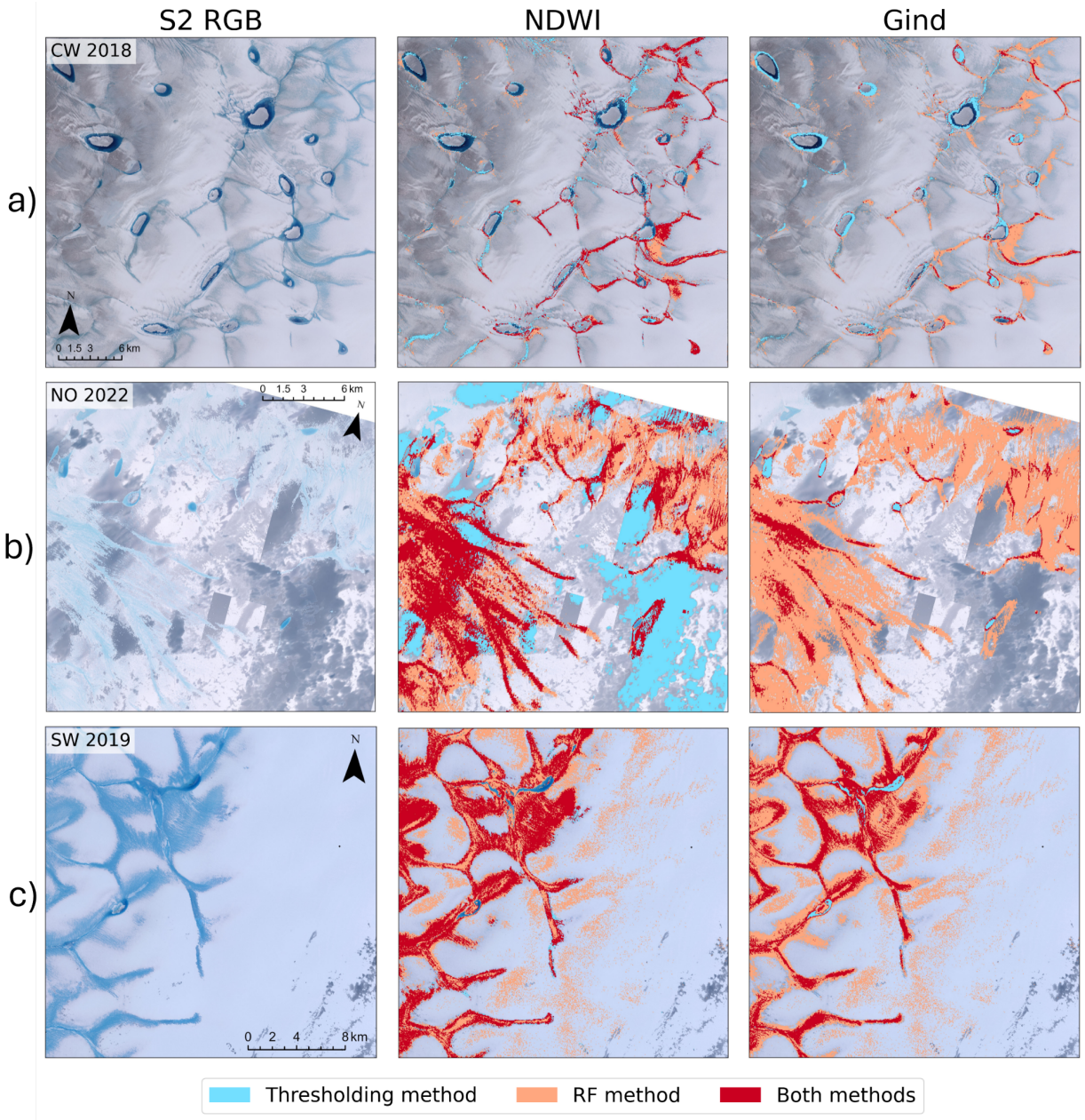

Figure 4.20: Visual comparison of RF with NDWI and Gind classification methods against S2 optical imagery across three **basins** ***and years: a) CW 2018, b) NO 2022, c) SW 2019. The left column displays the original S2 RGB images for reference. The middle column shows NDWI classifications, and the right column shows Gind classifications. Red indicates areas classified as slush by both RF and the thresholding method, orange represents slush identified only by RF, and blue indicates slush identified only by the thresholding method. Note: The NO 2022 image was intentionally selected as a complex case due to significant cloud cover and artifacts such as visible seams and spectral discontinuities between adjacent scenes resulting from the mosaicking process.***

4.4. Discussion

This study presents the first ice-sheet-wide investigation of slush distribution on the GrIS from 2016 to 2024. Using GEE and a combination of k-means clustering and RF classification, we were able to efficiently process large volumes of S2 imagery (329,229 scenes) and delineate slush at high spatial and temporal resolutions.

4.4.1. Spatial distribution of slush across the Greenland Ice Sheet

Our observations of slush distribution across the GrIS demonstrates clear regional variability, with greater areal extents observed in the western and northern basins compared to the eastern and southern basins. This pattern is consistent with previous Greenland-wide studies of supraglacial hydrology (e.g., Zhang et al., 2023; Dunmire et al., 2021). Slush predominantly occurs near the ice margins but is generally absent from the most crevassed areas along the very edge of the ice sheet, with notable inland penetration in the southwest. Among all basins, the SW exhibits the most extensive summer slush coverage, followed by the NO basin. Moderate coverage is observed in the NE, CW, and NW basins, while the SE consistently records the lowest slush presence in each summer. Our findings that slush coverage in the SW is more extensive than in any other GrIS basin is consistent with meltwater detected in previous studies (e.g., Selmes et al., 2011; Hu et al., 2022; Zhang et al., 2023; Fan et al., 2025), which report that the western ice sheet contains the largest area of SGLs.

The high slush coverage in the SW basin is driven by the basin’s favourable topographic conditions, including low relief, shallow surface slopes (Ignéczi et al., 2018), and extensive ablation zones (Ryan et al., 2019), combined with high melt rates (Mikkelsen et al., 2016; van As, 2017). These factors make the basin particularly susceptible to slush formation. However, within the SW basin, a distinct stripe along the western margin shows a notable absence of slush (Figure 4.5), in stark contrast to the surrounding areas. This absence corresponds to the "dark zone," a basin characterized by relatively low albedo and limited snow cover (Tedstone et al., 2017), which reduces slush formation. Other studies have shown that this dark zone is expanding, with a 12% expansion between 2000 and 2014 in SW Greenland (Shimada et al., 2016). As such, the future expansion of this dark area may further influence the spatial distribution of slush in the SW basin in the future. In contrast, SE Greenland's minimal slush presence reflects its steep slopes (up to 30% steeper and 1,000 m higher than the SW basin), small ablation zones, and high winter snowfall accumulation due to proximity to North Atlantic storm tracks (Morlighem et al., 2017; Noël et al., 2019;

Hanna et al., 2016; 2024). These factors limit early summer melt, constraining slush formation in this SE basin.

We find that, across the GrIS, approximately 40% of slush is spatially concurrent with subsurface features such as low-permeability ice slabs and firn aquifers. This includes the 30% (45,100 km²) of slush that we observe to be above ice slabs, which act as aquitards that restrict vertical meltwater percolation into the firn (Figure 4.21; Jullien et al., 2023; Miller et al., 2022). As a result, excess meltwater accumulates at the surface, promoting slush formation and the lateral transport of meltwater through the firn, enhancing runoff. At the end of the season, meltwater retained as slush may refreeze at the end of the season, thickening the near-surface ice slabs and contributing to their expansion. This process further reduces the firn's retention capacity, alters meltwater pathways, and amplifies runoff in subsequent melt seasons, creating a reinforcing feedback loop (Covi et al., 2022; Machguth et al., 2016; MacFerrin et al., 2019; Miller et al., 2022; Jullien et al., 2023). Similarly, ~10% (8,334 km²) of slush forms atop firn aquifers, which store liquid water year-round within firn layers. Slush formation may occur where excess meltwater saturates the surface layers during intense melt events through the upward movement of meltwater from subsurface reservoirs to the surface (Forster et al., 2014; Miege et al., 2016). Together, these processes highlight the dual role of slush as both a product and driver of hydrological changes on the GrIS.

In contrast, we observe 60% of slush in regions of the ice sheet without low-permeability layers. In these areas, slush develops during melt events when the rate of meltwater production exceeds the firn's capacity to absorb and facilitate water percolation. Achieving full firn saturation is more challenging under these conditions, as the firn must become saturated at depth, which typically occurs when preferential flow fingers are overwhelmed and a uniform wetting front saturates the surface layers (Clerx et al., 2022; 2024). Once saturation is achieved, slush may refreeze in place, reducing the firn's ability to fill and store meltwater and increasing the likelihood of supraglacial runoff during subsequent melt seasons. Additionally, the formation of infiltration ice alters the thermal and structural properties of the firn, influencing its permeability and modifying meltwater pathways in future years. When still liquid, meltwater from slush can travel laterally, contributing to enhanced runoff and redistribution of meltwater across the ice sheet.

Our study shows that slush is a dominant yet overlooked component of GrIS hydrology. In both the low-melt year of 2018 and the high-melt year of 2019, we detected a far larger melt area than in previous studies. For example, Zhang et al. (2023) mapped rivers, lakes, and water-filled crevasses but omitted slush. In 2018, we mapped 24,400 km² of slush versus their 4,900 km² of meltwater area–a fivefold increase. In 2019, we detected 144,800 km² of

slush compared to their 9,990 km² of total melt area, a 14.5-fold difference. Regionally, the discrepancy persists. In the NE basin, 11,700 km² of slush detected in our study in 2019 represents a 14.3-fold increase over the supraglacial meltwater features mapped by Zhang et al., while the NW basin exhibited the smallest increase, with 5,060 km² of slush–still more than double the previously mapped supraglacial melt extent. Additionally, Fan et al. (2025) reported that total lake areas rarely exceed 3,500 km² even in peak melt years, emphasizing that assessments focused solely on supraglacial lakes significantly underestimate melt-affected areas. While supraglacial lakes have long been a research focus, our findings indicate that slush plays an important role in meltwater storage and runoff. Similar Antarctic studies (Dell et al., 2024) show that slush and ponded water cover comparable areas on ice shelves, and incorporating their lower albedo into models increased simulated snowmelt by 2.8 times. Future research must integrate slush into hydrology assessments and further examine its effects on albedo and energy balance to refine melt models and improve ice-sheet mass balance projections.

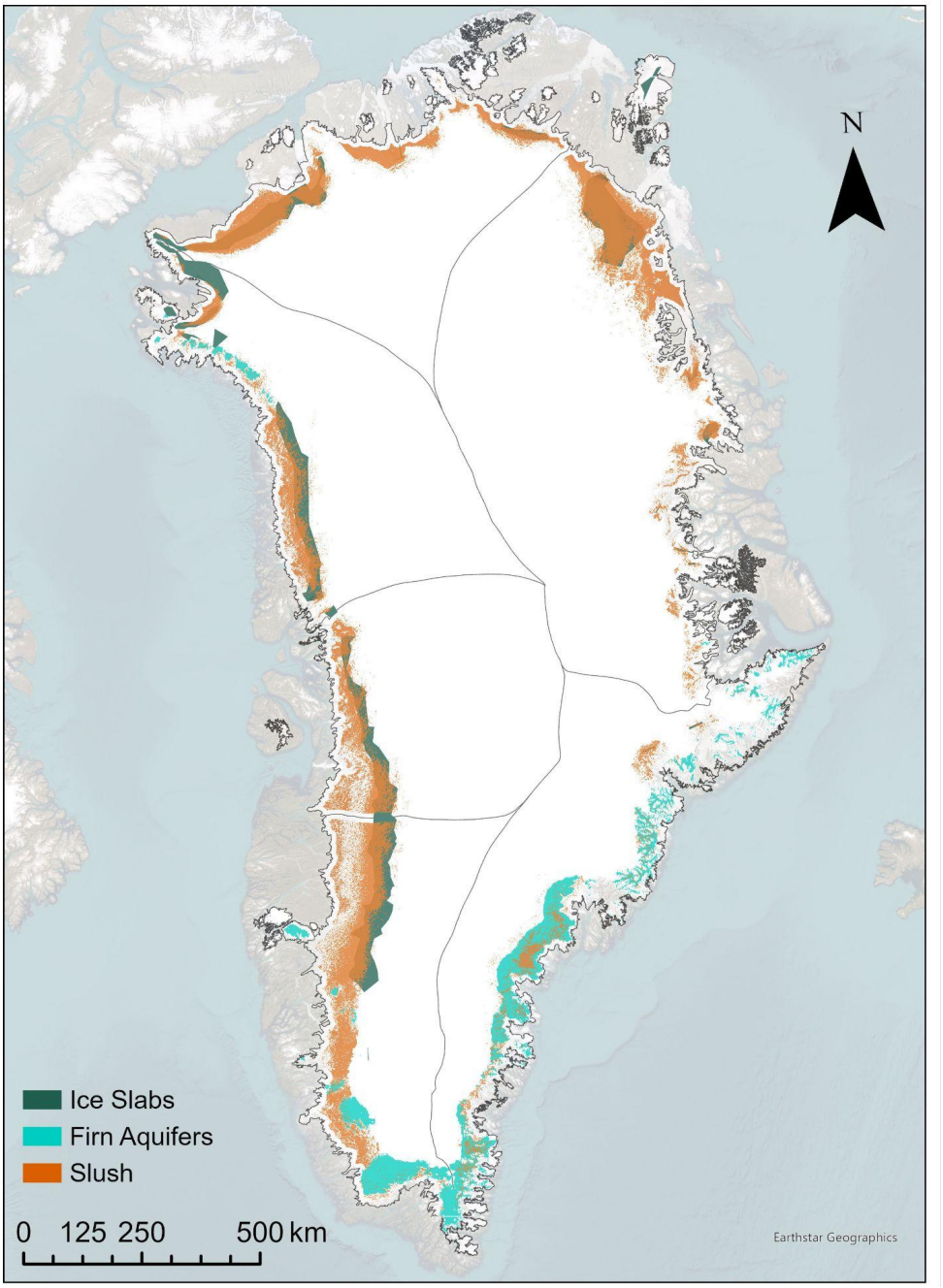

Figure 4.21: Maximum slush extent between 2016 - 2024 (orange), ice slab extent between 2010–2018 (Jullien et al., 2023) (dark green), and firn aquifers in 2010–2014 (Miège et al., 2016) (light green). Base map source: Earthstar Geographics.

4.4.2. Trends and variability in slush elevation

During warmer, and hence more intense melt years, such as 2019 and 2023, we observe slush extending to higher elevations than in cooler years with limited melt (Figures 4.9; 4.22). This pattern aligns with previous findings that SGLs also form at progressively higher elevations during warmer years of substantial melting (e.g., Sundal et al., 2009; Liang et al., 2012; Lüthje et al., 2006; Glen et al., 2025). Covi et al. (2022) further observed this pattern in the Kangerlussuaq sector of the western GrIS, where years with below-average melt, such as 2017, 2018, and 2020, blue slush was limited to lower elevations, and in contrast, years with intense melt, such as 2016, 2019, and 2021, saw expansion of blue slush to higher elevations. Generally, water percolating into subfreezing firn at higher elevations refreezes, modifying the thermal and physical properties of the firn and releasing latent heat that raises the firn temperature to a critical point where meltwater can begin to drain freely (Chu et al., 2013). Additionally, at these higher elevations, melting initiates structural changes within the snow and firn, including increased densification rates as liquid water infiltrates for the first time and drives snow grain metamorphosis.

We observe no significant trends in slush elevation over our study period, either at an ice sheet or regional scale. This aligns with Machguth et al. (2022), who reported no significant change in maximum slush elevation between 2012 and 2021 on the GrIS's western flank. Their findings also highlight considerable variability in maximum slush elevation during individual summers, which is consistent with our observations. However, our findings contrast with Tedstone and Machguth (2022), who documented a significant rise in the visible runoff limit (i.e., slush elevation) from 1985 to 2020, with average increases of 242 m in the west, 194 m in the north, and 59 m in the northeast. Additionally, the absence of a trend in maximum slush elevation is inconsistent with studies that documented the increasing elevations of SGLs (e.g., Howat et al., 2013; Gledhill and Williamson, 2017; Zhu et al., 2022).

Examining the relationship between maximum slush area and maximum slush elevation reveals that these two metrics often vary independently (Figure 4.11). For example, the SW basin exhibited synchronized peaks in both area and elevation during 2016 and 2019, reflecting widespread slush formation at higher elevations during intense melt seasons. In contrast, the NW basin in 2024 displayed extensive slush coverage concentrated at lower elevations, likely due to more localized meltwater retention. Similarly, the NE basin in 2017 recorded high slush elevation but limited area, suggesting favourable conditions for slush formation at elevation but insufficient meltwater to support horizontal expansion. Further study is required to better understand these processes.

4.4.3. Inter-annual variability of slush across Greenland

Slush presence across the GrIS from 2016 to 2024 exhibits dynamic fluctuations, with notable peaks and troughs in terms of areal extent, which correspond closely to modelled air temperature anomalies (Figure 4.22; 4.23). However, during our 9-year study period, the lack of a significant trend in slush area across the ice sheet prevents us from concluding consistent long-term changes. Fan et al. (2025), however, showed that from 1985 to 2023, SGL area across the entire GrIS increased by 50.5 km² per year. The fact that we did not observe an increase in slush area may be due to our relatively short 9-year study period. Or, although supraglacial melt has increased over this time period, increased meltwater storage in supraglacial hydrological features such as SGLs may have limited the expansion of slush area over this time period. Further work is needed to assess the partitioning of meltwater between slush and other supraglacial hydrological features, such as SGLs, to better understand the factors governing slush extent and persistence.

In 2020, passive microwave data suggest that the near-surface melt area across the ice sheet was lower compared to other relatively low-melt years, such as 2017 and 2018 (Figure 4.24). However, interestingly, we show that the slush extent in 2020 was double that of 2017 and 2018 (Figure 4.12). Regionally, this pattern was also evident, with the 2020 summer's slush extent surpassing 2017 across all basins, including a fourfold increase in the NO basin. This discrepancy may be linked to the extensive slush event in 2019, which recorded the highest observed slush coverage on the GrIS (~4%). It is plausible that the slush from 2019 refroze at the end of the melt season, forming a low-permeability layer beneath the surface. In the summer of 2020, only the seasonal winter snowpack on top of this layer needed to saturate to generate widespread slush. This preconditioning of the ice sheet surface enhances the potential for greater supraglacial runoff and meltwater ponding in subsequent years. Such surface preconditioning has also been identified by Rawlins et al. (2024), who observed this process at Humboldt Glacier in North Greenland. Their study showed earlier activation of the supraglacial hydrologic system and extended melt seasons in years following widespread slush events (Rawlins et al., 2023). Similarly, Covi et al. (2022) documented a substantial increase in slush extent in the Kangerlussuaq sector during 2020 compared to 2017 and 2018, despite 2020 experiencing the lowest positive degree days in the region. These findings align with our observations, indicative of prior widespread slush events causing widespread refreezing, which preconditions the surface for greater slush formation in subsequent years.

The NO basin exhibited a clear step-increase in slush area from 2019 onwards, with consistently elevated levels observed in subsequent years. It is possible that the widespread

refreezing event in 2019, which created extensive low-permeability ice layers across the ice sheet, had a long-term impact on this basin. This could explain the persistent slush formation in the NO basin even during years with relatively lower melt intensity, as the refrozen layers would require only the seasonal winter snowpack to saturate for slush to develop. This is also in combination with warming trends in the NO basin. As shown in Figure 4.23, the NO basin has experienced persistently positive temperature anomalies, particularly in years such as 2019. Such warming has driven a 46% expansion of the northern ablation zone–nearly double the 25% increase observed in the south (Noël et al., 2019, 2022). Northern Greenland also showed the greatest trends in number of extreme melt days across the GrIS from 1950 to 2022, attributed to positive anomalies in downward longwave radiation and a 5–10% rise in early-summer cloud cover since the 1990s, which have intensified melt rates (Bonsoms et al., 2024; Noël et al., 2019, 2022). Projections indicate northern Greenland will experience the greatest warming across the GrIS in the 21st century, further exacerbating its vulnerability in part due to relatively low winter accumulation rates compared to other ice sheet sectors (Hill et al., 2018; Goelzer et al., 2013). These factors make the NO basin a key basin for understanding and monitoring the impacts of future climatic changes (Rawlins et al., 2023).

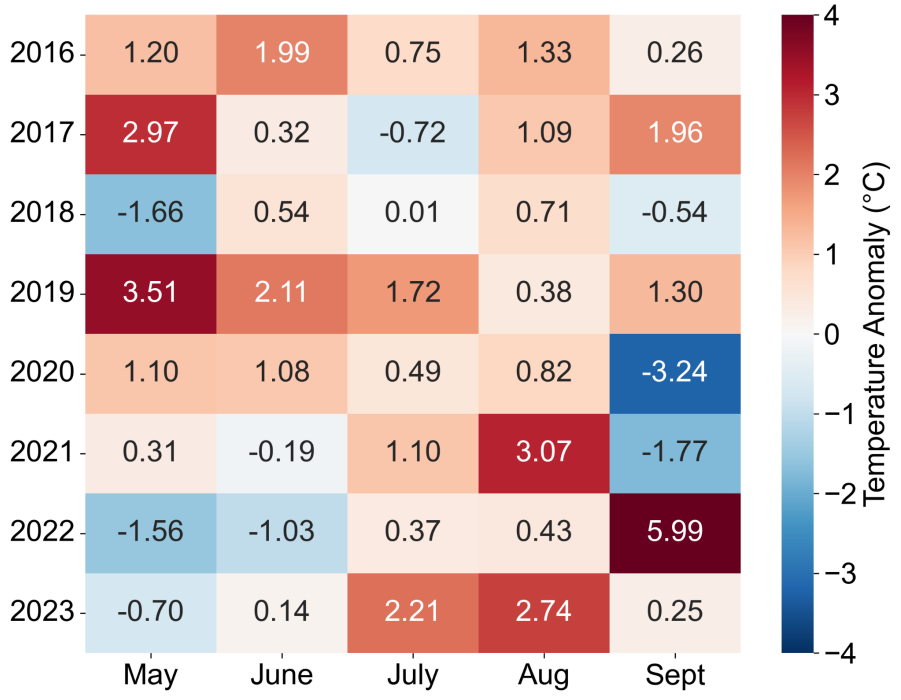

Figure 4.22: May to September monthly temperature anomalies (°C) from the 1958–2015 mean for the GrIS during 2016–2023. Data is derived from the RACMO climate model (Noel et al., 2019).

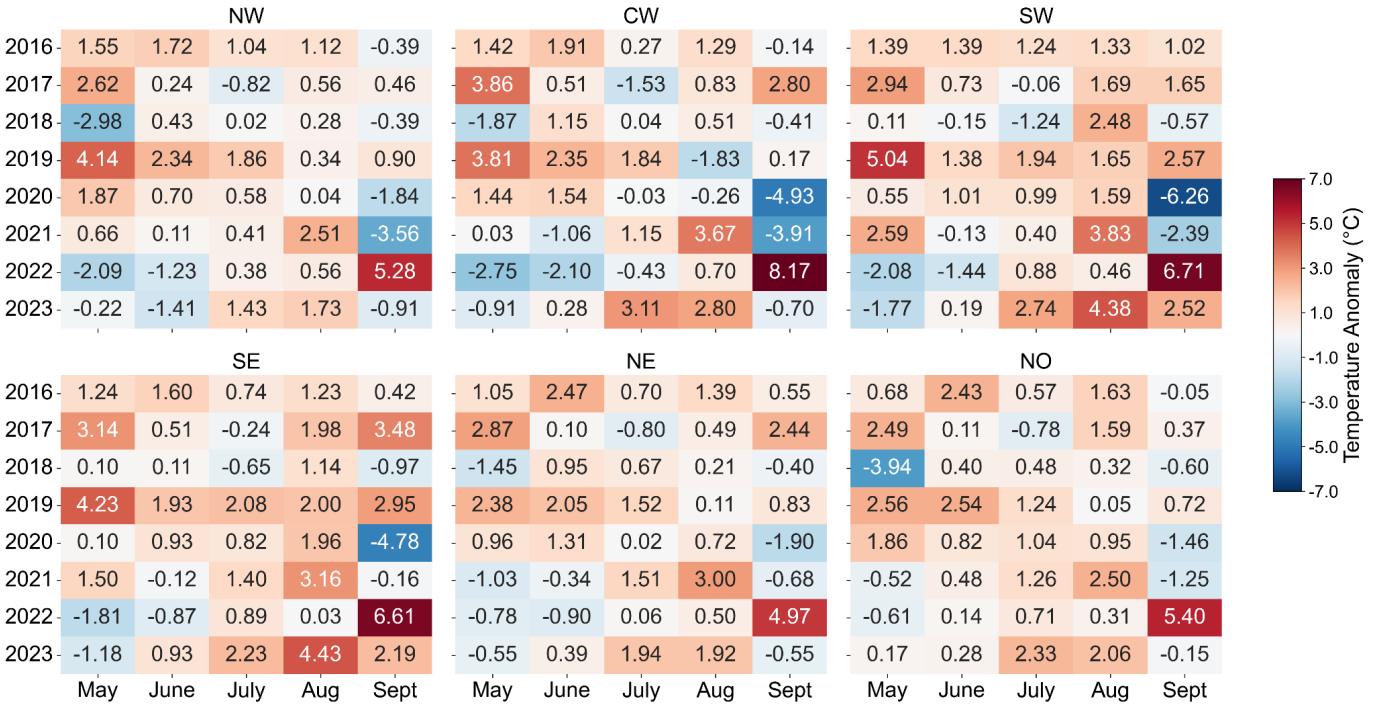

Figure 4.23: May to September monthly temperature anomalies (°C) from the 1958–2015 mean for each basin of the GrIS during 2016–2023. Data is derived from the RACMO climate model (Noel et al., 2019).

4.4.4 Intra-annual variability of slush across Greenland

The intra-annual variability of slush across Greenland from 2016 to 2024 reveals pronounced and anomalous patterns during years with extreme melt events and late-season warming. For instance, 2019 shows pronounced positive air temperature anomalies in the early-to-mid season (Figure 4.23), corresponding to an intense melt season that likely drove widespread slush formation which peaked at ~ 4% coverage of the ice sheet in August - the greatest seen throughout our study (Figure 4.14). Under typical conditions, slush follows a predictable seasonal cycle, forming in May, peaking in July, and retreating during the autumn freeze-up, similar to the behaviour of SGLs (e.g., Otto et al., 2022; Yang et al., 2021; Glen et al., 2024). However, during anomalous years such as 2019 and 2022, this cycle is disrupted by exceptional atmospheric and supraglacial melt conditions.

In 2019, persistent anticyclonic circulation and a strong Greenland Blocking Index led to one of the most extreme melt seasons on record, as seen in Figure 4.24. From May to July, consistently high positive temperature anomalies were observed, with May reaching +3.5°C above the 1958–2015 mean (Figure 4.22). These elevated temperatures drove prolonged and intense melt conditions, further exacerbated by melt-albedo feedbacks due to reduced

snowfall and the exposure of darker ice surfaces. As a result, slush fields expanded further inland and covered the largest proportions of the ice sheet during the study period, nearing 1900 m a.s.l and 4% ice sheet coverage (Sasgen et al., 2020; Tedesco and Fettweis, 2020; Hanna et al., 2021).

In September 2022, anomalously high temperatures and exceptional rainfall caused substantial ice-sheet wide melt (Figure 4.24), which disrupted the seasonal melt cycle by delaying the autumn freeze-up, resulting in sustained slush fields into October (Moon et al., 2022; C3S, 2023). This anomaly is reflected in air temperature records, with September 2022 showing temperature anomalies exceeding ~6°C across several basins, a sharp contrast to typical late summer cooling patterns (Figure 4.23). The persistence of late-season slush coverage in September 2022 may have had implications for ice dynamics. Acting as a transient reservoir, slush may have temporarily stored and released excess supraglacial runoff later in the summer than usual, overwhelming subglacial drainage systems. This hydrological disruption may have contributed to a brief acceleration of ice flow until the hydrological system adapted by channelizing the additional meltwater, stabilizing ice velocities (Ing et al., 2024).

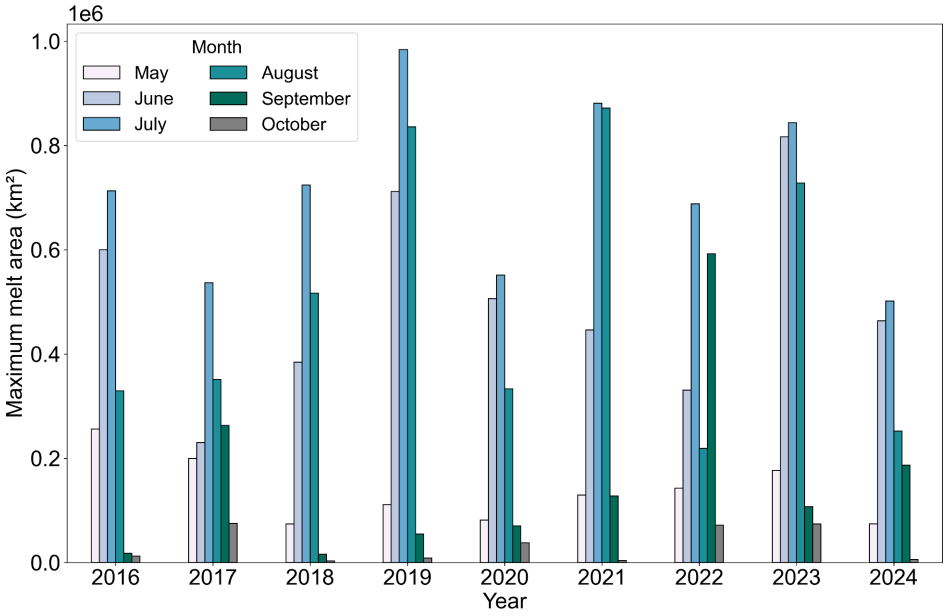

Figure 4.24: Monthly maximum area of surface and near-surface melt (km²) across the whole GrIS from 2016 to 2024, derived from passive microwave sensors. Each bar shows the maximum melt areal extent for a specific month, with colours representing May through October. Data used to make figure came from the National Snow and Ice Data Center/T. Mote, University of Georgia (Mote et al., 1995, 2007).

4.4.5 Method performance, comparison and limitations

Our ML method, following Dell et al. (2022; 2024), but adapted for the GrIS, integrates unsupervised k-means clustering with a supervised RF classifier, which enables automated slush detection across the GrIS. The k-means clustering step uncovers subtle spectral patterns in slush areas, while manual refinement of the training data ensures robustness, making it applicable for large-scale, multi-temporal analyses. To assess the performance of our approach, we quantitatively compared the RF classifier results with those from two other methods: NDWI and Gind, as well as qualitative visual comparison with optical imagery.

4.4.5.1 NDWI comparison

NDWI showed reasonable quantitative agreement with RF in some regions, particularly where surface conditions were relatively simple such as in the SW, but the performance of NDWI declined in areas with more complex topography such as SE. Visual comparisons supported these patterns: while NDWI and RF produced similar outputs in some cases like the CW basin, NDWI frequently overestimated slush, especially in challenging environments with variable terrain or cloud cover, where it misclassified clouds as slush. For example, in NO (2022), NDWI substantially overestimated slush by misclassifying clouds, an error that RF avoided. Together, these findings highlight that although NDWI can provide an approximation of slush extent in straightforward settings, its reliance on a static threshold limits its reliability across diverse conditions, reducing its suitability for consistent, large-scale slush mapping.

4.4.5.2 Gind comparison

In contrast to our comparison of NDWI results with those from the RF, Gind showed weaker spatial agreement with RF. For instance, in the CW basin (Table 4.5; 4.6), the overlap between RF and Gind was just 13% of the RF-detected slush area. In comparison, the overlap between RF and NDWI in the same basin was 48%, highlighting Gind's more limited slush detection capabilities relative to the RF method. This trend was consistent across other GrIS basins too. Visual comparisons support these results, showing that Gind missed large portions of slush areas identified by both RF and NDWI methods. For example, in the NO (Figure 4.20b), Gind detected very little slush, overlooking clear linear slush streams mapped by RF, while in the SE (Figure 4.20c), Gind underestimated slush extent where surface expressions were more subtle. These limitations demonstrate that while Gind can provide some useful information in basins containing relatively simpler surface spectral types and topography, its performance diminishes in areas with more challenging environmental conditions.

4.4.5.3 RF performance and limitations

Our RF approach demonstrates superior detection capabilities compared to both NDWI and Gind thresholding methods, particularly with regard to capturing the fine-scale spatial and temporal variability of slush. However, RF is not without its limitations. In a minority of cases, such as in the SW basin in 2019, the RF method appears to overestimate slush coverage (Figure 4.20). Additionally, the manual interpretation and refinement required during k-means clustering introduce a degree of subjectivity, as operator expertise and decision-making influences the selection and adjustment of clusters, potentially affecting classification consistency and efficiency. Despite the application of masking techniques to exclude clouds, crevasses, and exposed rock, commission errors persist, particularly in basins with complex environmental conditions, as our analysis has shown.

4.5. Conclusion

This study has provided the first comprehensive assessment of slush distribution across the GrIS from 2016 to 2024, offering insights into its variability, spatial patterns, and potential drivers. By combining RF classification with k-means clustering, we successfully mapped slush across the GrIS and within six basins at a high temporal and spatial and temporal resolution. While previous research has extensively examined meltwater storage in SGLs, and meltwater flow in rivers and streams, the spatial and temporal dynamics of slush–a critical yet often overlooked meltwater feature–have remained largely unexplored. By filling this gap, our analysis provides new insights into the distribution, extent, and persistence of slush across the GrIS over nearly a decade.

We found that slush coverage was most extensive in the SW, NE and NO basins, while the SE basin consistently exhibited minimal slush presence, a pattern also observed with SGL distribution in other studies. Slush showed highest interannual persistence in the NE and NO basins, which aligns with observed warming trends in North Greenland, and could suggest that these basins may continue to be particularly sensitive to future climate change.

Extreme events on the GrIS, including the record high melt seasons of 2019 and 2022 (Hanna et al. 2024), summers where we observed particularly large areal slush extents, highlight the sensitivity of slush production to atmospheric anomalies, highlighting its increasing prominence in a warming climate. As rapid climate warming in the Arctic continues, processes driving slush formation–such as prolonged and more intense supraglacial melting, as seen in August 2019 and September 2022–are projected to further intensify. This raises concerns about the role of slush in accelerating supraglacial runoff and influencing subglacial hydrology. If warmer conditions become the norm, slush could shift from being a seasonal anomaly to a defining feature of the ice sheet's melt season each year, with significant implications for en- and sub-glacial meltwater routing, ice dynamics, and sea-level rise contributions.

Our findings demonstrate that slush is a dominant yet often previously overlooked component of GrIS supraglacial hydrology. Our results show that slush-covered areas alone exceed previous estimates of total meltwater extent by up to 14.5 times. Even the most conservative difference–double the previous estimates–emphasizes the need to incorporate slush into models of meltwater hydrology and ice-sheet mass balance. The widespread presence of slush reduces surface albedo relative to snow and firn, increasing solar absorption relative to ice or snow and influencing the surface energy balance. As regional climate models do not currently account for albedo variations resulting from the presence of

slush, our results highlight the need for model refinements to better represent supraglacial melt processes. We also suggest that future mapping work should aim to assess all supraglacial meltwater features, including slush, SGLs, and streams, to provide a more comprehensive understanding of their combined hydrological impacts.

This study provides a foundation for further exploration of slush dynamics and their broader impacts on ice sheet behaviour. Both monitoring and modelling slush processes are essential for understanding the GrIS's response to future climate conditions, as well as refining predictions of supraglacial hydrology and ice sheet mass loss via runoff. With global temperatures projected to rise by up to 6.6°C by 2100 (Hanna et al., 2021), the intensification of slush formation and its refreezing into ice slabs may amplify runoff and accelerate the GrIS's contribution to sea-level rise.

Chapter 5

Assessing the performance of machine learning algorithms in Google Earth Engine for cloud-based supraglacial meltwater feature classification on the Greenland Ice Sheet

Emily Glen[1,2], Malcolm McMillan[1, 2], Amber Leeson[1,2], Alison F. Banwell[3], Diarmuid Corr[1,2], David Parkes[1,2]

[1] Lancaster Environment Centre, Lancaster University, Lancaster, UK

[2] UK Centre for Polar Observation & Modelling, Lancaster University, Lancaster, UK

[3] Cooperative Institute for Research in Environmental Sciences (CIRES), University of Colorado Boulder, Boulder, USA

Correspondence to: Emily Glen (e.glen@lancaster.ac.uk)

This following work is prepared for publication to be submitted as: ‘Assessing the performance of machine learning algorithms in Google Earth Engine for cloud-based supraglacial meltwater feature classification on the Greenland Ice Sheet’

EG and MM conceptualised the research. AL, AFB, DC, DP, and MM contributed to the scientific content, technical details, and overall structure of this paper. All co-authors contributed to discussion of results and editing of the manuscript.

Abstract

The Greenland Ice Sheet is losing mass at an accelerating rate, as climate warming increases supraglacial meltwater production, driving surface runoff and the formation of meltwater features. Supraglacial lakes, rivers, and slush form a dynamic, interconnected hydrological network that regulates how meltwater is stored, routed, and exported from the ice sheet–impacting surface mass balance, ice flow dynamics, and freshwater input to the ocean. However, large-scale mapping of this hydrological network remains challenging, as traditional remote sensing methods require location-specific tuning and extensive manual correction to address false positives and negatives. Machine learning (ML) offers a scalable alternative and is increasingly used in supraglacial hydrology, but the rapid development of new algorithms has outpaced their systematic evaluation in this context. This study addresses that gap by evaluating seven machine learning classifiers for supraglacial meltwater mapping in Google Earth Engine, comparing their accuracy, transferability, and sensitivity to training data characteristics. Random Forest (RF) and Gradient Boosted Decision Trees (GBDT) performed best: GBDT had the highest accuracy (0.99 ± 0.004) within the same region and year, but was sensitive to incorrect training labels, while RF had the most consistent performance across regions and melt seasons (0.96 ± 0.009), albeit with a slight loss in accuracy. Spectrally diverse training data–particularly from high-melt years and heterogeneous regions–enabled better model transfer in space and time. While larger training datasets improved performance, accuracy stabilized at ~16,000 randomly selected points (50% of the dataset), and accuracy also plateaued when using more than 3–7 spectral bands and indices as inputs. These findings provide clear guidance for efficient and effective ML-based monitoring of meltwater evolution and support the scalable, automated mapping of supraglacial hydrology as Greenland's climate continues to warm.

5.1. Introduction

Over recent decades, the Greenland Ice Sheet (GrIS) has experienced substantial net mass loss due to intensified surface melting and dynamic ice flow changes (Slater et al., 2021; Otosaka et al., 2023; IMBIE, 2020; Moon, 2020; Mouginot et al., 2019; van den Broeke et al., 2008). Between 1992 and 2020, the GrIS lost an average of 169 ± 9 Gt of ice annually, amounting to a total of 4892 ± 457 Gt, which contributed ~14 mm to global sea level rise (Otosaka et al., 2023). From 2007 to 2017, 64% of this mass loss resulted from increased surface melting, while the remaining 36% was driven by increases in dynamic ice loss (Otosaka et al., 2023). As the climate warms, the GrIS's contribution to global sea level is expected to increase; potentially adding 3–14 cm to global sea levels by 2100 under a range of emissions scenarios (IPCC, 2021; Morlighem et al., 2017; Otosaka et al., 2023).

Increased meltwater production on the GrIS over recent decades (Slater et al., 2021; Tedstone and Machguth, 2022) has been driven by rising air temperatures (Hanna et al., 2012, 2021), changing summertime atmospheric circulation patterns (van den Broeke, 2017), and the ongoing expansion (Noël et al., 2019) and darkening (Tedesco et al., 2016) of the bare ice zone. Surface meltwater on the GrIS forms complex networks of supraglacial lakes (SGLs), channels, and saturated firn, known as slush. Increased melting has resulted in the proliferation of supraglacial meltwater features, increasing in both area and number (Liang et al., 2012; Palmer et al., 2015; Howat et al., 2013). Notably, supraglacial meltwater features have been observed at progressively higher elevations across the ice sheet, reaching regions previously considered too cold for substantial melting (Howat et al., 2013; Leeson et al., 2015).

Supraglacial hydrology exerts a fundamental control on the behaviour of the GrIS, influencing both surface and basal processes that regulate mass loss across seasonal and multi-annual timescales. At the surface, networks of SGLs, channels, and slush fields develop across the ablation zone and lower accumulation zone during summer, routing large volumes of meltwater downslope. This water contributes directly to mass loss through runoff and reduces the ice sheet's albedo, enhancing the absorption of solar radiation and amplifying surface melt (Leidman et al., 2021). In addition, the refreezing of near-surface meltwater forms impermeable ice slabs that limit firn porosity and reduce meltwater storage capacity, further increasing runoff (MacFerrin et al., 2019). Meltwater generated at the surface can also exert powerful controls on basal processes when it is transferred to the bed via moulins and hydrofractures. Once at the base, this water can reduce basal friction and trigger transient accelerations in ice flow (Chu, 2014; Zwally et al., 2002; Joughin et al., 2008; Banwell et al., 2013; Hoffman et al., 2018), facilitating the delivery of ice to lower

elevations where it becomes more vulnerable to surface melt and calving. Over longer timescales, the sustained input of relatively warm meltwater can drive cryo-hydrologic warming, softening the ice and promoting enhanced internal deformation (Phillips et al., 2010, 2013). Rapid drainage of SGLs can induce ice–bed separation, temporarily enhancing basal lubrication and accelerating ice flow, while also reorganising subglacial drainage by opening new pathways to the bed (Banwell et al., 2016). Under sustained or extreme meltwater input, these processes can contribute to widespread and prolonged weakening of the subglacial bed, amplifying basal motion and ice loss (Maier et al., 2022).

Because of the range of processes through which supraglacial meltwater influences ice sheet behaviour, it is essential to monitor the distribution and evolution of surface hydrological features to improve understanding of how the ice sheet responds to atmospheric warming.

Much of the research on meltwater processes in the GrIS has focused on the delineation of SGLs (e.g., McMillan et al., 2007; Selmes et al., 2011; Williamson et al., 2017, 2018a; Miles et al., 2017; Yang et al., 2021; Lu et al., 2021; Turton et al., 2021; Zhang et al., 2023), and to a lesser extent, channels (e.g., Yang and Smith, 2012; Lu et al., 2020; Yang et al., 2016) and slush (e.g. Rawlins et al., 2023; Yang and Smith., 2013; Tedstone and Machguth 2022; Machguth et al., 2023). These delineation efforts have commonly been conducted using both manual methods (e.g., Leeson et al., 2013; Fitzpatrick et al., 2014; Lampkin and Vanderberg, 2014; Langley et al., 2016; Yang and Smith, 2016) and automated threshold based detection algorithms (Fitzpatrick et al., 2014; Miles et al., 2017; Williamson et al., 2018; Yang et al., 2021; Moussavi et al., 2020; Banwell et al., 2014; Box & Ski, 2007; Yang et al., 2017). The most commonly used semi-automated method to map supraglacial hydrology is the Normalised Difference Water Index (NDWI), which classifies pixels as ‘water’ or ‘non-water’ based on spectral characteristics (McFeeters, 1996). While NDWI-based approaches can be effective, they often require extensive additional filtering and manual intervention to correct for misclassifications, making it difficult to scale across large datasets (Corr et al., 2022; Moussavi et al., 2020).

Machine learning (ML) offers potential for automated, large-scale supraglacial hydrology mapping, addressing many of the limitations of traditional remote sensing methods that rely on manual or threshold-based techniques, which are impractical for large-scale, repeat monitoring. ML algorithms provide scalable, automated solutions capable of handling vast satellite datasets, leveraging spectral, spatial, and textural information from satellite imagery to improve classification accuracy. Despite promising results from algorithms like Random Forest (RF) (e.g., Dell et al., 2022; Dirscherl et al., 2020) and emerging deep learning

approaches (Hu et al., 2022; Lutz et al., 2024), ML remains underutilized in mapping supraglacial hydrology. The application of ML to supraglacial meltwater mapping is still in its early stages, with the first studies focusing on SGL detection emerging around 2020 (e.g., Dirscherl et al., 2020; Halberstadt et al., 2020), and slush classification receiving attention even more recently (e.g., Dell et al., 2022; 2024). Halberstadt et al. (2020) used Landsat 8 imagery and k-means-derived training data to evaluate classification methods for SGL mapping in Antarctica, where RF performed the best, achieving 99.3% overall accuracy. However, the study did not optimize hyperparameters or explore advanced techniques like boosted algorithms, and the reliance on 30-meter resolution imagery limited the detection of smaller SGLs, which higher-resolution Sentinel-2 (S2) data has the potential to address. More recently, deep learning techniques like Convolutional Neural Networks (CNNs) and U-Net architectures have shown promise in SGL mapping, with U-Net being applied to Sentinel-1 (S1) and S2 imagery for SGL detection in Greenland and Antarctica, often integrated with RF to improve segmentation performance (Dirscherl et al., 2021a; Niu et al., 2023). ML classification methods have also shown promise for slush mapping; for example, Dell et al. (2022; 2024) utilized a k-means clustering algorithm to create training classes from Landsat 8 imagery, subsequently training an RF classifier to delineate both slush and SGLs on Antarctic ice shelves. To date, there are no studies focused specifically on the classification of supraglacial rivers using ML, with the only example being Choukset et al. (2021), which applied SVM to classify surface features in East Antarctica, including some supraglacial hydrological features.

Despite the growing use of ML in supraglacial hydrology, several critical gaps remain. A key limitation is the availability of reliable training data, which is essential for developing, validating, and generalizing classification models. Generating high-quality ground truth data is challenging in polar environments due to logistical constraints and the dynamic nature of meltwater features. While manually enhancing existing datasets can help, this process is time-consuming and may introduce biases by relying on subjective decisions about which features to include and how to label them. Persistent misclassification issues, including shadow effects, partial SGL freezing, and cloud interference, also pose challenges, particularly when distinguishing meltwater features from surrounding ice (Dirscherl et al., 2020; Dell et al., 2022). Additionally, most ML studies focus on localized regions or specific melt seasons, limiting the spatial and temporal transferability of results across the GrIS. The scalability of ML approaches for large-scale, long-term monitoring remains underexplored, with computational constraints hindering the analysis of extensive satellite archives.

The advent of freely available cloud-based platforms like Google Earth Engine (GEE) has revolutionised the ability to analyse large-scale satellite data efficiently (Gorelick et al.,

2017), providing a powerful tool for studying supraglacial hydrology (e.g., Tuckett et al., 2021; Zhu et al., 2022; Wang et al., 2024; Dell et al., 2022, 2024; Dirscherl et al., 2020). Early applications focused on adapting traditional threshold-based methods, such as Tuckett et al. (2021), who mapped SGLs on the Amery Ice Shelf using reflectance thresholds and introduced visibility metrics to account for cloud cover, producing a multi-year time series of SGL area and number from 2005 to 2020. Dell et al. (2022) and Dell et al. (2024) leveraged GEE's built-in ML algorithms, combining k-means clustering with RF classification to distinguish slush from ponded water. Applied to the entire Landsat 8 catalogue, their method generated monthly records of meltwater features across 57 Antarctic ice shelves from 2013 to 2021, demonstrating the potential for large-scale, automated monitoring. In Greenland, Wang et al. (2024) utilized GEE's RF classifier with Landsat 8 and S2 imagery to map SGLs on Heilprin and Tracy Glaciers. Their automated workflow enabled sub-weekly tracking of SGL formation and evolution between 2014 and 2021, providing new insights into seasonal and interannual meltwater dynamics.

GEE's data catalogue offers access to multi-petabytes of high-resolution satellite imagery from sensors such as Landsat, Sentinel, and MODIS, covering several decades of Earth observation. Alongside advanced image processing capabilities, this makes GEE well-suited for analysing supraglacial hydrology at scale, facilitating real-time analysis across large spatial extents. The inclusion of both optical and radar datasets enables comprehensive monitoring, even in cloud-prone regions like Greenland and Antarctica. The integration of multi-sensor data within the GEE environment allows for cross-validation and improved temporal coverage, while ancillary datasets available through the GEE data catalogue–such as digital elevation models (DEMs), climate reanalysis products, and surface temperature records–provide additional context for analysing meltwater dynamics without the need to export data for external processing. Coupled with GEE's scalable computational infrastructure and built-in ML algorithms, these features make GEE an ideal solution for conducting large-scale, high-resolution, and temporally extensive analyses of ice sheet supraglacial hydrology.

Despite advancements in ML for supraglacial hydrology mapping within GEE, it is unclear how the choice of ML methods affects classification outcomes, and thus the design of future large-scale supraglacial meltwater monitoring systems. This study addresses this by performing a systematic comparison and performance evaluation of seven different ML classifiers within the GEE environment for the extraction of supraglacial meltwater features; Random Forest (RF), Support Vector Machine (SVM), Minimum Distance (MD), Classification and Regression Trees (CART), Maximum Entropy (ME), and Gradient Boosting Decision Trees (GBDT).

Specifically, we: (1) assess the performance of the classifiers through cross-validation and manual comparison with reference datasets; (2) evaluate the spatial and temporal transferability of these classifiers to determine their robustness across different melt seasons and geographic regions; and (3) investigate the influence of training data configurations, including dataset size, feature selection, and label quality, on classification outcomes. Finally, this work identifies the most effective and transferable ML approaches for large-scale supraglacial hydrology mapping and make recommendations for enhancing the accuracy, efficiency, and scalability of future meltwater monitoring on the GrIS.

5.2. Methods

In order to evaluate the effectiveness of ML classifiers for mapping supraglacial meltwater features on the GrIS, first a training dataset is prepared covering a range of geographic regions and melt seasons across the GrIS (Section 5.2.2). Seven supervised classifiers - detailed in table 5.1 - were then trained using these data (Section 5.2.2.3). Classifier performance was evaluated (Section 5.2.5.1), and their transferability to regions and melt seasons not included in the training sample was assessed (Section 5.2.5.2). Additional experiments were conducted to examine how factors such as training dataset size, input feature selection, and label inaccuracies affect model performance (Section 5.2.5.3). Finally, the trained classifiers were applied to Sentinel-2 imagery from two contrasting regions and melt seasons–the Northeast Greenland Ice Stream (NEGIS) in 2019 (a high-melt year) and the Watson River catchment in 2018 (a low-melt year)–to evaluate their practical utility for mapping supraglacial hydrology under differing glaciological settings and melt conditions (Section 5.2.6).

Table 5.1: Overview of supervised ML algorithms compared and evaluated in this study, detailing their corresponding GEE classifiers, references documenting their prior use in delineating SGLs, whether implemented within GEE or through other remote sensing approaches, algorithm descriptions, advantages, disadvantages, and tuneable hyperparameters with their purposes. This table is compiled from algorithm documentation and peer-reviewed studies that have applied these methods to supraglacial hydrology or similar remote sensing tasks.

Algorithm	GEE Classifier	SGL references	Description	Advantages	Disadvantages	Tuneable Hyperparameters (purpose)
Classification and Regression Trees (CART)	ee.Classifier .smileCart	Halberstadt et al. (2020)	Decision tree splitting data based on feature importance (Breiman et al., 1984).	Simple, interpretable, easy decision-making.	Prone to overfitting; sensitive to training data.	i. *maxNodes* (limits tree complexity), ii. *minLeafPopulation* (minimum samples per leaf node)
Gradient Boosting Decision Trees (GBDT)	ee.Classifier. smileGradient TreeBoost	N/A	Sequential decision trees correcting errors iteratively (Friedman, 2001).	Effective for complex tasks; iterative learning improves accuracy.	Computationally intensive; prone to overfitting if not properly tuned.	i. *numberOfTrees* (model complexity), ii. *shrinkage* (learning rate), iii. *samplingRate* (data usage per iteration), iv. *maxNodes* (tree depth)
k-Nearest Neighbors (KNN)	ee.Classifier. smileKNN	N/A	Classifies based on the most common class among k neighbors (Cover & Hart, 1967).	Simple, intuitive; effective with well-defined boundaries.	Computationally expensive for large datasets; sensitive to distance metric.	i. *k* (number of neighbors), ii. *searchMethod* (search strategy), iii. *metric* (distance calculation method)
Maximum Entropy (ME)	ee.Classifier. amnhMaxent	Halberstadt et al. (2020)	Estimates class probabilities via maximum entropy (Phillips et al., 2004).	Flexible; handles complex, high-dimensional data.	Computationally intensive; poor with sparse data.	i. *categoricalNames* (input categories), ii. *outputFormat* (probability output), iii. *autoFeature* (auto feature selection), iv. *betaMultiplier* (regularization strength), v. *randomTestPoints* (test data split)
Minimum Distance (MD)	ee.Classifier .minimum Distance	Halberstadt et al. (2020)	Assigns each pixel to the class with the closest mean value based on spectral distance.	Computationally efficient; quick application on large datasets.	Assumes uniform class distribution; low accuracy in complex data.	i. *metric* (distance measure, e.g., Euclidean), ii. *kNearest* (number of nearby classes considered)
Random Forest (RF)	ee.Classifier. smileRandom Forest	Dirscherl et al. (2020, 2021); Halberstadt et al. (2020); Yuan et al. (2020); Dell et al. (2022, 2024); Hu et al. (2022); Wangchuk et al. (2020)	Ensemble method using multiple decision trees with averaged predictions (Breiman, 2001)	Robust against overfitting; handles high-dimensional data well.	Computationally demanding; less interpretable than simpler models.	i. *numberOfTrees* (controls forest size), ii. *bagFraction* (data subset per tree), iii. *minLeafPopulation* (minimum samples per leaf), iv. *maxNodes* (tree depth), v. *enableOOBMode* (accuracy estimate)
Support Vector Machine (SVM)	ee.Classifier. libsvm	Halberstadt et al. (2020); Choukset et al. (2021)	Finds optimal hyperplane for class separation (Vapnik, 1995; Rüping, 2001).	Handles high-dimensional data well; effective for complex tasks with clear class boundaries.	Computationally expensive; struggles with noisy or overlapping data.	i. *decisionProcedure* (voting method), ii. *kernelType* (defines boundary shape), iii. *degree* (polynomial degree), iv. *gamma* (kernel influence), v. *coef0* (margin balancing), vi. *cost* (error-bound trade-off), vii. *nu* (margin size)

5.2.2. Training and validation data preparation

5.2.2.1. S2 imagery

A total of 93 high-resolution S2 Multispectral Instrument images were used in this study and accessed through the GEE data catalogue (Figure 5.1). 91 of these were used for training and validation (Section 5.2.3.1) with the remainder used to verify the results of the training and validation exercise (Section 5.2.3.2). These scenes, detailed in Table C.1, were acquired from 2017 to 2020 between May and September and were selected to encompass diverse geographic, temporal, and surface conditions. They cover all six major drainage basins of the GrIS (Mouginot and Rignot, 2019), representing environments from the ice sheet margin to over 200 km inland, multiple melt seasons, and varying solar elevation angles. The locations of these training and validation images are shown in Figure 5.1.

All images were processed to top-of-atmosphere reflectance using a scaling factor of 10,000 (ESA, 2015). The S2 instrument records 13 spectral bands across visible, near-infrared (NIR), and shortwave infrared (SWIR) wavelengths. The spectral bands utilized in this study included Coastal Aerosol (B1), Blue (B2), Green (B3), Red (B4), Red Edge (B5, B6, B7), NIR (B8), Narrow NIR (B8A), Water Vapor (B9), and SWIR (B10, B11, B12), as detailed in Table 5.2.

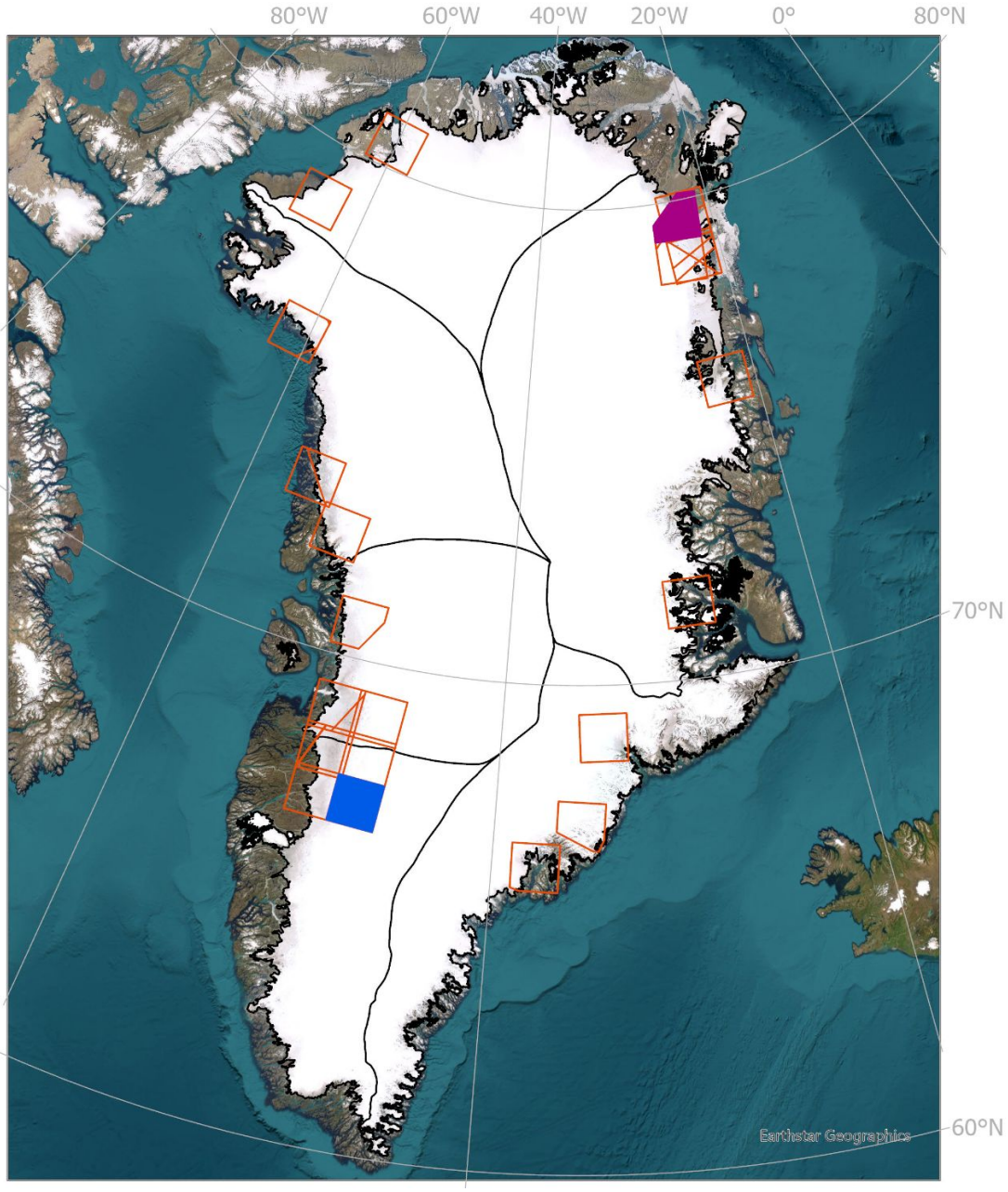

Figure 5.1: Overview map of the GrIS separated into six drainage basins: Southwest, Central West, Northwest, North, Northeast and Southeast (Mouginot and Rignot, 2019). Orange boxes indicate footprints of the 91 training/validation images used for the primary training and validation dataset used in this study. Note: Due to overlapping acquisitions across multiple years and regions, the total number of visible footprints appears fewer than the 91 images used. Blue filled box represents the S2 image for Watson, captured on 30th July 2018. The Purple filled box represents the S2 image for NEGIS, captured on 13th July 2019. Base map source: Earthstar Geographics.

5.2.2.2. Image masking

To ensure accurate classification, a cloud detection algorithm was applied to each S2 image based on thresholds outlined by Corr et al. (2022). A 1 km buffer was added around detected clouds to account for potential shadows. To exclude rock outcrops, a modified Normalized Difference Snow Index (NDSI) approach was used, following Moussavi et al. (2020), with an additional 1 km buffer applied to ensure complete removal of exposed rock.

5.2.2.3. Band indices

Using the S2 bands described above, a suite of spectral indices was calculated, as detailed in Table 5.3. These indices were selected based on their prior use in ML-based supraglacial meltwater classification studies (e.g., Corr et al., 2022; Dirscherl et al., 2021), where they are commonly included as input features. While the potential benefits of using spectral indices–such as highlighting water or snow-related surface characteristics–have been suggested in previous work, their actual impact on classification performance is assessed explicitly in this study. Combined with the original spectral bands, these indices were used to generate 25-band composite images.

Table 5.2 S2 bands, their central wavelengths, and spatial resolutions, and input feature order (see Section 5.2.5.3.3).

S2 Band (B)	Central Wavelength (μm)	Resolution (m)	Input Feature Order
B1 - Coastal aerosol	0.443	60	1
B2 - Blue	0.49	10	2
B3 - Green	0.56	10	3
B4 - Red	0.665	10	4
B5 - Vegetation Red Edge	0.705	20	5
B6 - Vegetation Red Edge	0.74	20	6
B7 - Vegetation Red Edge	0.783	20	7
B8 - NIR	0.842	10	8
B8A - Vegetation Red Edge	0.865	20	9
B9 - Water vapour	0.945	60	10
B10 - SWIR - Cirrus	1.375	60	11
B11 - SWIR	1.61	20	12
B12 - SWIR	2.19	20	13

Table 5.3. Spectral indices used in this study, including their formulas, target features, references, and input feature order (see Section 2.5.3.3). See table 5.2 for S2 Band information.

Index	Name	Formula	Target Features	Reference	Input Feature Order
$NDWI_{BlueRed}$	Normalized Difference Water Index (Blue/Red)	$\frac{Blue - Red}{Blue + Red}$	Surface water	Yang and Smith, 2013; McFeeters, 1996; Moussavi et al., 2020	14
$NDWI_{GreenNIR}$	Normalized Difference Water Index (Green/NIR)	$\frac{Green - NIR}{Green + NIR}$	Surface water	Glen et al., 2025; Corr et al. 2022	15
NWI	Normalized Water Index	$\frac{Blue - (NIR + SWIR_1 + SWIR_2)}{Blue + (NIR + SWIR_1 + SWIR_2)}$	Surface water, shadow	Feng, 2009	16
NDSI	Normalized Difference Snow Index	$\frac{Green - SWIR_1}{Green + SWIR_1}$	Rock, sediment, ice	Hall et al., 1995; Xu, 2006	17
SWI	Snow Water Index	$\frac{Blue - SWIR_1}{Blue + SWIR_1}$	Rock, sediment, ice	Dirscherl et al., 2020	18
NDGI	Normalized Difference Glacier Index	$\frac{Green - Red}{Green + Red}$	Rock, sediment, ice	Keshri et al., 2009	19
$SAVI_{mod}$	Soil Adjusted Vegetation Index	$2 \times \frac{Green - NIR}{1 + Green + NIR}$	Rock, sediment, ice, shadow	Huete et al., 1988	20
SI_{mod}	Sediment Index	$\frac{Blue - NIR}{Blue + NIR}$	Shaded snow and ice, shadow	Li et al., 2016	21
TC_{wet}	Tasselled Cap Wetness	$(0.1509 \times Blue) + (0.1973 \times Green) + (0.3279 \times Red) + (0.3406 \times NIR) - (0.7112 \times SWIR_1) - (0.4572 \times SWIR_2)$	Surface water	Kauth and Thomas, 1976; Schwatke et al., 2019	22
$AWEI_{sh}$	Automated Water Extraction Index (including shadow)	$Blue + (2.5 \times Green) - (1.5 \times (NIR + SWIR_1)) - (2.5 \times SWIR_2)$	Surface water, shadow	Feyisa et al., 2014	23
$AWEI_{nsh}$	Automated Water Extraction Index (not including shadow)	$4 \times (Green - SWIR_1) - (0.25 \times NIR) - (2.75 \times SWIR_2)$	Surface water	Feyisa et al., 2014	24
NDI	Normalized Difference Index	$\frac{Green - Blue}{Green + Blue}$	All features	Dirscherl et al., 2020	25

5.2.3. Label generation for model training and validation

Two distinct datasets were generated to support model training and validation: the *primary training and validation dataset* and the *manual verification dataset*. In this context, a label refers to the binary classification assigned to each pixel – either melt or non-melt. The

primary dataset was used for both model training and validation and the manual verification dataset provided an independent verification, based on two S2 images not used in training (NEGIS and Watson). The following sections explain how labels were created based on each dataset.

5.2.3.1. Primary training and validation dataset

Training and validation labels were created in two classes: surface water and non-surface water. Each class encompassed multiple distinct feature types. The surface water class included SGLs, channels, and slush. These features were delineated using NDWI-based water masks optimized for surface water detection, with thresholds suited for identifying SGLs and slush (as described in Chapter 3; Glen et al., 2025; Corr et al., 2022). Channels were extracted using an automatic river delineation method from Yang et al. (2017), which identifies river networks based on Gaussian-like cross-sections and longitudinal open-channel morphometry (see Chapter 3). These methods produced polygons representing diverse surface water features, all grouped under the single surface water class. The non-surface water class encompassed a variety of features not classified as surface water, including but not limited to bare ice, exposed rock, snow, clouds, sediment, and cryoconite. Polygons for these non-surface water features were manually delineated through visual interpretation of S2 true-colour imagery and merged to create a single class. Each image contained polygons representing both surface water and non-surface water. Within these polygons, approximately 2,000 pixels per scene were randomly sampled, evenly split between surface water (1,000 pixels) and non-surface water (1,000 pixels). Stratified random sampling was used to ensure that samples were evenly drawn from each class, preventing class imbalance in the training data.

5.2.3.2. Manual verification dataset

Two additional images, not included in the primary training and validation dataset, were selected for manual verification to represent contrasting melt conditions. One image from the Watson region in Southwest Greenland was captured on 30 July 2018, a low melt year, while the other, from the Northeast Greenland Ice Stream (NEGIS), was captured on 13 July 2019, a high melt year. These years were chosen to capture interannual variability in surface hydrology, with 2018 reflecting limited meltwater presence and 2019 characterized by widespread melt due to anomalously warm conditions. The Watson and NEGIS regions were selected to represent areas with distinct glaciological and environmental characteristics: Watson is located in southwest Greenland, influenced by a relatively warmer, maritime climate with dynamic supraglacial hydrology (e.g., Smith et al., 2015; Fitzpatrick et al., 2014; Yang et al., 2021), while NEGIS lies in northeast Greenland, within a colder, drier

environment dominated by fast-flowing ice streams and complex ice dynamics (Turton et al., 2021; Lu et al., 2021). The locations of these validation regions are shown in Figure 5.1.

For the manual verification dataset, polygons delineating water and non-water regions were manually drawn using two S2 images from NEGIS and Watson regions. A balanced sampling strategy was applied, with approximately 750 points randomly sampled for each class (water and non-water) per region, resulting in a total of ~1,500 validation points per image.

5.2.4. Hyperparameter tuning

To ensure optimal classifier performance, a nested cross-validation approach was employed for hyperparameter optimization across all classifiers. Nested cross-validation is a model evaluation technique that incorporates two loops: an inner loop for hyperparameter tuning and an outer loop for model performance assessment. This structure helps prevent information leakage between training and validation data, reducing the risk of overfitting (Hastie et al., 2001; Cawley and Talbot, 2010). In the outer loop, the dataset was divided into five folds, with one-fold used for validation and the remaining folds for training. The choice of five folds reflects a common practice in the literature, where 5 to 10 folds are typically used to balance computational efficiency and reliable performance estimation (Kohavi, 1995). Within each outer loop fold, the inner loop further split the training data into five additional folds to systematically evaluate various hyperparameter combinations. A random sampling strategy was applied to explore the hyperparameter combinations, selecting the combination with the highest mean accuracy across the inner folds as the optimal configuration. The optimised classifier was then trained on the full training data from the outer loop and validated on the held-out fold. Details of hyperparameters that are tuned are given in Table 5.1, with additional information regarding specific hyperparameter values given in Table C.2.

5.2.4. Validation metrics

Performance was evaluated using multiple accuracy metrics, including precision, recall, overall accuracy, and the Kappa coefficient, as detailed in Table 5.4. All metrics are derived from the confusion matrix, which compares predicted labels with actual ground-truth labels to provide a summary of classification outcomes. When performance evaluation is conducted over repeated runs, the confusion matrix is cumulative rather than averaged. This approach aggregates the classification results across all iterations, allowing for a more robust assessment of model performance. By summing the true positives, false positives, true negatives, and false negatives across runs, the cumulative confusion matrix reflects the overall trends and consistency in classification behaviour.

Table 5.4: Definitions and formulas of performance metrics used for evaluating the classification models.

Metric	Description	Formula
Precision	Represents the proportion of correctly classified positive instances out of all instances predicted as positive. Reflects the reliability of positive predictions.	$Precision = \frac{TP}{TP + FP}$
Recall	Indicates the proportion of actual positive instances correctly identified by the model. Reflects the model's ability to detect true positives	$Recall = \frac{TP}{TP + FN}$
Overall Accuracy (OA)	Measures the proportion of correctly classified instances across all classes. Provides a general performance metric but can be misleading for imbalanced datasets.	$OA = \frac{TP + TN}{TP + TN + FP + FN}$
Kappa Coefficient (κ)	Evaluates the level of agreement between classification results and reference data, accounting for random chance. Useful for assessing reliability across datasets.	$k = \frac{P_o - P_e}{1 - P_e}$

5.2.5. Classifier analysis

A series of experiments were conducted to 1) evaluate the performance of each classifier, 2) examine their transferability in both spatial and temporal contexts, and 3) analyse the influence of different training data configurations on classification.

5.2.5.1. Performance evaluation

Classifier performance was evaluated using three approaches, repeated validation, cross-validation and independent validation. These approaches were chosen in order to comprehensively understand how well each classifier performed under different conditions.

5.2.5.1.1. Repeated validation

Repeated validation tests how much the model's results vary with different random data splits, providing insight into its stability and sensitivity to data variability. Validation was conducted by splitting the primary dataset into 80% training and 20% testing subsets, ensuring equal class representation. This process was repeated 20 times with different random seeds, and performance metrics were calculated for each iteration. The 80/20 split is a standard ratio that provides a good balance between having enough data to train the model effectively and enough data to reliably evaluate its performance. This split minimizes the risk of bias from insufficient training data and reduces variability in performance estimates that can occur with small test sets. Repeating the process 20 times captures variability due to random data splits, allowing us to assess the consistency and stability of classifier performance. This helps determine whether observed performance differences are due to genuine model behaviour or simply random chance.

5.2.5.1.2. Cross-validation

Cross-validation measures how well the model performs across the entire dataset, offering a comprehensive assessment by ensuring all data points are used for both training and testing. A 10-fold cross-validation strategy was implemented by systematically dividing the dataset into 10 folds, where each fold represents a unique subset of the data containing one-tenth of the total samples. Each fold was used for validation once, while the remaining nine folds were used for training. Performance metrics were computed across all folds.10 folds were used as this number offers an effective balance between computational efficiency and performance reliability (e.g., Kohavi, 1995), compared to higher fold numbers, which can be less practical for large datasets.

5.2.5.1.3 Independent validation using manual datasets

Independent validation evaluates the model's accuracy on completely new data, helping to determine its real-world applicability and generalization to unseen conditions. Classifiers trained on the main dataset were tested on manually sampled points from images not used in the main training exercise (as described in Section 5.2.3.2), with the validation process repeated 20 times to ensure robust performance estimates.

5.2.5.2. Transferability of classifiers

In these experiments, spatial and temporal transferability of classifiers were assessed in order to evaluate their ability to generalize across distinct regions and years. This approach helps determine how well models trained on one set of data can perform when applied to new, unseen data. Transferability is a critical consideration in remote sensing applications, where models are often deployed in environments or time periods different from the training data.

5.2.5.2.1. Spatial transferability, i.e. across different regions of the ice sheet

Transferability tests are essential because the GrIS spans a wide range of climatological and glaciological settings, which can affect classifier performance. The ability of the classifiers to transfer between regions of the ice sheet was tested using data from the NEGIS region which is characterized by fast-flowing ice streams, colder and drier conditions, and complex ice dynamics (e.g., Turton et al., 2021; Lu et al., 2021) and the Watson River region which is situated in southwest Greenland and experiences a relatively warmer, maritime-influenced climate with more dynamic supraglacial hydrology (e.g., Smith et al., 2015; Fitzpatrick et al., 2014; Yang et al., 2021). Data covering May to September from 2017 to 2020 was used, with classifiers trained on the NEGIS [Watson] data and tested on the Watson [NEGIS] data. These contrasting glaciological settings–differing in location, climate, ice dynamics, and surface melt patterns–provide a robust framework for evaluating the adaptability of classifiers to varying geographical locations.

5.2.5.2.2. Temporal transferability across melt years

Since melt conditions vary between years, temporal transferability was assessed to test how well classifiers generalise across time. Temporal transferability was assessed in two scenarios to evaluate classifier performance under varying melt conditions across the entire primary dataset, which includes data from all six major drainage basins of the GrIS (Figure 5.1). Classifiers were trained on data from the high melt year (2019), characterized by extensive surface melt due to anomalously warm conditions, and tested on data from the low

melt year (2018). The reverse scenario was also conducted, with models trained on 2018 data and tested on 2019 data.

5.2.5.3. Training data configuration

Several experiments were conducted to explore the sensitivity of classifiers to training data configurations. This is important because creating high-fidelity training datasets is time-consuming and resource-intensive, representing a key limitation of current ML approaches. Understanding how factors like dataset size, input feature selection, and label quality affect model performance can help to optimize training strategies, reduce manual effort, and improve classifier performance. All training data experiments, described in further detail below, were trained and validated on the primary dataset.

5.2.5.3.1. Impact of training dataset size

To assess the impact of training dataset size, subsets ranging from 10% to 80% of the primary training dataset were created. Classifiers were trained on these subsets and validated against a fixed validation set (also from primary dataset), repeated 20 times to account for variability introduced by random sampling. Metrics were analysed to assess the trade-off between dataset size and reliable performance, and how this varied for each of the different classifiers, in order to understand the sensitivity of each classifier to the size of training dataset used.

5.2.5.3.2. Contributions of spectral bands and indices

This experiment aimed to evaluate the added value of including derived spectral indices alongside raw spectral bands in the classification process. To investigate this, three training scenarios were compared: one using only raw spectral bands (B1–B12, i.e. 12 features), one using only the derived spectral indices defined in Table 5.3 (13 features), and another combining these bands with all the spectral indices (25 features in total). The purpose of this experiment was to determine whether the potential improvement in classification accuracy offered by the inclusion of spectral indices justifies the additional effort required to compute these indices. Classifier performance in each scenario was assessed over 20 repeated runs to ensure robust results. This approach allowed us to determine whether the inclusion of spectral indices enhances classification accuracy or if similar performance can be achieved with fewer input features, thereby simplifying the model and reducing computational demands.

5.2.5.3.3. Feature subset analysis

Feature number–referring to the input variables used for classification (i.e., the 25 combined spectral bands and derived indices)–was assessed using an iterative approach, where classifiers were trained with progressively larger subsets of features, ranging from 1 to 25. Each configuration was evaluated over 20 repeated runs to ensure robustness. The feature order was based on the original sequence of the feature list, determined by the order in which the spectral bands and derived indices were introduced during data preparation, given in tables 2.2 and 2.3. This approach enabled an unbiased evaluation of model performance without making prior assumptions about the predictive power of individual features.

5.2.5.3.4. Sensitivity to label inaccuracies

ML classifiers are often trained on datasets where the labelled examples serve as ground truth. However, in real-world applications, some degree of label inaccuracy is inevitable due to human error or ambiguities in classification criteria. This experiment evaluates how different classifiers deal with label inaccuracies by systematically introducing noise into the training dataset and measuring the resulting performance degradation when tested on clean data. This methodology allowed for a systematic evaluation of classifier robustness to label noise, highlighting which models were more resilient to training inaccuracies.

To simulate labelling errors, a controlled proportion of training labels–ranging from 1% to 20%–was randomly altered, meaning that a fraction of correct labels was intentionally flipped to incorrect values. Once this alteration was performed, classifiers were then trained on the modified labels and validated against the original, uncorrupted dataset to quantify the impact of label noise on classification performance. Due to computational constraints, this experiment was conducted as a single-run analysis.

5.2.6. Application of classifiers

Finally, a comparative evaluation of the ability of the seven supervised ML classifiers was performed to detect supraglacial hydrological features in S2 imagery from two contrasting glaciological settings: NEGIS in 2019 (a high-melt year) and Watson in 2018 (a low-melt year). These classifiers were trained on the primary training dataset and optimized using the best-performing hyperparameters. Each classifier produced binary water/non-water masks for the respective regions, enabling us to explore similarities and differences in their detection of supraglacial hydrological features.

To assess classifier performance, both qualitative and quantitative evaluations were conducted. First, a visual comparison of classifier outputs against true-colour S2 imagery

was done, identifying areas of agreement and misclassification, such as the erroneous labelling of clouds or crevasses as meltwater. This qualitative analysis provided insight into classifier behaviour under different melt conditions and highlighted systematic over- or underestimation of melt extent.

To complement the visual assessment, classifier agreement was quantified using classification overlap maps, which illustrate regions of consensus and areas of increased divergence between different classifiers. Additionally, pairwise agreement using the Intersection over Union (IoU) metric was computed, measuring the extent to which classifiers detected the same meltwater pixels. These analyses provide a quantitative framework for evaluating classifier consistency, helping to identify methods that produced similar outputs across different conditions, though not necessarily confirming their absolute accuracy.

5.3. Results

This section presents the results of the meltwater classification analysis. It begins with the application of classifiers to real-world meltwater mapping scenarios in the NEGIS and Watson regions, providing visual outputs that offer an intuitive understanding of classifier performance and highlighting patterns of agreement and disagreement in meltwater detection. Following this, classifier performance is evaluated through repeated validations, cross-validation, and independent manual experiments. The analysis then explores the transferability of classifiers, both spatially and temporally, to assess their generalization across different regions and melt years. Next, the influence of training data characteristics is examined, including dataset size, input feature selection, the inclusion of spectral indices, and the impact of labelling inaccuracies. Finally, the section concludes with a ranking of classifiers, synthesizing performance metrics across all evaluation scenarios to identify the most robust models.

5.3.1. Visual Assessment of Classifier Outputs

Seven supervised ML classifiers were applied to S2 imagery from two contrasting GrIS scenarios: NEGIS in 2019 (a high-melt year) and Watson in 2018 (a low-melt year). These settings provide diverse glaciological and climatic conditions, enabling a robust test of each classifier's ability to detect and delineate SGLs, channels, and slush. This section presents a visual assessment of classifier outputs.

5.3.1.1. NEGIS

The NEGIS 2019 meltwater maps in Figure 5.2 show that all classifiers detect meltwater in plausible locations, consistently identifying slush, rivers, and SGLs. Slush formations appear particularly detailed, revealing distinct linear structures. However, some misclassifications are evident: all classifiers erroneously label a cloud area in the upper left as meltwater, and the MD classifier tends to misclassify crevasses as meltwater.

5.3.1.2. Watson

For Watson 2018, all classifiers exhibit comparable performance when assessed visually (Figure 5.3). While all methods appear to overpredict meltwater extent compared to the true-colour image they all reliably detect a network of SGLs and channels. Additionally, the cloudy region to the bottom right of the image is consistently classified as non-water by all methods.

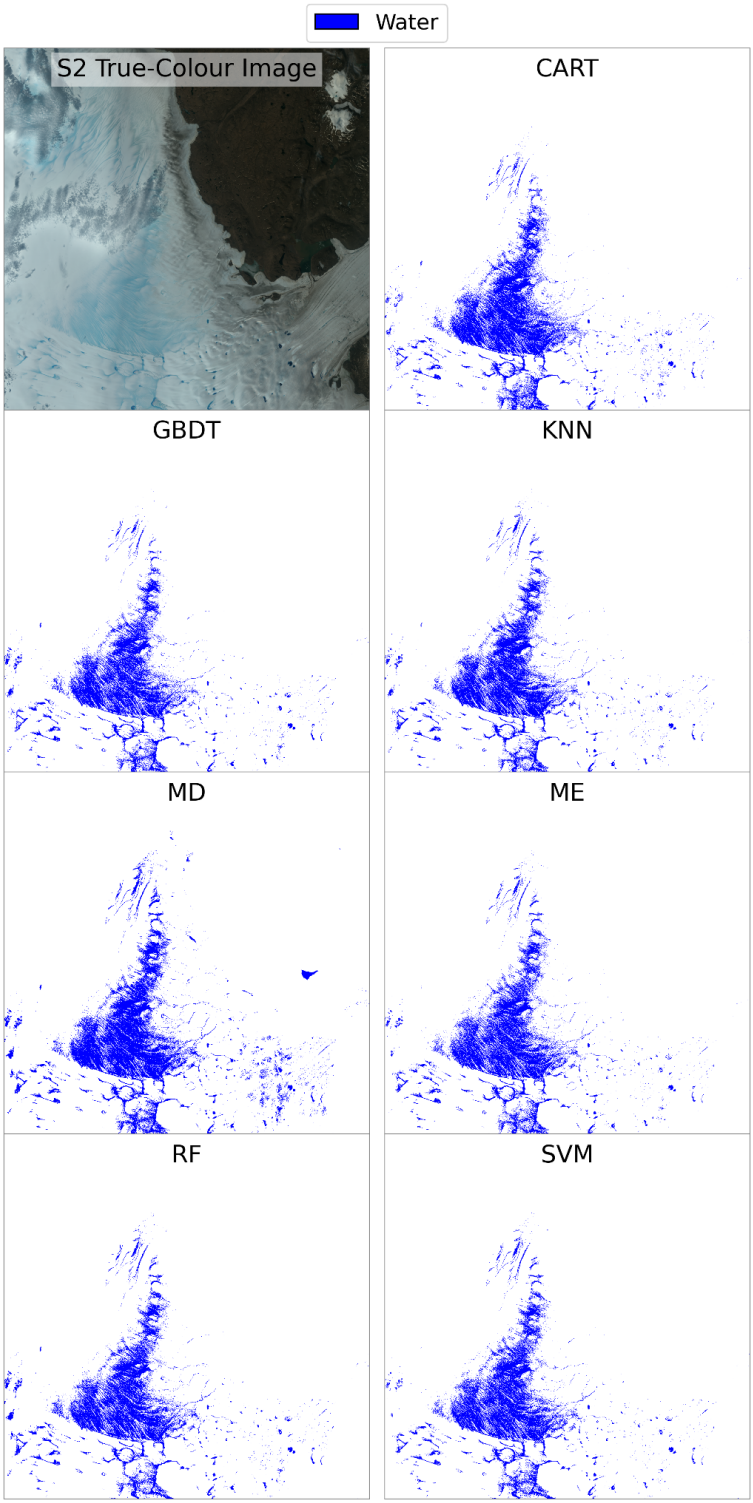

Figure 5.2: Comparison of classified meltwater maps generated by the seven classifiers for NEGIS 2019 alongside the S2 true-colour image for reference. Blue indicates water, and red represents non-water. White represents where the image was masked.

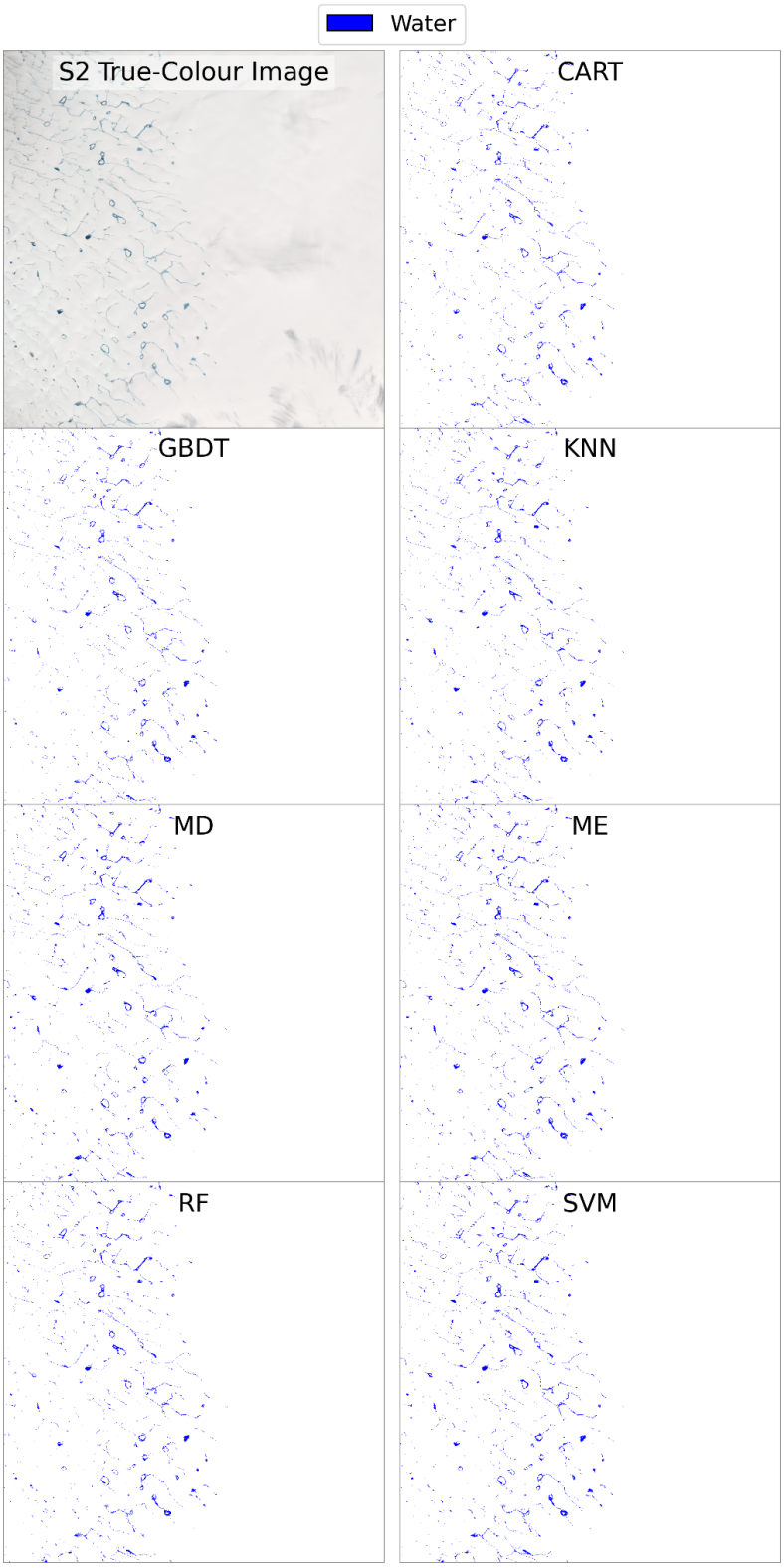

Figure 5.3: Comparison of classified meltwater maps generated by different classifiers (CART, GBDT, KNN, ME, MD, RF, and SVM) for Watson 2018 alongside the S2 true-colour image for reference. Blue indicates water, and red represents non-water.

5.3.2. Classifier Agreement

This section examines areas of consensus and disagreement among classifiers, quantifying the consistency of meltwater detection to evaluate the relative similarity of each method's outputs.

5.3.2.1. NEGIS

In regions characterized by clear and distinct surface types–such as dense slush fields, rivers, and SGLs–the classifiers exhibit a high level of agreement (i.e., all seven concur; Figure 5.4; Figure 5.5). This strong consensus suggests that well-defined features are readily detected by most methods. However, noticeable discrepancies emerge along feature boundaries where pixels are more scattered, leading to greater classification variability. Specific examples within Figure 5.4 and Figure 5.5 highlight these patterns. In panel (i), cloud-covered areas generally show strong classifier alignment, indicating that cloud pixels are consistently misclassified. In panel (ii), the linearity of slush fields is accurately captured by all classifiers. Panel (iii) shows that the linear slush features are well resolved, with good agreement between classifiers despite cloud cover. Panel (iv) demonstrates that areas with more diffuse or indistinct slush boundaries result in lower agreement between classifiers, suggesting that these gradual transition zones are more challenging to classify consistently. SGLs, as shown in panel (v), are also identified with high consensus; however, a single classifier (MD) uniquely misclassifies additional surrounding crevasses as water bodies.

Figure 5.6 presents the pairwise agreement between classifiers when applied to the NEGIS 2019 image, measured using IoU. This metric quantifies the proportion of shared water pixels between two classifiers relative to their total detected water pixels, ensuring a symmetric comparison. Assessing classifier agreement is important for evaluating the stability and reliability of meltwater classification methods, helping to identify which classifiers produce consistent results and which diverge. The highest agreement is observed between ME and SVM (0.94), followed closely by ME and RF (0.91) and RF and SVM (0.90), indicating strong consistency among these classifiers. In contrast, the lowest IoU values are recorded between CART and MD and between GBDT and MD (both 0.73), indicating notable disagreement in these pairs. More broadly, MD consistently exhibits lower pairwise agreement across multiple comparisons, supporting the observation that it diverges more than other classifiers in this setting.

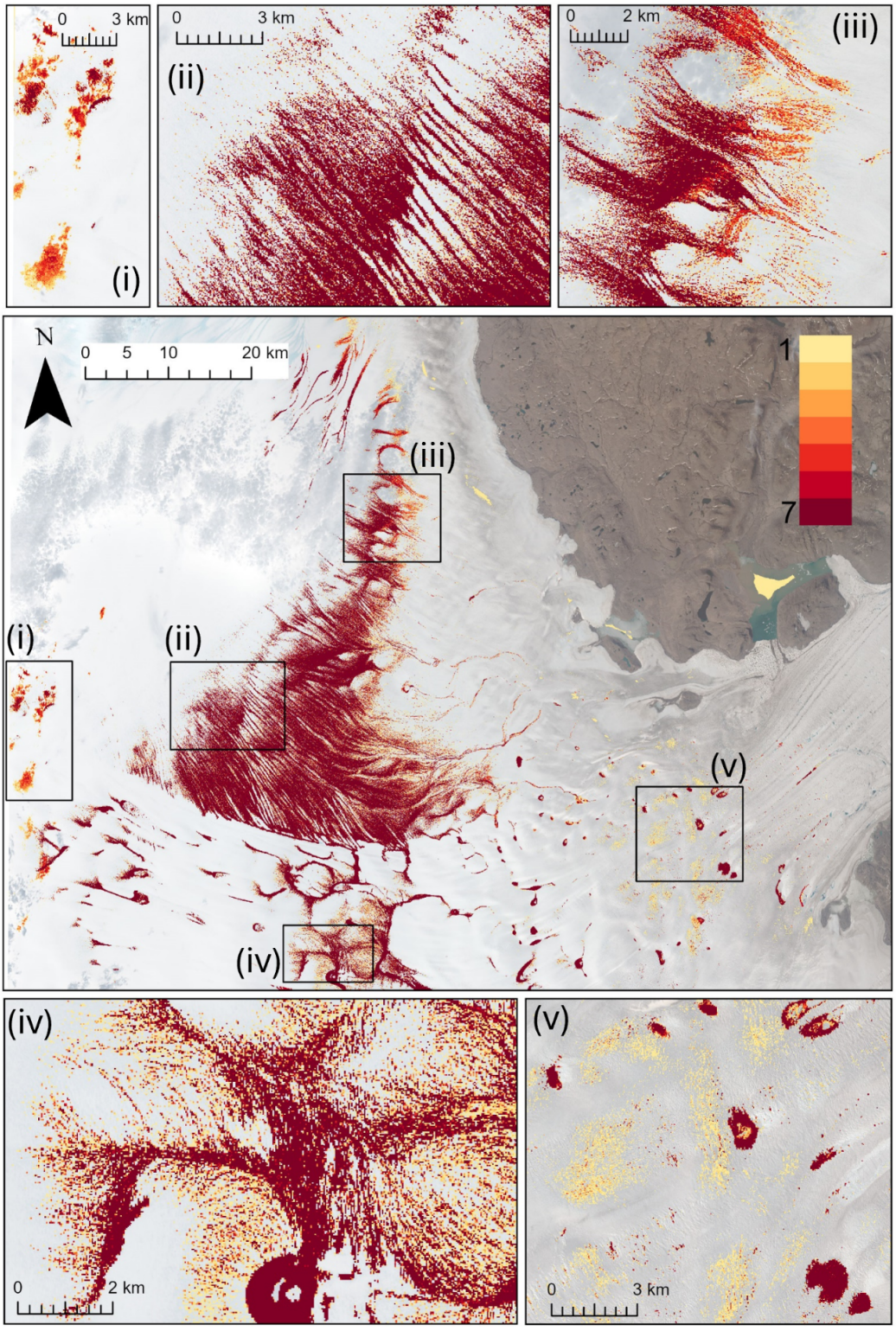

Figure 5.4: Classifier agreement map showing the overlap of classified meltwater features across all classifiers for NEGIS 13th July 2019. The values (1–7) represent the number of classifiers agreeing on the classification of each pixel. The corresponding true colour image panels are also shown on the following page.

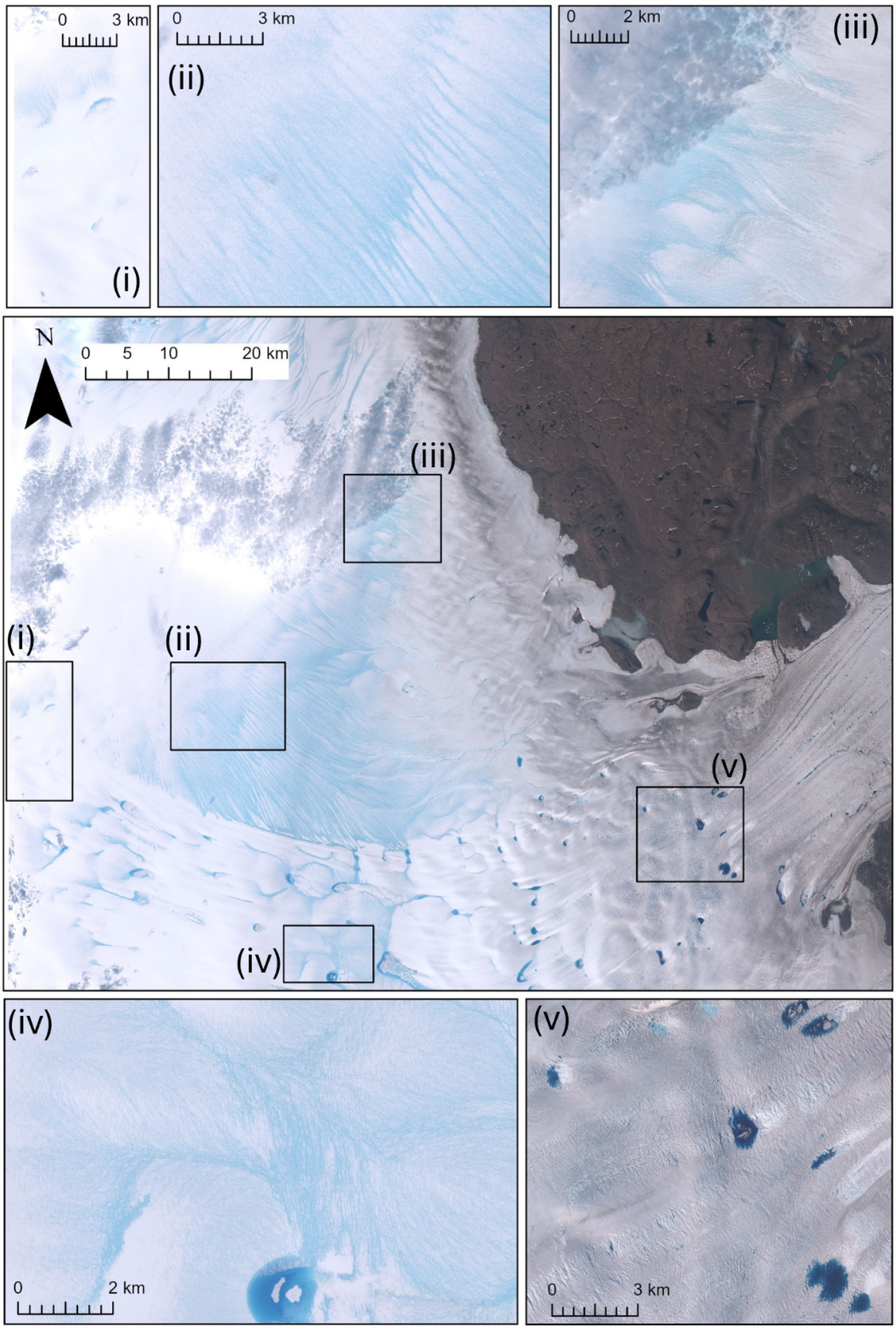

Figure 5.5: True colour image panels for Figure 5.4 (NEGIS 13th July 2019).

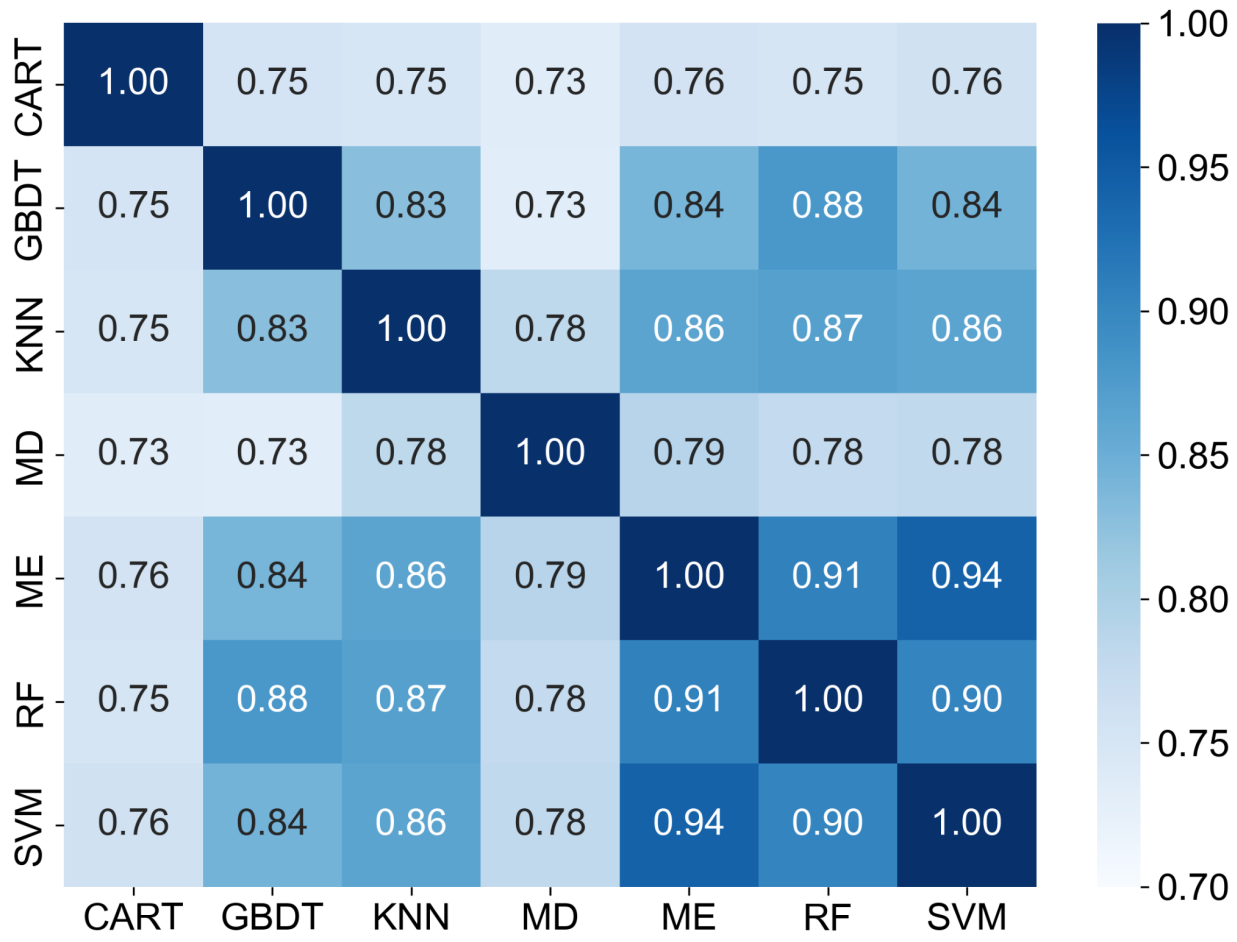

Figure 5.6: Pairwise agreement between classifiers applied to the NEGIS 2019 image, measured using IoU. This metric quantifies the proportion of shared water pixels between two classifiers relative to their total detected water pixels, providing a symmetric measure of classifier consistency. Darker blue indicates higher overlap, reflecting greater agreement between classifiers, while lighter blue represents lower overlap.

5.3.2.2. Watson

Figure 5.7 and 5.8 shows that classifiers generally agree on the most distinct SGLs and meltwater channels in the Watson region during the low-melt year of 2018. Although, there is less agreement between classifiers in frozen parts of SGLs. In panel (i), a partially frozen SGL is visible, with liquid water in the centre and frozen boundaries. Classifiers show strong agreement in the SGL's liquid region and along linear slushy streams connecting SGLs, but agreement decreases at the frozen edges. Similarly, in panel (ii), slushy streams linking SGLs–some with ice lids–are well-detected, with high agreement on these channels but slightly lower agreement on SGLs. panel (iii) highlights narrow meltwater channels, which are consistently identified across classifiers. However, agreement decreases in the partially frozen SGL into which these channels flow. Finally, panel (iv) shows isolated frozen SGLs, one with small, attached streams. Here, classifier agreement is strong.

Figure 5.9 presents the pairwise agreement between classifiers when applied to the Watson 2018 image, measured using IoU. The Watson IoU values are generally lower than those observed for NEGIS 2019, suggesting greater variability in classification agreement for Watson 2018. The highest agreement is observed between ME and SVM (0.93), followed by RF and GBDT (0.85), indicating strong consistency among these classifiers. In contrast, the lowest IoU value, 0.73 for CART and KNN, reflects the greatest classification discrepancies.

Comparing the two regions in contrasting melt years, ME and SVM consistently demonstrate the highest agreement, indicating a strong and stable alignment between these classifiers across contrasting glaciological settings and melt conditions. In contrast, the classifiers contributing to the lowest pairwise agreement differ between regions–MD in NEGIS and KNN in Watson.

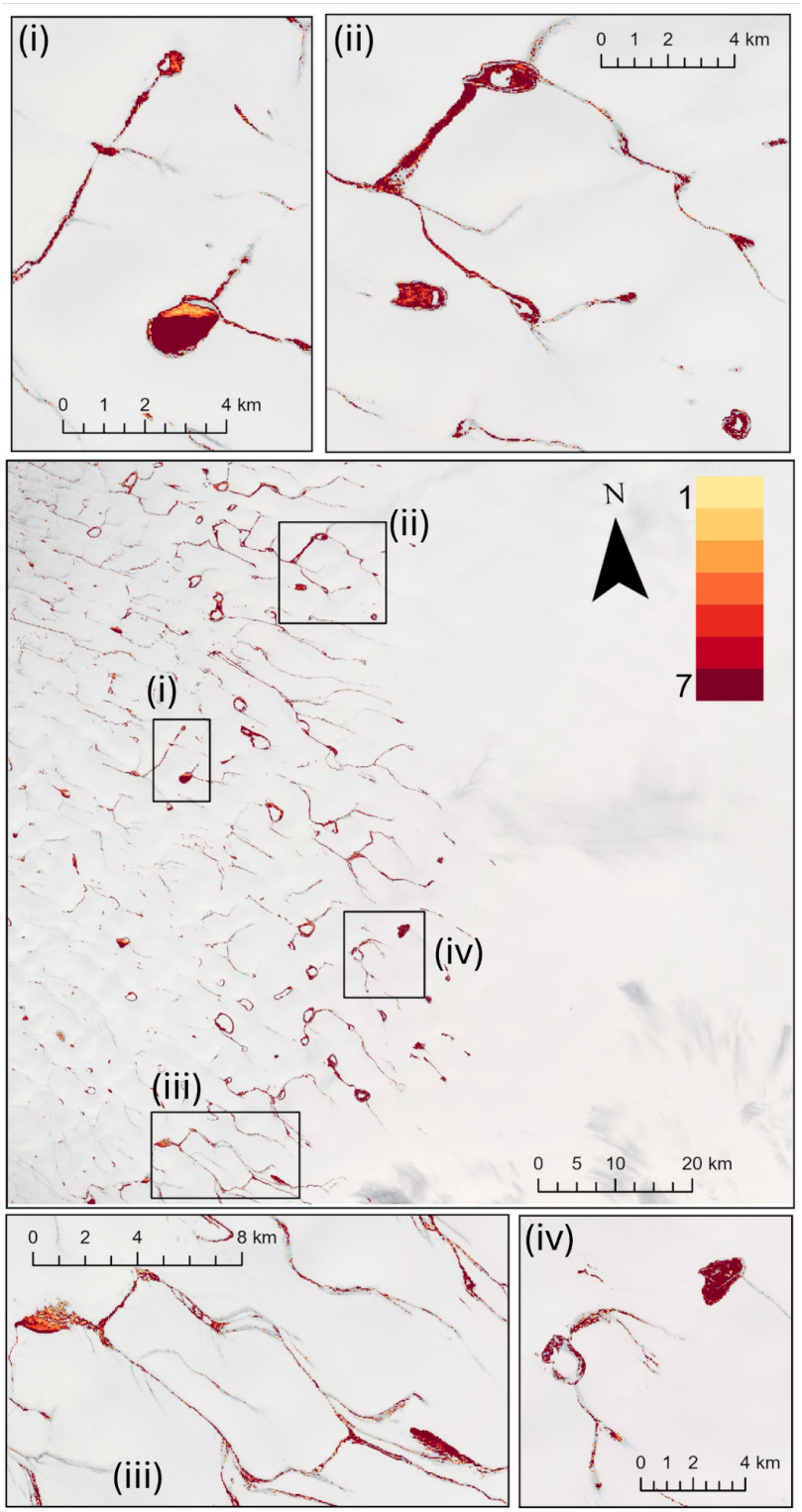

Figure 5.7: Classifier agreement map showing the overlap of classified meltwater features across all classifiers for Watson 30th July 2018. The values (1–7) represent the number of classifiers agreeing on the classification of each pixel. The corresponding true colour image panels are also shown on the following page.

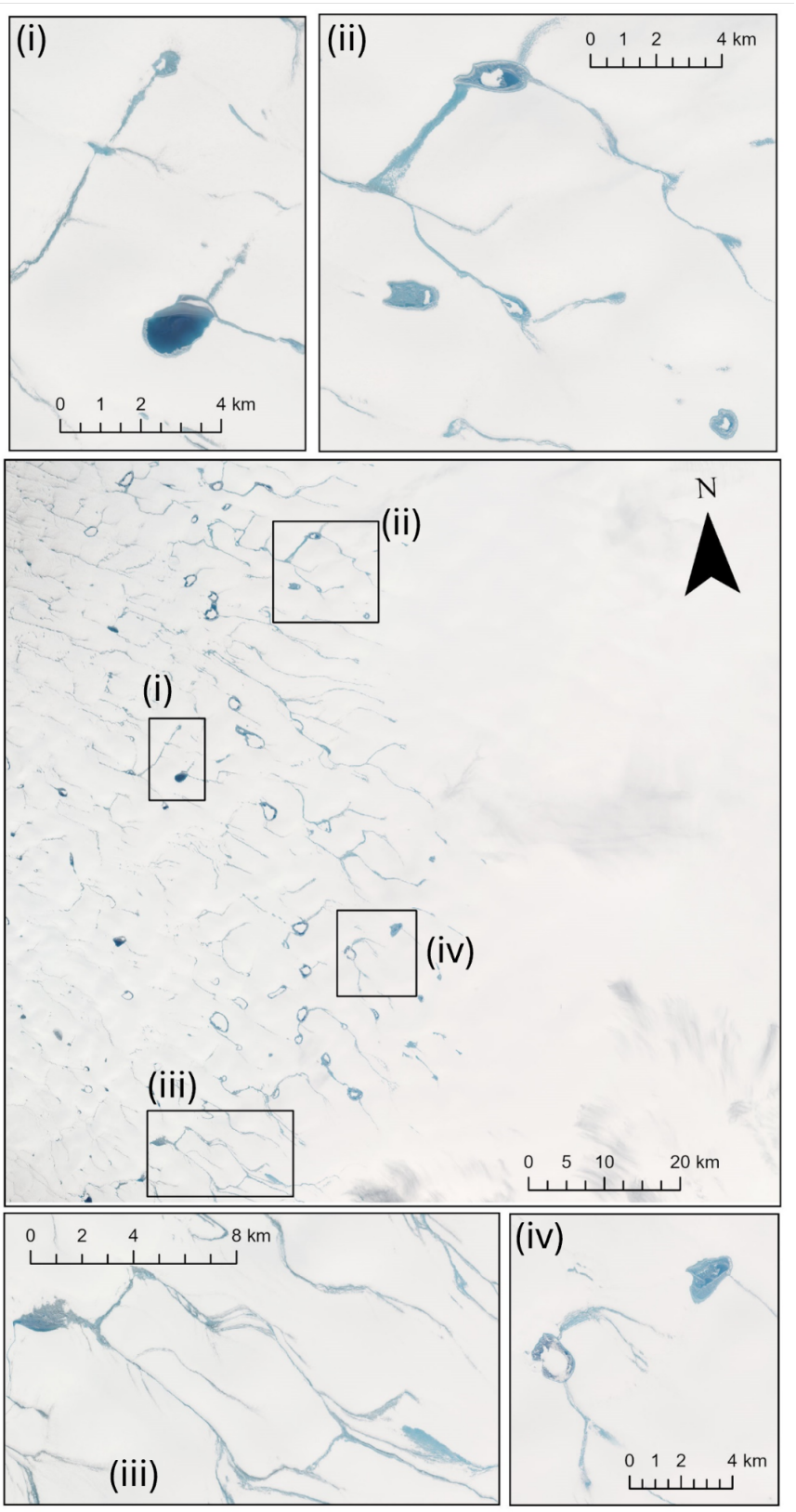

Figure 5.8: True colour image panels for Figure 5.7 (Watson 30th July 2018).

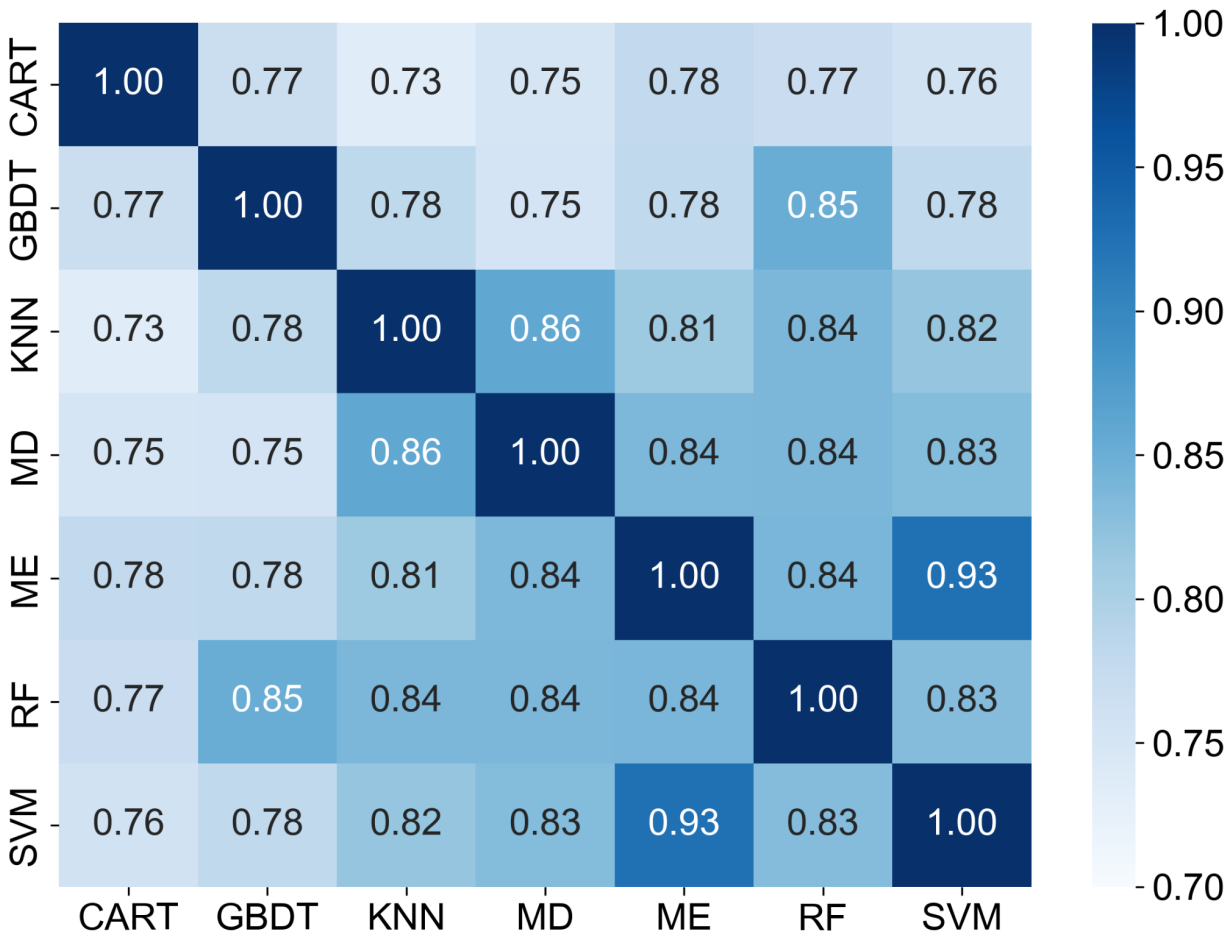

Figure 5.9: Pairwise agreement between classifiers applied to the Watson 2018 image, measured using IoU. Darker blue indicates higher overlap, reflecting greater agreement between classifiers, while lighter blue represents lower overlap.

5.3.3 Computational efficiency

Computational efficiency is a key consideration when selecting classifiers for large-scale or operational monitoring, where processing time may constrain feasibility. To assess this, the total execution time of each classifier was recorded during their application to S2 imagery from NEGIS and Watson (Table 5.5). The computational performance of classifiers varied considerably, with execution times ranging from under 5 seconds to over 50 seconds. ME (50.4 seconds) and MD (36.2 seconds) were the slowest, while GBDT (3.9 seconds) and RF (3.9 seconds) were the fastest, reflecting the efficiency of optimized tree-based processing. SVM (4.2 seconds) and KNN (5.2 seconds) showed moderate computational demand, whereas CART (11.8 seconds) was slower than the other decision tree models (RF and GBDT). This represents an order of magnitude difference between the fastest and slowest classifiers.

To evaluate scalability, Table 5.5 presents estimated processing times per image and projected totals for a GrIS periphery snapshot (~300 images) and a full melt season (~5400 images). These figures illustrate the practicality of each classifier in operational contexts, with RF and GBDT offering the greatest potential for time-efficient large-scale application.

Table 5.5. Estimated classifier execution times based on validation runs over two S2 images (NEGIS and Watson). Time per image was derived by halving the total execution time. Projections are shown for a GrIS-wide periphery snapshot (~300 images) and a full melt season (~5400 images).

Classifier	Time per image (s)	Time for snapshot (~300 images)	Time for a season (~5400 images)
RF	1.95	585 (9.75 min)	10,530 (2.9 hr)
GBDT	1.95	585 (9.75 min)	10,530 (2.9 hr)
SVM	2.10	630 (10.5 min)	11,340 (3.15 hr)
KNN	2.60	780 (13 min)	14,040 (3.9 hr)
CART	5.90	1,770 (29.5 min)	31,860 (8.85 hr)
MD	18.10	5,430 (1.5 hr)	97,740 (27.15 hr)
ME	25.20	7,560 (2.1 hr)	136,080 (37.8 hr)

5.3.4. Classifier performance evaluation

This section presents the results from the different evaluation methods to highlight how each classifier performs under various testing conditions. Classifier performance evaluation is important to understand how well ML models perform, not just in terms of raw accuracy, but also regarding their stability, generalization, and real-world applicability. By employing multiple evaluation methods–repeated validation, cross-validation, and comparison to manual datasets– models that are not only technically proficient but also robust under different data conditions can be identified. This multi-faceted approach helps uncover potential issues like overfitting, sensitivity to data variability, and performance consistency across diverse datasets.

5.3.4.1. Repeated classifier

This assessment evaluates the stability and robustness of classifiers when exposed to different random splits of the primary training dataset (Section 5.2.3.1). The primary training dataset includes labelled surface water and non-surface water pixels sampled from 91 S2 images, acquired between 2017 and 2020 across all six major drainage basins of the GrIS (Figure 5.1). Repeated validation provides insights into how consistently each model performs under varying data partitions, helping to identify classifiers that are resilient to data variability.

Most classifiers achieve accuracies between 0.95 and 0.99 (Figure 5.10), demonstrating stable performance. MD is the clear outlier, underperforming with an accuracy of 0.78 ± 0.01 and a Kappa of 0.56 ± 0.01, approximately 20% lower than the top classifiers. The ± values represent standard deviation, with lower values indicating more consistent performance. GBDT is the top-performing classifier, achieving the highest accuracy (0.99 ± 0.004) and Kappa (0.99 ± 0.004), with the lowest variability. RF follows with an accuracy of 0.97 ± 0.006 and a Kappa of 0.94 ± 0.007, while CART records an accuracy of 0.96 ± 0.008 and a Kappa of 0.93 ± 0.008.

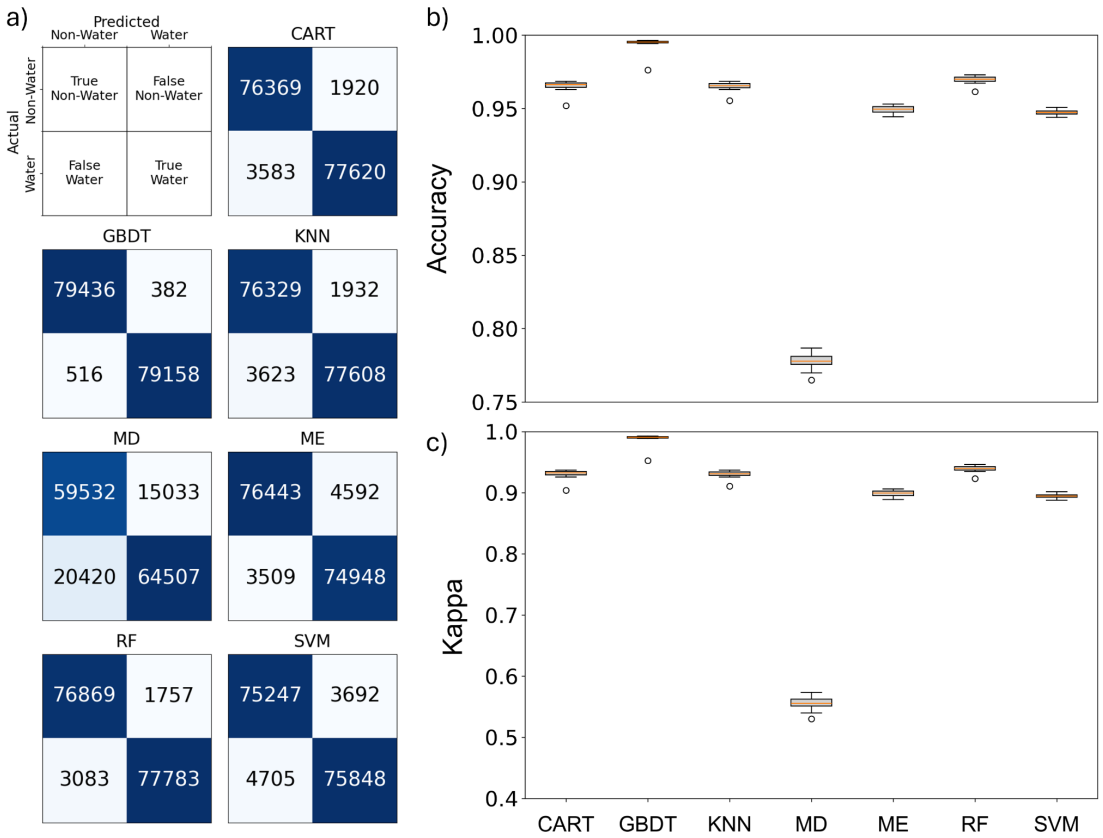

Figure 5.10: Results of the repeated classifier validation using the Primary training and validation dataset. a) Cumulative confusion matrices summarizing classification outcomes across 20 iterations. b) Accuracy distributions showing classifier performance consistency. c) Kappa coefficient distributions illustrating agreement with the main validation dataset. The orange horizontal line within each box represents the median value, indicating the central tendency of the classifier's performance. The box spans the interquartile range (IQR), representing the middle 50% of the data (from the 25th to the 75th percentile). The whiskers extend to 1.5 times the IQR, showing the range of most data points, while individual circles represent outliers, indicating performance deviations across iterations.

5.3.4.2. Cross-validation

In this assessment, the generalization capability of classifiers was evaluated using cross-validation. The cross-validation was performed on the primary dataset, which includes labelled S2 pixels between 2017 and 2020, spanning all six major drainage basins of the GrIS. This experiment is designed to test how well classifiers perform when exposed to different subsets of data, providing a measure of their ability to generalize beyond the specific conditions seen during training. Unlike single-split validation, cross-validation ensures that each data point is used for both training and validation, reducing the risk of biased results.

As shown in Figure 5.11, classifier accuracy generally ranges from 0.95 to 0.99, with MD as a clear outlier, achieving an accuracy of 0.78 ± 0.0055 and a Kappa of 0.56 ± 0.011– approximately 20% lower than the top classifiers. GBDT is the top-performing classifier, achieving the highest accuracy (0.99 ± 0.0009) and Kappa (0.99 ± 0.0018) with the lowest variability. RF and CART perform similarly (0.97 ± 0.0021 and 0.97 ± 0.0023 accuracy; 0.94 ± 0.0042 and 0.93 ± 0.0045 Kappa).

When comparing these results with the repeated validation outcomes discussed in Section 5.3.3.1, the performance patterns remain consistent. GBDT and RF continue to outperform other classifiers, while MD consistently underperforms. Accuracy and Kappa values remain nearly identical across both validation methods.

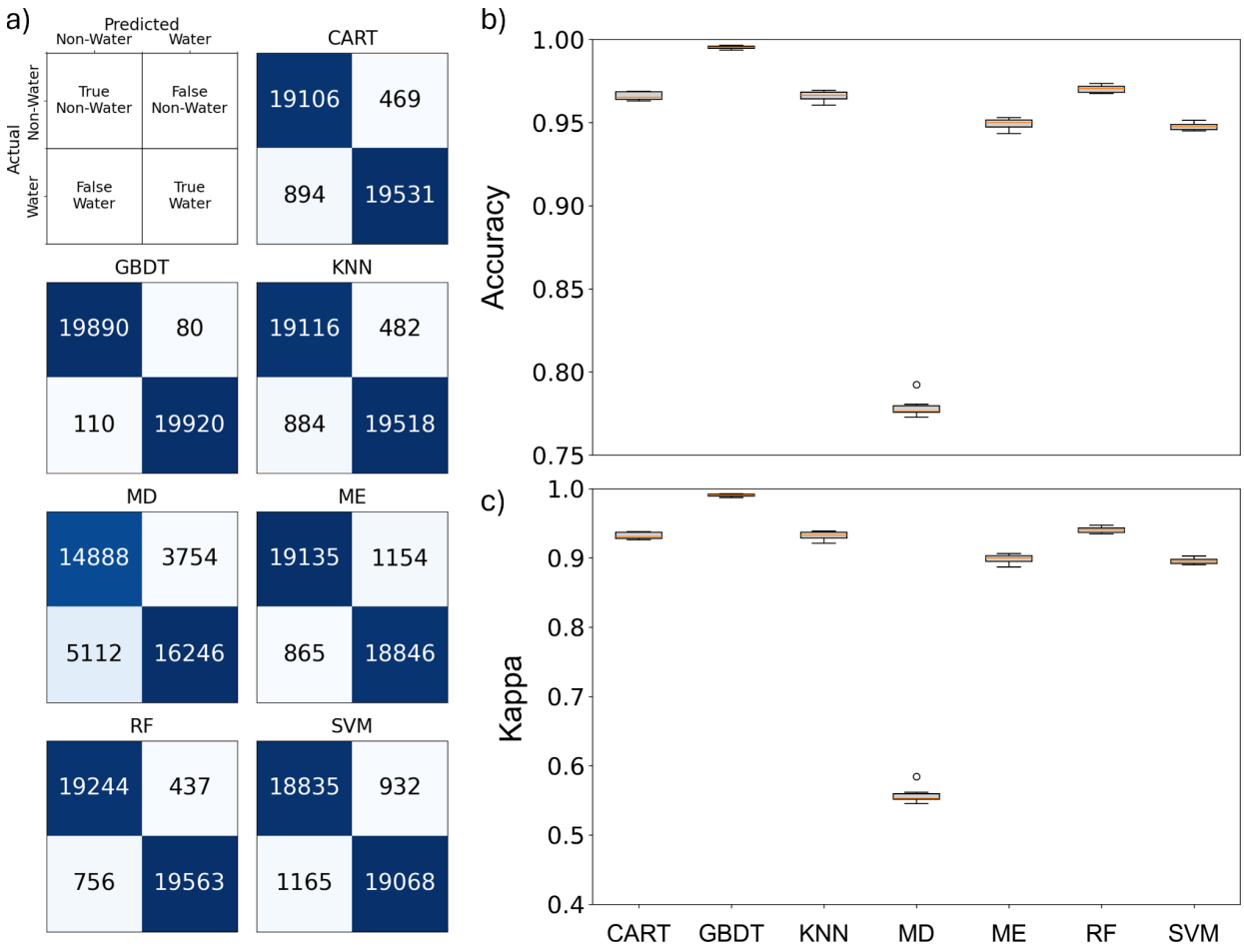

Figure 5.11: Results of the k-fold validation using the Primary training and validation dataset. a) Cumulative confusion matrices summarizing classification outcomes across 20 iterations. b) Accuracy distributions showing classifier performance consistency. c) Kappa coefficient distributions illustrating agreement with the main validation dataset. Note: The cumulative confusion matrices reflect the summed results across all folds, which differ from the 80/20 validation totals due to the nature of the k-fold cross-validation approach, where each fold is used for validation exactly once. The orange horizontal line within each box represents the median value, indicating the central tendency of the classifier's performance. The box spans the IQR, representing the middle 50% of the data (from the 25th to the 75th percentile). The whiskers extend to 1.5 times the IQR, showing the range of most data points, while individual circles represent outliers, indicating performance deviations across iterations.

5.3.4.3. Comparison to manual datasets

While repeated and cross-validation assess model stability and sensitivity to data variability within the primary dataset, comparison to manual datasets provides a more stringent test of generalization, revealing how well classifiers perform on previously unseen regions and melt conditions. To complement these internal evaluations, independent manual verification datasets were used, as described in Section 5.2.3.2. Classifiers trained on the primary dataset were tested on manually sampled points from independent images, with the validation process repeated 20 times to ensure robust performance estimates. This approach provides an assessment of the model's real-world performance by testing it on images that it has never encountered during training. The manual verification dataset was made from two images not trained on, with data derived using different methods to the primary dataset: one from the Watson region, captured in 2018 (a low melt year), and another from NEGIS, captured in August 2019 (a high melt year).

5.3.4.3.1. NEGIS

In evaluating classifier performance using manually derived datasets from NEGIS (Figure 5.12), accuracy scores ranging from 0.91 to 0.94 were observed. RF and ME consistently outperformed other classifiers, achieving accuracy rates of 0.94 ± 0.001 and 0.93 ± 0.001, respectively, with both Kappa values of 0.86 ± 0.001. GBDT and CART also performed well, both reaching 0.93 ± 0.002 accuracy with Kappa values close to 0.86 ± 0.001 and 0.85 ± 0.001, though they exhibited slightly more variability. SVM demonstrated the weakest performance, with an accuracy of 0.91 ± 0.0001 and a Kappa of 0.81 ± 0.0002.

When comparing these results to the automated validation outcomes of the repeated classifier (Section 5.3.3.1) and cross-validation (Section 5.3.3.2), performance patterns remain consistent in some aspects but diverge in others. GBDT and RF continue to outperform other classifiers, demonstrating strong generalization and low variability across datasets. MD consistently shows poor performance, aligning with its underperformance in earlier tests. SVM, which performed moderately in prior tests, shows weaker results in manual validation. ME shows strong performance in manual NEGIS, comparable to RF, even though ME had lower accuracy scores in earlier automated validations.

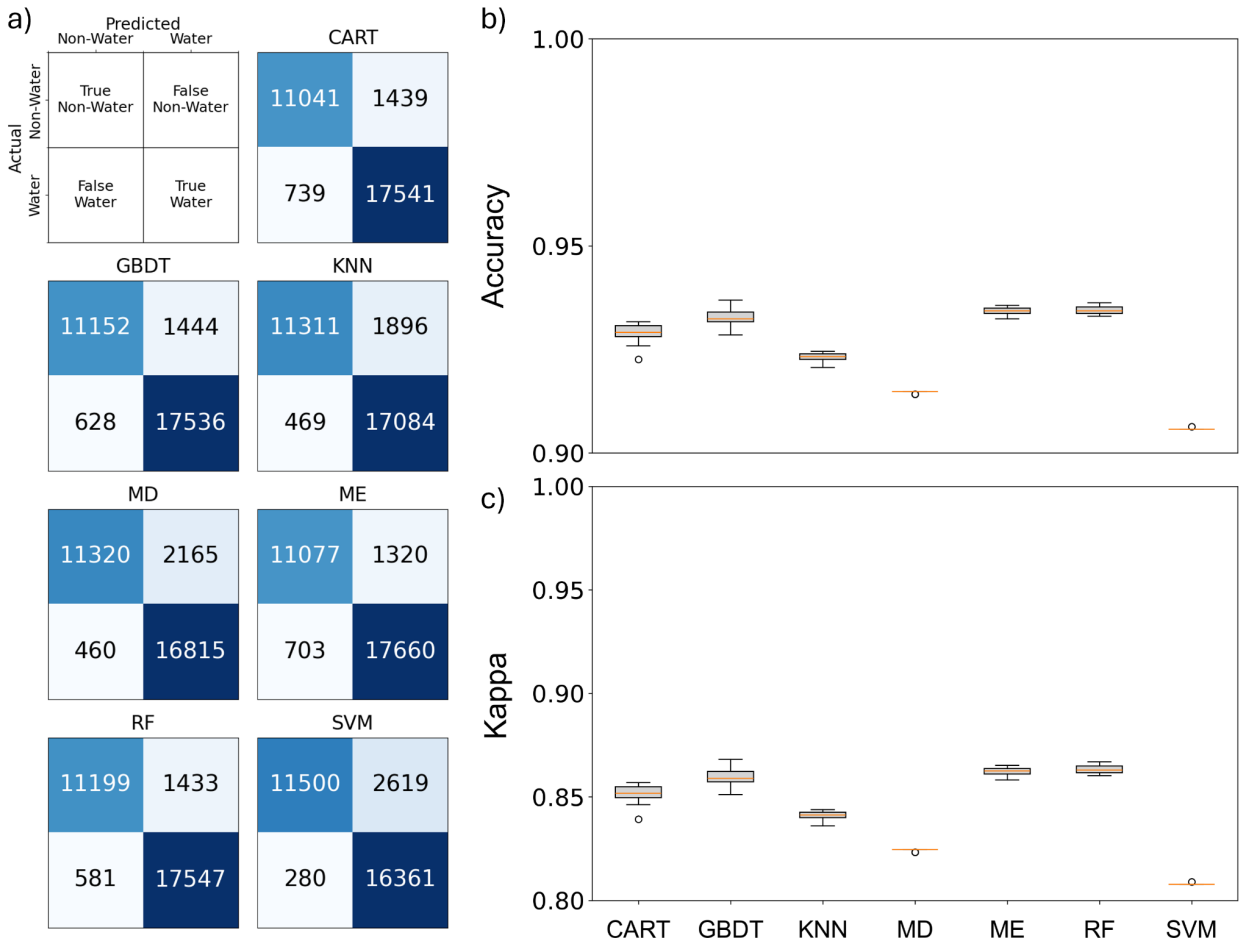

Figure 5.12: Results of the repeated classifier using manually derived data from NEGIS for validation. a) Cumulative confusion matrices summarizing classification outcomes across 20 iterations. b) Accuracy distributions showing classifier performance consistency. c) Kappa coefficient distributions illustrating agreement with the main validation dataset. The orange horizontal line within each box represents the median value, indicating the central tendency of the classifier's performance. The box spans the IQR, representing the middle 50% of the data (from the 25th to the 75th percentile). The whiskers extend to 1.5 times the IQR, showing the range of most data points, while individual circles represent outliers, indicating performance deviations across iterations.

5.3.4.3.2. Watson

The classifier performance, validated against manually derived Watson data (Figure 5.13), showed accuracies ranging from 0.70 to 0.87. Most classifiers achieved moderate accuracy, with the notable exception of MD, which underperformed with an accuracy of 0.70 ± 0.001–approximately 12–17% lower than the others. CART achieved the highest accuracy at 0.87 ± 0.02 with a Kappa of 0.75 ± 0.04, indicating strong classification performance, although with relatively large variability. Notably, RF ranked as the third-lowest performer, with moderate accuracy (0.82) and Kappa (0.65), diverging from its consistently strong performance in previous experiments.

Most classifiers are highly sensitive to meltwater features as shown by the confusion matrices where false negatives are 0% (except for ME). However, this comes at the cost of increased false positives, particularly for MD and KNN, which misclassify 30% and 17% of non-meltwater pixels as meltwater, respectively. This trade-off means that while these classifiers effectively capture meltwater features, they also overestimate meltwater extent by incorrectly labelling non-meltwater areas. The fact that this overestimation trend is observed across multiple classifiers suggests a systematic bias stemming from the training and validation data, rather than from classifier-specific behaviour.

When comparing these results to those obtained from the high melt year (manual NEGIS dataset), a few key differences emerge. In the low melt year (manual Watson dataset), accuracy ranged from 0.70 to 0.87, whereas NEGIS classifiers achieved a higher accuracy range of 0.91 to 0.94. This difference may reflect the improved detectability of abundant and spectrally distinct meltwater features during high melt conditions. However, while sparse meltwater in the low melt year presents challenges–such as fewer training examples and reduced spectral contrast with surrounding surfaces–it could also reduce ambiguity in boundary delineation due to less saturated firn and more stable surface conditions. The reduced accuracy in Watson suggests that, in this case, the limited spectral distinctiveness of meltwater features outweighed any potential advantages.

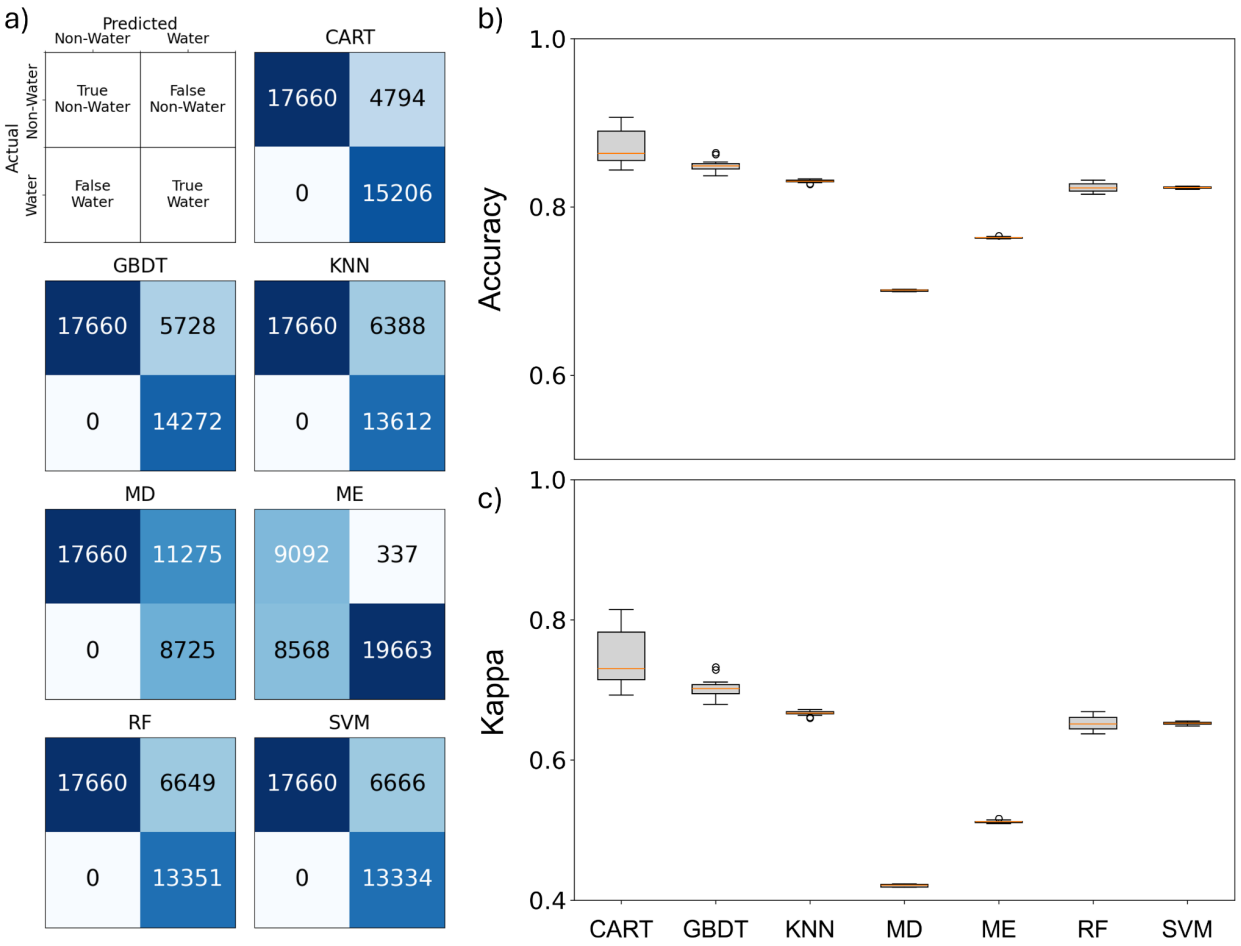

Figure 5.13: Results of the repeated classifier using manually derived data from Watson for validation. a) Cumulative confusion matrices summarizing classification outcomes across 20 iterations. b) Accuracy distributions c) Kappa coefficient distributions. The orange horizontal line within each box represents the median value, indicating the central tendency of the classifier's performance. The box spans the IQR, representing the middle 50% of the data (from the 25th to the 75th percentile). The whiskers extend to 1.5 times the IQR, showing the range of most data points, while individual circles represent outliers, indicating performance deviations across iterations.

Classifier performance was consistently higher in repeated and cross-validation tests (0.97–0.99 across classifiers) than in the independent manual validation datasets, where accuracy dropped to 0.91–0.94 for NEGIS (Figure 5.12) and 0.70–0.87 for Watson (Figure 5.13). This discrepancy reflects the difference between in-sample validation and independent testing: repeated and cross-validation draw from the same data distribution as the training set, often inflating metrics due to exposure to familiar spectral and spatial patterns. In contrast, the manual validation datasets consist of entirely separate images, introducing novel conditions and providing a more rigorous test of model generalizability.

Despite high automated accuracy, classifiers like RF and GBDT exhibited reduced accuracy and greater variability on the manual datasets. This suggests their strong performance in repeated and cross-validation does not fully translate to unseen imagery. Inspection of confusion matrices (Figures 5.12a and 5.13a) indicates that most errors stem from false positives, with non-water pixels incorrectly identified as water. This issue is most pronounced in SVM and MD, while top-performing classifiers like RF and GBDT maintain relatively low false negative rates, indicating they still reliably detect true water pixels under unfamiliar conditions.

5.3.5. Transferability analysis

In these experiments, we assessed the spatial and temporal transferability of classifiers by filtering the primary dataset accordingly. For spatial transferability, classifiers were trained on data from one region – either NEGIS or Watson – and tested on the other across all years. This simulates applying a model trained in one geographic area to a different, unseen area. For temporal transferability, classifiers were trained on data from either 2018 (a low melt year) or 2019 (a high melt year) and tested on the other across all regions. This setup evaluates how well models generalise across contrasting melt conditions. Together, these tests provide insight into classifier adaptability under varying spatial and temporal scenarios, supporting informed model selection for real-world applications.

5.3.5.1. Spatial transferability

Overall, classifiers performed better when trained on NEGIS and tested on Watson, achieving accuracies exceeding 0.9. In contrast, training on Watson and testing on NEGIS resulted in lower performance, with accuracies averaging closer to 0.8 (Figure 5.14).

In the NEGIS to Watson transfer, RF was the strongest performer, achieving the highest accuracy (0.96 ± 0.009), outperforming all other classifiers. SVM (0.96 ± 0.01) and GBDT (0.95 ± 0.01) followed closely, demonstrating strong generalization across regions. In contrast, ME performed the worst, achieving only 0.78 ± 0.013.

For the Watson to NEGIS transfer, GBDT achieved the highest accuracy (0.91 ± 0.01), with RF following closely (0.90 ± 0.01). However, SVM (0.75 ± 0.01) and KNN (0.78 ± 0.019) experienced the largest performance declines compared to their NEGIS to Watson results. ME remained the weakest performer (0.66 ± 0.009), reinforcing its poor transferability across spatial domains.

Among all classifiers, CART exhibited the highest variability, with a standard deviation of 0.052 for NEGIS to Watson and 0.020 for Watson to NEGIS, highlighting its inconsistent performance. RF was the most stable for NEGIS to Watson, showing the lowest variability (0.0089), while ME exhibited the least variability for Watson to NEGIS (0.009), despite its poor performance.

RF and GBDT were the most transferable classifiers, both with a combined average accuracy of 0.93 across both transfer directions. ME was the least transferable, with a low combined accuracies of 0.72 and larger performance drops when applied to new areas.

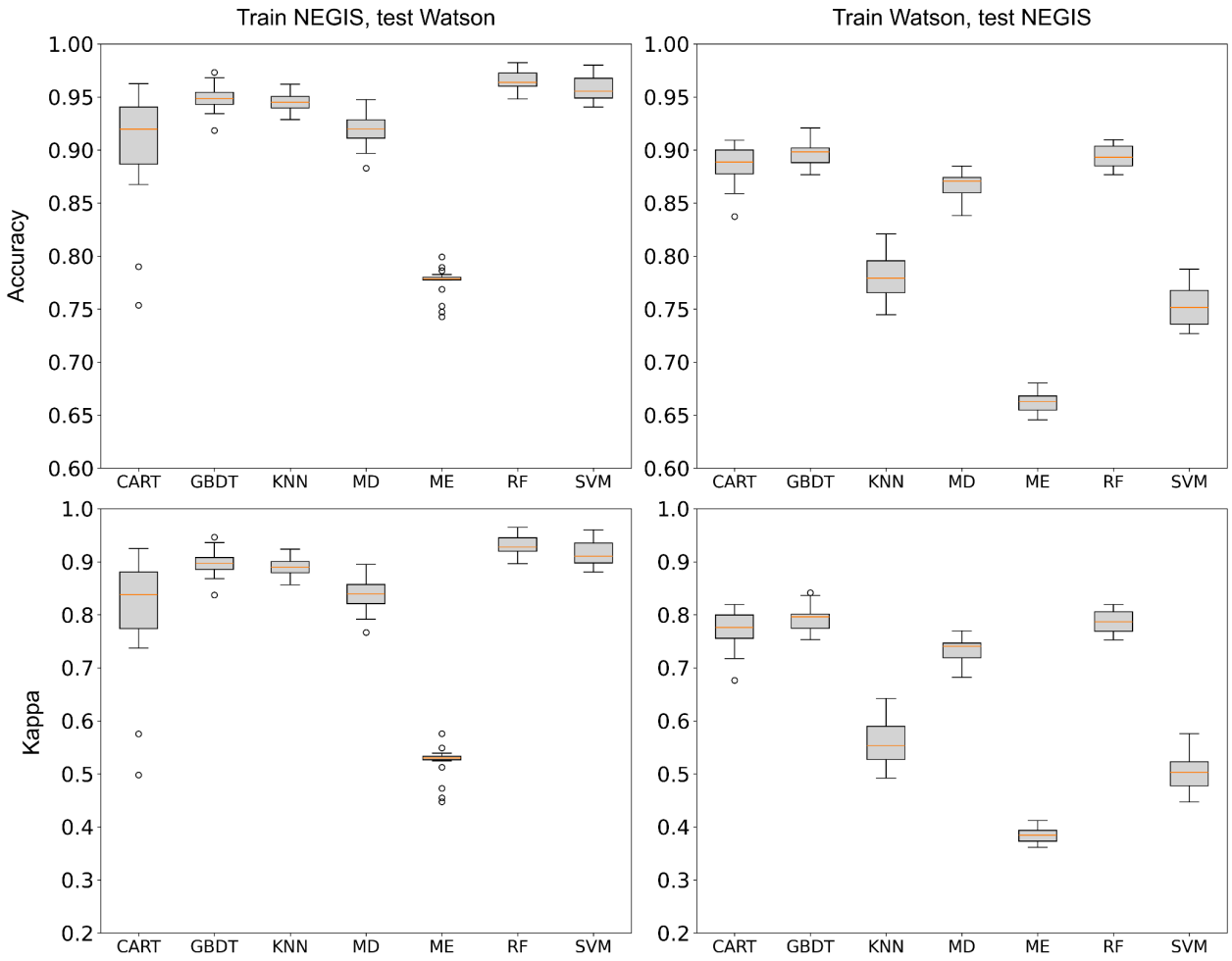

Figure 5.14: Results from 20 repeated runs evaluating spatial transfer scenarios. Accuracy (top) and Kappa (bottom) scores are displayed for models trained on NEGIS and tested on Watson (left) and models trained on Watson and tested on NEGIS (right).

Classification errors varied markedly between the two spatial transfer directions (Figure 5.15). When trained on NEGIS and tested on Watson, classifiers such as CART and KNN produced notably more false positives–for instance, CART misclassified 626 non-water pixels as water, while KNN recorded 333 false positives–indicating a tendency to over-predict water presence in the Watson region. This overprediction pattern was consistent across most classifiers in this transfer direction, with false negatives remaining relatively low (e.g., RF: 72 false negatives, GBDT: 71). In contrast, classifiers trained on Watson and tested on NEGIS showed a reversal in error profile, with substantially more false negatives. CART, for example, produced 752 false negatives–over four times more than its false positives–while SVM misclassified 1903 water pixels as non-water, reflecting a consistent under-prediction of water features in the NEGIS environment.

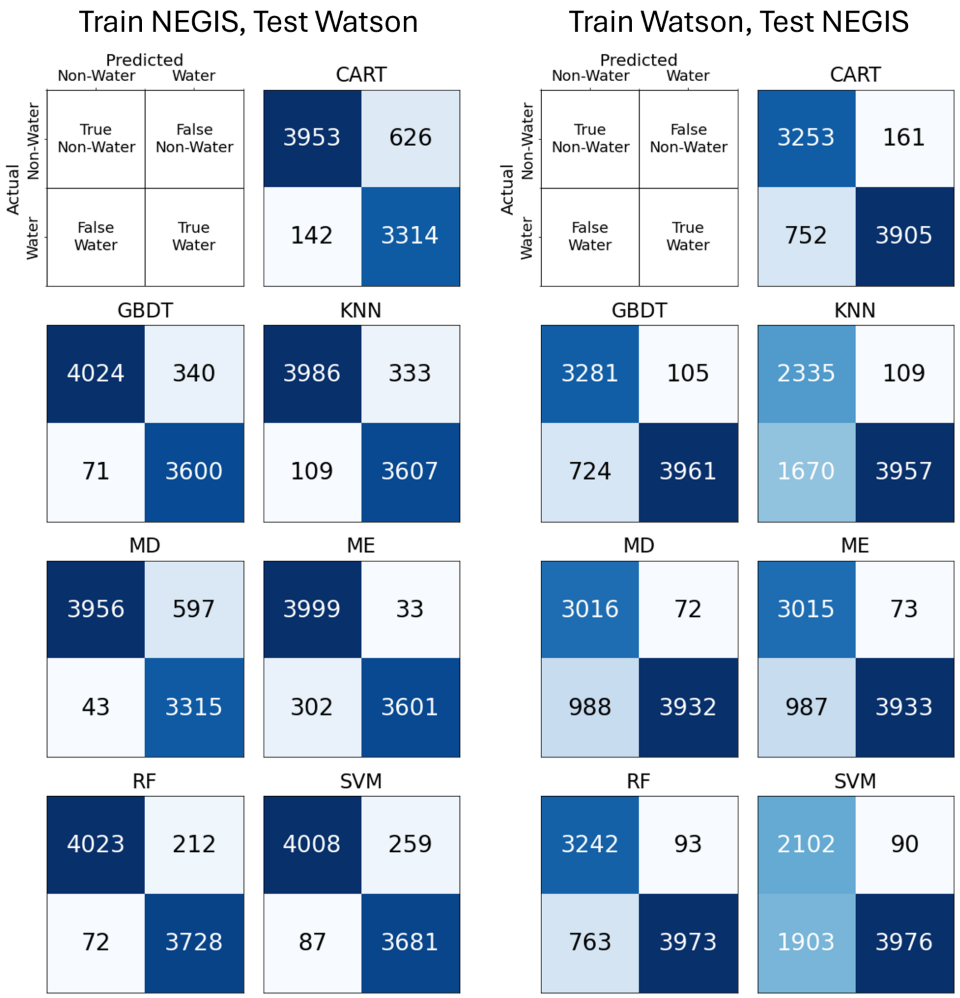

Figure 5.15: Cumulative confusion matrices summarizing classification outcomes from 20 repeated runs across two spatial transfer scenarios: models trained on NEGIS and tested on Watson (left) and models trained on Watson and tested on NEGIS (right).

5.3.5.2. Temporal transferability

The temporal transferability of classifiers was assessed by training on one year (2018 or 2019) and testing on the other (Figure 5.16). Overall, classifiers performed slightly better when trained on 2019 and tested on 2018 data, with an average accuracy of 0.96 compared to 0.94 for the reverse direction (2018 to 2019). However, the difference in performance between the two directions is minimal, indicating that classifiers can generalize well across years with only a small variation in accuracy.

When training on 2018 and testing on 2019 data, classifier performance varied. RF maintained strong and consistent accuracy at 0.96 ± 0.0007, followed closely by GBDT at 0.96 ± 0.0012. Both classifiers exhibited low standard deviation, indicating stable performance across iterations. In contrast, MD struggled in this transfer scenario, achieving the lowest accuracy (0.86 ± 0.0033) with the highest variability, reflecting its inconsistency in

adapting to changing melt conditions.

In the reverse direction, training on 2019 and testing on 2018 data, SVM emerged as the top performer with the highest accuracy (0.98 ± 0.0003) and the lowest standard deviation, suggesting good stability across temporal shifts. RF (0.96 ± 0.0007) and GBDT (0.96 ± 0.0011) maintained strong performance with similarly low variability, reinforcing their robustness in generalizing across years. MD remained the weakest performer (0.91 ± 0.0032), showing the highest variability among classifiers, further highlighting its poor adaptability to varying melt conditions.

Across both temporal transfer directions, SVM emerged as the most transferable classifier, achieving the highest average accuracy (0.97) and the lowest variability, demonstrating strong generalization across years. RF, GBDT, ME, and KNN all performed similarly (0.96 average accuracy), maintaining strong generalization but with slightly lower accuracy compared to SVM. In contrast, MD was the least transferable, with the lowest average accuracy (0.88) and the highest variability, indicating its difficulty in adapting to different temporal conditions.

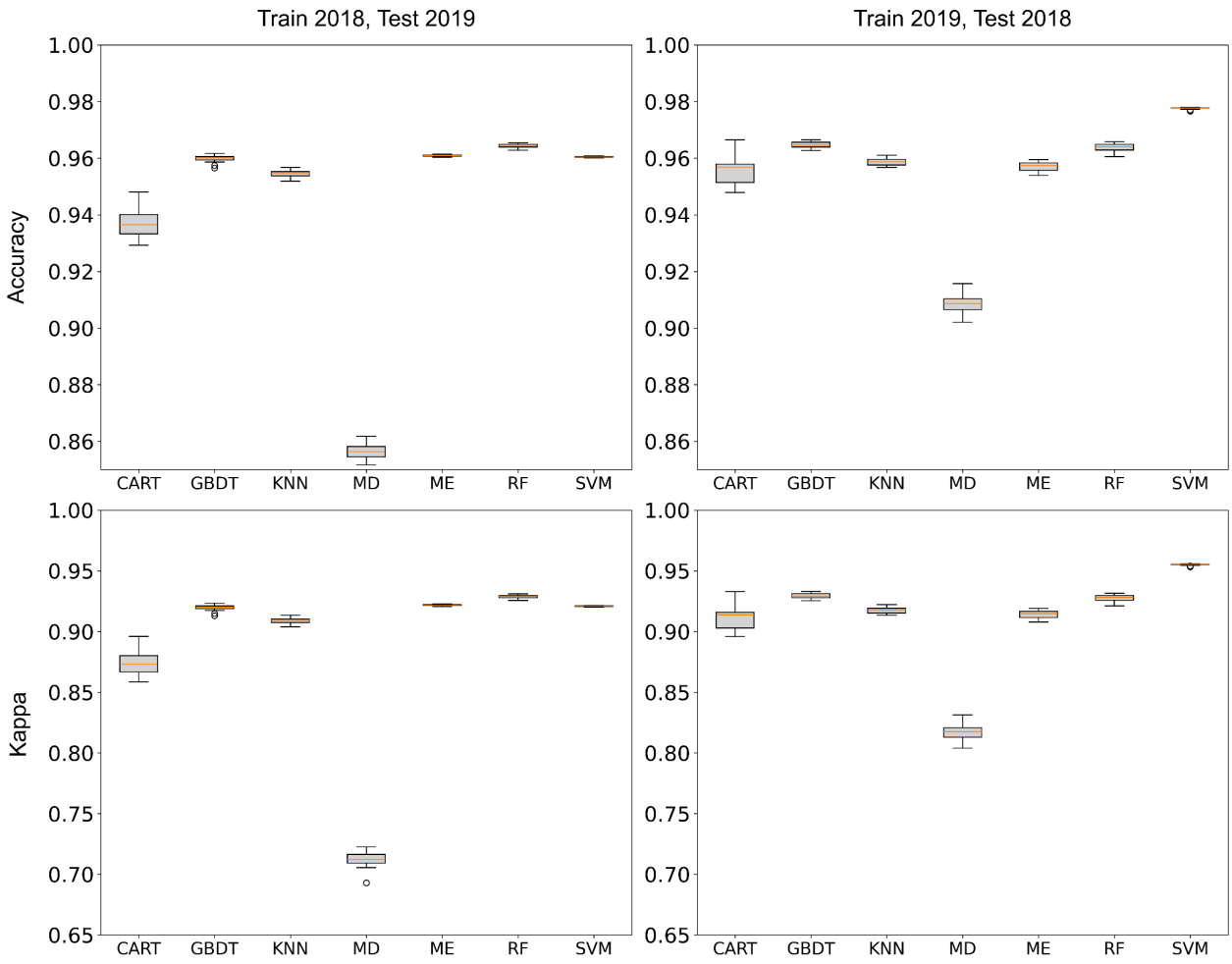

Figure 5.16: Results from 20 repeated runs evaluating temporal transfer scenarios. Accuracy (top) and Kappa (bottom) are displayed for models trained in 2018 and tested in 2019 (left) and trained in 2019 and tested in 2018 (right).

Classification errors revealed clear directional differences between the two interannual transfer scenarios (Figure 5.17). When trained on 2018 (the lower melt year) and tested on 2019 (the high melt year), classifiers tended to produce higher false positives, especially CART (23,139), MD (34,000), and SVM (10,260). This reflects a tendency to over-predict meltwater features. By contrast, when trained on 2019 and tested on 2018, classifiers more often under-predicted water, with higher false negatives observed in CART (6,063), and ME (5,850), indicating a struggle to detect the subtler melt features typical of 2018.

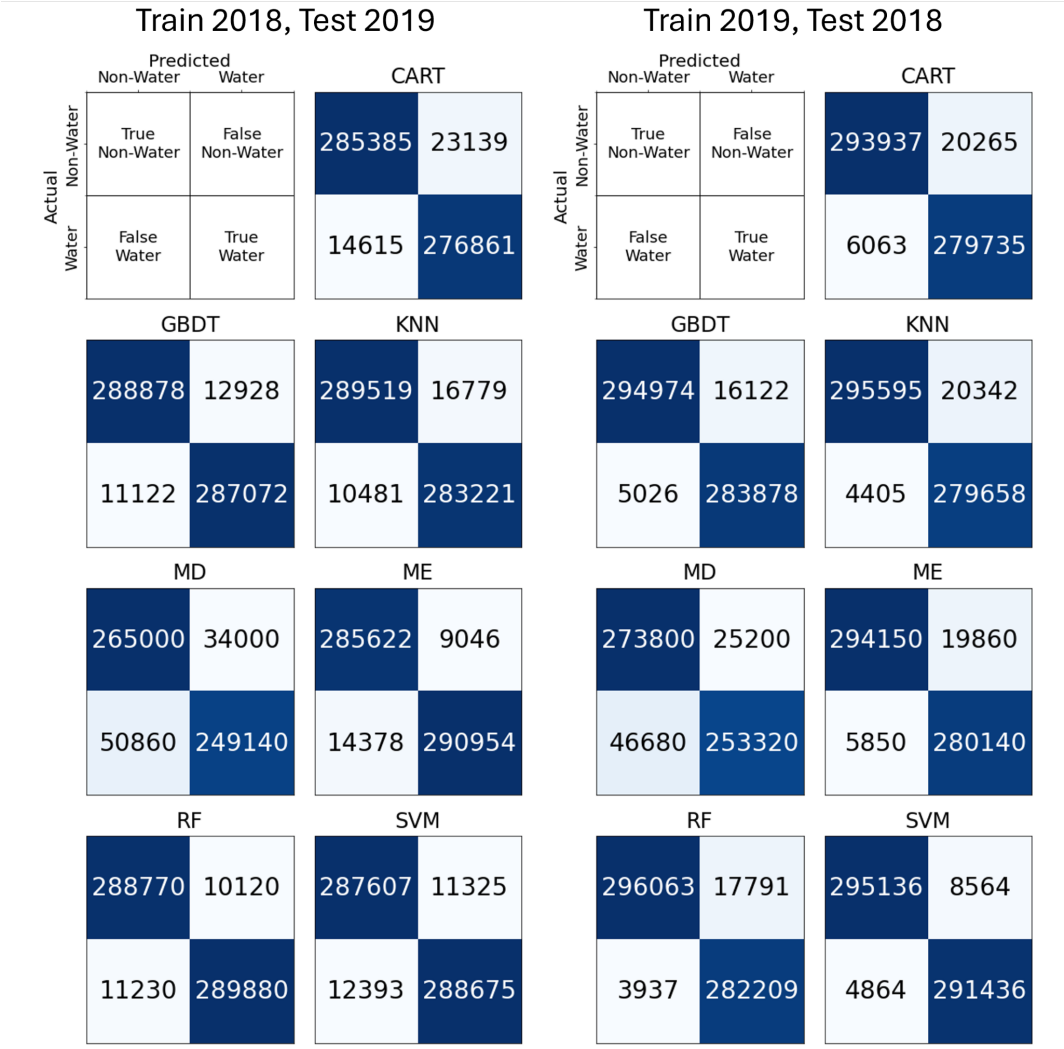

Figure 5.17: Cumulative confusion matrices summarizing classification outcomes from 20 repeated runs across two spatial transfer scenarios: models trained on NEGIS and tested on Watson (left) and models trained on Watson and tested on NEGIS (right).

5.3.5.3. Overall transferability

RF emerged as the most transferable classifier across both spatial and temporal domains, achieving the highest combined accuracy (0.92) with minimal variation, demonstrating strong generalization capabilities. SVM performed well in temporal transfer, particularly from 2019 to 2018 (0.98), but struggled with spatial transfer, dropping to 0.75 when tested from Watson to NEGIS, highlighting its sensitivity to spatial variability. GBDT performed well in spatial transfer from Watson to NEGIS (0.89) but showed a decline in the reverse direction (0.74). It also ranked second in temporal transfer, maintaining solid generalization across years. KNN performed well spatially but with slightly lower accuracy than the top classifiers, while ME and MD were the least transferable, with the lowest combined accuracies (0.72 for ME and 0.88 for MD), reflecting their difficulty in adapting to different spatial and temporal conditions.

The variability in classifier transferability aligns with spectral differences across datasets, highlighting the role of spectral diversity in shaping generalization performance. Section 5.3.5.4 explores these spectral influences in greater detail, examining how variability across key bands affects classifier adaptability across spatial and temporal domains.

5.3.5.4. Spectral variability and its impact on classifier transferability

Spectral variability appears to play a key role in classifier adaptability, with broader spectral distributions improving generalization.

In spatial transferability, classifiers trained on NEGIS outperformed those trained on Watson, reflecting higher spectral variability in NEGIS across B1–B12 (coastal blue to shortwave infrared) (Figure 5.18). B1 (443 nm) in NEGIS had a standard deviation of 0.162 compared to 0.115 in Watson, while B3 (560 nm) showed greater variability in NEGIS (0.153) than in Watson (0.112) (Figure 5.19). This broader spectral range provided a more diverse training set, improving classifier robustness when applied to Watson's more uniform spectral conditions. In contrast, Watson-trained classifiers struggled in NEGIS, where greater spectral variability, particularly in B3 (~560 nm) and B6 (~740 nm), led to higher misclassification rates.

In temporal transferability, classifiers trained on 2019 generalized better to 2018 than vice versa, aligning with higher spectral variability in 2019 across B2–B7 (blue to near-infrared) and B11–B12 (shortwave infrared) (Figures 5.20 and 5.21). B1 (443 nm) variability was higher in 2019 (std = 0.163) than in 2018 (0.128), and B11 (1610 nm) showed similar trends (0.153 vs. 0.132). This wider range of melt conditions in 2019 allowed classifiers to develop more adaptable decision boundaries, while 2018-trained models struggled with the more complex spectral conditions of 2019. However, the difference in accuracy between the two temporal transfer directions was minimal, indicating classifiers generalized well across years with only small variations in performance.

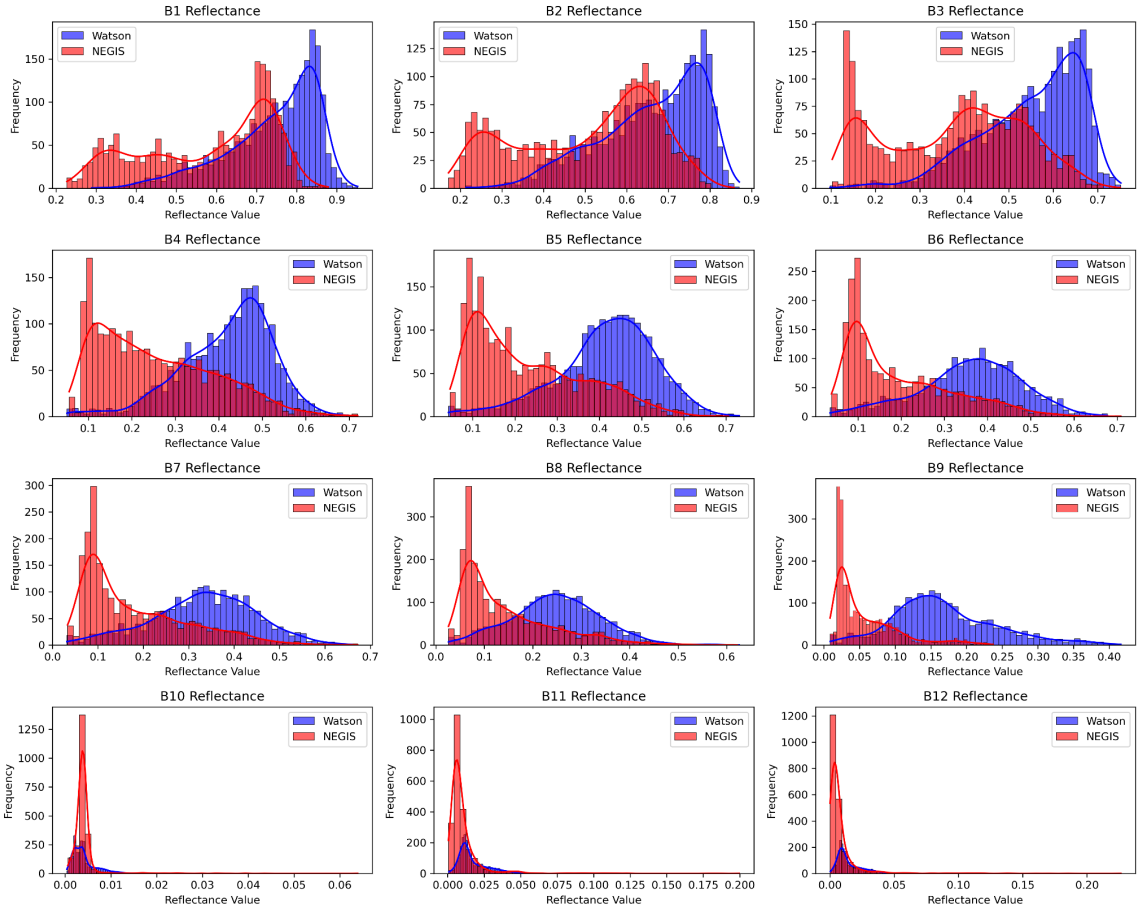

Figure 5.18: Histograms of reflectance values for water pixels across all 12 spectral bands, generated by extracting water pixel reflectance values from training datasets for NEGIS and Watson and binning them into frequency distributions for each spectral band.

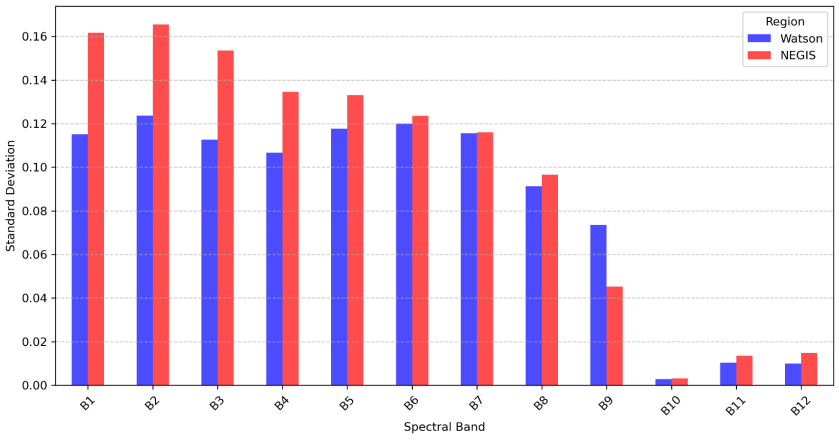

Figure 5.19: Standard deviation of reflectance values for water pixels across all 12 spectral bands in NEGIS and Watson, generated by computing the per-band standard deviation of reflectance values from water pixels in the training datasets for each year.

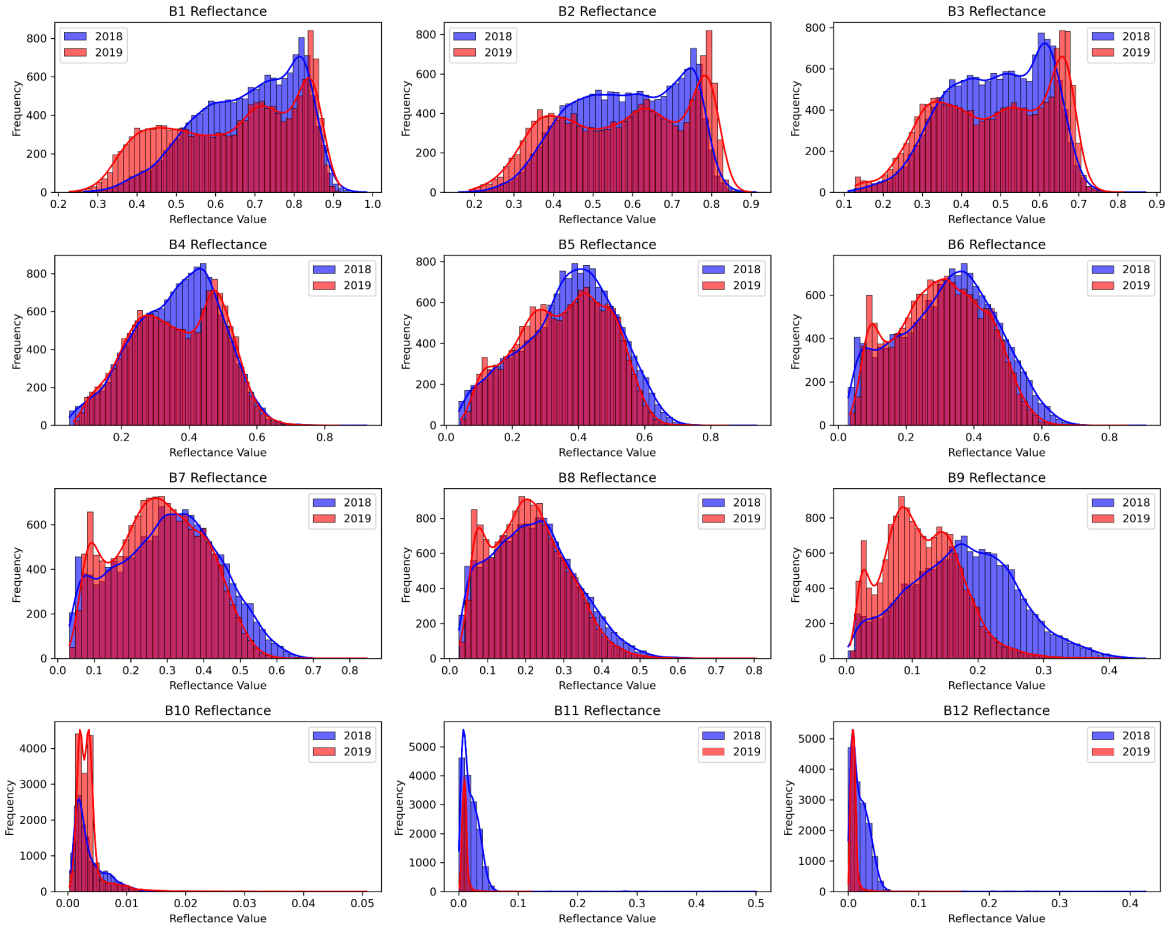

Figure 5.20: Histograms of reflectance values for water pixels across all 12 spectral bands, generated by extracting water pixel reflectance values from training datasets for 2018 and 2019 and binning them into frequency distributions for each spectral band.

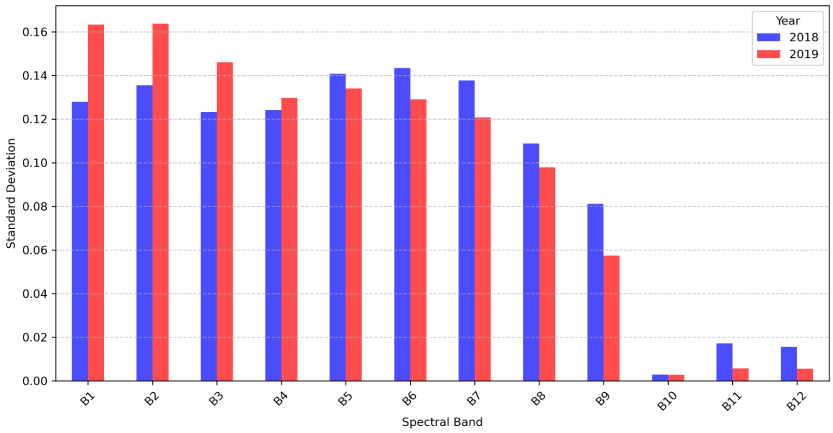

Figure 5.21: Standard deviation of reflectance values for water pixels across all 12 spectral bands in 2018 and 2019, generated by computing the per-band standard deviation of reflectance values from water pixels in the training datasets for each year.

5.3.6. Training data

Optimizing ML models for remote sensing requires a clear understanding of how training data configurations–including their size, composition, and quality–impact classification performance. Since creating high-quality training datasets is resource-intensive, this study systematically evaluated the effects of (1) dataset size, (2) input features derived from training data, and (3) label accuracy. These experiments explored how training dataset volume affects model reliability, how the selection of training features (e.g., raw bands vs indices) influences accuracy, and how robust different classifiers are to noisy or imperfect training labels. The following sections summarize key findings, highlighting the training data characteristics that most strongly influence classification accuracy and generalization.

5.3.6.1. Training data number

In this assessment, the degree to which the number of training data points influences classifier accuracy was evaluated, as well as variability in accuracy across repeated training runs. This was done, using the primary dataset described in Section 5.2.3.1, which spans multiple regions of the GrIS from 2017 to 2020.

Figure 5.22 illustrates the impact of increasing training data size from 20–80% of the primary dataset (8,000–32,000 samples) on classifier accuracy. While larger datasets generally improve performance, the rate of improvement varies across classifiers. GBDT and RF reach near-peak accuracy with relatively small datasets, compared to other classifiers that require more data to achieve similar performance. GBDT achieves 0.96 ± 0.002 accuracy with just 10% of the training data, increasing only 0.012 to 0.97 ± 0.001 at 50%, indicating diminishing returns beyond this point. Similarly, RF starts at 0.95 ± 0.001 (10%) and reaches 0.96 ± 0.001 (50%), showing stable performance even with limited data.

By contrast, CART and KNN rely more on larger training datasets, with accuracy continuing to increase across all training percentages. CART improves from 0.94 ± 0.004 (10%) to 0.95 ± 0.002 (50%), while KNN follows a similar trend, increasing from 0.94 ± 0.001 to 0.95 ± 0.001. This suggests that while they can achieve competitive accuracy, they require more data for stability. At the lower end, MD performs the worst, achieving 0.78 ± 0.004 accuracy with little improvement as training data increases, indicating difficulty in distinguishing between classes regardless of dataset size.

Interestingly RF shows a slight accuracy decline at higher training percentages, likely due to overfitting from redundant or noisy samples. This suggests that 80% training data may have

been excessive, and a smaller training size (50–60%) likely offers a better balance between accuracy and efficiency.

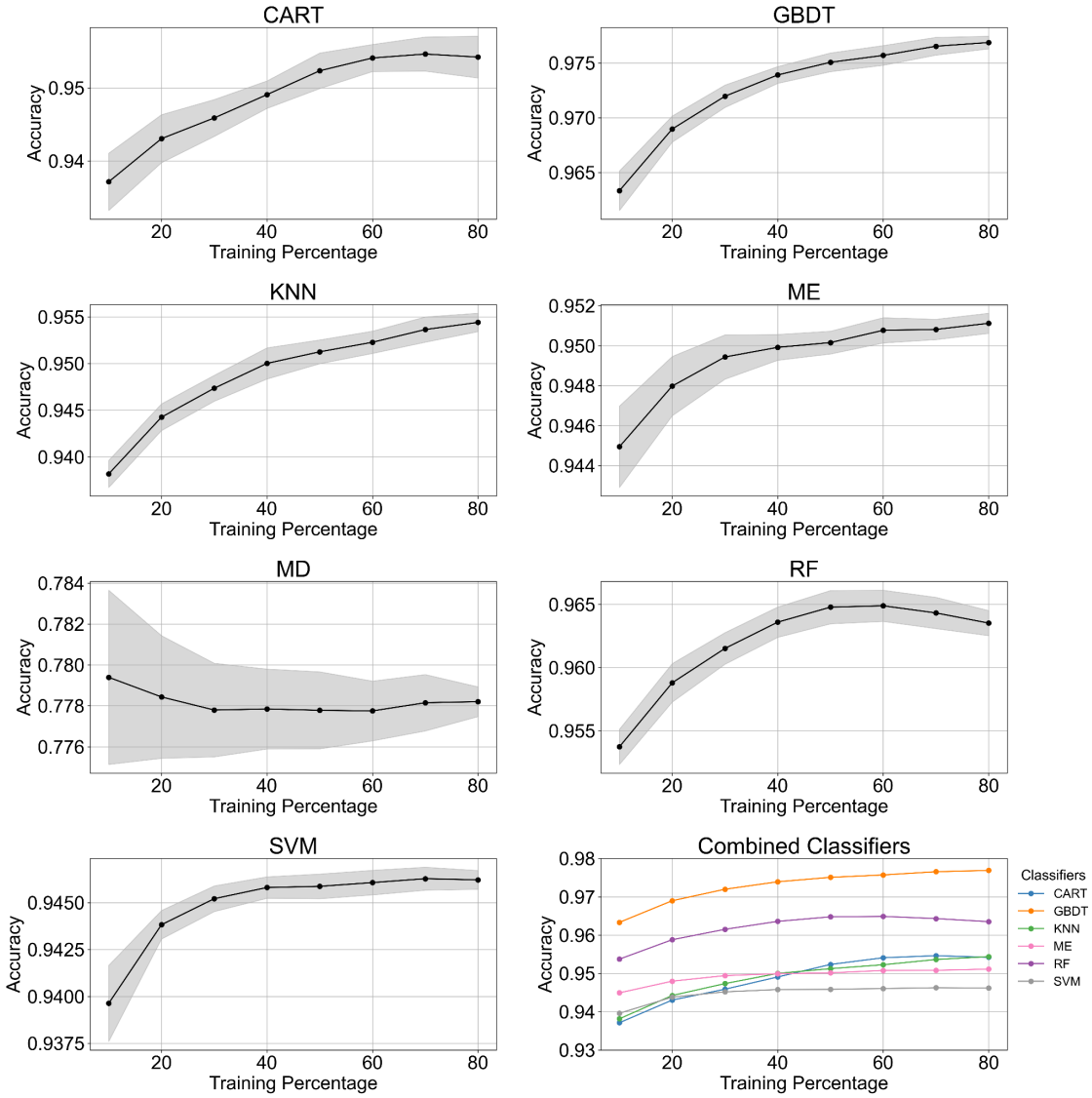

Figure 5.22: Accuracy trends for classifiers as a function of training dataset size. Each panel illustrates the accuracy progression for each classifier as the percentage of training data increases from 20% to 80%. The combined plot compares all classifiers except MD: blue for CART, orange for GBDT, green for KNN, pink for ME, purple for RF, and grey for SVM. Note: MD is excluded from the combined plot due to its significantly lower performance and higher variability.

5.3.6.2. Number of input features

As described in Section 5.2.5.3.3, the number of features refer to the number of spectral bands and derived indices used as input variables for classification. The feature subset analysis was conducted using an iterative approach, where classifiers were trained with progressively larger subsets of features, ranging from 1 to 25. The order of feature inclusion followed the original sequence in which spectral bands and indices were introduced during data preparation (Tables 2.2 and 2.3), providing a consistent and reproducible framework for evaluating classifier performance as feature numbers increase.

The results for this experiment indicate that classifier accuracy improves rapidly with the inclusion of the first few features before reaching a performance plateau (Figure 5.23). For example, GBDT achieves its highest accuracy (0.98 ± 0.003) with 7 features, while RF reaches near-optimal performance (0.95 ± 0.003) with just 3 features. As seen in Tables 2.2 and 2.3, these first three features correspond to B1 (Coastal aerosol), B2 (Blue), and B3 (Green). This suggests that both classifiers require relatively few input variables to perform well. In contrast, CART, KNN, and SVM exhibit a more gradual improvement, stabilizing at their peak accuracies of 0.96 ± 0.003, 0.962 ± 0.003, and 0.95 ± 0.005, respectively, only after incorporating 10–12 features. These models require more information to match the performance of GBDT and RF.

MD demonstrates lower accuracy compared to all other classifiers, stabilizing at just 0.78 ± 0.01 after four features. This performance is not only weak but also highly variable, with a standard deviation of approximately ± 0.01, indicating inconsistency across different runs. Similarly, ME shows a steady but slow increase in accuracy, reaching its highest performance (0.95 ± 0.004) only at the near maximum number of input features (24).

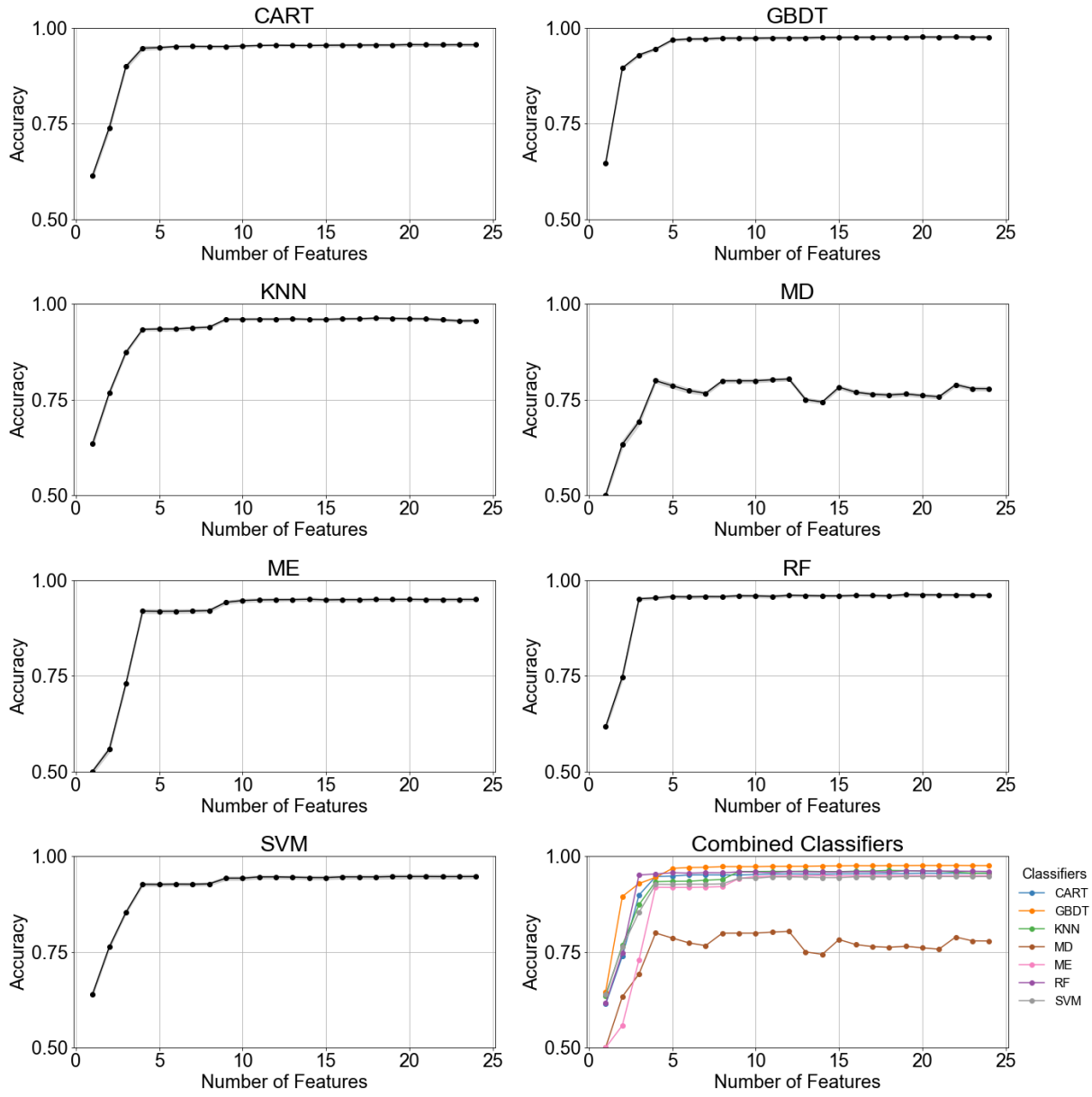

Figure 5.23: Accuracy trends for classifiers as a function of the number of features. Each panel illustrates the accuracy progression for each classifier as features are incrementally added. The combined plot compares all classifiers: blue for CART, orange for GBDT, green for KNN, pink for MD, maroon for ME, purple for RF, and grey for SVM.

5.3.6.3. Impact of spectral indices on classifier performance

This experiment assessed whether incorporating derived spectral indices alongside raw spectral bands improves classification accuracy sufficiently to justify the additional computational effort required for their calculation. To investigate this, three training configurations were compared: one using only the raw spectral bands (B1–B12, 12 features), one using only derived indices (Section 5.2.2.3, 13 features), and another combining these bands with all derived spectral indices (25 features in total).

Results indicate that incorporating spectral indices alongside raw spectral bands improves classification accuracy for most algorithms (Figure 5.24). RF and GBDT, which already perform well using only a small subset of spectral bands (accuracies of 0.974 ± 0.003 and 0.975 ± 0.003, respectively), exhibited modest but consistent gains when spectral indices were included, with improvements of 0.7% and 0.8%, respectively. Classifiers with lower baseline performance–such as CART and KNN–showed more variable responses. CART demonstrated the most pronounced improvement, increasing by 1.2% from 0.945 ± 0.005 to 0.956 ± 0.003 with the combined feature set, while KNN showed a marginal decline (−0.4%). MD was the only classifier to show a substantial drop in accuracy (−3.1%), indicating that the addition of spectral indices may introduce noise or redundancy for this distance-based method.

Spectral indices alone generally underperformed compared to raw bands, suggesting that while they capture some spectral information, they are most effective when used in conjunction with the full spectral profile. These findings suggest that the additional computational cost of calculating spectral indices may be justified, particularly when enhancing weaker classifiers or designing a general-purpose classification approach. However, for high-performing classifiers such as RF and GBDT, the marginal gains may not outweigh the increased processing demands in operational settings where speed or simplicity is prioritized.

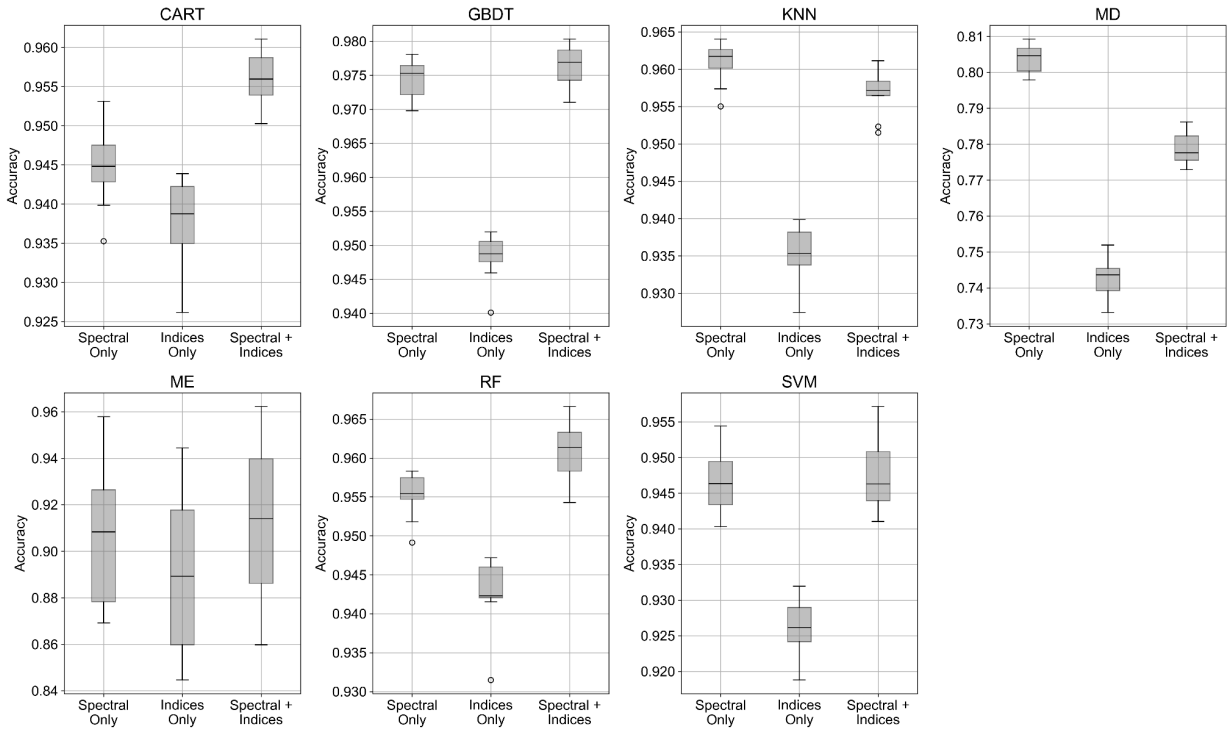

Figure 5.24: ***Comparison of classifier performance (accuracy) across models using spectral bands only, derived indices only and spectral bands combined with indices. The box spans the IQR, representing the middle 50% of the data (from the 25th to the 75th percentile). The whiskers extend to 1.5 times the IQR, showing the range of most data points, while individual circles represent outliers, indicating performance deviations across iterations.***

5.3.6.4. Label inaccuracies

By introducing increasing levels of noise and analysing performance degradation, this assessment provided insight into how much label error a classifier could tolerate before experiencing significant drops in accuracy. This is particularly important for real-world applications where perfectly labelled datasets are rarely available, and robustness to noise is an important factor in model selection.

As label inaccuracies increased from 1% to 20%, classifier performance exhibited a clear trend of gradual degradation, though the rate and extent of decline varied across models (Figure 5.25). GBDT and RF, which had the highest initial accuracy, responded differently to increasing inaccuracies. GBDT, which started at 0.99 at 1% inaccuracies, experienced a substantial drop to 0.88 at 20%, representing an 11 % accuracy loss. In contrast, RF, which began at 0.97, declined more gradually to 0.94, resulting in only a 2.6% decrease. These results indicate that while GBDT is the best-performing classifier in low-inaccuracy conditions, it is more susceptible to label inaccuracies than RF, which maintains better stability at higher levels of noise.

Among the other classifiers, KNN and CART exhibited moderate resilience. KNN experienced a 6.0% accuracy loss, showing that while it is affected by label inaccuracies, it degrades less severely than GBDT. CART demonstrated even greater robustness, with only a 2.3% decline. SVM also showed relatively stable performance, with a gradual decline from 0.95 at 1% inaccuracies to 0.93 at 20% inaccuracies.

Among the remaining classifiers, performance under label noise varied. MD, which had the lowest initial accuracy at 0.78, showed little variation but remained the weakest performer throughout, ending at 0.77 at 20% inaccuracies. ME, however, experienced the steepest decline of all classifiers, plummeting from 0.95 to 0.65–representing a 32% accuracy loss. This suggests that ME is highly sensitive to mislabelled data, struggling to maintain classification performance even at moderate levels of label inaccuracy.

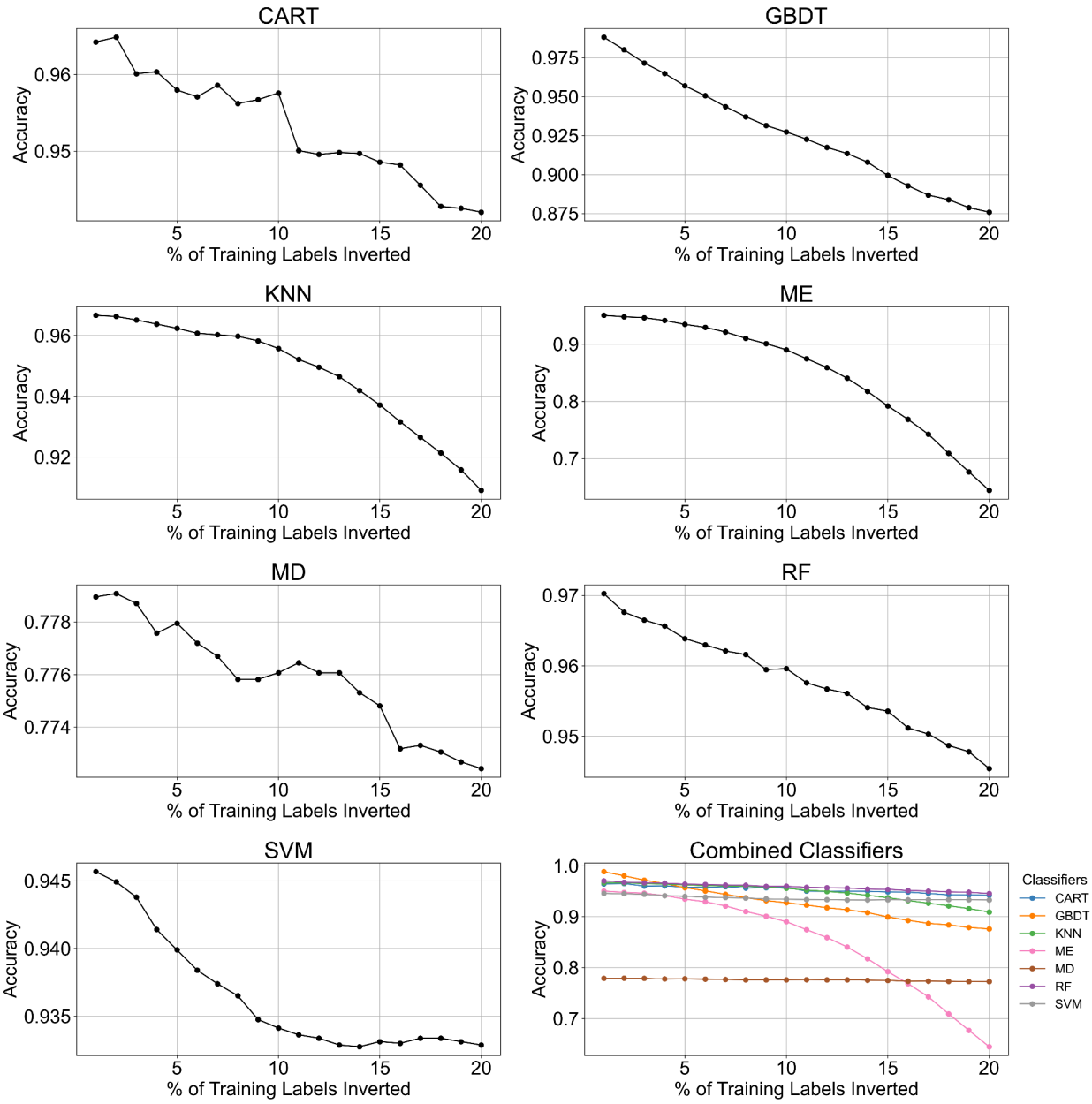

Figure 5.25: Accuracy of classifiers under increasing noise levels, showing individual performance trends for CART, GBDT, KNN, MD, ME, RF, and SVM, along with a combined overview. Note: No shading is included as this experiment was conducted with a single run due to computational constraints.

5.3.6. Ranking classifiers

To synthesize the results from all classification experiments, the seven classifiers were ranked based on their performance across multiple evaluation criteria. This ranking framework provides a holistic assessment of classifier reliability in supraglacial meltwater mapping, highlighting the most robust models for different applications. The evaluation considers ten key metrics derived from previous sections, including overall accuracy (Sections 5.3.3.1–5.3.3.3), spatial transferability (Section 5.3.4.1), temporal transferability (Section 5.3.4.2), sensitivity to training data size (Section 5.3.5.1), feature selection (Section 5.3.5.2), the impact of spectral indices (Section 5.3.5.3), and robustness to label noise (Section 5.3.3.4).

Both absolute performance and stability were considered, where absolute performance was determined through accuracy metrics and stability was assessed using the standard deviation of classifier performance across multiple experimental iterations, with lower values indicating greater reliability across datasets and conditions.

All evaluation tests are summarized in Table 5.6, with results detailed in Table 5.7, while Figures 5.26 and 5.27 provide a visual breakdown of classifier rankings across different assessment categories. The combined rankings in Figure 3.26 were derived by computing mean ranks across three key evaluation criteria: overall performance, transferability, and training data sensitivity, described in Table 3.1.

In terms of overall accuracy, GBDT emerged as the most accurate classifier, consistently achieving high accuracy across all validation tests. RF closely followed, demonstrating notable strength in generalizing to previously unseen datasets. CART ranked third, particularly excelling in manual verification for the Watson region. KNN achieved moderate yet stable accuracy, ranking fourth, while ME, ranked fifth, exhibited inconsistent results across validation tests. SVM performed less effectively, ranking sixth overall, and MD consistently demonstrated the lowest performance across all validation assessments.

Assessments of transferability indicated that RF was the top-performing classifier, excelling in both spatial and temporal transferability. GBDT ranked second, providing reliable results, though its adaptability was somewhat limited compared to RF. SVM demonstrated strength primarily in temporal transferability, securing third place, but struggled with spatial generalization. CART and KNN maintained moderate transferability rankings at fourth and fifth place, respectively. ME and MD showed poor transferability, ranking sixth and seventh due to consistent underperformance.

Evaluating sensitivity to variations in training data, RF again ranked highest, demonstrating robustness to changes in dataset size, feature selection, and label noise. GBDT ranked second, showing high sensitivity to label noise despite performing well in other sensitivity metrics. CART ranked third, maintaining stability across various tests, while KNN, in fourth place, required larger datasets to achieve optimal performance. SVM and ME ranked fifth and sixth, respectively, reflecting moderate to significant sensitivity to training data variations. MD was consistently the weakest performer across all sensitivity tests, ranking last.

The classifiers were finally categorized based on these evaluations into optimal, efficient, suboptimal, and inefficient groups. RF and GBDT were classified as optimal due to their strong generalization capabilities and high accuracy, respectively, even though GBDT was sensitive to label noise. CART and KNN were considered efficient, suitable under specific dataset conditions, though limited in flexibility. SVM and ME were categorized as suboptimal due to their inconsistent performance and limited generalization capabilities. MD was classified as inefficient, consistently underperforming across all evaluations and thus not recommended for supraglacial hydrology applications.

Table 5.6: Summary of classification evaluation tests, categorized by Overall Performance, Transferability, and Training Data Sensitivity. Overall Performance tests measure classifier accuracy and consistency across different validation techniques. Transferability tests evaluate the ability of classifiers to generalize across spatial and temporal domains. Training Data Sensitivity tests analyse how classifiers respond to variations in dataset size, input feature selection, spectral indices, and label noise. The reference section column provides links to detailed descriptions of each test in the main text.

Test name	**Test category**	**Description**	**Reference section**
Repeated Validation	Overall accuracy	Assesses classifier consistency across multiple random splits of the dataset, measuring stability in performance.	Section 5.3.3.1
K-Fold Validation	Overall accuracy	Evaluates classifier generalization by training and testing across multiple data folds, ensuring all samples are used for validation.	Section 5.3.3.2
NEGIS Manual Dataset	Overall accuracy	Compares classifier outputs against a manually labelled dataset from NEGIS (2019, high-melt year) to assess real-world accuracy.	Section 5.3.3.3.1
Watson Manual Dataset	Overall accuracy	Similar to NEGIS manual verification but applied to Watson (2018, low-melt year), testing classifier reliability under different melt conditions.	Section 5.3.3.3.2
Spatial Transferability	Transferability	Tests how well classifiers generalize when trained in one region (e.g., Watson) and applied to another (e.g., NEGIS).	Section 5.3.4.1
Temporal Transferability	Transferability	Evaluates how well classifiers trained in one melt year (e.g., 2018) perform when applied to another year (e.g., 2019).	Section 5.3.4.2
Training Data Number	Training data sensitivity	Analyses how classifier performance varies with different training dataset sizes, identifying models requiring more data for stability.	Section 5.3.5.1
Feature Number Sensitivity	Training data sensitivity	Examines how classification accuracy changes when different numbers of spectral bands and indices are used as input features.	Section 5.3.5.2
Derived Indices	Training data sensitivity	Tests whether including additional spectral indices alongside raw bands improves classifier performance.	Section 5.3.5.3
Noise Sensitivity	Training data sensitivity	Introduces increasing levels of label noise to evaluate classifier robustness under real-world uncertainties.	Section 5.3.5.4

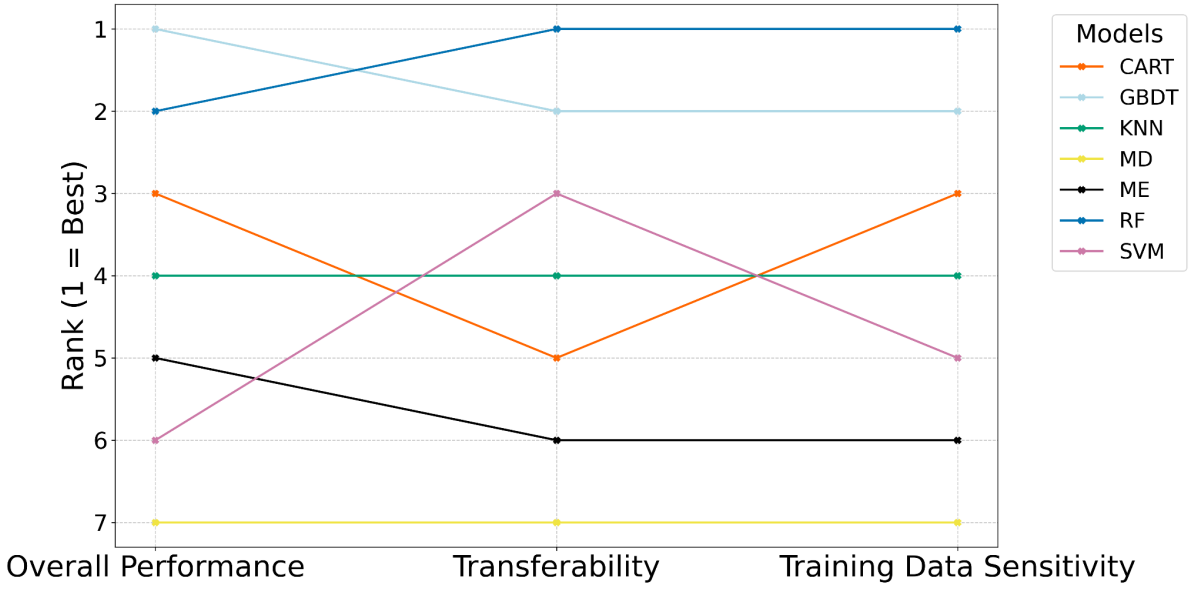

Figure 5.26: Combined rankings of all classifiers, where 1 represents the best-performing classifier and 7 the worst. CART is orange, GBDT is light blue, KNN is Green, MD is yellow, ME is black, RF is dark blue, SVM is pink. Classifiers are grouped into three evaluation categories: overall performance, Transferability, and Training Data Sensitivity. The final combined ranking is derived by assessing classifier consistency across multiple evaluation metrics within each category. Further details are provided in Table 5.6.

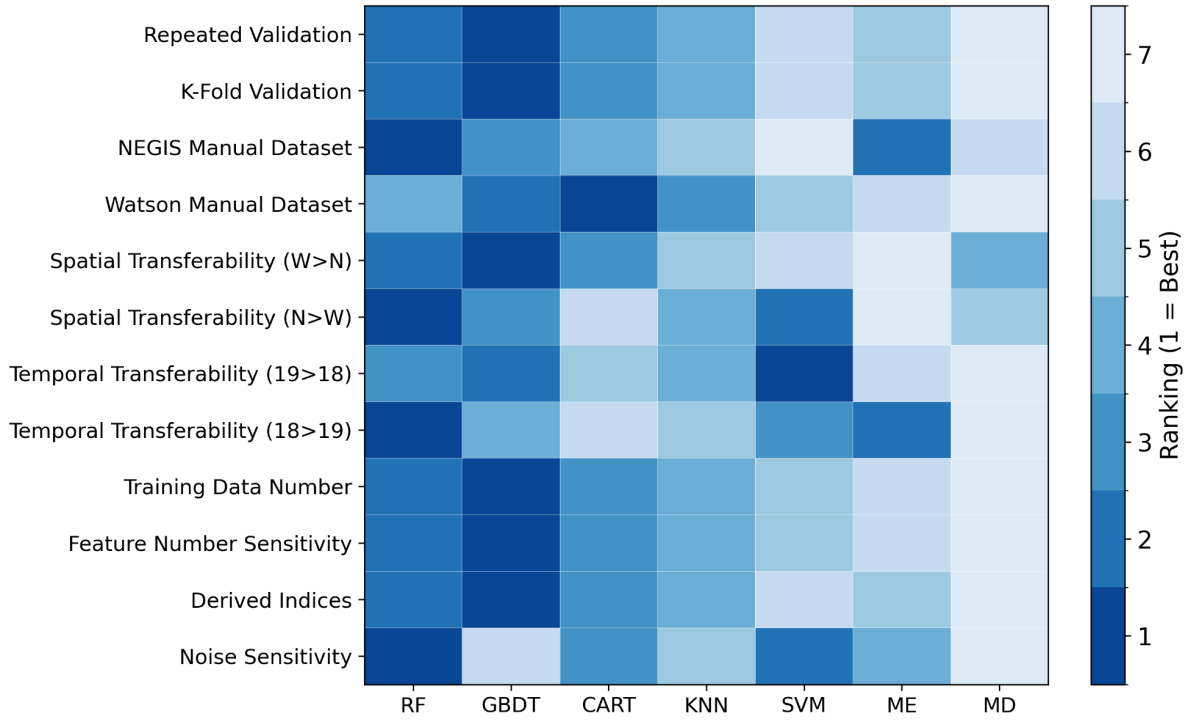

Figure 5.27: Rankings of all classifiers for each individual test, where 1 (dark blue) represents the best-performing classifier and 7 (light blue) represents the worst-performing. "W" refers to Watson, "N" refers to NEGIS, "19" denotes the 2019 dataset, and "18" denotes the 2018 dataset. ">" indicates the direction of transfer, with the classifier trained on the first dataset and tested on the second Refer to Table 5.6 for detailed descriptions of the individual tests.

Table 5.7: Summary of classifier rankings based on overall performance, transferability, and training data sensitivity. Each classifier is ranked from 1 (best) to 7 (worst), with strengths and weaknesses identified based on evaluation tests.

.

Classifier	**Rank**	**Strengths**	**Weaknesses**
RF	1	Best generalization; robust to spatial & temporal transfer; handles noisy data well	Slightly lower accuracy than GBDT; some sensitivity to dataset size; lower ranking in tests involving low melt conditions
GBDT	2	Highest accuracy in validation; performs well with small datasets	Struggles with label inaccuracies
CART	3	Consistent performance; robust to noise	Lower ranking in major accuracy tests; weaker temporal transferability
KNN	4	Moderate stability; decent spatial generalization	Requires larger training datasets; weaker temporal transferability
SVM	5	Strong temporal generalization; good manual verification performance	Struggles with spatial transferability; highly sensitive to feature selection
ME	6	Performed well in controlled manual validation	Poor transferability; inconsistent across datasets
MD	7	None	Underperforms in all tests; highly sensitive to noise and dataset variations

5.4. Discussion

ML is playing an ever-increasing role in remote sensing applications for supraglacial meltwater feature delineation, offering scalable, automated alternatives to traditional threshold-based methods, which often struggle to generalize across large datasets and variable melt conditions. However, the effectiveness of different ML algorithms in classifying meltwater features remains underexplored, particularly in the context of cloud-based processing environments like GEE. This study systematically evaluates multiple classifiers, assessing their accuracy, transferability across space and time, as well as their sensitivity to training data variation–key considerations for reliable large-scale hydrological mapping.

The following sections discuss the leading classifiers identified in this study, challenges in classifier performance, the role of spectral variability in transferability, and the optimization of training data selection. Additionally, the potential for holistic meltwater feature mapping was explored and the broader implications of the findings of this study for future research and operational applications.

5.4.1. Interpretation of evaluation approaches

In the context of large-scale supraglacial meltwater mapping on the GrIS, understanding how classifiers perform under varying data conditions is essential for both scientific and operational applications. Although all three evaluation methods used in this study–repeated validation, cross-validation, and independent manual comparison–report accuracy and Kappa scores, they assess distinct aspects of model performance.

Repeated and cross-validation test internal consistency and sensitivity to data variability within the primary dataset, helping to identify overfitting and assess how reliably a classifier performs when trained on different partitions of familiar data. The high scores achieved in these tests demonstrate how well models can replicate known patterns. In contrast, manual dataset comparisons offer a more stringent test of generalization, evaluating performance on fully independent images captured in different years and regions, and labelled using alternative methodologies. This simulates real-world deployment, where models encounter unfamiliar spectral and environmental conditions. Performance declines in these tests–particularly in cases like Watson 2018, where subtle melt signals and low spectral contrast lead to elevated false positive rates.

The divergence in outcomes between evaluation methods also highlights a key distinction: while internal validation emphasizes accuracy within known domains, independent validation better reflects a model’s precision and reliability in novel settings. For example, RF maintains

balanced recall and precision across diverse conditions, while classifiers like CART may overestimate meltwater extent in unfamiliar regions.

Ultimately, this multi-faceted framework offers a fuller picture of both technical capability and practical utility. Internal validation is best suited for model development and benchmarking, while independent validation provides a more realistic assessment for operational use. The relative weight placed on each should reflect the intended application–whether the goal is theoretical insight or robust deployment across space and time.

5.4.2. RF and GBDT as leading classifiers

A key aim of this study is to assess how different ML classifiers perform in supraglacial meltwater mapping. Among the classifiers evaluated, RF and GBDT emerged as the most effective models for supraglacial meltwater classification. RF has been widely used in remote sensing applications for SGL detection (e.g., Wangchuk & Bolch, 2020; Hu et al., 2021; Dirscherl et al., 2020, 2021; Dell et al., 2022, 2024; Yuan et al., 2020; Halberstadt et al., 2020; Wang & Sugiyama, 2024). This study reaffirms RF's strengths but also highlights the potential of GBDT, which has yet to be used for this purpose. GBDT ranked first in overall performance based on repeated validation and cross-validation accuracy, both of which are in-dataset validation methods that assess model consistency by resampling subsets of the same dataset. In contrast, RF ranked first in transferability, demonstrating superior spatial and temporal generalization–an essential capability for real-world supraglacial mapping, where models must accommodate variations in surface reflectance, illumination conditions, and meltwater expressions that were not represented in the training data. This distinction suggests that while GBDT is highly effective when applied to datasets with similar spectral characteristics to the training set, excelling in scenarios where the model does not need to extrapolate beyond familiar conditions, RF is better suited for large-scale, multi-year meltwater mapping due to its robustness across heterogeneous environments and its ability to generalize to unseen spectral and temporal variations.

A key limitation of GBDT is its sensitivity to label noise–an important factor in operational settings where training data quality may be variable. Although GBDT outperformed RF under ideal training conditions, its performance degraded more sharply when noise was introduced, limiting its suitability for large-scale applications without extensive label refinement. These findings indicate that RF and GBDT should not be viewed as competing classifiers but rather as complementary models with distinct strengths. A hybrid classification framework integrating GBDT's precision with RF's robustness could provide an optimized solution for large-scale supraglacial hydrology mapping. One potential approach would be to

use GBDT in regions with high spectral consistency, where its precision is most effective, while deploying RF in more heterogeneous or uncertain areas to ensure broader generalization. Alternatively, ensemble or meta-learning strategies could be explored, combining the strengths of both models through weighted predictions or context-aware switching to enhance classification accuracy across diverse conditions. This warrants further investigation to determine whether such an approach could improve supraglacial meltwater mapping on the GrIS.

5.4.3. Challenges in classifier performance for large-scale meltwater mapping

While RF and GBDT performed best, other classifiers struggled with key challenges that limit their usefulness for large-scale supraglacial meltwater mapping. MD was the weakest, failing to separate meltwater from ice and shadows, likely because it assumes clear differences between classes, which is not the case in complex supraglacial environments. This led to high misclassification rates and poor adaptability across regions and years, making MD unreliable for tracking meltwater changes. SVM showed promise in tracking year-to-year melt changes within the same region but struggled when applied to different locations, limiting its usefulness for large-scale studies. Previous work by Chouksey et al. (2021) and Halberstadt et al. (2020) found that SVM reduced false positives in challenging conditions like cloud shadows, yet these results show it has trouble handling different spectral patterns across space.

CART consistently overfit the training data, performing well in controlled conditions but failing when applied to different years or regions. This makes it unreliable for large-scale mapping, where adaptability is crucial. KNN required vast, high-quality training datasets to function effectively. Its accuracy improved with more data, but it remained computationally slow, making it impractical for real-time or large-scale applications in GEE. ME was inconsistent, occasionally producing strong results but highly sensitive to label inaccuracies. When training data contained moderate errors, the accuracy of ME dropped by over 30%, making it unreliable for real-world applications where perfect labels are rarely available. While some of these methods may still have niche uses–such as SVM for detailed multi-year regional studies –the results of this analysis show that RF and GBDT are the best choices for reliable, transferable meltwater classification on the GrIS.

5.4.4. The role of spectral variability in classifier transferability

This study finds that classifier performance was generally higher [lower] when trained on NEGIS [Watson] and tested on Watson [NEGIS], likely due to the greater spectral variability

present in NEGIS. In NEGIS, meltwater features coexist with fresh snow, providing a stronger contrast that aids classifier performance. In contrast, frozen-over SGLs in Watson offer a more subtle spectral contrast, which makes distinguishing meltwater from non-meltwater areas more challenging. Similarly, classifiers trained on the high melt year (2019) generalized more effectively to the low-melt year (2018) than vice versa, likely due to the highly variable melt conditions of 2019, which led to greater spectral variability. Greater spectral variability in the training data enables classifiers to develop a more adaptable decision boundary, improving performance when applied to the more spectrally uniform conditions of the low-melt year.

The manual verification experiments (Section 5.3.3.3), which tested classifiers on independent datasets from both NEGIS (2019) and Watson (2018), further reinforce these observations. For example, classifiers trained on spectrally homogeneous areas, like Watson (2018), where meltwater features are sparse and subtle, tend to be overly sensitive to the few visible meltwater areas, leading to the detection of all actual meltwater (reducing false negatives to 0%), but this sensitivity also causes the misclassification of non-meltwater areas as meltwater, resulting in an overestimation of meltwater extent. This overestimation was less pronounced in NEGIS, where the contrast between meltwater and non-water surfaces, such as snow, was stronger, allowing classifiers to more effectively distinguish between water and non-water areas. These patterns further highlight the importance of spectral diversity in training data.

5.4.5. Optimising training data selection

Optimizing training data for generalization involves more than just selecting scenes with high spectral variability; it also requires careful consideration of dataset size, feature selection, and tolerance to annotation error to ensure consistent performance across diverse conditions–especially given the challenges of large-scale classification in the dynamic and heterogeneous environments of the GrIS.

While increasing training data size generally improves classifier accuracy, the relationship is not linear, and additional data does not always yield proportional gains. The fact that GBDT and RF reached peak accuracy with only around half of the available training data–despite points being randomly selected–suggests that classifier performance does not necessarily depend on large volumes of data. This finding is particularly relevant for large-scale operational mapping, where computational efficiency and training data availability are key constraints. In contrast, lower-performing classifiers like CART and KNN appear to benefit more consistently from larger training datasets, with performance continuing to improve as more data are added. This suggests that some models are more reliant on volume than

others. The slight decline in RF accuracy at higher training percentages may also hint at overfitting, serving as a caution against assuming that larger training datasets will always lead to better performance.

Beyond dataset size, the choice of input features matters more than simply including every spectral band and index available, suggesting that adding more variables does not always translate to better results. Instead, a minimal subset of features–added in S2 band order–was often sufficient, reducing computational burden while maintaining accuracy. This is particularly relevant in cloud-based platforms like GEE, where efficiency is critical for large-scale classification. Interestingly, the inclusion of spectral indices had only a minor effect on accuracy. While some studies (e.g., Wang and Sugiyama, 2024; Dirscherl et al., 2020) have emphasized the importance of derived indices for meltwater delineation, the findings from this study suggest that RF and GBDT extract enough information from spectral bands alone, with only marginal improvements (~ 0.7%) when indices were included. This suggests that indices may not be essential for these classifiers in large-scale meltwater mapping.

Another important aspect of training data selection is its resilience to labelling inaccuracies, as real-world datasets are rarely free from annotation errors. Given the time-intensive nature of manual labelling, it is important to consider whether classifiers should be trained on highly refined datasets or if they can tolerate some level of noise. Findings from this study reveal that classifier performance declines as label noise increases, but not all classifiers are affected equally. GBDT is highly sensitive to annotation errors, while RF remains stable, suggesting that it can better handle the inconsistencies that inevitably arise in large-scale mapping efforts. This makes RF a strong candidate for operational applications, where absolute labelling consistency across all datasets may not be achievable.

These results provide a foundation for future efforts to optimise training data selection in ML-based supraglacial hydrology mapping. Increasing dataset size alone is unlikely to guarantee optimal performance across classifiers. Instead, improving the representativeness and spectral diversity of training data may be a more effective strategy, particularly for models applied across varied spatial and temporal domains.

5.4.5. Advancing holistic meltwater feature mapping

A key finding of this study is the ability of ML classifiers to consistently identify multiple supraglacial meltwater features–SGLs, rivers, and slush–across distinct environmental conditions, e.g. the high-melt year of NEGIS (2019) and the low-melt year of Watson (2018). This represents a shift from many previous studies, which have predominantly focused on mapping SGLs in isolation, often neglecting the interconnectivity of supraglacial hydrological

features. Recent research increasingly acknowledges that supraglacial hydrology functions as a coupled system, with SGLs, rivers, and slush collectively transporting meltwater across the ice surface and towards the bed (Glen et al., 2025; Rawlins et al., 2024; Yang and Smith, 2012; Chu, 2016). The ability of ML classifiers to capture the spatial extent of these features in a unified framework enhances the ability to quantify meltwater connectivity, improving representations of supraglacial drainage processes. The results from this highlight the potential for ML classifiers, when appropriately trained, to move beyond single-feature mapping and support a more integrated understanding of supraglacial hydrology. Further work will be needed to refine classifiers to better distinguish between feature types and their boundaries, but the ability to capture the broader meltwater network represents an important step forward.

5.4.6. Caveats and considerations

It should be noted that the findings presented here are based on specific datasets and methodological choices, including the use of S2 optical imagery, supervised classifiers available within GEE, and a training dataset derived from select regions of the GrIS. These factors shape the results, and while they offer valuable insights into classifier performance, they do not necessarily generalize to all supraglacial environments (e.g., Antarctica), different satellite sensors, or alternative classification approaches. Additionally, the evaluation is constrained by the spatial and temporal scope of the study. Differences in atmospheric conditions (e.g., variable cloud cover or low solar angles), ice sheet surface properties (e.g., the presence of cryoconite), and sensor data characteristics (e.g., differences in spatial resolution, spectral coverage, or revisit frequency across satellite platforms) could influence classification outcomes in other locations or time periods.

Moreover, while the study explores the impact of training data characteristics, the optimal balance between dataset size, feature selection, and label accuracy may vary depending on the specific goals of a given application. For example, while the classifiers evaluated here perform well within the scope of this study, different applications may impose different requirements. Large-scale monitoring initiatives may prioritise efficiency and robustness across diverse conditions, whereas targeted process studies may demand higher accuracy in resolving subtle feature differences. The optimal training strategy will therefore depend on the intended use case. These findings should therefore be interpreted as a guideline rather than a prescriptive rule. Future research incorporating additional regions, different sensors (e.g., radar, hyperspectral), and alternative classification strategies (e.g., deep learning - not currently supported by GEE) will be essential for further refining best practices in supraglacial meltwater mapping.

5.5. Practical implications and concluding remarks

This study provides a systematic assessment of ML classifiers for supraglacial meltwater mapping, advancing understanding of both model performance and the broader challenges of large-scale classification on the GrIS. While remote sensing has long been used to track supraglacial hydrology, traditional threshold-based approaches often struggle to generalize across regions and melt seasons. By evaluating multiple classifiers within a cloud-based framework, this study identifies RF and GBDT as the most effective models for large-scale supraglacial meltwater mapping, with RF excelling in transferability and robustness, while GBDT offers the highest classification accuracy under controlled conditions. The results reinforce that classifier selection should be guided by the intended application, with RF proving the most reliable for real-world, large-scale mapping, while GBDT may offer advantages in targeted, high-accuracy settings.

Beyond classifier rankings, this study highlights the critical role of spectral variability in training data selection, demonstrating that models trained on spectrally diverse datasets–such as those from high-melt years (2019) or spatially heterogeneous regions (NEGIS)–are more transferable across space and time. This finding challenges the common assumption that increasing dataset size alone leads to better generalization. Instead, these results emphasize that training data should be curated to maximize spectral diversity, rather than indiscriminately expanding labelled datasets. This insight has practical implications for future supraglacial meltwater studies, where efficiency in training data selection is crucial for scaling classification efforts to the full ice sheet.

A further contribution of this work is the shift towards a more holistic approach to supraglacial hydrology mapping. Unlike previous studies that have primarily focused on SGL segmentation, this study demonstrates that ML classifiers can reliably identify multiple meltwater features, including supraglacial SGLs, rivers, and slush. This supports the emerging view that supraglacial hydrology should be treated as an interconnected system, where different meltwater features interact to influence water storage, transport, and eventual drainage into the ice sheet. Moving forward, classification frameworks should move beyond isolated feature mapping to capture the dynamic evolution of supraglacial hydrology in a more integrated manner.

While this study advances ML-based supraglacial hydrology mapping, it also underscores several open challenges that should guide future research. A key limitation of current approaches is their reliance on optical imagery, which remains susceptible to cloud contamination and low-light conditions. Integrating multi-sensor datasets, such as S1 SAR or

thermal imagery, could improve classification accuracy, particularly in persistently cloudy regions. Additionally, while this study focuses on traditional ML classifiers, the growing accessibility of deep learning approaches, such as CNNs, presents new opportunities for feature extraction and classification in complex melt environments. However, deep learning models require large, labelled datasets and significant computational power, necessitating further research into their feasibility for supraglacial hydrology applications.

From an operational perspective, the findings of this study support the scalability of ML-based supraglacial meltwater classification for real-time monitoring. The strong transferability of RF, combined with its resilience to label noise, suggests that it is a viable candidate for integration into automated monitoring frameworks on cloud platforms such as GEE. A hybrid classification approach, leveraging RF's adaptability and GBDT's precision, could provide an optimal balance between generalization and accuracy, further enhancing large-scale monitoring efforts. The ability to track meltwater evolution over multiple seasons with minimal re-training represents an important step toward operationalizing ML for large-scale ice sheet hydrology studies. As the GrIS continues to experience increasing melt under a warming climate, robust and scalable classification approaches will be critical for monitoring evolving hydrological processes.

Chapter 6

Synthesis and conclusions

This thesis advances research on supraglacial hydrology mapping and monitoring on the Greenland Ice Sheet (GrIS) by applying semi-automated remote sensing and machine learning (ML) methods to identify, quantify, and track surface meltwater features across the ice sheet. These contributions enhance both the understanding of meltwater distribution and dynamics on the GrIS, and the methodological approaches used for supraglacial hydrology monitoring.

The overarching aim of this research was to improve understanding of supraglacial hydrology on the GrIS through three key objectives, as outlined in Chapter 2:

1. ***Better understand how the distribution, evolution, and morphology of supraglacial meltwater varies within, and between, high and low melt years.*** Chapter 3 offers insights into how increased surface meltwater may influence future ice sheet hydrology by comparing supraglacial meltwater features in southwest Greenland during a low-melt year (2018) and a high-melt year (2019), a study which is published in *the Cryosphere* (Glen et al., 2025).

2. ***Better understand the spatial and temporal distribution of slush on the GrIS.*** Chapter 4 provides the first near-decadal, ice-sheet-wide assessment of slush distribution, revealing its seasonal and regional variability.

3. ***Optimize the performance of and understand the trade-offs between ML classifiers deployed in the cloud.***
   Chapter 5 presents a systematic comparison of the accuracy, transferability, and training data dependencies of ML classifiers within Google Earth Engine (GEE). This evaluation highlights the strengths and limitations of different classification approaches, providing a framework for informing the selection of optimal methods for future supraglacial meltwater mapping studies.

This thesis was designed to address knowledge gaps in process understanding, methodological approaches, and technological scalability in supraglacial hydrology. While SGLs and channels have been extensively studied, slush remains underexplored despite its critical role in hydrological connectivity and runoff. As the Earth's climate warms, increasingly frequent extreme melt years further complicate understanding of how these meltwater features interact and evolve within hydrological drainage systems. Despite forming a connected system, meltwater features have often been studied in isolation (e.g., Box & Ski, 2007; Selmes et al., 2011; Williamson et al., 2017; Sundal et al., 2009), and holistic approaches remain limited in spatial and temporal scope.

Methodological challenges arise from the difficulty of distinguishing SGLs, channels, and slush from one another. Many classification methods apply generalized approaches that fail to account for their distinct spectral and morphological characteristics of different meltwater features, leading to incomplete or inaccurate results. While ML presents a promising solution, its application to supraglacial hydrology has so far been relatively limited, with previous studies relying on random forest (RF) or select deep learning models, often without critical comparison to alternative models (e.g., Wangchuk & Bolch, 2020; Hu et al., 2021; Dell et al., 2024). Additionally, key uncertainties persist in prior ML-based studies of supraglacial meltwater, particularly regarding optimal training data requirements and the transferability of classification models across different regions and melt seasons – a gap that has not yet been systematically addressed in existing research.

Technological limitations further constrain large-scale supraglacial hydrology mapping. Traditional approaches relying on locally stored satellite imagery are computationally inefficient, limiting large-scale analysis. Cloud-based ML frameworks, such as GEE, offer scalable solutions but remain underutilized in this field. Expanding the use of cloud-based processing and deep learning frameworks could significantly improve the efficiency and accuracy of supraglacial meltwater classification.

This final Chapter synthesizes the key contributions of this thesis to supraglacial hydrology research on the GrIS, summarizing principal findings, emerging research themes, and pathways for refining and expanding supraglacial meltwater monitoring. It then discusses study limitations and outlines priorities for future work. While this research is focused on the GrIS, the findings may also inform supraglacial hydrology studies on mountain glaciers and the Antarctic Ice Sheet, where similar remote sensing and classification challenges arise.

6.1. Summary of key findings

This thesis directly addresses the knowledge gaps outlined in Chapter 2 and as briefly explained above, the three interconnected studies each contribute to a more comprehensive understanding of supraglacial hydrology on the GrIS.

Chapter 3 compares the distribution, evolution, and morphology of supraglacial meltwater features in southwest Greenland during a low-melt year (2018) and a high-melt year (2019). By examining the entire supraglacial meltwater system–including SGLs, channels, and slush–this research provides new insights into how increased melt influences meltwater feature characteristics, SGL behaviour and hydrological connectivity. The results reveal that in 2019, meltwater covered 20.8% of the catchment area, compared to only 6.3% in 2018, with slush playing a significant role in surface water distribution. Additionally, the study highlights the increasing prevalence of small SGLs, which influence early-season surface-to-bed connections and may impact ice sheet dynamics. These findings emphasize the importance of considering all meltwater components in hydrological models and climate projections.

Building on the findings of slush from Chapter 3, the fourth Chapter presents the first near-decadal, ice-sheet-wide assessment of slush distribution, mapping its extent from 2016 to 2024 using Sentinel-2 (S2) imagery and RF classification. The results indicate that slush is a dominant component of supraglacial hydrology, covering an average of 4.2% of the GrIS annually, with strong regional and interannual variability. The SW and NO basins exhibit the highest slush coverage, with annual averages of 5.5% and 4.8%, respectively, while the SE consistently shows the lowest at just 0.6%. The NO basin stands out as an area of increasing slush presence, particularly since 2019. During extreme melt years, slush expands significantly, reaching higher elevations than previously observed and exceeding prior surface meltwater extent estimates by as much as 14.5 times. Even the lowest increase doubles previous estimates. Interannual variability reflects its sensitivity to atmospheric conditions, with coverage peaking at 8.3% (144,800 km²) in 2019 and contracting to just 1.4% (24,400 km²) in 2018. This study also demonstrates the advantages of ML-based classification over traditional thresholding techniques, offering a more robust and scalable approach for detecting slush. Our results also highlight the need to integrate slush into hydrological and climate models to improve predictions of meltwater storage, runoff, and hence ice-sheet mass balance.

The fifth Chapter systematically evaluates a variety of ML classifiers for supraglacial meltwater delineation in GEE. By comparing classifier accuracy, transferability, and training

data requirements, this work identifies RF and Gradient Boosting Decision Trees (GBDT) as the most effective classifiers for large-scale, automated meltwater mapping. The study also demonstrates that training data diversity is critical for improving classifier performance, with models trained on spectrally variable environments generalizing more effectively to new regions and melt conditions. These findings contribute to the development of scalable, ML-based classification frameworks that enhance the efficiency and accuracy of supraglacial hydrology monitoring.

6.2. Synthesis of key findings

This thesis advances the study of supraglacial hydrology on the GrIS by addressing key knowledge gaps in the observation, classification, and understanding of supraglacial meltwater features and drainage systems. While previous research has largely focused on individual components of supraglacial hydrology–such as SGLs or streams–this work contributes a broader, system-level perspective, emphasizing the spatial and temporal complexity of meltwater processes and the methodological innovations required to monitor them effectively. Through a combination of comparative melt year analysis, ice-sheet-wide mapping, and ML algorithm development, this thesis contributes to both the scientific understanding of supraglacial hydrology and the tools needed to study it at scale. Several key themes emerge from this work.

This work highlights the pronounced interannual variability and climate sensitivity of supraglacial hydrology. By contrasting meltwater features in 2018 and 2019, and mapping slush over nearly a decade, this research shows how quickly, and dramatically surface hydrology can reorganize in response to extreme melt seasons. The differences between low- and high-melt years are stark: slush coverage, meltwater connectivity, and the prevalence of small SGLs all increase significantly during warmer conditions. These findings reinforce the idea that Greenland's hydrology is highly sensitive to climate forcing, with extreme years like 2019 offering a glimpse into the future behaviour of the ice sheet as climate warming continues. Importantly, this melt variability is not just a matter of areal extent but also of system structure–extreme years foster more connected, more saturated, and more dynamic hydrological networks.

A central contribution is the focus on slush, an ephemeral and often-overlooked feature of Greenland's meltwater system. Despite its widespread presence, slush has historically been neglected in large-scale remote sensing studies due to its spectral ambiguity and transient nature. By first identifying that slush is more widespread in a high-melt year compared to a low-melt year, this thesis then presents the first near-decadal, GrIS-wide assessment of

slush, revealing its dominance as a key component of surface hydrology during extreme melt years and a persistent feature in certain regions. By quantifying slush coverage, elevation, and interannual variability, this research suggests that slush plays a critical role in meltwater storage, surface albedo reduction, and runoff generation. These findings elevate slush from a peripheral to a central feature of supraglacial hydrology, highlighting the need for its inclusion in future process studies and predictive models of hydrology and ice sheet mass balance.

Building on the theme described above, the thesis advances a holistic, interconnected view of supraglacial hydrology. Rather than treating SGLs, channels, and slush as discrete features, this work emphasizes their co-evolution and interdependence. Through comparative analysis of low- and high-melt years, and across different spatial regions, it becomes clear that meltwater features respond collectively to changing atmospheric conditions. Slush frequently forms along the margins of SGLs and channels, small SGLs feed into supraglacial streams, and widespread surface saturation can influence drainage efficiency across entire catchments. This integrated perspective highlights the importance of viewing supraglacial hydrology as a continuum of water storage and transport pathways, where transitions between features are fluid and dynamic. Such a framework is essential for accurately modelling meltwater routing, predicting subglacial inputs, and understanding the broader response of the ice sheet to climate forcing.

An important finding of this thesis is the upward migration of meltwater features to higher elevations on the ice sheet. Traditionally, supraglacial hydrology has been thought of as concentrated in the lower elevations of the ice sheet, where melt is most intense. However, this thesis documents the upward expansion of SGLs and slush, with features appearing at elevations above 1900 m a.s.l. during extreme melt years. This shift has significant implications for the stability of the firn zone and the capacity of high-elevation areas to buffer meltwater through refreezing. As melt penetrates further inland and upward, the hydrological and thermal structure of the ice sheet is being reshaped, with potential feedbacks for runoff generation, firn densification, and mass loss. These findings contribute to growing evidence that the spatial limits of active surface hydrology are expanding, challenging long-held assumptions about the vertical structure of the GrIS's hydrological system.

This thesis also argues that ML is not just a useful tool, but an essential component of supraglacial hydrology research going forward. The complexity and scale of supraglacial hydrology cannot be captured through manual delineation or threshold-based methods alone. ML provides a scalable, adaptable, and transferable solution to the challenges of classifying diverse meltwater features across varying atmospheric and surface conditions.

Beginning with the identification of ML as a necessary methodological advance, the research develops, tests, and implements classifiers capable of distinguishing SGLs, channels, and slush, even in challenging environments with partial cloud cover or subtle spectral differences. These contributions move the field toward operational, ice-sheet-wide monitoring, where supraglacial hydrology can be tracked consistently across years and regions.

Finally, underpinning the scientific advances outlined above is a commitment to methodological scalability and operational monitoring. The approaches developed in this thesis–integrating ML within cloud-based platforms like GEE–demonstrate that large-scale, repeatable mapping of supraglacial hydrology is not only possible but essential as melt seasons grow more dynamic and satellite archives expand.

6.3. Limitations and directions for future research

While this thesis provides significant advancements in the study of supraglacial hydrology on the GrIS, several limitations must be acknowledged. These limitations stem from data constraints, methodological challenges, and broader issues related to scalability and generalization. Addressing these challenges in future research will improve supraglacial meltwater mapping and enhance our ability to monitor and predict ice sheet hydrology under ongoing climate change.

6.3.1. Limitations of optical imagery

The availability of optical images is primarily constrained by sensor revisit times. S2, with its twin satellites, has a 5-day revisit cycle, while Landsat 8 (L8) has a 16-day cycle. The shorter revisit time of S2 improves temporal resolution, aiding the capture of dynamic supraglacial hydrology. However, meltwater can be transported across, or drain through, the ice sheet within hours or days, meaning even a 5-day revisit cycle may not capture all hydrological variability.

In Chapter 3, we identify that the availability of satellite imagery varies between years, with more frequent image acquisitions in 2019 (~2-day intervals) compared to 2018 (~5-day intervals). This disparity limits the ability to differentiate between rapid and slow drainage events, which can have distinct effects on supraglacial, englacial, and subglacial hydrology. While this thesis utilizes both S2 and L8 data, future work should integrate additional remote sensing datasets, such as Synthetic Aperture Radar (SAR) from Sentinel-1, to improve temporal resolution. SAR's ability to penetrate cloud cover provides more consistent observations, particularly for tracking rapid drainage events.

Additionally, optical sensors can only detect surface slush, while subsurface layers remain invisible, meaning our reported slush extents likely represent a minimum bound. SAR offers a potential solution, as it can penetrate cloud cover and detect subsurface slush, similar to its use in mapping SGLs (e.g., Miles et al., 2017; Dunmire et al., 2021). By combining SAR with optical methods, future work has the potential to provide a more comprehensive assessment of slush distribution, its seasonal evolution, and its impact on meltwater transport.

Another challenge of optical image usage lies in errors introduced by cloud cover and cloud shadows. Despite the use of cloud masks, misclassifications occur, particularly when cloud edges or thin clouds resemble slush in spectral imagery. These errors lead to false positives, where clouds are mistakenly classified as slush, inflating the detected extent. A potential

solution is time-series filtering, where classifications with low persistence (i.e., pixels identified as slush only once in a season) are excluded (e.g., Dell et al., 2022). However, this approach risks removing real, short-lived slush events, potentially underestimating true coverage. Developing more effective cloud-masking techniques or post-classification filtering methods will be necessary to improve classification accuracy.

6.3.2. Interannual variability and climate sensitivity

A central theme of this thesis is the pronounced interannual variability and climate sensitivity of supraglacial hydrology. Chapter 3 highlights the contrast between the low-melt year (2018) and the high-melt year (2019), using 2019 as a proxy for intensified future melt conditions. However, while this comparison illustrates the hydrological response to extreme surface melt, it does not capture the long-term evolution of ice-sheet surface properties. Chapter 4 expands the temporal scope through a nine-year analysis of slush, yet the record is limited to observations from 2016 onward. As a result, it remains unclear whether the observed patterns reflect short-term variability or indicate sustained changes driven by climate forcing. Multi-year processes such as firn densification, ice slab formation, and cumulative meltwater retention will play an important role in the GrIS's response to climate change. Future research should examine extended melt records, incorporating historical datasets from the 1980s onward using Landsat imagery. This will allow for a clearer distinction between interannual variability and long-term climate-driven trends in supraglacial hydrology.

6.3.3. Challenges in supraglacial lake behaviour and depth estimation

Distinguishing between SGL drainage and refreezing also remains difficult. Chapter 3 classified drainage and refreezing based on changes in SGL area and volume, supplemented by modelled air temperature data. However, without in situ validation, some SGLs identified as refreezing may have partially drained or retained liquid water beneath an impermeable ice surface', leading to classification uncertainties. Incorporating thermal imaging or radar-based techniques, such as SAR penetration depth analysis, could help differentiate between refrozen and partially drained SGLs. The framework developed by Dunmire et al. (2025) provides a promising automated classification approach for capturing SGL behaviour by incorporating higher-temporal-resolution datasets and sophisticated ML-based analyses.

SGLs depth estimation presents another challenge. Depth calculations based on optical reflectance are limited by a saturation threshold, typically between 1 and 3 m (Melling et al.,

2024). This constraint affects volume estimates, introducing uncertainty into calculations of meltwater storage capacity. Our calculated 21.2% uncertainty associated with SGL volume estimates underscores the need for improved depth retrieval methods. Future research should explore alternative techniques, such as ICESat-2 laser altimetry. The empirical depth estimation model proposed by Lutz et al. (2024), which combines S2 reflectance with ICESat-2 and sonar-derived depth calibrations, represents a promising approach. Additionally, incorporating DEM derived SGL basin bathymetry post-drainage could provide further validation of optical-based estimates. Expanding field-based measurements across a wider range of SGL types and locations would also improve model accuracy.

6.3.4. Methodological challenges in meltwater classification

A key limitation of our current method used in Chapter 4 is its reliance on K-means clustering for generating training data, which may not be the most optimal approach for distinguishing slush from other hydrological features. This is, however, the method Dell et al (2022, 2024) used for detecting slush on Antarctic ice shelves. While K-means is a widely used unsupervised technique, it assigns clusters based purely on spectral similarity without considering the physical properties of meltwater or its spatial context. This can lead to heterogeneous class definitions, where slush pixels are grouped with spectrally similar but physically distinct features like wet firn or thin ice layers. A more refined approach would involve semi-supervised or active learning methods, where an initial classifier is iteratively improved through expert-labelled corrections. Alternatively, self-supervised learning techniques could leverage large unlabelled datasets to learn more meaningful representations of slush without relying on predefined clustering. Exploring these alternatives could improve the consistency and generalizability of training data, ultimately leading to more robust slush classification.

Beyond training data generation, the choice of classification algorithm itself presents a methodological challenge. While this thesis primarily uses traditional ML methods–RF in Chapter 4 and various cloud-based classifiers in Chapter 5–it remains uncertain whether these are the most effective approaches for meltwater classification. Emerging techniques such as convolutional neural networks, transformer models, and hybrid approaches may better capture complex spatial patterns and reduce errors in mixed-pixel environments. Future research should evaluate whether deep learning models trained on multi-modal datasets (e.g., optical, radar, and topographic data) can outperform traditional classifiers, particularly in dynamically evolving melt conditions. Additionally, uncertainty quantification methods, such as Bayesian inference, should be explored to provide confidence estimates for classification outputs, improving the interpretability of large-scale meltwater assessments.

Additionally, there is currently a notable lack of an explicit ML method for distinguishing between all types of supraglacial meltwater features (i.e., SGLs, channels, and slush), though some studies do use ML techniques to delineate one or two of these meltwater feature types. Chapter 3 employed multiple thresholding methods and manual delineation, which, while effective for localized analysis, is impractical for large-scale mapping across the GrIS. Meanwhile, the classifiers tested in Chapter 5 delineated meltwater extent as a binary classification but did not differentiate between these features. A promising approach would be to use the dataset developed in Chapter 3 as training data for ML models, enabling automated classification of supraglacial hydrological features while preserving the ability to distinguish between different meltwater components, and connectivity between them. Additionally, the addition of automated post-processing techniques, such as spatial filtering, morphological analysis, or object-based image classification, could facilitate large-scale identification of distinct hydrological features.

Computational demands remain a significant challenge for large-scale, ice-sheet-wide meltwater monitoring. Chapter 5 found that while GEE enables cloud-based processing, classifier efficiency varies, with some models (e.g., Minimum Distance, Maximum Entropy) being computationally expensive without offering substantial performance gains. Future research should focus on optimizing ML workflows for large-scale classification, potentially leveraging cloud-based deep learning frameworks (not currently supported by GEE) such as TensorFlow or PyTorch to enhance scalability and efficiency. Automating classifier selection based on dataset characteristics could further streamline processing, enabling models to dynamically select the most suitable algorithm for specific classification tasks.

6.4. Concluding remarks

This thesis has significantly advanced our understanding of supraglacial hydrology on the GrIS by integrating satellite remote sensing with ML techniques to address key observational and methodological challenges. It presents three major contributions: (i) a comparative analysis of meltwater evolution during contrasting melt years (Chapter 3), (ii) the first near-decadal, ice-sheet-wide mapping of slush using S2 imagery and random forest classification (Chapter 4), and (iii) a systematic evaluation of supervised ML classifiers for automated delineation of supraglacial meltwater features using cloud-based platforms (Chapter 5).

To achieve these outcomes, this thesis employed a progression of remote sensing and classification approaches, from semi-automated thresholding to scalable ML-based workflows. The results demonstrate that high melt years, such as 2019, drive increased hydrological connectivity, increased upslope migration of lakes and slush, and the expansion of surface meltwater storage. Slush is shown to be a widespread and climatically sensitive meltwater component on the GrIS but was previously underrepresented in large-scale hydrological studies. As a result of this thesis, its spatial distribution, interannual variability, and elevation migration have now been quantified at the ice-sheet scale. Furthermore, the performance of seven ML classifiers was assessed across multiple regions and melt seasons, with RF and GBDT emerging as the most effective methods for delineating supraglacial meltwater features from optical satellite imagery. This work establishes a robust, transferable framework for automated supraglacial meltwater mapping within platforms such as GEE, enabling near-real-time monitoring across broad spatial and temporal ice sheet domains.

The findings mentioned above carry several important implications. First, they reinforce our understanding that the interannual variability of supraglacial hydrology is strongly sensitive to climate, with extreme melt seasons offering insight into the ice sheet's potential response to ongoing warming. Second, they establish slush as an integral and dynamic component of the surface hydrological system, underrepresented in prior studies. Third, this thesis demonstrates that scalable ML-based classification, when implemented in cloud-based environments, can overcome key limitations of traditional remote sensing approaches–such as location-specific tuning, extensive manual correction for false positives and negatives, and constraints on processing time and storage–enabling efficient, high-resolution monitoring of supraglacial hydrology.

Together, the key findings in this thesis enhance our ability to monitor, model, and predict the future state of supraglacial hydrology on the GrIS, laying the foundation for continued

research in an era of accelerating climate change. Continued observation, and better understanding, of these processes is essential for improving projections of future ice sheet mass loss under a warming climate.

Appendix A

A comparison of supraglacial meltwater features throughout contrasting melt seasons: Southwest Greenland

Table A.1: details of all Sentinel-2 (S2) and Landsat 8 (L8) satellite imagery used in this study.

Scene ID	Date	Satellite	Cloud Cover (%)
S2A_MSIL1C_20180516T150041_N0206_R125_T22WEV_20180516T170011	16-May-18	S2	9.8
S2A_MSIL1C_20180516T150041_N0206_R125_T22WFV_20180516T170011	16-May-18	S2	87.7
S2A_MSIL1C_20180526T145921_N0206_R125_T22WEV_20180526T201815	26-May-18	S2	68.6
S2A_MSIL1C_20180526T145921_N0206_R125_T22WFV_20180526T201815	26-May-18	S2	60.2
LC08_L1TP_008013_20180605_20200831_02_T1	05-Jun-18	L8	35.4
S2B_MSIL1C_20180610T150009_N0206_R125_T22WEV_20180610T183746	10-Jun-18	S2	16.1
S2B_MSIL1C_20180610T150009_N0206_R125_T22WFV_20180610T183746	10-Jun-18	S2	82.8
S2A_MSIL1C_20180615T145911_N0206_R125_T22WEV_20180615T170226	15-Jun-18	S2	34.3
S2A_MSIL1C_20180615T145911_N0206_R125_T22WFV_20180615T170226	15-Jun-18	S2	43.1
S2A_MSIL1C_20180618T150911_N0206_R025_T22WEV_20180618T185402	18-Jun-18	S2	4.9
S2A_MSIL1C_20180618T150911_N0206_R025_T22WFV_20180618T185402	18-Jun-18	S2	22.6
S2B_MSIL1C_20180703T150909_N0206_R025_T22WEV_20180703T201427	03-Jul-18	S2	71.9
S2B_MSIL1C_20180703T150909_N0206_R025_T22WFV_20180703T201427	03-Jul-18	S2	19.6
LC08_L1TP_008013_20180707_20200831_02_T1	07-Jul-18	L8	31.2
S2B_MSIL1C_20180710T150009_N0206_R125_T22WEV_20180710T202212	10-Jul-18	S2	5.0
S2B_MSIL1C_20180710T150009_N0206_R125_T22WFV_20180710T202212	10-Jul-18	S2	94.5
S2B_MSIL1C_20180713T151139_N0206_R025_T22WEV_20180713T200909	13-Jul-18	S2	4.3
S2B_MSIL1C_20180713T151139_N0206_R025_T22WFV_20180713T200909	13-Jul-18	S2	0.3
S2A_MSIL1C_20180725T145911_N0206_R125_T22WEV_20180725T185310	25-Jul-18	S2	89.9
S2A_MSIL1C_20180725T145911_N0206_R125_T22WFV_20180725T185310	25-Jul-18	S2	25.1
S2B_MSIL1C_20180730T150009_N0206_R125_T22WEV_20180730T202856	30-Jul-18	S2	0.1
S2B_MSIL1C_20180730T150009_N0206_R125_T22WFV_20180730T202856	30-Jul-18	S2	0.2
S2A_MSIL1C_20180810T151911_N0206_R068_T22WEV_20180810T202556	10-Aug-18	S2	2.5
S2A_MSIL1C_20180810T151911_N0206_R068_T22WFV_20180810T202556	10-Aug-18	S2	0.0
S2B_MSIL1C_20180819T145959_N0206_R125_T22WEV_20180819T200111	19-Aug-18	S2	26.2

S2B_MSIL1C_20180819T145959_N0206_R125_T22WFV_20180819T200111	19-Aug-18	S2	9.3
S2A_MSIL1C_20180824T145911_N0206_R125_T22WEV_20180824T190305	24-Aug-18	S2	59.8
S2A_MSIL1C_20180824T145911_N0206_R125_T22WFV_20180824T190305	24-Aug-18	S2	65.3
S2A_MSIL1C_20180913T145911_N0206_R125_T22WEV_20180913T171024	13-Sep-18	S2	0.0
S2A_MSIL1C_20180913T145911_N0206_R125_T22WFV_20180913T171024	13-Sep-18	S2	0.0
S2B_MSIL1C_20180918T145959_N0206_R125_T22WEV_20180918T200337	18-Sep-18	S2	0.0
S2B_MSIL1C_20180918T145959_N0206_R125_T22WFV_20180918T200337	18-Sep-18	S2	6.9
S2A_MSIL1C_20180919T151911_N0206_R068_T22WEV_20180919T191221	19-Sep-18	S2	17.2
S2A_MSIL1C_20180919T151911_N0206_R068_T22WFV_20180919T191221	19-Sep-18	S2	0.0
S2B_MSIL1C_20180921T151119_N0206_R025_T22WEV_20180921T201342	21-Sep-18	S2	28.2
S2B_MSIL1C_20180921T151119_N0206_R025_T22WFV_20180921T201342	21-Sep-18	S2	95.4
S2B_MSIL1C_20180924T152029_N0206_R068_T22WEV_20180924T202449	24-Sep-18	S2	1.2
S2B_MSIL1C_20180924T152029_N0206_R068_T22WFV_20180924T202449	24-Sep-18	S2	0.0
S2A_MSIL1C_20190501T145921_N0207_R125_T22WEV_20190501T165756	01-May-19	S2	1.6
S2A_MSIL1C_20190501T145921_N0207_R125_T22WFV_20190501T165756	01-May-19	S2	45.5
S2B_MSIL1C_20190502T151809_N0207_R068_T22WEV_20190502T190011	02-May-19	S2	0.0
S2B_MSIL1C_20190502T151809_N0207_R068_T22WFV_20190502T190011	02-May-19	S2	0.0
S2B_MSIL1C_20190506T150019_N0207_R125_T22WEV_20190506T195836	06-May-19	S2	2.4
S2B_MSIL1C_20190506T150019_N0207_R125_T22WFV_20190506T195836	06-May-19	S2	0.7
LC08_L1TP_008013_20190507_20200828_02_T1	07-May-19	L8	3.8
S2B_MSIL1C_20190509T150809_N0207_R025_T22WEV_20190509T184714	09-May-19	S2	0.6
S2B_MSIL1C_20190509T150809_N0207_R025_T22WFV_20190509T184714	09-May-19	S2	13.4
S2A_MSIL1C_20190517T151911_N0207_R068_T22WEV_20190517T171614	17-May-19	S2	29.3
S2A_MSIL1C_20190517T151911_N0207_R068_T22WFV_20190517T171614	17-May-19	S2	0.0
S2B_MSIL1C_20190519T150809_N0207_R025_T22WEV_20190519T184819	19-May-19	S2	6.3
S2B_MSIL1C_20190519T150809_N0207_R025_T22WFV_20190519T184819	19-May-19	S2	7.9
S2B_MSIL1C_20190522T151919_N0207_R068_T22WEV_20190522T171829	22-May-19	S2	0.0
S2B_MSIL1C_20190522T151919_N0207_R068_T22WFV_20190522T171829	22-May-19	S2	0.0
LC08_L1TP_008013_20190523_20200830_02_T1	23-May-19	L8	4.5
S2A_MSIL1C_20190524T150911_N0207_R025_T22WEV_20190524T170812	24-May-19	S2	7.9
S2A_MSIL1C_20190524T150911_N0207_R025_T22WFV_20190524T170812	24-May-19	S2	17.3
LC08_L1TP_006013_20190525_20200828_02_T1	25-May-19	L8	0.7
S2B_MSIL1C_20190526T150019_N0207_R125_T22WEV_20190526T183734	26-May-19	S2	0.6
S2B_MSIL1C_20190526T150019_N0207_R125_T22WFV_20190526T183734	26-May-19	S2	79.1

S2A_MSIL1C_20190527T151911_N0207_R068_T22WEV_20190527T202622	27-May-19	S2	0.1
S2A_MSIL1C_20190527T151911_N0207_R068_T22WFV_20190527T202622	27-May-19	S2	0.0
S2B_MSIL1C_20190529T150809_N0207_R025_T22WEV_20190529T201431	29-May-19	S2	7.6
S2B_MSIL1C_20190529T150809_N0207_R025_T22WFV_20190529T201431	29-May-19	S2	94.1
S2A_MSIL1C_20190531T145921_N0207_R125_T22WEV_20190531T165832	31-May-19	S2	3.7
S2A_MSIL1C_20190531T145921_N0207_R125_T22WFV_20190531T165832	31-May-19	S2	22.6
S2B_MSIL1C_20190601T151809_N0207_R068_T22WEV_20190601T184204	01-Jun-19	S2	13.6
S2B_MSIL1C_20190601T151809_N0207_R068_T22WFV_20190601T184204	01-Jun-19	S2	0.0
S2B_MSIL1C_20190605T150019_N0207_R125_T22WEV_20190605T200407	05-Jun-19	S2	10.1
S2B_MSIL1C_20190605T150019_N0207_R125_T22WFV_20190605T200407	05-Jun-19	S2	94.0
S2B_MSIL1C_20190608T150809_N0207_R025_T22WEV_20190608T184815	08-Jun-19	S2	10.1
S2B_MSIL1C_20190608T150809_N0207_R025_T22WFV_20190608T184815	08-Jun-19	S2	14.1
LC08_L1TP_006013_20190610_20200828_02_T1	10-Jun-19	L8	1.2
S2A_MSIL1C_20190613T150911_N0207_R025_T22WEV_20190613T170639	13-Jun-19	S2	52.6
S2A_MSIL1C_20190613T150911_N0207_R025_T22WFV_20190613T170639	13-Jun-19	S2	0.9
LC08_L1TP_007013_20190617_20200828_02_T1	17-Jun-19	L8	10.5
S2A_MSIL1C_20190620T145921_N0207_R125_T22WEV_20190620T183937	20-Jun-19	S2	0.1
S2A_MSIL1C_20190620T145921_N0207_R125_T22WFV_20190620T183937	20-Jun-19	S2	0.0
S2A_MSIL1C_20190703T150921_N0207_R025_T22WEV_20190703T184907	03-Jul-19	S2	13.9
S2A_MSIL1C_20190703T150921_N0207_R025_T22WFV_20190703T184907	03-Jul-19	S2	31.8
S2A_MSIL1C_20190707T144921_N0207_R082_T22WEV_20190707T164746	07-Jul-19	S2	23.2
S2A_MSIL1C_20190707T144921_N0207_R082_T22WFV_20190707T164746	07-Jul-19	S2	3.8
S2B_MSIL1C_20190708T150809_N0208_R025_T22WEV_20190708T185223	08-Jul-19	S2	0.0
S2B_MSIL1C_20190708T150809_N0208_R025_T22WFV_20190708T185223	08-Jul-19	S2	0.1
S2B_MSIL1C_20190712T144759_N0208_R082_T22WEV_20190712T164159	12-Jul-19	S2	0.0
S2B_MSIL1C_20190712T144759_N0208_R082_T22WFV_20190712T164159	12-Jul-19	S2	0.0
S2B_MSIL1C_20190715T150019_N0208_R125_T22WEV_20190715T200825	15-Jul-19	S2	0.3
S2B_MSIL1C_20190715T150019_N0208_R125_T22WFV_20190715T200825	15-Jul-19	S2	5.9
S2B_MSIL1C_20190725T150019_N0208_R125_T22WEV_20190725T183725	25-Jul-19	S2	21.1
S2B_MSIL1C_20190725T150019_N0208_R125_T22WFV_20190725T183725	25-Jul-19	S2	0.8
S2B_MSIL1C_20190801T144759_N0208_R082_T22WEV_20190801T164915	01-Aug-19	S2	0.0
S2B_MSIL1C_20190801T144759_N0208_R082_T22WFV_20190801T164915	01-Aug-19	S2	1.8
S2A_MSIL1C_20190802T150921_N0208_R025_T22WEV_20190802T170710	02-Aug-19	S2	0.0
S2A_MSIL1C_20190802T150921_N0208_R025_T22WFV_20190802T170710	02-Aug-19	S2	7.3

S2B_MSIL1C_20190804T150019_N0208_R125_T22WEV_20190804T165643	04-Aug-19	S2	4.2
S2B_MSIL1C_20190804T150019_N0208_R125_T22WFV_20190804T165643	04-Aug-19	S2	17.7
S2A_MSIL1C_20190809T145921_N0208_R125_T22WEV_20190809T165708	09-Aug-19	S2	0.6
S2A_MSIL1C_20190809T145921_N0208_R125_T22WFV_20190809T165708	09-Aug-19	S2	0.0
S2B_MSIL1C_20190811T144759_N0208_R082_T22WEV_20190811T164246	11-Aug-19	S2	0.0
S2B_MSIL1C_20190811T144759_N0208_R082_T22WFV_20190811T164246	11-Aug-19	S2	0.0
S2A_MSIL1C_20190812T150921_N0208_R025_T22WEV_20190812T201743	12-Aug-19	S2	0.0
S2A_MSIL1C_20190812T150921_N0208_R025_T22WFV_20190812T201743	12-Aug-19	S2	11.3
S2B_MSIL1C_20190817T150809_N0208_R025_T22WEV_20190817T202054	17-Aug-19	S2	52.7
S2B_MSIL1C_20190817T150809_N0208_R025_T22WFV_20190817T202054	17-Aug-19	S2	16.4
LC08_L1TP_007013_20190820_20200827_02_T1	20-Aug-19	L8	11.1
S2B_MSIL1C_20190824T150009_N0208_R125_T22WEV_20190824T201004	24-Aug-19	S2	5.2
S2B_MSIL1C_20190824T150009_N0208_R125_T22WFV_20190824T201004	24-Aug-19	S2	27.8
S2A_MSIL1C_20190825T151911_N0208_R068_T22WEV_20190825T185502	25-Aug-19	S2	3.4
S2A_MSIL1C_20190825T151911_N0208_R068_T22WFV_20190825T185502	25-Aug-19	S2	0.0
LC08_L1TP_008013_20190827_20200826_02_T1	27-Aug-19	L8	42.5
S2A_MSIL1C_20190829T145921_N0208_R125_T22WEV_20190829T183408	29-Aug-19	S2	11.2
S2A_MSIL1C_20190829T145921_N0208_R125_T22WFV_20190829T183408	29-Aug-19	S2	99.5
S2B_MSIL1C_20190830T151809_N0208_R068_T22WEV_20190830T185641	30-Aug-19	S2	33.3
S2A_MSIL1C_20190901T150911_N0208_R025_T22WEV_20190901T170819	01-Sep-19	S2	34.5
S2A_MSIL1C_20190901T150911_N0208_R025_T22WFV_20190901T170819	01-Sep-19	S2	24.2
S2B_MSIL1C_20190909T151809_N0208_R068_T22WEV_20190909T202539	09-Sep-19	S2	14.6
S2A_MSIL1C_20190918T150011_N0208_R125_T22WEV_20190918T201931	18-Sep-19	S2	24.1
S2A_MSIL1C_20190918T150011_N0208_R125_T22WFV_20190918T201931	18-Sep-19	S2	98.3
S2B_MSIL1C_20190923T150009_N0208_R125_T22WEV_20190923T200537	23-Sep-19	S2	21.1
S2B_MSIL1C_20190923T150009_N0208_R125_T22WFV_20190923T200537	23-Sep-19	S2	26.7
S2B_MSIL1C_20190926T150949_N0208_R025_T22WEV_20190926T184849	26-Sep-19	S2	0.5
S2B_MSIL1C_20190926T150949_N0208_R025_T22WFV_20190926T184849	26-Sep-19	S2	0.0
S2A_MSIL1C_20190928T150011_N0208_R125_T22WEV_20190928T165931	28-Sep-19	S2	0.0
S2A_MSIL1C_20190928T150011_N0208_R125_T22WFV_20190928T165931	28-Sep-19	S2	18.8

Table A.2: Maximum areal coverage and median elevation a.s.l. of all SGL, channel and slush features in 2018 (left) and 2019 (right).

	2018	2019
Maximum areal coverage		
SGLs	1.5%	2.1%
Channels	4.5%	6.4%
Slush	0.3%	12.3%
Median elevation		
SGLs	1350 m	1250 m
Channels	1350 m	1500 m
Slush	1600 m	1700 m

Section A.1.

Supplementary animations 1 and 2 can be found here:
https://tc.copernicus.org/articles/19/1047/2025/tc-19-1047-2025-supplement.zip

Appendix B

Supervised classification of slush on the Greenland Ice Sheet using Sentinel-2 satellite imagery

Table B.1: List of selected S2 images used for training and validation across basins. Image IDs correspond to GEE asset identifiers from the 'COPERNICUS/S2' collection (Gorelick et al., 2017).

Sentinel 2 Image ID
ee.Image('COPERNICUS/S2/20190721T151809_20190721T151812_T23WMS')
ee.Image('COPERNICUS/S2/20220704T140739_20220704T140740_T25WDS')
ee.Image('COPERNICUS/S2/20230716T185919_20230716T185920_T21XWK')
ee.Image('COPERNICUS/S2/20220825T180919_20220825T181113_T19XEH')
ee.Image('COPERNICUS/S2/20190802T164901_20190802T164904_T26XMP')
ee.Image('COPERNICUS/S2/20210621T144749_20210621T144900_T22WES')
ee.Image('COPERNICUS/S2/20190801T144759_20190801T144759_T22WFV')
ee.Image('COPERNICUS/S2/20190713T150921_20190713T150916_T26XNP')
ee.Image('COPERNICUS/S2/20230703T161831_20230703T161832_T21XWC')
ee.Image('COPERNICUS/S2/20200726T180919_20200726T180916_T20XMN')
ee.Image('COPERNICUS/S2/20210805T135729_20210805T135732_T25WFS')
ee.Image('COPERNICUS/S2/20230702T150801_20230702T150959_T22WEC')
ee.Image('COPERNICUS/S2/20180604T143919_20180604T143920_T26XNJ')
ee.Image('COPERNICUS/S2/20200613T161829_20200613T161831_T21XWD')
ee.Image('COPERNICUS/S2/20160503T180920_20160503T231352_T20XMP')
ee.Image('COPERNICUS/S2/20230501T142741_20230501T142742_T23WPN')
ee.Image('COPERNICUS/S2/20170616T151911_20170616T152036_T22WED')
ee.Image('COPERNICUS/S2/20160516T145922_20160516T150205_T22WEA')
ee.Image('COPERNICUS/S2/20210822T143931_20210822T144327_T22WFS')
ee.Image('COPERNICUS/S2/20180913T145911_20180913T145910_T26XNM')
ee.Image('COPERNICUS/S2/20230815T171859_20230815T171900_T20XML')
ee.Image('COPERNICUS/S2/20220816T164851_20220816T164854_T25XDL')

ee.Image('COPERNICUS/S2/20210823T141011_20210823T141007_T24WWV')
ee.Image('COPERNICUS/S2/20170815T151911_20170815T152131_T22WFB')

Appendix C

Assessing the performance of machine learning algorithms in Google Earth Engine for cloud-based supraglacial meltwater feature classification on the Greenland Ice Sheet

Table C.1: Sentinel 2 image images used for training and validation. Image IDs correspond to GEE asset identifiers from the 'COPERNICUS/S2' collection (Gorelick et al., 2017).

S2 Image ID
ee.Image('COPERNICUS/S2/20170530T152911_20170530T152909_T22WEB')
ee.Image('COPERNICUS/S2/20170531T145921_20170531T150133_T22WEA')
ee.Image('COPERNICUS/S2/20170531T145921_20170531T150133_T22WEV')
ee.Image('COPERNICUS/S2/20170531T145921_20170531T150133_T22WFA')
ee.Image('COPERNICUS/S2/20170531T145921_20170531T150133_T22WFV')
ee.Image('COPERNICUS/S2/20170612T153911_20170612T153906_T26XNN')
ee.Image('COPERNICUS/S2/20170615T141011_20170615T141200_T25WDS')
ee.Image('COPERNICUS/S2/20170619T234731_20170619T234734_T21XWB')
ee.Image('COPERNICUS/S2/20170710T145911_20170710T150120_T22WEA')
ee.Image('COPERNICUS/S2/20170710T145911_20170710T150120_T22WEV')
ee.Image('COPERNICUS/S2/20170710T145911_20170710T150120_T22WFA')
ee.Image('COPERNICUS/S2/20170722T171901_20170722T171857_T20XNK')
ee.Image('COPERNICUS/S2/20170723T150911_20170723T151115_T22WEB')
ee.Image('COPERNICUS/S2/20170724T143921_20170724T143924_T27XVE')
ee.Image('COPERNICUS/S2/20170724T175911_20170724T175913_T20XMN')
ee.Image('COPERNICUS/S2/20170730T145921_20170730T150103_T22WFB')
ee.Image('COPERNICUS/S2/20170730T145921_20170730T145915_T26XNN')
ee.Image('COPERNICUS/S2/20170731T160901_20170731T160903_T21XWB')
ee.Image('COPERNICUS/S2/20170809T145921_20170809T150205_T22WEV')

ee.Image('COPERNICUS/S2/20170812T150911_20170812T150912_T22WEA')
ee.Image('COPERNICUS/S2/20170812T150911_20170812T150912_T22WEV')
ee.Image('COPERNICUS/S2/20170812T150911_20170812T150912_T22WFA')
ee.Image('COPERNICUS/S2/20170812T150911_20170812T150912_T22WFV')
ee.Image('COPERNICUS/S2/20170825T165851_20170825T170139_T20XNK')
ee.Image('COPERNICUS/S2/20170830T142931_20170830T142933_T27XVE')
ee.Image('COPERNICUS/S2/20170908T145911_20170908T150039_T22WEA')
ee.Image('COPERNICUS/S2/20170908T145911_20170908T150039_T22WEV')
ee.Image('COPERNICUS/S2/20170908T145911_20170908T150039_T22WFA')
ee.Image('COPERNICUS/S2/20170908T145911_20170908T150039_T22WFV')
ee.Image('COPERNICUS/S2/20180526T145921_20180526T150107_T22WEA')
ee.Image('COPERNICUS/S2/20180526T145921_20180526T150107_T22WEV')
ee.Image('COPERNICUS/S2/20180526T145921_20180526T150107_T22WFA')
ee.Image('COPERNICUS/S2/20180526T145921_20180526T150107_T22WFV')
ee.Image('COPERNICUS/S2/20180913T145911_20180913T145910_T22WEA')
ee.Image('COPERNICUS/S2/20180913T145911_20180913T145910_T22WEV')
ee.Image('COPERNICUS/S2/20180913T145911_20180913T145910_T22WFA')
ee.Image('COPERNICUS/S2/20180913T145911_20180913T145910_T22WFV')
ee.Image('COPERNICUS/S2/20190601T160901_20190601T160904_T27XVH')
ee.Image('COPERNICUS/S2/20190712T153911_20190712T154146_T21XXA')
ee.Image('COPERNICUS/S2/20190713T164901_20190713T164901_T27XVJ')
ee.Image('COPERNICUS/S2/20190901T150911_20190901T150911_T22WEA')
ee.Image('COPERNICUS/S2/20190901T150911_20190901T150911_T22WEV')
ee.Image('COPERNICUS/S2/20190901T150911_20190901T150911_T22WFA')
ee.Image('COPERNICUS/S2/20190901T150911_20190901T150911_T22WFA')
ee.Image('COPERNICUS/S2/20190901T150911_20190901T150911_T22WFV')
ee.Image('COPERNICUS/S2/20190903T154911_20190903T154905_T27XVJ')
ee.Image('COPERNICUS/S2/20200518T150921_20200518T150916_T22WEB')

ee.Image('COPERNICUS/S2/20200528T150921_20200528T150917_T22WEV')
ee.Image('COPERNICUS/S2/20200623T170901_20200623T170857_T20XNK')
ee.Image('COPERNICUS/S2/20200702T142001_20200702T141956_T27XVE')
ee.Image('COPERNICUS/S2/20200717T150921_20200717T150916_T22WEB')
ee.Image('COPERNICUS/S2/20200717T150921_20200717T150916_T22WEV')
ee.Image('COPERNICUS/S2/20200717T150921_20200717T150916_T26XNN')
ee.Image('COPERNICUS/S2/20200718T161911_20200718T161905_T21XWB')
ee.Image('COPERNICUS/S2/20200803T145921_20200803T145920_T27XVH')
ee.Image('COPERNICUS/S2/20180622T185919_20180622T185915_T20XNQ')
ee.Image('COPERNICUS/S2/20180710T150009_20180710T150006_T22WEA')
ee.Image('COPERNICUS/S2/20180710T150009_20180710T150006_T22WEV')
ee.Image('COPERNICUS/S2/20180710T150009_20180710T150006_T22WFA')
ee.Image('COPERNICUS/S2/20180710T150009_20180710T150006_T22WFV')
ee.Image('COPERNICUS/S2/20180715T140739_20180715T140733_T24WWU')
ee.Image('COPERNICUS/S2/20180819T145959_20180819T150250_T22WEA')
ee.Image('COPERNICUS/S2/20180819T145959_20180819T150250_T22WEV')
ee.Image('COPERNICUS/S2/20180819T145959_20180819T150250_T22WFA')
ee.Image('COPERNICUS/S2/20180819T145959_20180819T150250_T22WFV')
ee.Image('COPERNICUS/S2/20180822T150749_20180822T150752_T22WEB')
ee.Image('COPERNICUS/S2/20180921T151119_20180921T151122_T22WEV')
ee.Image('COPERNICUS/S2/20190529T150809_20190529T151155_T22WEA')
ee.Image('COPERNICUS/S2/20190529T150809_20190529T151155_T22WEV')
ee.Image('COPERNICUS/S2/20190529T150809_20190529T151155_T22WFA')
ee.Image('COPERNICUS/S2/20190529T150809_20190529T151155_T22WFV')
ee.Image('COPERNICUS/S2/20190601T151809_20190601T151812_T27XVJ')
ee.Image('COPERNICUS/S2/20190613T141749_20190613T141745_T24WXV')
ee.Image('COPERNICUS/S2/20190708T150809_20190708T150808_T22WEA')
ee.Image('COPERNICUS/S2/20190708T150809_20190708T150808_T22WEV')

ee.Image('COPERNICUS/S2/20190708T150809_20190708T150808_T22WFA')
ee.Image('COPERNICUS/S2/20190708T150809_20190708T150808_T22WFV')
ee.Image('COPERNICUS/S2/20190713T155829_20190713T155829_T27XVH')
ee.Image('COPERNICUS/S2/20190804T150019_20190804T150015_T22WEA')
ee.Image('COPERNICUS/S2/20190804T150019_20190804T150015_T22WEV')
ee.Image('COPERNICUS/S2/20190804T150019_20190804T150015_T22WFA')
ee.Image('COPERNICUS/S2/20190804T150019_20190804T150015_T22WFV')
ee.Image('COPERNICUS/S2/20190813T152819_20190813T152814_T27XVH')
ee.Image('COPERNICUS/S2/20190813T152819_20190813T152814_T27XVJ')
ee.Image('COPERNICUS/S2/20190903T150009_20190903T150010_T27XVH')
ee.Image('COPERNICUS/S2/20200614T140739_20200614T140737_T26WME')
ee.Image('COPERNICUS/S2/20200620T142749_20200620T142745_T27XVE')
ee.Image('COPERNICUS/S2/20200718T170849_20200718T170849_T20XNK')
ee.Image('COPERNICUS/S2/20200905T155829_20200905T160134_T21XWB')
ee.Image('COPERNICUS/S2/20200909T153819_20200909T153853_T22WED')
ee.Image('COPERNICUS/S2/20200909T153819_20200909T153853_T26XNN')

Table C.2: Best hyperparameters and corresponding outer accuracy and kappa values for each classifier across five cross-validation folds

	Best Hyperparameters	**Outer Accuracy**	**Outer Kappa**
CART			
1	{minLeafPopulation=4.0, maxNodes=200.0}	0.961827	0.923646
2	{minLeafPopulation=4.0, maxNodes=200.0}	0.95606	0.912119
3	{minLeafPopulation=4.0, maxNodes=200.0}	0.958199	0.916369
4	{minLeafPopulation=3.0, maxNodes=200.0}	0.954168	0.908347
5	{minLeafPopulation=3.0, maxNodes=200.0}	0.954585	0.909181
GBDT			
1	{seed=3, numberOfTrees=150.0, samplingRate=0.9, maxNodes=150.0, shrinkage=0.2}	0.977096	0.954189

2	{seed=3, numberOfTrees=150.0, samplingRate=0.9, maxNodes=150.0, shrinkage=0.2}	0.972912	0.945826
3	{seed=2, numberOfTrees=200.0, samplingRate=0.7, maxNodes=200.0, shrinkage=0.1}	0.978481	0.956947
4	{seed=2, numberOfTrees=200.0, samplingRate=0.7, maxNodes=200.0, shrinkage=0.1}	0.974692	0.949384
5	{seed=2, numberOfTrees=200.0, samplingRate=0.7, maxNodes=200.0, shrinkage=0.1}	0.97654	0.953079
KNN			
1	{metric=EUCLIDEAN, searchMethod=AUTO, k=5}	0.959324	0.918636
2	{metric=EUCLIDEAN, searchMethod=AUTO, k=5}	0.950568	0.90115
3	{metric=EUCLIDEAN, searchMethod=AUTO, k=3}	0.956963	0.913872
4	{metric=EUCLIDEAN, searchMethod=AUTO, k=5}	0.956434	0.912884
5	{metric=EUCLIDEAN, searchMethod=AUTO, k=5}	0.955464	0.910933
ME			
1	{randomTestPoints=5.0, betaMultiplier=1.0, doClamp=false, extrapolate=false}	0.95219	0.904385
2	{randomTestPoints=5.0, betaMultiplier=1.0, doClamp=false, extrapolate=false}	0.944576	0.889142
3	{randomTestPoints=5.0, betaMultiplier=1.0, doClamp=false, extrapolate=false}	0.949542	0.899078
4	{randomTestPoints=5.0, betaMultiplier=1.0, doClamp=false, extrapolate=false}	0.949761	0.899499
5	{randomTestPoints=5.0, betaMultiplier=1.0, doClamp=false, extrapolate=false}	0.951574	0.903132
RF			
1	{minLeafPopulation=4.0, seed=1, numberOfTrees=200.0, bagFraction=0.5, maxNodes=200.0, variablesPerSplit=4.0}	0.965457	0.930902
2	{minLeafPopulation=4.0, seed=1, numberOfTrees=200.0, bagFraction=0.5, maxNodes=200.0, variablesPerSplit=4.0}	0.955436	0.910883

3	{minLeafPopulation=4.0, seed=1, numberOfTrees=200.0, bagFraction=0.5, maxNodes=200.0, variablesPerSplit=4.0}	0.964259	0.928477
4	{minLeafPopulation=4.0, seed=1, numberOfTrees=200.0, bagFraction=0.5, maxNodes=200.0, variablesPerSplit=4.0}	0.961974	0.923955
5	{minLeafPopulation=4.0, seed=1, numberOfTrees=200.0, bagFraction=0.5, maxNodes=200.0, variablesPerSplit=4.0}	0.959854	0.919715
SVM			
1	{svmType = 'C_SVC', kernelType: 'Linear', shrinking=true, cost=10, decisionProcedure=Voting}	0.950688	0.901367
2	{svmType = 'C_SVC', kernelType: 'Linear', shrinking=false, cost=10, decisionProcedure=Margin}	0.942329	0.88467
3	{svmType = 'C_SVC', kernelType: 'Linear', shrinking=true, cost=10, decisionProcedure=Voting}	0.950408	0.900771
4	{svmType = 'C_SVC', kernelType: 'Linear', shrinking=false, cost=10, decisionProcedure=Margin}	0.947746	0.895495
5	{svmType = 'C_SVC', kernelType: 'Linear', shrinking=true, cost=10, decisionProcedure=Voting}	0.946682	0.89337

References

Alley, R. B.: Towards a hydrological model for computerized ice-sheet simulations, Hydrological Processes, 10, 649–660, https://doi.org/10.1002/(SICI)1099-1085(199604)10:4<649::AID-HYP397>3.0.CO;2-1, 1996.

Alley, R., T. Dupont, B. Parizek, and S. Anandakrishnan (2005), Access of surface meltwater to beds of sub-freezing glaciers: Preliminary insights, Ann. Glaciol., 40, 8–14.

Arndt, P. S. and Fricker, H. A.: A framework for automated supraglacial lake detection and depth retrieval in ICESat-2 photon data across the Greenland and Antarctic ice sheets, The Cryosphere, 18, 5173–5206, https://doi.org/10.5194/tc-18-5173-2024, 2024.

Arnold, N. S., Banwell, A. F., and Willis, I. C.: High-resolution modelling of the seasonal evolution of surface water storage on the Greenland Ice Sheet, The Cryosphere, 8, 1149–1160, https://doi.org/10.5194/tc-8-1149-2014, 2014.

Arthur, J. F., Shackleton, C., Moholdt, G., Matsuoka, K., and van Oostveen, J.: Evidence of active subglacial lakes under a slowly moving coastal region of the Antarctic Ice Sheet, The Cryosphere, 19, 375–392, https://doi.org/10.5194/tc-19-375-2025, 2025.

Arthur, J. F., Stokes, C. R., Jamieson, S. S. R., Carr, J. R., and Leeson, A. A.: Distribution and seasonal evolution of supraglacial lakes on Shackleton Ice Shelf, East Antarctica, The Cryosphere, 14, 4103–4120, https://doi.org/10.5194/tc-14-4103-2020, 2020.

Bamber, J. L., Westaway, R. M., Marzeion, B., and Wouters, B.: The land ice contribution to sea level during the satellite era, Environmental Research Letters, 13, 063008, https://doi.org/10.1088/1748-9326/aac2f0, 2018.

Banwell, A. F., Arnold, N. S., Willis, I. C., Tedesco, M., and Ahlstrøm, A. P.: Modeling supraglacial water routing and lake filling on the Greenland Ice Sheet, J. Geophys. Res., 117, F04012, https://doi. org/10. 1029/2012JF002393, 2012.

Banwell, A. F., Caballero, M., Arnold, N., Glasser, N., Mac Cathles, L., and MacAyeal, D.: Supraglacial lakes on the Larsen B ice shelf, Antarctica, and at Paakitsoq, West Greenland: A comparative study. Annals of Glaciology, 55(66), 1-8, https://doi. org/10. 3189/2014AoG66A049, 2014.

Banwell, A. F., Datta, R. T., Dell, R. L., Moussavi, M., Brucker, L., Picard, G., Shuman, C. A., and Stevens, L. A.: The 32-year record-high surface melt in 2019/2020 on the northern George VI Ice Shelf, Antarctic Peninsula, The Cryosphere, 15, 909–925, https://doi.org/10.5194/tc-15-909-2021, 2021.

Banwell, A. F., Hewitt, I., Willis, I. C., and Arnold, N.: Moulin density controls drainage development beneath the Greenland ice sheet, J. Geophys. Res. Earth Surf., 121, 2248–2269, https://doi. org/10. 1002/2015JF003801, 2016.

Banwell, A. F., I. C. Willis, I. C., and Arnold N. S.: Modeling subglacial water routing at Paakitsoq, W Greenland, J. Geophys. Res. Earth Surf., 118, 1282–1295, https://doi. org/10. 1002/jgrf. 20093, 2013.

Banwell, A. F., Willis, I. C., Macdonald, G. J., Goodsell, B., and MacAyeal, D. R.: Direct measurements of ice-shelf flexure caused by surface meltwater ponding and drainage. Nat Commun 10, 730, https://doi. org/10. 1038/s41467-019-08522-5, 2019.

Bartholomaus, T. C., Anderson, R. S., and Anderson, S. P.: Response of glacier basal motion to transient water storage, Nature Geoscience, 1, 33–37, https://doi.org/10.1038/ngeo.2007.52, 2008.

Bartholomew, I., Nienow, P., Mair, D., Hubbard, A., King, M. A., and Sole, A.: Seasonal evolution of subglacial drainage and acceleration in a Greenland outlet glacier, Nat. Geosci., 3, 408–411, https://doi. org/10. 1038/ngeo863, 2010.

Bartholomew, I., Nienow, P., Sole, A., Mair, D., Cowton, T., and King, M. A.: Short-term variability in Greenland Ice Sheet motion forced by time-varying meltwater drainage: Implications for the relationship between subglacial drainage system behavior and ice velocity, J. Geophys. Res., 117, F03002, https://doi:10.1029/2011JF002220, 2012.

Beckmann, J. and Winkelmann, R.: Effects of extreme melt events on ice flow and sea level rise of the Greenland Ice Sheet, The Cryosphere, 17, 3083–3099, https://doi.org/10.5194/tc-17-3083-2023, 2023.

Bell, R., Chu, W., Kingslake, J., Das, I., Tedesco, M., Tinto, K. J., Zappa, C. J., Frezzotti, M., Boghosian, A., and Lee, W. S.: Antarctic ice shelf potentially stabilized by export of meltwater in surface river. Nature 544, 344–348, https://doi. org/10. 1038/nature22048, 2017.

Benedek, C. L. and Willis, I. C.: Winter drainage of surface lakes on the Greenland Ice Sheet from Sentinel-1 SAR imagery, The Cryosphere, 15, 1587–1606, https://doi.org/10.5194/tc-15-1587-2021, 2021.

Benn, D., and Evans, D. J. A.: Glaciers and Glaciation, 2nd ed., Hodder Education, London, 2010.

Benson, C. S.: Stratigraphic studies in the snow and firn of the Greenland ice sheet, U.S. Army Snow, Ice and Permafrost Research Establishment, Corps of Engineers, Research Report 70, 120 pp., 1962.

Berk, R. A.: Classification and regression trees (CART), in: Statistical learning from a regression perspective, Springer International Publishing, Cham, 129–186, https://doi.org/10.1007/978-3-319-44048-4_3, 2016.

Bishop, C. M.: Pattern recognition and machine learning, Springer, New York, 2006.

Bonsoms, J., Oliva, M., López-Moreno, J. I., and Fettweis, X.: Rising extreme meltwater trends in Greenland Ice Sheet (1950–2022): Surface energy balance and large-scale circulation changes. J. Clim., 37, 4851–4866, https://doi.org/10.1175/JCLI-D-23-0396.1, 2024.

Boulton, G. S., and Jones, A. S.: Stability of temperate ice caps and ice sheets resting on beds of deformable sediment, Journal of Glaciology, 24, 29–43, https://doi.org/10.1017/S0022143000014623, 1979.

Bowling, J. S., Livingstone, S. J., Sole, A. J., and Chu, W.: Distribution and dynamics of Greenland subglacial lakes, Nature Communications, 10, 2810, https://doi.org/10.1038/s41467-019-10821-w, 2019.

Box, J. E. and Ski, K.: Remote sounding of Greenland supra-glacial melt lakes: Implications for subglacial hydraulics, Journal of glaciology, 53(181), 257−264, https://doi. org/10. 3189/172756507782202883, 2007.

Box, J. E., Fettweis, X., Stroeve, J. C., Tedesco, M., Hall, D. K., and Steffen, K.: Greenland ice sheet albedo feedback: thermodynamics and atmospheric drivers, The Cryosphere, 6, 821–839, https://doi.org/10.5194/tc-6-821-2012, 2012.

Box, J. E., Hubbard, A., Bahr, D. B., Colgan, W. T., Fettweis, X., Mankoff, K. D., Wehrlé, A., Noël, B., van den Broeke, M. R., Wouters, B., Bjørk, A. A., and Fausto, R. S.: Greenland ice sheet climate disequilibrium and committed sea-level rise, Nature Climate Change, 12, 808–813, https://doi.org/10.1038/s41558-022-01441-2, 2022.

Box, J. E., Yang, L., Bromwich, D. H., and Bai, L.-S.: Greenland Ice Sheet surface air temperature variability: 1840–2007, Journal of Climate, 22, 4029–4049, https://doi.org/10.1175/2009JCLI2816.1, 2009.

Brabec, B., and Meister, R.: A nearest-neighbor model for regional avalanche forecasting, Annals of Glaciology, 32, 130–134, https://doi.org/10.3189/172756401781819247, 2001.

Breiman, L., Friedman, J., Olshen, R. A., and Stone, C. J.: Classification and Regression Trees, 1st Edn., Chapman and Hall/CRC, New York, https://doi.org/10.1201/9781315139470, 1984.

Breiman, L.: Random forests, Mach. Learn., 45, 5–32, https://doi.org/10.1023/A:1010933404324, 2001.

Briner, J. P., Cuzzone, J. K., Badgeley, J. A., Young, N. E., Steig, E. J., Morlighem, M., Schlegel, N.-J., Hakim, G. J., Schaefer, J. M., Johnson, J. V., Lesnek, A. J., Thomas, E. K., Allan, E., Bennike, O., Cluett, A. A., Csatho, B., de Vernal, A., Downs, J., Larour, E., and Nowicki, S.: Rate of mass loss from the Greenland Ice Sheet will exceed Holocene values this century, Nature, 586, 70–74, https://doi.org/10.1038/s41586-020-2742-6, 2020.

Burges, C. J. C.: A tutorial on support vector machines for pattern recognition, Data Mining and Knowledge Discovery, 2, 121–167, 1998.

Cardille, J. A., Crowley, M. A., Saah, D., and Clinton, N. E. (Eds.): Cloud-Based Remote Sensing with Google Earth Engine: Fundamentals and Applications, Springer, Cham, https://doi.org/10.1007/978-3-031-26588-4, 2024.

Catania, G., Neumann, T., and Price, S.: Characterizing englacial drainage in the ablation zone of the Greenland Ice Sheet, Journal of Glaciology, 54, 567–578, https://doi.org/10.3189/002214308786570854, 2008.

Cawley, G. C., and Talbot, N. L. C.: On over-fitting in model selection and subsequent selection bias in performance evaluation, Journal of Machine Learning Research, 11, 2079–2107, 2010.

Chandler, D.M., Hubbard, A.: Widespread partial-depth hydrofractures in ice sheets driven by supraglacial streams, Nat. Geosci, 16, 605–611, https://doi.org/10.1038/s41561-023-01208-0, 2023.

Charalampidis, C., van As, D., Box, J. E., van den Broeke, M. R., Colgan, W. T., Doyle, S. H., Hubbard, A. L., MacFerrin, M., Machguth, H., and Smeets, C. J. P. P.: Changing surface–atmosphere energy exchange and refreezing capacity of the lower accumulation area, West Greenland, The Cryosphere, 9, 2163–2181, https://doi.org/10.5194/tc-9-2163-2015, 2015.

Choukset, A., Thakur, P. K., Sahni, G., Swain, A. K., Aggarwal, S. P., & Kumar, A. S.: Mapping and identification of ice-sheet and glacier features using optical and SAR data in parts of central Dronning Maud Land (cDML), East Antarctica, Polar Science, 30, 100740, https://doi.org/10.1016/j.polar.2021.100740, 2021.

Christoffersen, P., Bougamont, M., Hubbard, A., Doyle, S. H., Grigsby, S., and Pettersson, R.: Cascading lake drainage on the Greenland Ice Sheet triggered by tensile shock and fracture, Nature Communications, 9, 1064, https://doi.org/10.1038/s41467-018-03420-8, 2018.

Chu, V. W.: Greenland ice sheet hydrology: A review, Prog. Phys. Geogr., 38, 19–54, https://doi.org/10.1177/0309133313507075, 2014.

Chudley, T. R., Christoffersen, P., Doyle, S. H., Dowling, T. P. F., Law, R., Schoonman, C. M., Bougamont, M., and Hubbard, B.: Controls on water storage and drainage in crevasses on the Greenland Ice Sheet, J. Geophys. Res. Earth Surf., 126, e2021JF006287, https://doi.org/10.1029/2021JF006287, 2021.

Chudley, T. R., Howat, I. M., King, M. D., and MacKie, E. J.: Increased crevassing across accelerating Greenland Ice Sheet margins, Nature Geoscience, 18, 148–153, https://doi.org/10.1038/s41561-024-01636-6, 2025.

Clerx, N., Machguth, H., Tedstone, A., and van As, D.: Modelling lateral meltwater flow and superimposed ice formation atop Greenland's near-surface ice slabs. J. Glaciol., 70, e54, https://doi.org/10.1017/jog.2024.69, 2024.

Clerx, N., Machguth, H., Tedstone, A., Jullien, N., Wever, N., Weingartner, R., and Roessler, O.: 'In situ measurements of meltwater flow through snow and firn in the accumulation zone of the SW Greenland ice sheet', The Cryosphere, 16, 4379–4401. https://doi.org/10.5194/tc-16-4379-2022, 2022.

Cogley, J. G., Arendt, A. A., Bauder, A., Braithwaite, R. J., Hock, R., Jansson, P., Kaser, G., Möller, M., Nicholson, L., Rasmussen, L. A., and Zemp, M.: Glossary of glacier mass balance and related terms, IHP-VII Technical Documents in Hydrology, International Hydrological Programme, 2010.

Colgan, W., Rajaram, H., Abdalati, W., McCutchan, C., Mottram, R., Moussavi, M. S., and Grigsby, S.: Glacier crevasses: Observations, models, and mass balance implications, Reviews of Geophysics, 54, 119–161, https://doi.org/10.1002/2015RG000504, 2016.

Cook, J. M., Tedstone, A. J., Williamson, C., McCutcheon, J., Hodson, A. J., Dayal, A., Skiles, M., Hofer, S., Bryant, R., McAree, O., McGonigle, A., Ryan, J., Anesio, A. M., Irvine-Fynn, T. D. L., Hubbard, A., Hanna, E., Flanner, M., Mayanna, S., Benning, L. G., van As, D., Yallop, M., McQuaid, J. B., Gribbin, T., and Tranter, M.: Glacier algae accelerate melt rates on the south-western Greenland Ice Sheet, The Cryosphere, 14, 309–330, https://doi.org/10.5194/tc-14-309-2020, 2020.

Copernicus Climate Change Service (C3S): European State of the Climate 2022, Summary, https://climate.copernicus.eu/sites/default/files/custom-uploads/ESOTC2022/PR/ESOTCsummary2022_final.pdf, last access: December 2024.

Corr, D., Leeson, A., McMillan, M., Zhang, C., and Barnes, T.: An inventory of supraglacial lakes and channels across the West Antarctic Ice Sheet, Earth Syst. Sci. Data, 14, 209–228, https://doi. org/10. 5194/essd-14-209-2022, 2022.

Corr, D., Leeson, A., McMillan, M., Zhang, C., and Barnes, T.: An inventory of supraglacial lakes and channels across the West Antarctic Ice Sheet, Earth Syst. Sci. Data, 14, 209–228, https://doi. org/10. 5194/essd-14-209-2022, 2022.

Corr, D.: Monitoring Greenland and Antarctic supraglacial hydrology from space, PhD thesis, Lancaster Environment Centre, Lancaster University, 2023.

Cortes, C., and Vapnik, V.: Support-vector networks, Machine Learning, 20, 273–297, https://doi.org/10.1007/BF00994018, 1995.

Cover, T., and Hart, P.: Nearest neighbor pattern classification, IEEE Transactions on Information Theory, 13, 21–27, 1967.

Covi, F.: Processes in the percolation zone in southwest Greenland: challenges in modeling surface energy balance and melt, and the role of topography in the formation of ice slabs. PhD dissertation, University of Alaska Fairbanks, 2022. Available at: https://hdl.handle.net/11122/13116, 2022.

Cuffey, K. M., and Paterson, W. S. B.: The physics of glaciers, 4th edn., Academic Press, Amsterdam, 704 pp., ISBN: 978-0-12-369461-4, 2010.

Cuffey, K. M., and Paterson, W. S. B.: The Physics of Glaciers, Fourth Edition. Academic Press, Amsterdam, 704 pp., ISBN10: 0123694612, ISBN13: 9780123694614, 2010.

Culberg, R., Michaelides, R. J., and Miller, J. Z.: Sentinel-1 detection of ice slabs on the Greenland Ice Sheet, The Cryosphere, 18, 2531–2555, https://doi.org/10.5194/tc-18-2531-2024, 2024.

Culberg, R., Schroeder, D. M., and Chu, W: Extreme melt season ice layers reduce firn permeability across Greenland, Nat Commun 12, 2336, https://doi. org/10. 1038/s41467-021-22656-5, 2021.

Das, S. B., Joughin, I., Behn, M. D., Howat, I. M., King, M. A., Lizarralde, D., and Bhatia, M. P.: Fracture propagation to the base of the Greenland Ice Sheet during supraglacial lake drainage, Science, 320, 778–781, https://doi. org/10. 1126/science. 1153360, 2008.

Davison, B. J., Sole, A. J., Livingstone, S. J., Cowton, T. R., and Nienow, P. W.: The influence of hydrology on the dynamics of land-terminating sectors of the Greenland Ice Sheet, Front. Earth Sci., 7, 10, https://doi.org/10.3389/feart.2019.00010, 2019.

Dell, R. L., Banwell, A. F., Willis, I. C., Arnold, N. S., Halberstadt, A. R. W., Chudley, T. R., and Pritchard, H. D.: Supervised classification of slush and ponded water on Antarctic ice shelves using Landsat 8 imagery, Journal of Glaciology, 68, 401–414, 2022.

Dell, R., Arnold, N., Willis, I., Banwell, A., Williamson, A., Pritchard, H., and Orr, A.: Lateral meltwater transfer across an Antarctic ice shelf, The Cryosphere, 14, 2313–2330, https://doi. org/10. 5194/tc-14-2313-2020, 2020.

Dell, R.L., Willis, I.C., Arnold, N.S., Banwell, A., de Roda Husman, S.: Substantial contribution of slush to meltwater area across Antarctic ice shelves. Nat. Geosci. 17, 624–630, https://doi.org/10.1038/s41561-024-01466-6, 2024.

Dirscherl, M. C., Dietz, A. J., and Kuenzer, C.: Seasonal evolution of Antarctic supraglacial lakes in 2015–2021 and links to environmental controls, The Cryosphere, 15, 5205–5226, https://doi.org/10.5194/tc-15-5205-2021, 2021a.

Dirscherl, M., Dietz, A. J., Kneisel, C., and Kuenzer, C.: A novel method for automated supraglacial lake mapping in Antarctica using Sentinel-1 SAR imagery and deep learning, Remote Sensing, 13, 197, https://doi.org/10.3390/rs13020197, 2021b.

Dirscherl, M., Dietz, A. J., Kneisel, C., and Kuenzer, C.: Automated Mapping of Antarctic Supraglacial Lakes Using a Machine Learning Approach. Remote Sens., 12, 1203, https://doi.org/10.3390/rs12071203, 2020.

Doyle, S. H., Hubbard, A. L., Dow, C. F., Jones, G. A., Fitzpatrick, A., Gusmeroli, A., Kulessa, B., Lindback, K., Pettersson, R., and Box, J. E.: Ice tectonic deformation during the rapid in situ drainage of a supraglacial lake on the Greenland Ice Sheet, The Cryosphere, 7, 129–140, https://doi.org/10.5194/tc-7-129-2013, 2013.

Doyle, S. H., Hubbard, A., Fitzpatrick, A. A. W., van As, D., Mikkelsen, A. B., Pettersson, R., and Hubbard, B.: Persistent flow acceleration within the interior of the Greenland ice sheet, Geophys. Res. Lett., 41, 899–905, https://doi.org/10.1002/2013GL058933, 2014.

Dumont, M., Brun, E., Picard, G., Michou, M., Libois, Q., Petit, J.-R., Geyer, M., Morin, S., and Josse, B.: Contribution of light-absorbing impurities in snow to Greenland's darkening since 2009, Nature Geoscience, 7, 509–512, https://doi.org/10.1038/ngeo2180, 2014.

Dunmire, D., Banwell, A. F., Wever, N., Lenaerts, J. T. M., and Datta, R. T.: Contrasting regional variability of buried meltwater extent over 2 years across the Greenland Ice Sheet, The Cryosphere, 15, 2983–3005, https://doi.org/10. 5194/tc-15-2983-2021, 2021.

Dunmire, D., Subramanian, A. C., Hossain, E., Gani, M. O., Banwell, A. F., Younas, H., and Myers, B.: Greenland Ice Sheet wide supraglacial lake evolution and dynamics: Insights from the 2018 and 2019 melt seasons, Earth and Space Science, 12, e2024EA003793, https://doi.org/10.1029/2024EA003793, 2025.

Echelmeyer, K., Clarke, T. S., and Harrison, W. D.: Surficial glaciology of Jakobshavns Isbræ, West Greenland: Part I. Surface morphology, Journal of Glaciology, 37, 368–382, https://doi.org/10.3189/S0022143000005803, 1991.

Edwards, T. L., Nowicki, S., Marzeion, B., Hock, R., Goelzer, H., Seroussi, H., Jourdain, N. C., Slater, D., Turner, F., Smith, C. J., McKenna, C. M., Simon, E., Abe-Ouchi, A., Gregory, J. M., Larour, E., Lipscomb, W. H., Payne, A. J., Shepherd, A., Agosta, C., Alexander, P., Albrecht, T., Anderson, B., Asay-Davis, X., Aschwanden, A., Barthel, A., Bliss, A., Calov, R., Chambers, C., Champollion, N., Choi, Y., Cullather, R., Cuzzone, J., Dumas, C., Felikson, D., Fettweis, X., Fujita, K., Galton-Fenzi, B. K., Gladstone, R., Golledge, N. R., Greve, R., Hattermann, T., Hoffman, M. J., Humbert, A., Huss, M., Huybrechts, P., Immerzeel, W., Kleiner, T., Kraaijenbrink, P., Le Clec'h, S., Lee, V., Leguy, G. R., Little, C. M., Lowry, D. P., Malles, J.-H., Martin, D. F., Maussion, F., Morlighem, M., O'Neill, J. F., Nias, I., Pattyn, F., Pelle, T., Price, S., Quiquet, A., Radić, V., Reese, R., Rounce, D. R., Ruckamp, M., Sakai, A., Shafer, C., Schlegel, N.-J., Shannon, S., Smith, R. S., Straneo, F., Sun, S., Tarasov, L., Trusel, L. D., Breedam, J. V., van de Wal, R., van den Broeke, M., Winkelmann, R., Zekollari, H., Zhao, C., Zhang, T., and Zwinger, T.: Projected land ice contributions to 21st century sea level rise, Nature, 593, 74–82, https://doi.org/10.1038/s41586-021-03302-y, 2021.

Enderlin, E. M., Howat, I. M., Jeong, S., Noh, M.-J., van Angelen, J. H., and van den Broeke, M. R.: An improved mass budget for the Greenland ice sheet, Geophysical Research Letters, 41, 866–872, https://doi.org/10.1002/2013GL059010, 2014.

European Space Agency (ESA), Sentinel-2 User Handbook, https://sentinel.esa.int/documents/247904/685211/Sentinel-2_User_Handbook, 2015

Everett, A., Murray, T., Selmes, N., Rutt, I. C., Luckman, A., James, T. D., Clason, C., O'Leary, M., Karunarathna, H., Moloney, V., and Reeve, D. E.: Annual down-glacier drainage of lakes and water-filled crevasses at Helheim Glacier, southeast Greenland, Journal of Geophysical Research: Earth Surface, 121, 1819–1833, https://doi.org/10.1002/2016JF003831, 2016.

Fan, Y., Ke, C.-Q., Luo, L., Shen, X., Livingstone, S. J., and Lea, J. M.: Expansion of supraglacial lake area, volume, and extent on the Greenland Ice Sheet from 1985 to 2023, Journal of Glaciology, 71, e4, https://doi.org/10.1017/jog.2024.87, 2025.

Fausto, R. S., Box, J. E., Vandecrux, B., van As, D., Steffen, K., MacFerrin, M. J., Machguth, H., Colgan, W., Koenig, L. S., McGrath, D., Charalampidis, C., and Braithwaite, R. J.: A snow density dataset for improving surface boundary conditions in Greenland Ice Sheet firn modeling, Front. Earth Sci., 6, 51, https://doi.org/10.3389/feart.2018.00051, 2018.

Feng, D.: Study on information extraction of water body with a new water index (NWI), Science of Surveying and Mapping, 2009, https://api.semanticscholar.org/CorpusID:132605452.

Ferguson, R. I.: Sinuosity of supraglacial streams, Geological Society of America Bulletin, 84, 251–256, https://doi.org/10.1130/0016-7606(1973)84<251:SOSS>2.0.CO;2, 1973.

Fettweis, X., Franco, B., Tedesco, M., van Angelen, J. H., Lenaerts, J. T. M., van den Broeke, M. R., and Gallée, H.: Estimating the Greenland ice sheet surface mass balance contribution to future sea level rise using the regional atmospheric climate model MAR, The Cryosphere, 7, 469–489, https://doi.org/10.5194/tc-7-469-2013, 2013.

Fettweis, X., Tedesco, M., van den Broeke, M. and Ettema, J.: Melting trends over theGreenland ice sheet (1958-2009) from spaceborne microwave data and regional climate Models, The Cryosphere, 5(2), 359-375, ISSN 19940416, doi: 10.5194/tc-5-359-2011, 2011.

Feyisa, G. L., Meilby, H., Fensholt, R., and Proud, S. R.: Automated Water Extraction Index: A new technique for surface water mapping using Landsat imagery, Remote Sensing of Environment, 140, 23–35, https://doi.org/10.1016/j.rse.2013.08.029, 2014.

Fichefet, T., Poncin, C., Goosse, H., Huybrechts, P., Janssens, I., and Le Treut, H.: Implications of changes in freshwater flux from the Greenland ice sheet for the climate of the 21st century, Geophysical Research Letters, 30, 17, https://doi.org/10.1029/2003GL017826, 2003.

Fitzpatrick, A. A. W., Hubbard, A. L., Box, J. E., Quincey, D. J., van As, D., Mikkelsen, A. P. B., Doyle, S. H., Dow, C. F., Hasholt, B., and Jones, G. A.: A decade (2002–2012) of supraglacial lake volume estimates across Russell Glacier, West Greenland, The Cryosphere, 8, 107–121, https://doi.org/10. 5194/tc-8-107-2014, 2014.

Flowers, G. E.: Hydrology and the future of the Greenland Ice Sheet, Nat. Commun., 9, 2729, https://doi.org/10.1038/s41467-018-05002-0, 2018.

Forster, R. R., Box, J. E., van den Broeke, M. R., Miège, C., Burgess, E. W., van Angelen, J. H., Lenaerts, J. T. M., Koenig, L. S., Paden, J., Lewis, C., Gogineni, S. P., Leuschen, C., and McConnell, J. R.: Extensive liquid meltwater storage in firn within the Greenland ice sheet. Nat. Geosci., 7, 95–98, https://doi.org/10.1038/ngeo2043, 2014.

Fricker, H. A., Scambos, T., Bindschadler, R., and Padman, L.: An active subglacial water system in West Antarctica mapped from space, Science, 315, 1544–1548, https://doi.org/10.1126/science.1136897, 2007.

Friedman, J. H.: Greedy function approximation: A gradient boosting machine, The Annals of Statistics, 29, 1189–1232, https://doi.org/10.1214/aos/1013203451, 2001.

Gantayat, P., Banwell, A. F., Leeson, A. A., Lea, J. M., Petersen, D., Gourmelen, N., and Fettweis, X.: A new model for supraglacial hydrology evolution and drainage for the Greenland Ice Sheet (SHED v1.0), Geoscientific Model Development, 16, 5803–5823, https://doi.org/10.5194/gmd-16-5803-2023, 2023.

Ghatkar, J. G., Singh, R. K., and Shanmugam, P.: Classification of algal bloom species from remote sensing data using an extreme gradient boosted decision tree model, International Journal of Remote Sensing, 40, 9412–9438, https://doi.org/10.1080/01431161.2019.1633696, 2019.

Gleason, C. J., Smith, L. C., Chu, V. W., Legleiter, C. J., Pitcher, L. H., Overstreet, B. T., Rennermalm, A. K., Forster, R. R., and Yang, K.: Characterizing supraglacial meltwater channel hydraulics on the Greenland Ice Sheet from in situ observations, Earth Surf. Process. Landf., 41, 2111–2122, https://doi.org/10.1002/esp.3977, 2016.

Gledhill, L. A., and Williamson, A. G.: Inland advance of supraglacial lakes in north-west Greenland under recent climatic warming. Ann. Glaciol., 59, 66–82, https://doi.org/10.1017/aog.2017.31, 2018.

Glen, E., Leeson, A., Banwell, A. F., Maddalena, J., Corr, D., Atkins, O., Noël, B., and McMillan, M.: A comparison of supraglacial meltwater features throughout contrasting melt seasons: southwest Greenland, The Cryosphere, 19, 1047–1066, https://doi.org/10.5194/tc-19-1047-2025, 2025.

Glen, E.: Dataset for: A comparison of supraglacial meltwater features throughout contrasting melt seasons: Southwest Greenland [data set], https://doi.org/10.5281/zenodo.11645884, 2024.

Goelzer, H., Huybrechts, P., Fürst, J. J., Nick, F. M., Andersen, M. L., Edwards, T. L., Fettweis, X., Payne, A. J., and Shannon, S.: Sensitivity of Greenland Ice Sheet Projections to Model Formulations. J. Glaciol., 59, 733–749, https://doi.org/10.3189/2013JoG12J182, 2013.

Goelzer, H., Nowicki, S., Payne, A., Larour, E., Seroussi, H., Lipscomb, W. H., Gregory, J., Abe-Ouchi, A., Shepherd, A., Simon, E., Agosta, C., Alexander, P., Aschwanden, A., Barthel, A., Calov, R., Chambers, C., Choi, Y., Cuzzone, J., Dumas, C., Edwards, T., Felikson, D., Fettweis, X., Golledge, N. R., Greve, R., Humbert, A., Huybrechts, P., Le clec'h, S., Lee, V., Leguy, G., Little, C., Lowry, D. P., Morlighem, M., Nias, I., Quiquet, A., Rückamp, M., Schlegel, N.-J., Slater, D. A., Smith, R. S., Straneo, F., Tarasov, L., van de Wal, R., and van den Broeke, M.: The future sea-level contribution of the Greenland ice sheet: a multi-model ensemble study of ISMIP6, The Cryosphere, 14, 3071–3096, https://doi.org/10.5194/tc-14-3071-2020, 2020.

Gorelick, N., Hancher, M., Dixon, M., Ilyushchenko, S., Thau, D., and Moore, R.: Google Earth Engine: Planetary-scale geospatial analysis for everyone, Remote Sensing of Environment, 202, 18–27, https://doi.org/10.1016/j.rse.2017.06.031, 2017.

Greuell, W. and Knap, W. H.: 'Remote sensing of the albedo and detection of the slush line on the Greenland ice sheet', J. Geophys. Res.-Atmos., 105, 15567–15576, https://doi.org/10.1029, 2000.Halberstadt, A.R.W., Gleason, C.J., Moussavi, M.S., Pope, A., Trusel, L.D., DeConto, R.M. Antarctic Supraglacial Lake Identification Using Landsat-8 Image Classification, Remote Sens, 12, 1327, https://doi.org/10.3390/rs12081327, 2020

Greuell, W., Reijmer, C. H., and Oerlemans, J.: Narrowband-to-broadband albedo conversion for glacier ice and snow based on aircraft and near-surface measurements, Remote Sens. Environ., 82, 48–63, https://doi.org/10.1016/S0034-4257(02)00029-6, 2002.

Groh, A., Horwath, M., Horvath, A., Meister, R., Sørensen, L. S., Barletta, V. R., Forsberg, R., Wouters, B., Ditmar, P., Ran, J., Klees, R., Su, X., Shang, K., Guo, J., Shum, C. K., Schrama, E., and Shepherd, A.: Evaluating GRACE mass change time series for the Antarctic and Greenland Ice Sheet–methods and results, Geosciences, 9, 415, https://doi.org/10.3390/geosciences9100415, 2019.

Gudmundsson, G. H.: Transmission of basal variability to a glacier surface, Journal of Geophysical Research: Solid Earth, 108, B5, https://doi.org/10.1029/2002JB002107, 2003.

Halberstadt, A. R. W., Gleason, C. J., Moussavi, M. S., Pope, A., Trusel, L. D., and DeConto, R. M.: Antarctic Supraglacial Lake Identification Using Landsat-8 Image Classification. Remote Sens., 12, 1327, https://doi.org/10.3390/rs12081327, 2020.

Hall, D. K., Comiso, J. C., DiGirolamo, N. E., Shuman, C. A., Box, J. E., and Koenig, L. S.: Variability in the surface temperature and melt extent of the Greenland ice sheet from MODIS, Geophys. Res. Lett., 40, 2114–2120, https://doi.org/10.1002/grl.50240, 2013.

Hall, D. K., Salomonson, V. V., and Riggs, G. A.: Development of methods for mapping global snow cover using moderate resolution imaging spectroradiometer data, Remote Sensing of Environment, 54, 127-140, https://10. 1016/0034-4257, 1995.

Hanna E, Cappelen J, Fettweis X, Mernild, S. H., Mote, T. L., Mottram, R., Steffen, K., Ballinger, and T. J., Hall, R. J: Greenland surface air temperature changes from 1981 to 2019 and implications for ice-sheet melt and mass-balance change. Int J Climatol. 2021;41 (Suppl. 1), E1336–E1352, https://doi.org/10.1002/joc.6771, 2021.

Hanna, E., Cropper, T. E., Hall, R. J., and Cappelen, J.: Greenland Blocking Index 1851–2015: a regional climate change signal, Int. J. Climatol., 36, 4847–4861, https://doi.org/10.1002/joc.4673, 2016.

Hanna, E., Cropper, T. E., Hall, R. J., Cornes, R. C., and Barriendos, M.: Extended North Atlantic Oscillation and Greenland Blocking Indices 1800–2020 from new meteorological reanalysis, Atmosphere, 13, 436, https://doi.org/10.3390/atmos13030436, 2022.

Hanna, E., Huybrechts, P., Steffen, K., Cappelen, J., Huff, R., Shuman, C., Irvine-Fynn, T., Wise, S., and Griffiths, M.: Increased runoff from melt from the Greenland Ice Sheet: A response to global warming, Journal of Climate, 21, 331–341, https://doi.org/10.1175/2007JCLI1964.1, 2008.

Hanna, E., Mernild, S. H., Cappelen, J., and Steffen, K.: Recent warming in Greenland in a long-term instrumental (1881–2012) climatic context: I. Evaluation of surface air temperature records, Environmental Research Letters, 7, 045404, https://doi.org/10.1088/1748-9326/7/4/045404, 2012.

Hanna, E., Topál, D., Box, J. E., Buzzard, S., Christie, F. D. W., Hvidberg, C., Morlighem, M., De Santis, L., Silvano, A., Colleoni, F., Sasgen, I., Banwell, A. F., van den Broeke, M. R., DeConto, R., De Rydt, J., Goelzer, H., Gossart, A., Gudmundsson, G. H., Lindbäck, K., Miles, B., Mottram, R., Pattyn, F., Reese, R., Rignot, E., Srivastava, A., Sun, S., Toller, J., Tuckett, P. A., and Ultee, L.: Short- and long-term variability of the Antarctic and Greenland ice sheets, Nat. Rev. Earth Environ., 5, 193–210, https://doi.org/10.1038/s43017-024-00438-8, 2024.

Harper, J., Humphrey, N., Pfeffer, W. T., Brown, J., and Fettweis, X.: Greenland ice-sheet contribution to sea-level rise buffered by meltwater storage in firn. Nature, 491, 240–243, https://doi.org/10.1038/nature11566, 2012.

Hastie, T., Tibshirani, R., and Friedman, J.: The Elements of Statistical Learning: Data Mining, Inference, and Prediction, Springer, 2001.

Herron, M. M., and Langway, C. C. Jr.: Firn densification: An empirical model, Journal of Glaciology, 25, 373–385, https://doi.org/10.3189/S0022143000015239, 1980.

Hill, E. A., Carr, J. R., Stokes, C. R., and Gudmundsson, G. H.: Dynamic changes in outlet glaciers in northern Greenland from 1948 to 2015, The Cryosphere, 12, 3243–3263, https://doi.org/10.5194/tc-12-3243-2018, 2018.

Hochreuther, P., Neckel, N., Reimann, N., Humbert, A., and Braun, M.: Fully automated detection of supraglacial lake area for Northeast Greenland using Sentinel-2 time-series, Remote Sensing, 13, 205, https://doi.org/10.3390/rs13020205, 2021.

Hock, R.: Glacier melt: a review of processes and their modelling, Progress in Physical Geography: Earth and Environment, 29, 3, 362–391, https://doi.org/10.1191/0309133305pp453ra, 2005.

Hofer, S., Tedstone, A. J., Fettweis, X., and Bamber, J. L.: Decreasing cloud cover drives the recent mass loss on the Greenland Ice Sheet, Science Advances, 3, e1700584, https://doi.org/10.1126/sciadv.1700584, 2017.

Hoffman, M. J., Andrews, L. C., Price, S. F., Catania, G. A., Neumann, T. A., Lüthi, M. P., Gulley, J., Ryser, C., Hawley, R. L., and Morriss, B.: Greenland subglacial drainage evolution regulated by weakly connected regions of the bed, Nature Communications, 7, 13903, https://doi.org/10.1038/ncomms13903, 2016.

Hoffman, M. J., Catania, G. A., Neumann, T. A., Andrews, L. C., and Rumrill, J. A.: Links between acceleration, melting, and supraglacial lake drainage of the western Greenland Ice Sheet, Journal of Geophysical Research: Earth Surface, 116, F04035, https://doi.org/10.1029/2010JF001934, 2011.

Hoffman, M., Perego, M., Andrews, L., Price, S., Neumann, T., Johnson, J., Catania, G., and Lüthi, M.: Widespread moulin formation during supraglacial lake drainages in Greenland, Geophys. Res. Lett., 45, 778–788, https://doi. org/10. 1002/2017GL075659, 2018.

Holland, D. M., Thomas, R. H., de Young, B., Ribergaard, M. H., and Lyberth, B.: Acceleration of Jakobshavn Isbræ triggered by warm subsurface ocean waters, Nature Geoscience, 1, 659–664, https://doi.org/10.1038/ngeo316, 2008.

Holmes, C. W.: ‘Morphology and Hydrology of the Mint Julep Area, Southwest Greenland. In: Project Mint Julep Investigation of Smooth Ice Areas of the Greenland Ice Cap, 1953; Part II Special Scientific Reports.’, Arctic, Desert, Tropic Information Center; Research Studies Institute; Air University, 1955.

Howat, I. M., Ahn, Y., Joughin, I., van den Broeke, M. R., Lenaerts, J. T. M., and Smith, B.: Mass balance of Greenland's three largest outlet glaciers, 2000–2010, Geophysical Research Letters, 38, L12501, https://doi.org/10.1029/2011GL047565, 2011.

Howat, I. M., de la Peña, S., van Angelen, J. H., Lenaerts, J. T. M., and van den Broeke, M. R.: Brief Communication "Expansion of meltwater lakes on the Greenland Ice Sheet", The Cryosphere, 7, 201–204, https://doi. org/10. 5194/tc-7-201-2013, 2013.

Hu, J., Huang, H., Chi, Z., Cheng, X., Wei, Z., Chen, P., Xu, X., Qi, S., Xu, Y., and Zheng, Y.: Distribution and evolution of supraglacial lakes in Greenland during the 2016–2018 melt seasons, Remote Sensing, 14, 55, 2021.

Huang, J., Lu, J., and Ling, C. X.: Comparing naive Bayes, decision trees, and SVM with AUC and accuracy, in: Proceedings of the Third IEEE International Conference on Data Mining, IEEE, 553–556, 2003.

Hubbard, B. P., Sharp, M. J., Willis, I. C., Nielsen, M. T., and Smart, C. C.: Borehole water-level variations and the structure of the subglacial hydrological system of Haut Glacier d'Arolla, Valais, Switzerland, Journal of Glaciology, 41, 572–583, https://doi.org/10.1017/S0022143000034894, 1995.

Hubbard, B., and Nienow, P.: Alpine subglacial hydrology, Quaternary Science Reviews, 16, 939–955, https://doi.org/10.1016/S0277-3791(97)00031-0, 1997.

Huete, A. R.: A soil-adjusted vegetation index (SAVI), Remote Sensing of Environment, 25, 295–309, https://doi.org/10.1016/0034-4257(88)90106-X, 1988.

Ignéczi, Á., Sole, A. J., Livingstone, S. J., Leeson, A. A., Fettweis, X., Selmes, N., Gourmelen, N., and Briggs, K.: Northeast sector of the Greenland Ice Sheet to undergo the greatest inland expansion of supraglacial lakes during the 21st century, Geophys. Res. Lett., 43, 9729–9738, https://doi.org/10.1002/2016GL070338, 2016.

Ing, R. N., Nienow, P. W., Sole, A. J., Tedstone, A. J., and Mankoff, K. D.: Minimal Impact of Late-Season Melt Events on Greenland Ice Sheet Annual Motion, Geophys. Res. Lett., 51, e2023GL106520, https://doi.org/10.1029/2023GL106520, 2024.

IPCC: Climate Change 2021: The Physical Science Basis. Contribution of Working Group I to the Sixth Assessment Report of the Intergovernmental Panel on Climate Change [Masson-Delmotte, V., Zhai, P., Pirani, A., Connors, S. L., Péan, C., Berger, S., Caud, N., Chen, Y., Goldfarb, L., Gomis, M. I., Huang, M., Leitzell, K., Lonnoy, E., Matthews, J. B. R., Maycock, T. K., Waterfield, T., Yelekçi, O., Yu, R., and Zhou, B. (eds.)], Cambridge University Press, Cambridge, United Kingdom and New York, NY, USA, https://doi.org/10.1017/9781009157896, 2021.

IPCC, Climate Change 2023: Synthesis Report. Contribution of Working Groups I, II and III to the Sixth Assessment Report of the Intergovernmental Panel on Climate Change [Core Writing Team, H. Lee, and J. Romero (eds.)]. IPCC, Geneva, Switzerland, https://doi.org/10.59327/IPCC/AR6-9789291691647, 2023.

Irvine-Fynn, T. D. L., Hodson, A. J., Moorman, B. J., Vatne, G., and Hubbard, A. L.: Polythermal glacier hydrology: a review, Reviews of Geophysics, 49, RG4002, https://doi.org/10.1029/2010RG000350, 2011.

Jenkins, A.: Convection-driven melting near the grounding lines of ice shelves and tidewater glaciers, J. Phys. Oceanogr., 41, 2279–2294, https://doi.org/10.1175/JPO-D-11-03.1, 2011.

Jiang, D., Li, X., Zhang, K., Marinsek, S., Hong, W., and Wu, Y.: Automatic supraglacial lake extraction in Greenland using Sentinel-1 SAR images and attention-based U-Net. Remote Sens., 14, 4998, https://doi.org/10.3390/rs14194998, 2022.

Johansson, A. M., Jansson, P., and Brown, I. A.: Spatial and temporal variations in lakes on the Greenland Ice Sheet, J. Hydrol. 476, 314–320, doi: 10.1016/j.jhydrol.2012.10.045, 2013.

Joughin, I., Das, S. B., Flowers, G. E., Behn, M. D., Alley, R. B., King, M. A., Smith, B. E., Bamber, J. L., van den Broeke, M. R., and van Angelen, J. H.: Influence of ice-sheet geometry and supraglacial lakes on seasonal ice-flow variability, The Cryosphere, 7, 1185–1192, https://doi.org/10.5194/tc-7-1185-2013, 2013.

Joughin, I., Howat, I. M., Fahnestock, M., Smith, B., Krabill, W., Alley, R. B., Stern, H., and Truffer, M.: Continued evolution of Jakobshavn Isbræ following its rapid speedup, J. Geophys. Res.,113, F04006, https://doi. org/10. 1029/2008JF001023, 2008.

Jullien, N., Tedstone, A. J., Machguth, H., Karlsson, N. B., and Helm, V.: Greenland Ice Sheet ice slab expansion and thickening, Geophys. Res. Lett., 50, e2022GL100911, https://doi.org/10.1029/2022GL100911, 2023.

Kamb, B.: Glacier surge mechanism based on linked cavity configuration of the basal water conduit system, Journal of Geophysical Research: Solid Earth, 92, 9083–9100, https://doi.org/10.1029/JB092iB09p09083, 1987.

Kauth, R., and Thomas, G.: The tasseled cap – A graphic description of the spectral-temporal development of agricultural crops as seen by Landsat, Proceedings of the Symposium on Machine Processing of Remotely Sensed Data, Purdue University, West Lafayette, Indiana, 1976.

Keshri, A. K., Shukla, A., and Gupta, R. P.: ASTER ratio indices for supraglacial terrain mapping, International Journal of Remote Sensing, 30, 519–524, https://doi.org/10.1080/01431160802339460, 2009.

King, M. D., Howat, I. M., Candela, S. G., Noh, M. J., Jeong, S., Noël, B. P. Y., van den Broeke, M. R., Wouters, B., and Negrete, A.: Dynamic ice loss from the Greenland Ice Sheet driven by

sustained glacier retreat, Communications Earth & Environment, 1, 1, https://doi.org/10.1038/s43247-020-0001-2, 2020.

Kingslake, J., Ely, J. C., Das, I., and Bell, R. E.: Widespread movement of meltwater onto and across Antarctic ice shelves, Nature, 544, 349–352, https://doi.org/10.1038/nature22049, 2017.

Koenig, L. S., Lampkin, D. J., Montgomery, L. N., Hamilton, S. L., Turrin, J. B., Joseph, C. A., Moutsafa, S. E., Panzer, B., Casey, K. A., Paden, J. D., Leuschen, C., and Gogineni, P.: Wintertime storage of water in buried supraglacial lakes across the Greenland Ice Sheet, The Cryosphere, 9, 1333–1342, https://doi.org/10.5194/tc-9-1333-2015, 2015.

Koenig, L. S., Miège, C., Forster, R. R., and Brucker, L.: Initial in situ measurements of perennial meltwater storage in the Greenland firn aquifer, Geophys. Res. Lett., 41, 81–85, https://doi.org/10.1002/2013GL058083, 2014.

Kohavi, R.: A study of cross-validation and bootstrap for accuracy estimation and model selection, in: Proceedings of the 14th International Joint Conference on Artificial Intelligence (IJCAI), 1137–1143, 1995.

Koziol, C., Arnold, N., Pope, A., and Colgan, W.: Quantifying supraglacial meltwater pathways in the Paakitsoq region, West Greenland, Journal of Glaciology, 1–13, https://doi.org/10.1017/jog.2017.5, 2017.

Krawczynski, M., Behn, M., Das, S. and Joughin, I.: Constraints on the lake volume required for hydro-fracture through ice sheets, Geophys. Res. Lett., 36, L10501, doi:10.1029/2008gl036765, 2009.

Kuipers Munneke, P., Ligtenberg, S. R. M., Noël, B. P. Y., Howat, I. M., Box, J. E., Mosley-Thompson, E., McConnell, J. R., Steffen, K., Harper, J. T., Das, S. B., and van den Broeke, M. R.: Elevation change of the Greenland Ice Sheet due to surface mass balance and firn processes, 1960–2014, The Cryosphere, 9, 2009–2025, https://doi.org/10.5194/tc-9-2009-2015, 2015.

Lampkin, D. J.: Supraglacial lake spatial structure in western Greenland during the 2007 ablation season, Journal of Geophysical Research: Earth Surface, 116, F4, https://doi.org/10.1029/2010JF001725, 2011.

Lampkin, D. L., and VanderBerg, J.: A preliminary investigation of the influence of basal and surface topography on supraglacial lake distribution near Jakobshavn Isbræ, western Greenland, Hydrological Processes, 25, 3347–3355, https://doi.org/10.1002/hyp.8170, 2011.

Langley, E. S., Leeson, A. A., Stokes, C. R., and Jamieson, S. S. R.: Seasonal evolution of supraglacial lakes on an East Antarctic outlet glacier, Geophys. Res. Lett., 43,8563–8571, https://doi. org/10. 1002/2016GL069511, 2016.

Leeson, A. A., Shepherd, A., Briggs, K., Howat, I., Fettweis, X., Morlighem, M., and Rignot, E.: Supraglacial lakes on the Greenland ice sheet advance inland under warming climate, Nat Clim Chang, 5, 51–55. https://doi. org/10.1038/nclimate2463, 2015.

Leeson, A. A., Shepherd, A., Palmer, S., Sundal, A., and Fettweis, X.: Simulating the growth of supraglacial lakes at the western margin of the Greenland ice sheet, The Cryosphere, 6, 1077–1086, https://doi. org/10. 5194/tc-6-1077-2012, 2012.

Leidman, S. Z., Rennermalm, Å. K., Muthyala, R., Guo, Q., and Overeem, I.: The presence and widespread distribution of dark sediment in Greenland Ice Sheet supraglacial streams implies substantial impact of microbial communities on sediment deposition and albedo, Geophysical Research Letters, 48, e2020GL088444, https://doi.org/10.1029/2020GL088444, 2020.

Lenaerts, J. T. M., and van den Broeke, M. R.: Modeling drifting snow in Antarctica with a regional climate model: 2. Results, Journal of Geophysical Research: Atmospheres, 117, D05103, https://doi.org/10.1029/2010JD015419, 2012.

Lenaerts, J. T. M., Camron, M. D., Wyburn-Powell, C. R., and Kay, J. E.: Present-day and future Greenland Ice Sheet precipitation frequency from CloudSat observations and the Community Earth System Model, The Cryosphere, 14, 2253–2265, https://doi.org/10.5194/tc-14-2253-2020, 2020.

Lenaerts, J. T. M., Le Bars, D., van Kampenhout, L., Vizcaino, M., Enderlin, E. M., and van den Broeke, M. R.: Representing Greenland ice sheet freshwater fluxes in climate models, Geophys. Res. Lett., 42, 6373–6381, https://doi.org/10.1002/2015GL064738, 2015.

Lenaerts, J. T. M., Medley, B., van den Broeke, M. R., and Wouters, B.: Observing and modeling ice sheet surface mass balance, Reviews of Geophysics, 57, 376–420, https://doi.org/10.1029/2018RG000622, 2019.

Levermann, A. and Winkelmann, R.: A simple equation for the melt elevation feedback of ice sheets, The Cryosphere, 10, 1799–1807, https://doi.org/10.5194/tc-10-1799-2016, 2016.

Li, H., Xu, L., Shen, H., and Zhang, L.: A general variational framework considering cast shadows for the topographic correction of remote sensing imagery, ISPRS Journal of Photogrammetry and Remote Sensing, 117, 161–171, https://doi.org/10.1016/j.isprsjprs.2016.03.021, 2016.

Liang, Y.-L., Colgan, W., Lv, Q., Steffen, K., Abdalati, W., Stroeve, J., Gallaher, D., and Bayou, N.: A decadal investigation of supraglacial lakes in West Greenland using a fully automatic detection and tracking algorithm, Remote Sensing of Environment, 123, 127–138, https://doi.org/10.1016/j.rse.2012.03.020, 2012.

Lin, Y., Yang, Q., Li, X., Yang, C.-Y., Wang, Y., Wang, J., Liu, J., Chen, S., and Liu, J.: Optimization of the k-nearest-neighbors model for summer Arctic sea ice prediction, Frontiers in Marine Science, 10, 1260047, https://doi.org/10.3389/fmars.2023.1260047, 2023.

Lindbäck, K., R. Pettersson, A. L. Hubbard, S. H. Doyle, D. van As, A. B. Mikkelsen, and Fitzpatrick, A. A.: Subglacial water drainage, storage, and piracy beneath the Greenland ice sheet, Geophys. Res. Lett., 42, 7606–7614, https://doi.org/10.1002/2015GL0653, 2015.

Livingstone, S. J., Li, Y., Rutishauser, A., Sanderson, R. J., Winter, K., Mikucki, J. A., Björnsson, H., Bowling, J. S., Chu, W., Dow, C. F., Fricker, H. A., McMillan, M., Ng, F. S. L., Ross, N., Siegert, M. J., Siegfried, M., and Sole, A. J.: Subglacial lakes and their changing role in a warming climate, Nature Reviews Earth & Environment, 3, 106–124, https://doi.org/10.1038/s43017-021-00240-7, 2022.

Loeb, N. A., Crawford, A., Herrington, A., McCrystall, M., Stroeve, J., and Hanesiak, J.: Projections and physical drivers of extreme precipitation in Greenland & Baffin Bay, Journal of Geophysical Research: Atmospheres, 129, e2024JD041375, https://doi.org/10.1029/2024JD041375, 2024.

Lu, Y., Yang, K., Lu, X., Li, Y., Gao, S., Mao, W. and Li, M.: Response of supraglacial rivers and lakes to ice flow and surface melt on the Northeast Greenland ice sheet during the 2017 melt season, J. Hydrol. 602, 126750, https://doi.org/10.1016/j.jhydrol.2021.126750 , 2021.

Lüthje, M., Pedersen, L. T., Reeh, N., and Greuell, W.: Modelling the evolution of supraglacial lakes on the West Greenland ice-sheet margin, J. Glaciol., 52, 608–618, https://doi.org/10.3189/172756506781828386, 2006.

Lutz, K., Bever, L., Sommer, C., Humbert, A., Scheinert, M., and Braun, M.: Assessing supraglacial lake depth using ICESat-2, Sentinel-2, TanDEM-X, and in situ sonar measurements over Northeast Greenland, EGUsphere [preprint], https://doi.org/10.5194/egusphere-2024-1244, 2024.

Lutz, K., Tabone, I., Humbert, A., and Braun, M.: Multi-annual patterns of rapidly draining supraglacial lakes in Northeast Greenland, EGUsphere [preprint], https://doi.org/10.5194/egusphere-2024-3056, 2024.

Lutz, S., Bohleber, P., and Eisen, O.: Deep learning-based supraglacial lake classification on the Greenland ice sheet using multi-sensor remote sensing data. Remote Sens., 15, 4360, https://doi.org/10.3390/rs15174360, 2023.

Macdonald, G., Banwell, A., and MacAyeal, D.: Seasonal evolution of supraglacial lakes on a floating ice tongue, Petermann Glacier, Greenland. Annals of Glaciology, 59(76pt1), 56-65, https://doi.org/10.1017/aog.2018.9, 2018.

MacFerrin, M., Machguth, H., As, D. V., Charalampidis, C., Stevens, C. M., Heilig, A., Vandecrux, B., Langen, P. L., Mottram, R., Fettweis, X., van den Broeke, M. R., Pfeffer, W. T., Moussavi, M. S., Abdalati, W.: Rapid expansion of Greenland's low-permeability ice slabs, Nature, 573, 403–407, https://doi.org/10.1038/s41586-019-1550-3, 2019.

Machguth, H., Box, J. E., Fausto, R. S., and Pfeffer, W. T.: Editorial: Meltwater retention processes in snow and firn on ice sheets and glaciers: Observations and modeling, Frontiers in Earth Science, 6, 105, https://doi.org/10.3389/feart.2018.00105, 2018.

Machguth, H., MacFerrin, M., van As, D., Box, J. E., Charalampidis, C., Colgan, W., Fausto, R, S., Meijer, H. A. J., Mosley-Thompson., and van de Wal, R. S. W.: Greenland meltwater storage in firn limited by near-surface ice formation. Nature Clim Change 6, 390–393, https://doi.org/10. 1038/nclimate2899, 2016.

Machguth, H., Tedstone, A., and Mattea, E.: Daily variations in Western Greenland slush limits, 2000–2021, Journal of Glaciology, 69(273), 191-203, https://doi.org/10.1017/jog.2022.65, 2023.

Maffezzoli, N., Rignot, E., Barbante, C., Petersen, T., and Vascon, S.: A gradient-boosted tree framework to model the ice thickness of the World's glaciers (IceBoost v1), EGUsphere [preprint], https://doi.org/10.5194/egusphere-2024-2455, 2024.

Maier, N., Gimbert, F., and Gillet-Chaulet, F.: Threshold response to melt drives large-scale bed weakening in Greenland, Nature, 607, 714–720, https://doi.org/10.1038/s41586-022-04901-9, 2022.

Malczyk, G., Gourmelen, N., Goldberg, D., Wuite, J., and Nagler, T.: Repeat subglacial lake drainage and filling beneath Thwaites Glacier, Geophysical Research Letters, 47, e2020GL089658, https://doi.org/10.1029/2020GL089658, 2020.

Mankoff, K. D. and Tulaczyk, S. M.: The past, present, and future viscous heat dissipation available for Greenland subglacial conduit formation, The Cryosphere, 11, 303–317, https://doi.org/10.5194/tc-11-303-2017, 2017.

Mankoff, K. D., Fettweis, X., Langen, P. L., Stendel, M., Kjeldsen, K. K., Karlsson, N. B., Noël, B., van den Broeke, M. R., Solgaard, A., Colgan, W., Box, J. E., Simonsen, S. B., King, M. D., Ahlstrøm, A. P., Andersen, S. B., and Fausto, R. S.: Greenland Ice Sheet mass balance from 1840 through next week, Earth System Science Data, 13, 5001–5025, https://doi.org/10.5194/essd-13-5001-2021, 2021.

Mattingly, K. S., Mote, T. L., and Fettweis, X.: Atmospheric river impacts on Greenland Ice Sheet surface mass balance, Journal of Geophysical Research: Atmospheres, 123, 8538–8560, https://doi.org/10.1029/2018JD028714, 2018.

Mattingly, K. S., Ramseyer, C. A., Rosen, J. J., Mote, T. L., and Muthyala, R.: Increasing water vapor transport to the Greenland Ice Sheet revealed using self-organizing maps, Geophysical Research Letters, 43, 9250–9258, https://doi.org/10.1002/2016GL070424, 2016.

McFeeters, S. K.: The use of the Normalized Difference Water Index (NDWI) in the delineation of open water features', International Journal of Remote Sensing, 17(7), 1425–1432, https://doi.org/10.1080/01431169608948714., 1996.

McLeod, J. T., and Mote, T. L.: Linking interannual variability in extreme Greenland blocking episodes to the recent increase in summer melting across the Greenland ice sheet, International Journal of Climatology, 36, 1484–1499, https://doi.org/10.1002/joc.4440, 2015.

McManus, J., Francois, R., Gherardi, J. M., Keigwin, L. D., and Brown-Leger, S.: Collapse and rapid resumption of Atlantic meridional circulation linked to deglacial climate changes, Nature, 428, 834–837, https://doi.org/10.1038/nature02494, 2004.

McMillan, M., Nienow, P., Shepherd, A., Benham, T., and Sole, A.: Seasonal evolution of supra-glacial lakes on the Greenland Ice Sheet, Earth and Planetary ScienceLetters, 262, 484−492, https://doi.org/10.1016/j.epsl.2007.08.002, 2007.

Melling, L., Leeson, A., McMillan, M., Maddalena, J., Bowling, J., Glen, E., Sandberg Sørensen, L., Winstrup, M., and Lørup Arildsen, R.: Evaluation of satellite methods for estimating supraglacial lake depth in southwest Greenland, The Cryosphere Discuss. [preprint], https://doi.org/10.5194/tc-2023-103, 2023.

Miège, C., Forster, R. R., Brucker, L., Koenig, L. S., Solomon, D. K., Paden, J. D., Box, J. E., Burgess, E. W., Miller, J. Z., McNerney, L., and Brautigam, N.: Spatial extent and temporal variability of Greenland firn aquifers detected by ground and airborne radars, J. Geophys. Res. Earth Surf., 121, 2381–2398, https://doi.org/10.1002/2016JF003869, 2016.

Mikkelsen, A. B., Hubbard, A., MacFerrin, M., Box, J. E., Doyle, S. H., Fitzpatrick, A., Hasholt, B., Bailey, H. L., Lindbäck, K., and Pettersson, R.: Extraordinary runoff from the Greenland ice

sheet in 2012 amplified by hypsometry and depleted firn retention, The Cryosphere, 10, 1147–1159, https://doi.org/10.5194/tc-10-1147-2016, 2016.

Miles K. E., Willis I. C., Benedek, C. L., Williamson, A. G., and Tedesco, M.: Toward Monitoring Surface and Subsurface Lakes on the Greenland Ice Sheet Using Sentinel-1 SAR and Landsat-8 OLI Imagery, Front. Earth Sci. 5:58, https://doi.org/10.3389/feart.2017.00058, 2017.

Miller, J. Z., Culberg, R., Long, D. G., Shuman, C. A., Schroeder, D. M., and Brodzik, M. J.: An empirical algorithm to map perennial firn aquifers and ice slabs within the Greenland Ice Sheet using satellite L-band microwave radiometry, The Cryosphere, 16, 103–125, https://doi.org/10.5194/tc-16-103-2022, 2022.

Miller, O., Solomon, D. K., Miège, C.,Koenig, L., Forster, R., Schmerr, N., Ligtenberg, S. R. M., Legchenko, A., Voss, C. I., Montgomery, L., and McConnell, J., R.: Hydrology of a perennial firn aquifer in southeast Greenland: an overview driven by field data, Water Resources Research 56, 4–8. https://doi.org /10.1029/2019WR026348, 2020.

Miller, O., Solomon, D. K., Miège, C.,Koenig, L., Forster, R., Schmerr, N., Ligtenberg, S. R. M., and Montgomery, L.: Direct evidence of meltwater flow within a firn aquifer in southeast Greenland, Geophysical Research Letters, 45, 207–215, https://doi.org/10.1002/2017GL075707, 2018.

Miller, O., Solomon, D. K., Miège, C.,Koenig, L., Forster, R., Schmerr, N., Ligtenberg, S. R. M., Legchenko, A., Voss, C. I., Montgomery, L., and McConnell, J., R.: Hydrology of a perennial firn aquifer in southeast Greenland: an overview driven by field data, Water Resources Research 56, 4–8. https://doi.org /10.1029/2019WR026348, 2020.

Mohajerani, Y.: Record Greenland mass loss, Nat. Clim. Chang, 10, 803–804, https://doi.org/10.1038/s41558-020-0887-9, 2020.

Montgomery, L. N., Schmerr, N., Burdick, S., Forster, R. R., Koenig, L., Ligtenberg, S., and Legchenko, A.: Investigation of firn aquifer structure in southeastern Greenland using active source seismology, Front. Earth Sci., 5, 10, https://doi.org/10.3389/feart.2017.00010, 2017.

Moon, T. A., Gardner, A. S., Csatho, B., Parmuzin, I., and Fahnestock, M. A.: Rapid Reconfiguration of the Greenland Ice Sheet Coastal Margin, Journal of Geophysical Research: Earth Surface, 125, e2020JF005585, https://doi.org/10.1029/2020JF005585, 2020.

Moon, T., Mankoff, K., Fausto, R., Fettweis, X., Loomis, B., Mote, T., et al.: Arctic Report Card 2022: Greenland Ice Sheet, NOAA Technical Report OAR ARC 22-05, https://doi.org/10.25923/c430-hb50, 2022.

Morlighem, M., C. Williams, E. Rignot, L. An, J. E. Arndt, J. Bamber, G. Catania, N. Chauché, J. A. Dowdeswell, B. Dorschel, I. Fenty, K. Hogan, I. Howat, A. Hubbard, M. Jakobsson, T. M. Jordan, K. K. Kjeldsen, R. Millan, L. Mayer, J. Mouginot, B. Noël, C. O'Cofaigh, S. J. Palmer, S. Rysgaard, H. Seroussi, M. J. Siegert, P. Slabon, F. Straneo, M. R. van den Broeke, W. Weinrebe, M. Wood, and K. Zinglersen.: BedMachine v3: Complete bed topography and ocean bathymetry mapping of Greenland from multi-beam echo sounding combined with mass conservation, Geophysical Research Letters. 44, https://doi.org/10.1002/2017GL074954, 2017.

Morriss, B. F., Hawley, R. L., Chipman, J. W., Andrews, L. C., Catania, G. A., Hoffman, M. J., Lüthi, M. P., and Neumann, T. A.: A ten-year record of supraglacial lake evolution and rapid drainage in West Greenland using an automated processing algorithm for multispectral imagery, The Cryosphere, 7, 1869–1877, https://doi.org/10.5194/tc-7-1869-2013, 2013.

Mote, T. L.: Greenland surface melt trends 1973–2007: Evidence of a large increase in 2007. Geophys. Res. Lett., 34, L22507, https://doi.org/10.1029/2007GL031976, 2007.

Mote, T., and Anderson, M.: Variations in snowpack melt on the Greenland ice sheet based on passive-microwave measurements, J. Glaciol., 41, 51–60, https://doi.org/10.3189/S0022143000017755, 1995.

Mouginot, J., Rignot, E., Bjørk, A. A., van den Broeke, M., Millan, R., Morlighem, M., Noël, B., Scheuchl, B., and Wood, M.: Forty-six years of Greenland Ice Sheet mass balance from 1972 to 2018, Proceedings of the National Academy of Sciences of the United States of America, 116, 9239–9244, https://doi.org/10.1073/pnas.1904242116, 2019.

Mountrakis, G., Im, J., and Ogole, C.: Support vector machines in remote sensing: a review, ISPRS Journal of Photogrammetry and Remote Sensing, 66, 247–259, https://doi.org/10.1016/j.isprsjprs.2010.11.001, 2011.

Moussavi, M., Pope, A., Halberstadt, A. R. W., Trusel, L. D., Cioffi, L., and Abdalati, W.: Antarctic supraglacial lake detection using Landsat 8 and Sentinel-2 imagery: Towards continental generation of lake volumes. Remote Sens., 12(1), 134, https://doi.org/10.3390/rs12010134, 2020.

Ng, F. S., Ignéczi, Á., Sole, A. J., and Livingstone, S. J.: Response of surface topography to basal variability along glacial flowlines, J. Geophys. Res.-Earth, 123, 2319–2340, https://doi.org/10.1029/2017JF004555, 2018.

Nias, I. J., Nowicki, S., Felikson, D., and Loomis, B.: Modeling the Greenland Ice Sheet's committed contribution to sea level during the 21st century, Journal of Geophysical Research: Earth Surface, 128, e2022JF006914, https://doi.org/10.1029/2022JF006914, 2023.

Nienow, P. W., Sole, A. J., Slater, D. A. and Cowton, T. R: Recent advances in our understanding of the role of meltwater in the Greenland Ice Sheet system, Current Climate Change Reports, 3(4), 330-344, https://doi.org/10.1007/s40641-017-0083-9 2017.

Niu, L., Tang, X., Yang, S., Zhang, Y., Zheng, L., and Wang, L.: Detection of Antarctic surface meltwater using Sentinel-2 remote sensing images via U-net with attention blocks: a case study over the Amery Ice Shelf, IEEE Transactions on Geoscience and Remote Sensing, 61, 1–13, https://doi.org/10.1109/TGRS.2023.3275076, 2023.

Niwano, M., Hashimoto, A. and Aoki, T.: Cloud-driven modulations of Greenland ice sheet surface melt. Sci Rep 9, 10380, https://doi. org/10. 1038/s41598-019-46152-5, 2019.

Noël, B., Lenaerts, J. T. M., Lipscomb, W. H., Thayer-Calder, K., and van den Broeke, M. R.: Peak refreezing in the Greenland firn layer under future warming scenarios, Nat. Commun., 13, 6870, https://doi.org/10.1038/s41467-022-34584-5, 2022.

Noël, B., van de Berg, W. J., Lhermitte, S., and van den Broeke, M. R.: Rapid ablation zone expansion amplifies North Greenland mass loss. Science Advances, 5(9), 2–11. https://doi.org/10.1126/sciadv.aaw0123, 2019.

Noël, B., van de Berg, W. J., van Meijgaard, E., Kuipers Munneke, P., van de Wal, R. S. W., and van den Broeke, M. R.: Evaluation of the updated regional climate model RACMO2.3: summer snowfall impact on the Greenland Ice Sheet, The Cryosphere, 9, 1831–1844, https://doi.org/10.5194/tc-9-1831-2015, 2015.

Noël, B., van de Berg, W. J., van Wessem, J. M., van Meijgaard, E., van As, D., Lenaerts, J. T. M., Lhermitte, S., Kuipers Munneke, P., Smeets, C. J. P. P., van Ulft, L. H., van de Wal, R. S. W., and van den Broeke, M. R.: Modelling the climate and surface mass balance of polar ice sheets using RACMO2 – Part 1: Greenland (1958–2016), The Cryosphere, 12, 811–831, https://doi.org/10.5194/tc-12-811-2018, 2018.

Nolin, A. W., and Payne, M. C.: Classification of glacier zones in western Greenland using albedo and surface roughness from the Multi-angle Imaging SpectroRadiometer (MISR), Remote Sensing of Environment, 107, 264–275, https://doi.org/10.1016/j.rse.2006.11.004, 2007.

Nye, J. F., Water flow in glaciers: jökulhlaups, tunnels and veins, Journal of Glaciology, 17, 181–207, https://doi.org/10.3189/S002214300001354X, 1976.

Oerlemans, J.: Some basic experiments with a vertically-integrated ice sheet model, Tellus A: Dynamic Meteorology and Oceanography, 33, 1–11, https://doi.org/10.3402/tellusa.v33i1.10690, 1981.

Okolie, C., Mills, J., Adeleke, A., Smit, J., and Maduako, I.: The explainability of gradient-boosted decision trees for digital elevation model (DEM) error prediction, Int. Arch. Photogramm. Remote Sens. Spatial Inf. Sci., XLVIII-M-3-2023, 161–168, https://doi.org/10.5194/isprs-archives-XLVIII-M-3-2023-161-2023, 2023.

O'Leary, M. and Christoffersen, P.: Calving on tidewater glaciers amplified by submarine frontal melting, The Cryosphere, 7, 119–128, https://doi.org/10.5194/tc-7-119-2013, 2013.

Oltmanns, M., Straneo, F., and Tedesco, M.: Increased Greenland melt triggered by large-scale, year-round cyclonic moisture intrusions, The Cryosphere, 13, 815–825, https://doi.org/10.5194/tc-13-815-2019, 2019.

Onesti, L. J., and Hestnes, E.: Slush-flow questionnaire, Annals of Glaciology, 13, 226–230, https://doi.org/10.3189/1989AoG13-1-226-230, 1989.

Onesti, L. J.: Meteorological conditions that initiate slushflows in the Central Brooks Range, Alaska, Annals of Glaciology, 6, 23–25, https://doi.org/10.3189/1985AoG6-1-23-25, 1985.

Oppenheimer, M., Glavovic, B. C., Hinkel, J., van de Wal, R., Magnan, A. K., Abd-Elgawad, A., Cai, R., Cifuentes-Jara, M., DeConto, R. M., Ghosh, T., Hay, J., Isla, F., Marzeion, B., Meyssignac, B., and Sebesvari, Z.: Sea level rise and implications for low-lying islands, coasts and communities, In: IPCC Special Report on the Ocean and Cryosphere in a Changing Climate, , 2019. [Pörtner, H.-O., Roberts, D. C., Masson-Delmotte, V., Zhai, P., Tignor, M., Poloczanska, E., Mintenbeck, K., Alegría, A., Nicolai, M., Okem, A., Petzold, J., Rama, B., and Weyer, N. M. (eds.)], In press. Accessed 1 December 2024.

Otosaka, I. N., Shepherd, A., Ivins, E. R., Schlegel, N.-J., Amory, C., van den Broeke, M. R., Horwath, M., Joughin, I., King, M. D., Krinner, G., Nowicki, S., Payne, A. J., Rignot, E., Scambos, T., Simon, K. M., Smith, B. E., Sørensen, L. S., Velicogna, I., Whitehouse, P. L., A, G., Agosta, C., Ahlstrøm, A. P., Blazquez, A., Colgan, W., Engdahl, M. E., Fettweis, X., Forsberg, R., Gallée, H., Gardner, A., Gilbert, L., Gourmelen, N., Groh, A., Gunter, B. C., Harig, C., Helm, V., Khan, S. A., Kittel, C., Konrad, H., Langen, P. L., Lecavalier, B. S., Liang, C.-C., Loomis, B. D., McMillan, M., Melini, D., Mernild, S. H., Mottram, R., Mouginot, J., Nilsson, J., Noël, B., Pattle, M. E., Peltier, W. R., Pie, N., Roca, M., Sasgen, I., Save, H. V., Seo, K.-W., Scheuchl, B., Schrama, E. J. O., Schröder, L., Simonsen, S. B., Slater, T., Spada, G., Sutterley, T. C., Vishwakarma, B. D., van Wessem, J. M., Wiese, D., van der Wal, W., and Wouters, B.: Mass balance of the Greenland and Antarctic ice sheets from 1992 to

2020, Earth Syst. Sci. Data, 15, 1597–1616, https://doi.org/10.5194/essd-15-1597-2023, 2023.

Otto J, Holmes, F. A. and Kirchner, N.: Supraglacial lake expansion, intensified lake drainage frequency, and first observation of coupled lake drainage, during 1985–2020 at Ryder Glacier, Northern Greenland, Front. Earth Sci.,10:978137, https://doi.org/10.3389/feart.2022.978137, 2022.

Palmer, S., McMillan, M. and Morlighem, M: Subglacial lake drainage detected beneath the Greenland ice sheet, Nat Commun 6, 8408, https://doi.org/10.1038/ncomms9408, 2015.

Pfeffer, W. T., Meier, M. F., and Illangasekare, T. H.: Retention of Greenland runoff by refreezing: Implications for projected future sea level change, Journal of Geophysical Research: Atmospheres, 96, 22117–22124, https://doi.org/10.1029/91JC02502, 1991.

Pham, T. D., Le, N. N., Ha, N. T., Nguyen, L. V., Xia, J., Yokoya, N., To, T. T., Trinh, H. X., Kieu, L. Q., and Takeuchi, W.: Estimating Mangrove Above-Ground Biomass Using Extreme Gradient Boosting Decision Trees Algorithm with Fused Sentinel-2 and ALOS-2 PALSAR-2 Data in Can Gio Biosphere Reserve, Vietnam, Remote Sensing, 12, 777, https://doi.org/10.3390/rs12050777, 2020.

Phillips, S. J., Dudík, M., and Schapire, R. E.: A maximum entropy approach to species distribution modeling, Proceedings of the Twenty-First International Conference on Machine Learning, Banff, Alberta, Canada, 1015412, 655–662, ACM, 2004.

Phillips, T., Rajaram, H., and Steffen, K.: Cryo-hydrologic warming: A potential mechanism for rapid thermal response of ice sheets, Geophys. Res. Lett., 37, https://doi.org/10.1029/2010GL044397, 2010.

Phillips, T., Rajaram, H., Colgan, W., Steffen, K., and Abdalati, W.: Evaluation of cryo-hydrologic warming as an explanation for increased ice velocities in the wet snow zone, Sermeq Avannarleq, West Greenland, J. Geophys. Res.-Earth Surf., 118, 1241–1256, https://doi.org/10.1002/jgrf.20079, 2013.

Pitcher, L. H., and Smith, L. C.: Supraglacial streams and rivers, Annual Review of Earth and Planetary Sciences, 47, 421–452, https://doi.org/10.1146/annurev-earth-053018-060302, 2019.

Poinar, K., Dow, C. F., and Andrews, L. C.: Long-term support of an active subglacial hydrologic system in southeast Greenland by firn aquifers, Geophys. Res. Lett., 46, 4772–4781, https://doi.org/10.1029/2019GL082786, 2019.

Poinar, K., Joughin, I., Das, S. B., Behn, M. D., Lenaerts, J. T. M., and van den Broeke, M. R.: Limits to future expansion of surface-melt-enhanced ice flow into the interior of western Greenland, Geophysical Research Letters, 42, 1800–1807, https://doi.org/10.1002/2015GL063192, 2015.

Poinar, K., Joughin, I., Lilien, D., Brucker, L., Kehrl, L., and Nowicki, S.: Drainage of Southeast Greenland firn aquifer water through crevasses to the bed, Front. Earth Sci., 5, https://doi.org/10.3389/feart.2017.00005, 2017.

Pope, A., Scambos, T. A., Moussavi, M., Tedesco, M., Willis, M., Shean, D., and Grigsby, S.: Estimating supraglacial lake depth in West Greenland using Landsat 8 and comparison with other multispectral methods, The Cryosphere, 10, 15–27, https://doi.org/10.5194/tc-10-15-2016, 2016.

Porter, C., Morin, P., Howat, I., Noh, M.-J., Bates, B., Peterman, K., Keesey, S., Schlenk, M., Gardiner, J., Tomko, K.,Willis, M., Kelleher, C., Cloutier, M., Husby, E., Foga, S.,Nakamura, H., Platson, M., Wethington, M. Jr., Williamson,C., Bauer, G., Enos, J., Arnold, G., Kramer, W., Becker, P.,Doshi, A., D'Souza, C., Cummens, P., Laurier, F., and Bo-jesen, M.: ArcticDEM, v3.0, Harvard Dataverse [data set], https://doi.org/10.7910/DVN/OHHUKH, 2018 [Date Accessed: April 2024].

Qayyum, N., Ghuffar, S., Ahmad, H., Yousaf, A., and Shahid, I.: Glacial Lakes Mapping Using Multi Satellite PlanetScope Imagery and Deep Learning. ISPRS Int. J. Geo-Inf., 9, 560, https://doi.org/10.3390/ijgi9100560, 2020.

Rahmani, S., Strait, M., Merkurjev, D., Moeller, M., and Wittman, T.: An Adaptive IHS Pan-Sharpening Method, IEEE Geosci. Remote S., 7, 746–750, https://doi.org/10.1109/LGRS.2010.2046715, 2010.

Rahmstorf, S., Box, J. E., Feulner, G., Mann, M. E., Robinson, A., Rutherford, S., et al.: Exceptional twentieth-century slowdown in Atlantic Ocean overturning circulation, Nature Climate Change, 5, 475–480, https://doi.org/10.1038/nclimate2554, 2015.

Rawlins, L. D., Rippin, D. M., Sole, A. J., Livingstone, S. J., and Yang, K.: Seasonal evolution of the supraglacial drainage network at Humboldt Glacier, North Greenland, between 2016 and 2020, The Cryosphere Discuss., https://doi. org/10. 5194/tc-2023-23, 2023.

Raymond, C., and Nolan, M.: Drainage of a glacial lake through an ice spillway, International Association of Hydrological Sciences Publications, 264, 199–210, available at: http://iahs.info/uploads/dms/iahs_264_0199.pdf, 2000.

Razaque, A., Ben Haj Frej, M., Almi'ani, M., Alotaibi, M., and Alotaibi, B.: Improved support vector machine enabled radial basis function and linear variants for remote sensing image classification, Sensors, 21, 4431, https://doi.org/10.3390/s21134431, 2021.

Rignot, E., Mouginot, J., Scheuchl, B., van den Broeke, M., van Wessem, M. J., and Morlighem, M.: Four decades of Antarctic Ice Sheet mass balance from 1979–2017, Proceedings of the National Academy of Sciences of the United States of America, 116, 1095–1103, https://doi.org/10.1073/pnas.1812883116, 2019.

Riihelä, A., King, M. D., and Anttila, K.: The surface albedo of the Greenland Ice Sheet between 1982 and 2015 from the CLARA-A2 dataset and its relationship to the ice sheet's surface mass balance, The Cryosphere, 13, 2597–2614, https://doi. org/10. 5194/tc-13-2597-2019, 2019.

Rippin, D. and Rawlins, L.: Supraglacial River Networks, In International Encyclopedia of Geography, edited by: Richardson, D., Castree, N., Goodchild, M. F., Kobayashi, A., Liu, W., and Marston, R. A., https://doi.org/10.1002/9781118786352.wbieg2072, 2021

Röthlisberger, H.: Water pressure in intra- and subglacial channels, Journal of Glaciology, 11, 177–204, https://doi.org/10.3189/S0022143000022188, 1972.

Rüping, S.: Incremental learning with support vector machines, ICDM: Proceedings of the IEEE International Conference on Data Mining, 2001, 641–642, https://doi.org/10.1109/ICDM.2001.989602.

Ryan, J. C., Smith, L. C., van As, D., Cooley, S. W., Cooper, M. G., Pitcher, L. H., and Hubbard, A.: Greenland Ice Sheet surface melt amplified by snowline migration and bare ice exposure. Sci. Adv., 5, eaav3738, https://doi.org/10.1126/sciadv.aav3738, 2019.

Sasgen, I., van den Broeke, M., Bamber, J. L., Rignot, E., Sørensen, L. S., Wouters, B., Martinec, Z., Velicogna, I., and Simonsen, S. B.: Timing and origin of recent regional ice-mass loss in Greenland, Earth and Planetary Science Letters, 333–334, 293–303, https://doi.org/10.1016/j.epsl.2012.03.033, 2012.

Sasgen, I., Wouters, B., Gardner, A. S., King, M. D., Tedesco, M., Landerer, F. W., Dahle, C., Save, H., and Fettweis, X.: Return to rapid ice loss in Greenland and record loss in 2019 detected by the GRACE-FO satellites, Communications Earth & Environment, 1, 8, https://doi.org/10.1038/s43247-020-0001-2, 2020.

Schoof, C.: Ice-sheet acceleration driven by melt supply variability, Nature, 468, 803–806, https://doi.org/10.1038/nature09618, 2010.

Schwatke, C., Scherer, D., and Dettmering, D.: Automated extraction of consistent time-variable water surfaces of lakes and reservoirs based on Landsat and Sentinel-2, Remote Sensing, 11, 1010, https://doi.org/10.3390/rs11091010, 2019.

Selmes, N., Murray, T., and James T. D.: Fast draining lakes on the Greenland ice sheet. Geophys Res Lett, 38, L15501, https://doi. org/10. 1029/2011GL047872, 2011.

Selmes, N., Murray, T., and James, T. D.: Characterizing supraglacial lake drainage and freezing on the Greenland Ice Sheet, The Cryosphere Discuss., 7, 475–505, https://doi.org/10.5194/tcd-7-475-2013, 2013.

Shepherd, A., Hubbard, A., Nienow, P., King, M., McMillan, M., and Joughin, I.: Greenland ice sheet motion coupled with daily melting in late summer, Geophys. Res. Lett., 36, https://doi.org/10.1029/2008GL035758, 2009.

Shepherd, A., Ivins, E. R., A, G., Barletta, V. R., Bentley, M. J., Bettadpur, S., Briggs, K. H., Bromwich, D. H., Forsberg, R., Galin, N., Horwath, M., Jacobs, S., Joughin, I., King, M. A., Lenaerts, J. T. M., Li, J., Ligtenberg, S. R. M., Luckman, A., Luthcke, S. B., McMillan, M., Meister, R., Milne, G., Mouginot, J., Muir, A., Nicolas, J. P., Paden, J., Payne, A. J., Pritchard, H., Rignot, E., Rott, H., Sørensen, L. S., Scambos, T. A., Scheuchl, B., Schrama, E. J. O., Smith, B., Sundal, A. V., van Angelen, J. H., van de Berg, W. J., van den Broeke, M. R., Vaughan, D. G., Velicogna, I., Wahr, J., Whitehouse, P. L., Wingham, D. J., Yi, D., Young, D., and Zwally, H. J.: A reconciled estimate of ice-sheet mass balance, Science, 338, 1183–1189, https://doi.org/10.1126/science.1228102, 2012.

Shimada, R., Takeuchi, N., and Aoki, T.: Inter-annual and geographical variations in the extent of bare ice and dark ice on the Greenland ice sheet derived from MODIS satellite images, Front. Earth Sci., 4, 43, https://doi.org/10.3389/feart.2016.00043, 2016.

Siegert, M. J., Ross, N., and Le Brocq, A. M.: Recent advances in understanding Antarctic subglacial lakes and hydrology, Philosophical Transactions of the Royal Society A: Mathematical, Physical and Engineering Sciences, 374, 20140306, https://doi.org/10.1098/rsta.2014.0306, 2016.

Siegfried, M. R., and Fricker, H. A.: Thirteen years of subglacial lake activity in Antarctica from multi-mission satellite altimetry, Annals of Glaciology, 59, 42–55, https://doi.org/10.1017/aog.2017.36, 2018.

Simonsen, S. B., Barletta, V. R., Colgan, W. T., and Sørensen, L. S.: Greenland Ice Sheet mass balance (1992–2020) from calibrated radar altimetry, Geophysical Research Letters, 48, e2020GL091216, https://doi.org/10.1029/2020GL091216, 2021.

Slater, D. A. and Straneo, F.: Submarine melting of glaciers in Greenland amplified by atmospheric warming, Nat. Geosci., 15, 794–799, https://doi.org/10.1038/s41561-022-01012-2, 2022.

Slater, D. A., Carroll, D., Oliver, H., Hopwood, M. J., Straneo, F., Wood, M., Willis, J. K., and Morlighem, M.: Characteristic depths, fluxes, and timescales for Greenland's tidewater glacier fjords from subglacial discharge-driven upwelling during summer, Geophysical Research Letters, 49, e2021GL097081, https://doi.org/10.1029/2021GL097081, 2022.

Slater, D. A., Straneo, F., Das, S. B., Richards, C. G., Wagner, T. J. W., and Nienow, P. W.: Localized plumes drive front-wide ocean melting of a Greenlandic tidewater glacier, Geophys. Res. Lett., 45, 12,350–12,358, https://doi.org/10.1029/2018GL080763, 2018.

Slater, T., Shepherd, A., McMillan, M. Leeson, A., Gilbert, L., Muir, A., Kuipers Munneke, P., Noel, B., Fettweis, X., van den Broeke, M., Briggs, K.: Increased variability in Greenland Ice Sheet runoff from satellite observations. Nat Commun 12, 6069 (2021). https://doi.org/10.1038/s41467-021-26229-4

Smith, L. C., Andrews, L. C., Pitcher, L. H., Overstreet, B. T., Rennermalm, Å. K., Cooper, M. G.: Supraglacial river forcing of subglacial water storage and diurnal ice sheet motion. Geophysical Research Letters, 48, e2020GL091418, https://doi.org/10.1029/2020GL091418, 2021.

Smith, L. C., Chu, V. W., Yang, K., Gleason, C. J., Pitcher, L. H., Rennermalm, A. K., Legleiter, C. J., Behar, A. E., Overstreet, B. T., Moustafa, S. E., Tedesco, M., Forster, R. R., LeWinter, A. L., Finnegan, D.C., Sheng, Y., Balog, J.: Efficient meltwater drainage through supraglacial streams and rivers on the southwest Greenland ice sheet, PNAS, 112, 4, 1001 – 1006, https://doi.org/10.1073/pnas.1413024112, 2015.

Smith, L. C., Yang, K., Pitcher, L. H., Overstreet, B. T., Chu, V. W., Rennermalm, Å. K., Ryan, J. C., Cooper, M., Gleason, C. J., Tedesco, M., Jeyaratnam, J., Van As, D., van den Broeke, M. R., van de Berg, W. J., Noël, B., Langen, P. L., Cullather, R. I., Zhao, B., Willis, M. J., and Hubbard, A.: Direct measurements of meltwater runoff on the Greenland ice sheet surface, Proceedings of the National Academy of Sciences of the United States of America, 114, E10622–E10631, https://doi.org/10.1073/pnas.1707743114, 2017.

Sneed, W. A. and Hamilton, G. S.: Evolution of melt pond volume on the surface of the Greenland Ice Sheet, Geophys. Res. Lett., 34, L03501, https://doi.org/10.1029/2006GL028697, 2007.

Sneed, W. and Hamilton, G.: Validation of a method for determining the depth of glacial melt ponds using satellite imagery, Ann. Glaciol., 52, 15–22, https://doi.org/10.3189/172756411799096240, 2011.

Sneed, W. D: Bathymetric mapping with passive multispectral imagery, Appl. Opt. 28, 1569-1578, https://doi. org/10.1364/AO.28.001569, 1989.

Sole, A., Mair, D. W. F., Nienow, P. W., Bartholomew, I. D., King, M. A., Burke, M. J., and Joughin, I.: Seasonal speedup of a Greenland marine-terminating outlet glacier forced by surface melt-induced changes in subglacial hydrology, J. Geophys. Res. Earth, 116, F03014, https://doi. org/10. 1029/2010JF001948, 2011.

Sole, A., Nienow, P., Bartholomew, I., Mair, D., Cowton, T., Tedstone, A., and King, M. A.: Winter motion mediates dynamic response of the Greenland Ice Sheet to warmer summers, Geophys. Res. Lett., 40, 3940–3944, https://doi.org/10.1002/grl.50764, 2013.

Sørensen, L. S., Simonsen, S. B., Nielsen, K., Lucas-Picher, P., Spada, G., Adalgeirsdóttir, G., Forsberg, R., and Hvidberg, C. S.: Mass balance of the Greenland Ice Sheet (2003–2008) from ICESat data – the impact of interpolation, sampling, and firn density, The Cryosphere, 5, 173–186, https://doi.org/10.5194/tc-5-173-2011, 2011.

Stevens, L. A., Behn, M. D., Das, S. B., Joughin, I., Noël, B. P. Y., van den Broeke, M. R., and Herring, T.: Greenland Ice Sheet flow response to runoff variability, Geophys. Res. Lett., 43, 11295–11303, https://doi.org/10.1002/2016GL070414, 2016.

Stokes, C. R., Sanderson, J. E., Miles, B. W. J., Jamieson, S. S. R., and Leeson, A, A.: Widespread distribution of supraglacial lakes around the margin of the East Antarctic Ice Sheet, Sci Rep 9, 13823, https://doi. org/10. 1038/s41598-019-50343-57, 2019.

Straneo, F., Sutherland, D. A., Holland, D., Gladish, C., Hamilton, G. S., Johnson, H. L., Rignot, E., Xu, Y., and Koppes, M.: Characteristics of ocean waters reaching Greenland's glaciers, Annals of Glaciology, 53, 202–210, https://doi.org/10.3189/2012AoG60A059, 2012.

Su, J., and Zhang, H.: A fast decision tree learning algorithm, in: Proceedings of the 21st National Conference on Artificial Intelligence, Boston, MA, USA, 16–20 July 2006, Volume 6, 500–505, 2006.

Sundal, A. V., Shepherd, A., Nienow, P., Hanna, E., Palmer, S., and Huybrechts, P.: Evolution of supra-glacial lakes across the Greenland ice sheet, Remote Sens. Environ., 113(10), 2164–2171, https://doi.org/10.1016/j.rse.2009.05.018, 2009.

Suykens, J. A., and Vandewalle, J.: Least squares support vector machine classifiers, Neural Processing Letters, 9, 293–300, 1999.

Tedesco, M. (Ed.): Remote Sensing of the Cryosphere, John Wiley & Sons, Ltd, Chichester, UK, https://doi.org/10.1002/9781118368909, 2015.

Tedesco, M. and Fettweis, X.: Unprecedented atmospheric conditions (1948–2019) drive the 2019 exceptional melting season over the Greenland ice sheet, The Cryosphere, 14, 1209-1223, https://doi.org/10.5194/tc-14-1209-2020, 2020.

Tedesco, M. and Steiner, N.: In-situ multispectral and bathymetric measurements over a supraglacial lake in western Greenland using a remotely controlled watercraft, The Cryosphere, 5, 445–452, https://doi.org/10.5194/tc-5-445-2011, 2011.

Tedesco, M., Box, J. E., Cappelen, J., Fausto, R. S., Fettweis, X., Anderson, J. K., Mote, T., Smeets, C. J. P. P., van As, D., and van de Wal, R. S. W, NOAA Arctic Report Card 2018: Greenland Ice Sheet in Arctic Report Card 2018. Available online: https://arctic.noaa.gov/Report-Card/Report-Card-2018, 2018, last access 13th April 2023.

Tedesco, M., Doherty, S., Fettweis, X., Alexander, P., Jeyaratnam, J., and Stroeve, J.: The darkening of the Greenland ice sheet: trends, drivers, and projections (1981–2100), The Cryosphere, 10, 477–496, https://doi.org/10.5194/tc-10-477-2016, 2016.

Tedesco, M., Fettweis, X., van den Broeke, M. R., van de Wal, R. S. W., Smeets, C. J. P. P., van de Berg, W. J., Serreze, M. C., and Box, J. E.: The role of albedo and accumulation in the 2010 melting record in Greenland, Environmental Research Letters, 6, 014005, https://doi.org/10.1088/1748-9326/6/1/014005, 2011.

Tedesco, M., Moon, T., Anderson, J. K., Box, J. E., Cappelen, J., Fausto, R. S., Fettweis, X., Loomis, B., Mankoff, K. D., Mote, T., Smeets, C. J. P. P., van As, D., and van de Wal, R. S. W. Greenland Ice Sheet in Arctic Report Card 2019; Available online: https://arctic.noaa.gov/Report-Card/Report-Card-2019, 2019, last access 13th April 2023.

Tedesco, M., Mote, T., Fettweis, X., Hanna, E., Jeyaratnam, J., Booth, J. F., and Datta, R.: Arctic cut-off high drives the poleward shift of a new Greenland melting record, Nature Communications, 7, 11723, https://doi.org/10.1038/ncomms11723, 2016.

Tedesco, M., Willis, I. C., Hoffman, M. J., Banwell, A. F., Alexander, P., and Arnold, N. S.: Ice dynamic response to two modes of surface lake drainage on the Greenland ice sheet, Environ. Res. Lett., 8, 034007, https://doi.org/10.1088/1748-9326/8/3/034007, 2013.

Tedesco, M.: Snowmelt detection over the Greenland ice sheet from SSM/I brightness temperature daily variations, Geophysical Research Letters, 34(2), 1-6, ISSN 00948276, doi: 10.1029/2006GL028466, 2007.

Tedstone, A. and Machguth, H.: Increasing surface runoff from Greenland's firn areas, Nature Climate Change 12, 672–676, https://doi.org/10.1038/s41558-022-01371-z, 2022.

Tedstone, A. J., Bamber, J. L., Cook, J. M., Williamson, C. J., Fettweis, X., Hodson, A. J., and Tranter, M.: Dark ice dynamics of the south-west Greenland Ice Sheet, The Cryosphere, 11, 2491–2506, https://doi.org/10.5194/tc-11-2491-2017, 2017.

Tedstone, A. J., Nienow, P. W., Gourmelen, N., Dehecq, A., Goldberg, D., and Hanna, E.: Decadal slowdown of a land-terminating sector of the Greenland Ice Sheet despite warming, Nature, 526, 692–695, https://doi.org/10.1038/nature15722, 2015.

Tedstone, A. J., Nienow, P. W., Sole, A. J., Mair, D. W. F., Cowton, T. R., Bartholomew, I. D., and King, M. A.: Greenland ice sheet motion insensitive to exceptional meltwater forcing, Proc. Natl. Acad. Sci. U.S.A., 110, 19719–19724, https://doi.org/10.1073/pnas.1315843110, 2013.

The Firn Symposium team: Firn on ice sheets, Nat. Rev. Earth Environ., 5, 79–99, https://doi.org/10.1038/s43017-023-00502-0, 2024.

The IMBIE Team.: Mass balance of the Greenland Ice Sheet from 1992 to 2018, Nature, 579, 233-239, https://doi.org/10.1038/s41586-019-1855-2, 2020.

Trusel, L. D., Das, S. B., Osman, M. B., Evans, M. J., Smith, B. E., Fettweis, X., McConnell, J. R., Noël, B. P., and van den Broeke, M. R.: Nonlinear rise in Greenland runoff in response to post-industrial Arctic warming, Nature, 564, 104-108, https://doi.org/10.1038/s41586-018-0752-4, 2018.

Tuckett, P. A., Ely, J. C., Sole, A. J., Booth, A. D., Gourmelen, N., Hawley, R. L., and Cowton, T. R.: Automated mapping of the seasonal evolution of surface meltwater and its links to climate on the Amery Ice Shelf, Antarctica, The Cryosphere, 15, 5785–5804, https://doi.org/10.5194/tc-15-5785-2021, 2021.

Turton, J. V., Hochreuther, P., Reimann, N., and Blau, M. T.: The distribution and evolution of supraglacial lakes on 79° N Glacier (north-eastern Greenland) and interannual climatic controls, The Cryosphere, 15, 3877–3896, https://doi.org/10.5194/tc-15-3877-2021, 2021.

Uddin, S., Khan, A., Hossain, M. E., and Moni, M. A.: Comparing different supervised machine learning algorithms for disease prediction, BMC Medical Informatics and Decision Making, 19, 281, https://doi.org/10.1186/s12911-019-1004-8, 2019.

USGS: Landsat 8 Data Users Handbook, Version 5.0, U.S. Geological Survey, 1–105, https://www.usgs.gov/media/files/lsds-1574l8datausershandbook-v50pdf, 2019.

van As, D., Bech Mikkelsen, A., Holtegaard Nielsen, M., Box, J. E., Claesson Liljedahl, L., Lindbäck, K., Pitcher, L., and Hasholt, B.: Hypsometric amplification and routing moderation of

Greenland ice sheet meltwater release, The Cryosphere, 11, 1371–1386, https://doi.org/10.5194/tc-11-1371-2017, 2017.

Van As, D., Hasholt, B., Ahlstrøm, A.P., Box, J.E., Cappelen, J., Colgan, W., Fausto, R.S., Mernild, S.H., Mikkelsen, A.B., Noël, B.P.Y., Petersen, D. and Van den Broeke, M.R.: Reconstructing Greenland Ice Sheet meltwater discharge through the Watson River (1949-2017), Arctic, Antarctic, and Alpine Research, 50 (1), doi: 10.1080/15230430.2018.1433799, 2018.

van As, D., Hubbard, A. L., Hasholt, B., Mikkelsen, A. B., van den Broeke, M. R., and Fausto, R. S.: Large surface meltwater discharge from the Kangerlussuaq sector of the Greenland ice sheet during the record-warm year 2010 explained by detailed energy balance observations, The Cryosphere, 6, 199–209, https://doi.org/10.5194/tc-6-199-2012, 2012.

van de Wal R. S. W., Boot W., Smeets C. J. P. P., Snellen H., van den Broeke M. R., Oerlemans J., Twenty-one years of mass balance observations along the K-transect, West Greenland. Earth Syst. Sci. Data 4, 31–35, 2012.

van den Broeke, M. R., Enderlin, E. M., Howat, I. M., Kuipers Munneke, P., Noël, B. P. Y., van de Berg, W. J., van Meijgaard, E., and Wouters, B.: On the recent contribution of the Greenland ice sheet to sea level change, The Cryosphere, 10, 1933–1946, https://doi. org/10.5194/tc-10-1933-2016, 2016.

van den Broeke, M., Box, J., Fettweis, X., Hanna, E., Noël, B., Tedesco, M., van As, D., van de Berg, W. J., and van Kampenhout, L.: Greenland Ice Sheet surface mass loss: recent developments in observation and modeling, Curr. Clim. Change Rep., 3, 345–356, https://doi.org/10.1007/s40641-017-0084-8, 2017.

van den Broeke, M., Smeets, P., Ettema, J., van der Veen, C., van de Wal, R., and Oerlemans, J.: Partitioning of melt energy and meltwater fluxes in the ablation zone of the west Greenland ice sheet, The Cryosphere, 2, 179–189, https://doi.org/10.5194/tc-2-179-2008, 2008.

van der Veen, C. J.: Fracture propagation as a means of rapidly transferring surface meltwater to the base of glaciers, Geophysical Research Letters, 34, L01501, https://doi.org/10.1029/2006GL028385, 2007.

van Wessem, J. M., van de Berg, W. J., Noël, B. P. Y., van Meijgaard, E., Amory, C., Birnbaum, G., Jakobs, C. L., Krüger, K., Lenaerts, J. T. M., Lhermitte, S., Ligtenberg, S. R. M., Medley, B., Reijmer, C. H., van Tricht, K., Trusel, L. D., van Ulft, L. H., Wouters, B., Wuite, J., and van den Broeke, M. R.: Modelling the climate and surface mass balance of polar ice sheets using RACMO2 – Part 2: Antarctica (1979–2016), The Cryosphere, 12, 1479–1498, https://doi.org/10.5194/tc-12-1479-2018, 2018.

Vandecrux, B., Mottram, R., Langen, P. L., Fausto, R. S., Olesen, M., Stevens, C. M., Verjans, V., Leeson, A., Ligtenberg, S., Kuipers Munneke, P., Marchenko, S., van Pelt, W., Meyer, C. R., Simonsen, S. B., Heilig, A., Samimi, S., Marshall, S., Machguth, H., MacFerrin, M., Niwano, M., Miller, O., Voss, C. I., and Box, J. E.: The firn meltwater Retention Model Intercomparison Project (RetMIP): evaluation of nine firn models at four weather station sites on the Greenland ice sheet, The Cryosphere, 14, 3785–3810, https://doi.org/10.5194/tc-14-3785-2020, 2020.

Velicogna, I., Mohajerani, Y., A, G., Landerer, F., Mouginot, J., Noël, B., Rignot, E., Sutterley, T., van den Broeke, M., van Wessem, M., and Wiese, D.: Continuity of ice sheet mass loss in Greenland and Antarctica from the GRACE and GRACE Follow-On missions, Geophysical Research Letters, 47, e2020GL087291, https://doi.org/10.1029/2020GL087291, 2020.

Vick-Majors, T. J., Michaud, A. B., Skidmore, M. L., Turetta, C., Barbante, C., Christner, B. C., Dore, J. E., Christianson, K., Mitchell, A. C., and others: Biogeochemical connectivity between freshwater ecosystems beneath the West Antarctic Ice Sheet and the sub-ice marine environment, Global Biogeochemical Cycles, 34, e2019GB006446, https://doi.org/10.1029/2019GB006446, 2020.

Wang, Y., and Sugiyama, S.: Supraglacial lake evolution on Tracy and Heilprin Glaciers in northwestern Greenland from 2014 to 2021, Remote Sensing of Environment, 303, 114006, https://doi.org/10.1016/j.rse.2024.114006, 2024.

Wangchuk, S. and Bolch, T.: Mapping of glacial lakes using Sentinel-1 and Sentinel-2 data and a random forest classifier: Strengths and challenges. Sci. Remote Sens., 2, 100008, https://doi.org/10.1016/j.srs.2020.100008, 2020.

Weertman, J.: Catastrophic glacier advances, in: Symposium of Obergurgl – Variations of the Regime of Existing Glaciers, International Association of Scientific Hydrology, 31–39, 1962.

Williamson, A. G., Banwell, A. F., Willis, I. C., and Arnold, N. S.: Dual-satellite (Sentinel-2 and Landsat 8) remote sensing of supraglacial lakes in Greenland, The Cryosphere, 12, 3045–3065, https://doi.org/10.5194/tc-12-3045-2018, 2018a.

Williamson, A. G., Willis, I. C., Arnold, N. S and Banwell, A. F.: Controls on rapid supraglacial lake drainage in West Greenland: An Exploratory Data Analysis approach. Journal of Glaciology, 64(244), 208-226, https://doi.org/10.1017/jog.2018.8 2018b.

Williamson, A., Arnold, N., Banwell, A., and Willis, I.: A Fully Automated Supraglacial lake area and volume Tracking (“FAST”) algorithm: Development and application using MODIS imagery of

West Greenland, Remote Sens. Environ., 196, 113–133, https://doi.org/10.1016/j.rse.2017.04.032, 2017.

Williamson, A.: Full source code for the Fully Automated Supraglacial lake Tracking at Enhanced Resolution (“FASTER”) algorithm, version 1 [software], https://doi.org/10.17863/CAM.25769, 2018.

Woollings, T., Barriopedro, D., Methven, J., Son, S.-W., Martius, O., Harvey, B., Sillmann, J., Lupo, A., and Seneviratne, S. I.: Blocking and its response to climate change, Current Climate Change Reports, 4, 287–300, https://doi.org/10.1007/s40641-018-0108-z, 2018.

Wu, R., Liu, G., Zhang, R., Wang, X., Li, Y., Zhang, B., Cai, J., and Xiang, W.: A Deep Learning Method for Mapping Glacial Lakes from the Combined Use of Synthetic-Aperture Radar and Optical Satellite Images. Remote Sens., 12, 4020, https://doi.org/10.3390/rs12244020, 2020.

Xu, H.: Modification of normalised difference water index (NDWI) to enhance open water features in remotely sensed imagery, International Journal of Remote Sensing, 27, 3025–3033, https://doi.org/10.1080/01431160600589179, 2006.

Yang, K., and Smith, L. C.: Supraglacial Streams on the Greenland Ice Sheet Delineated From Combined Spectral–Shape Information in High-Resolution Satellite Imagery, IEEE Geoscience and Remote Sensing Letters, 10(4), 801-805, https://doi. org/10. 1109/LGRS. 2012. 2224316, 2012.

Yang, K., Smith, L. C, Chu, V. W., Pitcher, L. H., Gleason, C. J., Rennermalm, A. K., and Li, M: Fluvial morphometry of supraglacial river networks on the southwest Greenland Ice Sheet, GIScience and Remote Sensing, 53:4, 459-482, https://doi. org/10. 1080/15481603. 2016. 1162345, 2016.

Yang, K., Smith, L. C., Cooper, M. G., Pitcher, L. H., Van As, D., Lu, Y., Lu, X., and Li, M.: Seasonal evolution of supraglacial lakes and rivers on the southwest Greenland Ice Sheet, Journal of Glaciology, 67, 592-602, https://doi.org/10.1017/jog.2021.10, 2021.

Yang, K., Smith, L. C., Sole, A., Livingstone, S. J., Cheng, X., Chen, Z., and Li, M.: Supraglacial rivers on the northwest Greenland Ice Sheet, Devon Ice Cap, and Barnes Ice Cap mapped using Sentinel-2 imagery, Int. J. Appl. Earth Obs., 78, 1–13, https://doi.org/10.1016/j.jag.2019.01.008, 2019.

Yuan, J., Chi, Z., Cheng, X., Zhang, T., Li, T., and Chen, Z.: Automatic Extraction of Supraglacial Lakes in Southwest Greenland during the 2014–2018 Melt Seasons Based on Convolutional Neural Network. Water, 12, 891, https://doi.org/10.3390/w12030891, 2020.

Zhang, W., Yang, K., Smith, L. C., Wang, Y., van As, D., Noël, B., Lu, Y., Liu, J.: Pan-Greenland mapping of supraglacial rivers, lakes, and water-filled crevasses in a cool summer (2018) and a warm summer (2019), Remote Sensing of Environment, 297, 113781, https://doi.org/10.1016/j.rse.2023.113781, 2023.

Zhang, Y., Song, Z., Lin, Y., Shi, Q., Hao, Y., Fu, Y., Wu, J., and Zhang, Z.: Predicting mechanical properties of CO2 hydrates: Machine learning insights from molecular dynamics simulations, Journal of Physics: Condensed Matter, 36, 015101, https://doi.org/10.1088/1361-648X/acfa55, 2024.

Zhu, D., Zhou, C., Zhu, Y., and Peng, B.: Evolution of supraglacial lakes on Sermeq Avannarleq glacier, Greenland using Google Earth Engine. J. Hydrol. Reg. Stud., 44, 101246, https://doi.org/10.1016/j.ejrh.2022.101246, 2022.

Zwally, H. J., Abdalati, W., Herring, T., Larson, K., Saba, J., and Steffen, K.: Surface melt-induced acceleration of Greenland ice-sheet flow, Science, 297, 218-222, https://doi.org/10.1126/science.1072708, 2002.